UNIVERSITY OF LEICESTER

DOCTORAL THESIS

Spectral Analysis of GRBs Observed by *Swift* and *Fermi* Satellites

---

Author:
Eman M. Moneer

Supervisors:
Prof. Paul O'Brien
&
Prof. Richard Willingale

A Thesis Submitted in Fulfillment of The Requirements for The Degree of Doctor of Philosophy

At The University of Leicester.

X-ray and Observation Astronomy Group (XROA)
Physics and Astronomy Department

December 9, 2019

Declaration of Authorship

I, Eman MONEER, declare that this thesis titled, "Spectral Analysis of GRBs Observed by *Swift* and *Fermi* Satellites" and the work presented in it are my own. I confirm that:

- This work was done wholly or mainly while in candidature for a research degree at this University.
- Where any part of this thesis has previously been submitted for a degree or any other qualification at this University or any other institution, this has been clearly stated.
- Where I have consulted the published work of others, this is always clearly attributed.
- Where I have quoted from the work of others, the source is always given. With the exception of such quotations, this thesis is entirely my own work.
- I have acknowledged all main sources of help.
- Where the thesis is based on work done by myself jointly with others, I have made clear exactly what was done by others and what I have contributed myself.

Signed:

Date:

UNIVERSITY OF LEICESTER

Abstract

Eman M. Moneer
Physics and Astronomy Department

Doctor of Philosophy

Spectral Analysis of GRBs Observed by *Swift* and *Fermi* Satellites

by Eman MONEER

Gamma-ray bursts (GRBs) one of the most energetic phenomena in the Universe that have been observed in distant galaxies. For the short period of time generally less than 30s, GRB can release energy about 10^{54} erg. The intense radiation of most observed GRBs is thought to be released within a massive explosions 'supernovae' that are associated with the most catastrophic stellar events that ever detected to form a neutron star or a black hole. Two types of GRBs (long/short) are associated with different emission processes. Studying the GRB spectral analysis of a joint fit time-integrated or time-resolved spectra assist to investigate further spectral properties, via two observatories *Swift* and *Fermi*. The thesis chapter outlines two different spectral joint fit analysis with the time-integrated and the time-resolved spectra as applied to two datasets. Two spectral models are used throughout this analysis, namely the low-energy power law with an exponential high-energy cutoff (CPL) and the Band function (Band). The joint-fit shows a significant difference in the spectral parameters compared to the GBM-only. Resulting that, adding *Swift* (BAT) data obtained a higher E_{peak} and a softer α than what it found when applying *Fermi* (GBM-only). The evolution of E_{peak} is discussed for the spectral joint-fit time-resolved spectra, and found that the E_{peak} evolution follow two trends; the hard-to-soft ratio and the intensity-tracking trend. A further interesting area of study is the Amati ($E_{peak,rest} - E_{iso,\gamma}$) and Yonetoku ($E_{peak,rest} - L_{iso,\gamma}$) relations, which are examined to investigate whether these two relations are in general agreement with the analysis given herein. A strong Amati relation was found for the time-integrated data, whereas the time-resolved Amati relation data was scattered above the Amati best fit. The Yonetoku relation was found to show a few scattered data shifted towards lower luminosity, $L_{iso,\gamma}$, in the time-integrated spectra, whilst showing a good correlation for the time-resolved spectra. Fermi (GBM+LLE) joint-fit analysis provides high-quality data through which to search for such a cutoff, E_c, from the LLE high energy bands (30 MeV - 130 MeV), and hence estimate Lorentz factor Γ for three GRBs in the sample.

Acknowledgements

Firstly, I would like to express my sincere thanks to my supervisor Prof.O'Brien and Prof. Willingale for the continuous support, patience and kindness. Their guidance helped me throughout my research and the writing up of this thesis. I really appreciate every single moment they spent time with me answering my questions and clearing up misconceptions. Without their great support, it would not be possible to conduct this research.

It's a pleasure to thank my thesis committee: Prof. Kobayashi Shiho and Dr. Starling Rhaana, for their valuable comments and encouragements, with their intelligent questions that increased my awareness from various perspectives. My gratefulness goes to Dr. Kim for teaching me the technicalities of *Swift* data and for her kind manner and generous time given when I first arrived. I am also extremely grateful to Dr. Gor Ogansyain for his support and help during my last year.

My thanks also go to the XROA IT services for their help in technical computer issues. A special thanks to Mark Mahabir who helped me set up the spectral fitting programs and other useful tools for my data analysis.

I would like to express my thanks to the doctoral college of the University of Leicester for their guidance and support throughout my four years there. My thesis will not be as polished without the final touches of Dr. Mark Watkins for his help with proofreading this thesis.

I dearly thank my friends and colleagues in Princess Nourah Bint Abdulrahman University (PNU) in Riyadh, Saudi Arabia for their help and support, and the Ministry of Higher Education for providing me the opportunity to continue my studies and the chance to be awarded my Ph.D degree. Thanks to the royal embassy of Saudi Arabia Cultural Bureau in London for their aid.

Lastly, my deep gratitude to my lovely husband for his extreme support spiritually throughout these years and to my children who I have been away from for half of this journey. A special thanks to my parents for everything they provided for me, it was more than I ever wished for. I dedicate this milestone to them. And I am forever indebted to my sister Sarah for accompanying me all these years.

I cannot express my happiness and gratitude towards finally arriving at the end of this tiring yet rewarding journey. I can honestly say from beginning to end, I faced a lot of setbacks and hardships that at the time felt impossible to overcome, but with the strength provided by Allah and the constant support from the amazing people in my life, I can finally say I arrived.

Contents

List of Figures

List of Tables

Chapter 1

Introduction

1.1 Gamma-Ray Bursts (GRBs) Overview

Sudden flashes of gamma-ray photons, or Gamma Ray Bursts (GRBs), are the most luminous events in the Universe, briefly releasing very high energies on very short timescales. GRBs are one of the most debated of astrophysical objects, not least because their emission mechanism is still, to a greater extent, a matter of conjecture. The discovery of GRBs (Klebesadel et al., 1973a) has opened a new field of science that has enabled astronomers to better understand the nature of the Universe. Several of the physical properties of the electromagnetic radiation arising from GRBs have been investigated and explained through a variety of experiments. Astronomers believe that GRBs are the result of catastrophic events involving massive compact objects, perhaps stellar mass black holes (BHs). GRB events are classified as being either long (lasting > 2 s) or short (lasting < 2 s), with long GRBs (LGRBs) believed to be associated with the deaths of collapsed massive stars (Woosley 1993; MacFadyen & Woosley 1999), whilst short GRBs (SGRBs) more likely to be the result of either the merger of binary neutron stars (NSs) or the merger of a neutron star with a black hole (Li & Paczyński 1998; Metzger et al. 2010; Metzger & Berger 2012;Kasen et al. 2013;Tanvir et al. 2013). GRBs are considered amongst the most extreme transient phenomena ever detected, a few examples of which are summarized below:

• GRBs are typically the most luminous objects observed (e.g., LGRB $\sim 10^{52}$ erg s^{-1}). The associated flux can be hundreds of times brighter than that of a supernova.

• The majority of the associated energy is released over a very short timescale, typically a few milliseconds to hundreds of seconds in the observer frame, in a phase known as the *prompt emission* in which the radiation emitted is primarily in the gamma ray region and peaks at energies ranging from a few keV to tens of MeV. Usually, the prompt emission is followed by an afterglow phase, which extends to longer wavelengths (from X-ray to optical and beyond, and which can be observed over a few days to several months).

• Because GRBs are extremely luminous, they are detectable even at extreme cosmological distances. GRBs emit intense beams that move toward the observer with an opening angle of 3-30 degrees (Frail et al. 2001; Ghirlanda et al. 2004a). Most GRB events have been observed as arising in distant star-forming galaxies (Zhang & Mészáros, 2004). Not all GRBs have a

measured redshift, but the highest redshifts currently recorded are for GRB 090429B at z = 9.4 (Cucchiara et al., 2011) and GRB 090423 at z = 8.2 (Tanvir et al., 2009); in general, GRB redshifts range from z = 0.0085 to z = 9, with a mean value of $\sim$ 2.4 (Jakobsson et al., 2006).

• The very high luminosity of GRBs arises from a high relativistic bulk motion with a high Lorentz factor Γ (in the order of a few hundred), as inferred due to the highly variable non-thermal emission.

There are many different aspects to GRB studies, some emphasizing an understanding of the GRB mechanism, others investigating various properties using GRBs as tools, e.g., the cosmological formation of stars using GRBs as indicators. The primary aspect is to study the prompt emission and the afterglow phases in order to investigate the physics of GRBs. In prompt emission, the durations of GRBs are variable and their time profiles are complex and distinct; furthermore, they can be observed to vary on timescales of milliseconds (section 1.2.1) (Bhat et al. 1992; Fishman & Meegan 1995; Koshut 1996). This variability exists whether a burst is classified as a SGRB ($<$ 2 s) or a long GRBs ($>$ 2 s). The duration of GRBs are characterized by two parameters: T_{90}, which includes the range from 5% to 95% of the integrated counts, or T_{50} which includes 25% to 75% (Kouveliotou et al., 1993).

Upon a catastrophic event such as those described above, an energetic jet is accelerated, while a relativistic prompt emission phase, this is possibly due to internal shocks within the jet in the fireball (Kobayashi et al., 1997). These shocks occur when two shells of material, as launched by the central engine, collide. While the internal shock travels outward, an external shock is formed due to the interaction between the ejecta and the surrounding cosmic medium. Accelerated electron shocks are believed to emit energy via synchrotron radiation, forming an afterglow (Katz 1994; Tavani 1996; Tavani 1997).

In contrast with the prompt emission, afterglows have been more widely studied and their data are well described by the "fireball" model (see, Mészáros & Rees 1997a; Reichart 1997; Waxman 1997; Vietri 1997; Tavani 1997; Wijers et al. 1997). After four decades of GRB investigations, some outstanding studies have been published that have attempted to unravel the mysteries of GRB prompt emission mechanisms and their progenitors, though various models of such have been suggested (e.g., Mészáros et al. 1994; Rees & Mészáros 1994a; Thompson 1994; Daigne & Mochkovitch 1998; Pilla & Loeb 1998; Medvedev & Loeb 1999; Piran 1999; Lloyd & Petrosian 2000; Ghisellini et al. 2000; Panaitescu & Mészáros 2000; Spruit et al. 2001; Zhang & Mészáros 2002; Pe'er & Waxman 2004a; Ryde 2004; Ryde 2005; Rees & Mészáros 2005; Pe'er et al. 2005; Pe'Er et al. 2006).

Together, *Swift* and *Fermi* help us to understand the physics of GRB emission and to maximise the scientific returns from such studies. *Swift* can detect GRBs with its very high sensitivity detectors over a large field of view, and can provide accurate GRB localization to enable redshift measurements. *Fermi* provides high-quality and high-resolution data across a wide range of energies extending to the tens of MeV. However, *Fermi* (LAT) data have suggested that in the high

energy domain beyond 100 MeV (e.g., Beniamini et al. 2011; Ackermann et al. 2012), most GRBs do not show strong emission.

1.2 GRB Theoretical Models

1.2.1 The Fireball Concept

Understanding the physics of GRBs and describing their models is one of the most debated subjects in astronomy. Different models exist, and each has its own particular characteristics to explain GRB observational signatures. Due to the general difficulties encountered in understanding GRB mechanisms and their high-energy radiations over cosmological distances, scientists have developed theoretical models that attempt to explain two main aspects of GRBs: first, what causes the prompt gamma ray and afterglow emission? and secondly, what is the progenitor energy source? For the GRB progenitor, there are two leading models for LGRBs and SGRBs: the core collapse of a massive star and the merger of binary neutron stars (NSs) or a neutron star with a black hole (NS-BH), respectively.

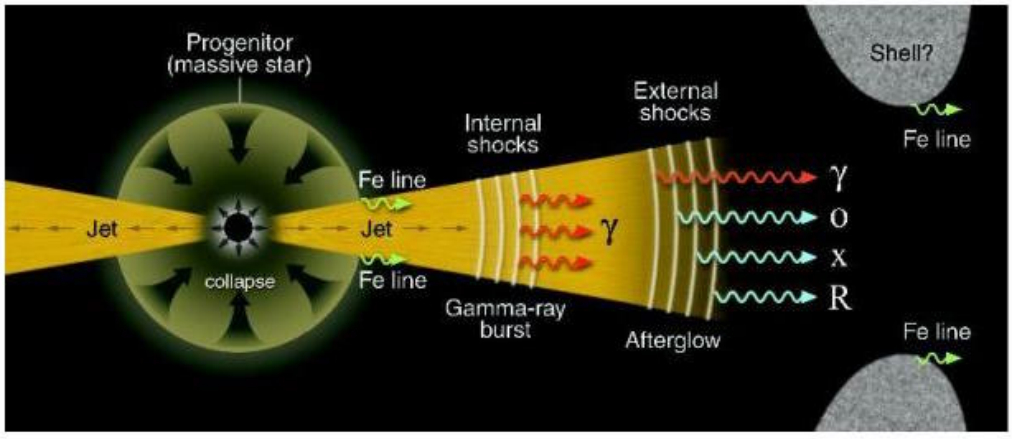

Figure 1.1: Schematic GRB of the fireball model showing the prompt emission and the afterglow during the jet, resulting from a relativistic jet with the internal shock and external shock. Iron lines 'Fe' may arise from X-ray illumination of a pre-ejected shell, for example a supernova remnant. This figure has been adapted from Mészáros (2001).

After the discovery of GRBs, the so-called "compactness problem" (Schmidt 1978; Ruderman & Sutherland 1975) was extensively discussed. The compactness problem is that the observed variability timescale ($\delta T \sim 1$ ms) of the prompt emission implies that the source emitting region is compact, with a linear dimension of $\delta R \sim c\delta T \sim 300$ km, and thus that its radius must be small at $\sim 10^{10}$ cm. However, the observed luminosity at cosmological distances indicates that at the source the high-energy photon density becomes extremely high ($\geq 10^{51}$ erg) in just

few seconds; in other words, the compactness problem is that the small size implied by the variability combined with the high photon density should result in a thermal spectrum. This rapid and intense energy release in a compact region can indeed form a very high energy ($\geq$ MeV) fireball (Paczynski 1986; Goodman 1986). As the fireball is essentially an optically thick plasma made of electron-positron pairs, radiation and a small number of baryons fill the surroundings of the central engine. This should result in a thermal spectrum, whereas a non-thermal spectrum is observed.

The solution to this problem can be found by considering a relativistic expansion of the fireball where the source moves relativistically with a Lorentz factor $\Gamma = 10^2$ (e.g., Fenimore et al. 1993a) for two reasons; i) the compactness condition becomes: the emission radius can be as large as $R < c\Gamma^2\delta t$ which introduce an additional factor of Γ^{-2} in the expression of $\tau_{\gamma\gamma}$, which is decreased by a factor of $\sim \Gamma^{2(\alpha+1)}$ since the typical $\alpha \sim 2$ - 3, this is generally implies $\Gamma > 100$ in order to have $\tau_{\gamma\gamma} < 1$ and to overcome the compactness argument. ii) the energy of the photons in the rest frame should be smaller by a factor of Γ, thus only a small fraction can create pairs, and the optical depth $\tau < 1$ provided that $\Gamma > 100$. As the optical depth decreases, the pair production becomes inefficient. This is again required that the emission radius should be large at about 10^{14} cm from the central engine suggesting that the emission occurs in an optically thin region which is above the photosphere. This is particularly required by the slow component pulses and the typical Lorentz factor Γ that is imposed from GRB observations by the observed duration (Uhm & Zhang, 2016).

One of a number of models that explains and develops GRB properties from a theoretical standpoint is derived from the concept of an opaque plasma, which has a small mass in the rest frame compared with its initial energy (Piran, 1999). Cavallo & Rees (1978), Goodman (1986) and Paczynski (1986) demonstrated that the fireball model is applicable to GRBs, which occurs as a result of the massive number of (gamma ray) photons being released by the outflow from a compact region leading to the formation of an optically thick fireball via electron-positron pair production. This model is widely used for predicting GRB properties.

The main prediction of the fireball model is when the expanding plasma becomes optically thin and hence the emitted radiation escapes within the burst formation. As noted above, this mechanism would generate a quasi-thermal spectrum rather than the observed power-law spectra, thus indicating the difficulty inherent to explaining the duration of the GRB having such a small timescale (just a few seconds). Moreover, the fireball baryonic load is another model (Shemi & Piran 1990; Paczynski 1990) which converts all its energy into kinetic energy rather than into luminosity to produce a quasi-thermal spectrum. This model, however, does not explain the efficient production of radiation.

Rees & Mészáros (1992) and Mészáros & Rees (1994) have argued that the process of reconverting the baryonic kinetic energy into heat that is hence radiated as gamma rays essentially

results in the fireball shock model, which is believed to occur in the outflow. The fireball-shock expansion is believed to have two phases: a matter-dominated, and a radiation-dominated phase. The assumption that the fireball is matter-dominated is widely used, and which consists of baryons, electrons and positrons, and photons resulting from the merger of binary neutron stars (Narayan et al., 1992) or a collapse of massive stars (Narayan et al. 1992; Woosley 1993). The emitted energy is higher than the mass of the baryon in the rest frame by a factor of ~ 100, with the baryon accelerated within an expanding fireball to a higher Lorentz factor, Γ. During this process, two major outcomes can be seen: at the photosphere, a fraction of the thermal energy is radiated away and the accelerated electrons produce a non-thermal gamma ray spectrum by a synchrotron or an IC processes in the internal shock at large jet radius. Rather, the outflows that form from the central engine are believed to be dominated by Poynting flux (e.g., Usov 1994; Katz 1997; Mészáros & Rees 1997b; Lyutikov & Blandford 2003; Zhang & Yan 2011a).

The shocks in the fireball model are collisionless, whereby the particles involved are accelerated and scattered within the *Fermi* process when crossing the shock interaction (Blandford & Eichler, 1987). This can result in the type of energy distribution that can be described by a power law ($\alpha \sim 2$ - 3). In such a situation, the electrons emit a non-thermal radiation of photons via two different mechanisms, synchrotron and IC, that extend to very high energy (GeV bands). There are two kinds of shock dissipation models, the external and internal shock models (Rees & Mészáros, 1992) and (Rees & Mészáros, 1994a), which successfully interpret the low-energy "afterglow" and the high-energy "prompt emission", respectively. In particular, the origin of the emission associated with the two phases is produced by two different mechanisms.

1.2.2 Dissipation Processes

I. External Shock

Due to its interaction with the interstellar medium (ISM), the expanding fireball decelerates and hence produces an external shock (Rees & Mészáros 1992; Mészáros & Rees 1993). Any model developed for this process had to be capable of describing a burst lasting a few tenths of a second. Generally, this model did seem be able to explain the type of GRB light curves observed, which show simple and smooth light curves resulting from a single pulse (Fenimore et al. 1996; Sari & Piran 1997; Panaitescu & Mészáros 1998). However, many GRBs show a very complex light curve across highly variable timescales whose durations could last up to ~ 100 s. This time variability may be the case where the external shock is difficult to explain; the internal shock model was later suggested by (Rees & Mészáros, 1994a) to resolve the time variability issue.

In fact, the external shock model has seen some considerable success in explaining the afterglow emission, which is significant in the sense that this is a direct extension of GRB activity. Emission of GRBs might also be expected to be associated with the relativistic jet through their interaction with the ISM, resulting in a much less variable timescale at a radius of $\sim 10^{17}$ cm. (In the external shock phase other shocks are generated, namely the forward shock and the reverse

shock.) The forward shock is highly relativistic, propagating into the external medium. It produces a prompt hard spectrum that shows an evolution of the power law that with time produces an optical, and then a radio spectrum. The reverse shock, however, moves back into the fireball (Rees & Mészáros, 1993). When deceleration becomes significant and external matter is swept up by the fireball, at some later time a reverse shock will start and the fireball then reconverts its small amount of the kinetic energy into thermal energy (Rees & Mészáros, 1992).

The reverse shock is not generally sufficient to slow down the fireball to any significant degree as it usually very weak. Moreover, in both shocks, the kinetic energy of the outflow dissipates when the ejecta is decelerated by the surrounding medium. The candidate observation for the reverse shock is believed to be associated with an optical flash (e.g., Sari & Piran 1999a, Sari & Piran 1999b; McMahon et al. 2006).

II. Internal Shock

The internal shock is produced within the GRB jet due to its gradient velocity being non-zero. This model is believed to produce a prompt GRB emission, and it was first introduced to explain the short timescale variability which occurs on the millisecond timescale that is seen in the prompt GRB light curves. This short timescale variability, as seen in GRB light curves and afterglows, is not easy to explain in terms of the external shock as a result of special relativistic effects (Fenimore et al. 1996; Sari & Piran 1997; Fenimore 1998).

In the particular scenario of prompt emission when the central engine is intermittent, there are a number of energy releases produced within the fireball which consequently lead to large-velocity variations within the outflow. Hence multiple shells can be emitted from the central engine. In fact, relativistic baryonic outflow speeds where the Γ is effectively time-independent, etc., are required to create the shock, which occurs when a fast-moving shell (e.g., the fireball ejecta) overtakes a slower-moving one in the comoving frame, and multiple shocks occur during the outflow at a radius of $\sim 10^{13}$ cm from the central engine (Mészáros & Rees 1993; Kobayashi et al. 1997; Sari & Piran 1997; Daigne & Mochkovitch 1998). The internal shock radius should be large, and hence the optical depth for pair production will be less than unity $\tau_{\gamma\gamma} < 1$. In particular, the photon emission associated with the internal shock scenario can explain the conversion of the vast kinetic energy of the outflow (baryonic jet) into the internal energy of non-thermal (gamma ray) particles (Narayan et al. 1992; Rees & Mészáros 1994b; Kumar 1999; Kobayashi & Sari 2001) via synchrotron and Inverse Compton (IC) processes.

This model is favoured because of its simplicity and ability to explain both the GRB prompt emission phase and its duration; other advantages are the natural appearance of internal shocks in the baryonic outflow, and the fact that it provides an excellent explanation for the diverse and variable light curves observed during the prompt emission phase. This is due to the small separation between the internal shock and the central engine. Nevertheless, a disadvantage of

this model is its inability to explain the observed spectrum, such as the spectral photon index below the peak (e.g., Piran 1999; Mészáros 2002; Zhang & Mészáros 2004; Mészáros 2006a). Figure 1.1 shows a schematic of the model of an ultra-relativistic fireball being emitted from the central engine (Goodman 1986; Paczynski 1986).

III. Magnetic Reconnection

In contrast to the internal shock model, which has been discussed comprehensively in the literature, magnetic reconnection is still poorly studied and understood. There are two different reconnection models, which have been reviewed by Beniamini & Granot (2016). The first model is associated with a quasi-spherical thin reconnection, while the second invokes relativistic turbulence (Lyutikov & Blandford 2003; Kumar & Narayan 2009; Lazarian et al. 2009; Inoue et al. 2011; Zrake 2014; Zrake & East 2016a; Lazarian et al. 2015; East et al. 2015; Zrake & East 2016b). Assuming GRBs emission is generated by magnetic reconnection, consider the relativistic bulk motions produced in the rest frame of the jet. A model of quasi-spherical thin reconnection layers between different regions of a reverse magnetic field is suggested when the magnetic field (produced away from the source) is perpendicular to the radial direction. From the emission region of the central source, the energy is achieved either in the form of baryonic jets (kinetic energy) (Shemi & Piran, 1990) or from Poynting flux "highly magnetized" (Usov 1992; Thompson 1994; Mészáros & Rees 1997; Lyutikov & Blandford 2003; Granot et al. 2015). With regards to the magnetic reconnection mechanism that is dominated by Poynting flux in any relativistic outflow jets, a possible magnetic reconnection appears when there is a high magnetization parameter outwith the reconnection region that remains in the outflow. Thus, the plasma holds the inflow within the reconnection layer.

1.2.3 Radiative Processes

I. Synchrotron Radiation

Synchrotron emission is the non-thermal radiation produced when a relativistic electron gyrates in a magnetic field. Synchrotron radiation can explain the GRB prompt emissions, and is considered to be one of the more important mechanisms in various astrophysical phenomena. The synchrotron shock mechanism, which is produced by the optically thin plasma in a weak magnetic field, can be used to predict the form of the observed spectra (Tavani 1996; Sari et al. 1998).

Synchrotron emission can be classified as having two regimes: the "fast-cooling" phase, which describes when the timescale for the cooling of the electrons is shorter than the dynamical lifetime of the source, resulting in an electron that cools quickly compared to the low-level injection of energy; conversely, "slow-cooling" occurs when the timescale for the cooling of the electrons is longer than the dynamical lifetime of the source (Sari et al. 1998; Wijers & Galama 1999). The differences between these two regimes are associated with the emission's radiative

timescale. The peak frequency, the cooling frequency, and the self-absorption frequencies set the characteristic break frequencies in the synchrotron spectra. These frequencies evolve with time; indeed, their evolution is reflected in the complexities observed in the shapes of the light curves at certain band energies (Sari et al. 1998; Wijers & Galama 1999). This model can successfully describe the afterglow. Thus, the optically thin synchrotron spectrum is currently considered the best spectral fitting model for most GRBs. The first synchrotron model was applied to the spectral fitting of GRBs by Tavani (1996), and subsequently by Baring & Braby (2004).

II. Synchrotron Self-Compton

Inelastic collisions between low-energy photons and ultra-relativistic electrons are known as the IC processes (e.g., Mészáros et al. 1994; Pilla & Loeb 1998; Razzaque et al. 2004; Pe'er & Waxman 2004b; Pe'er & Waxman 2005; Pe'er et al. 2005; Pe'Er et al. 2006). Each astrophysical source has an Synchrotron Self-Compton (SSC) scattering component when the synchrotron radiation that energizes it provides the means to scatter its seed photons to high energies and across a large frequency range. Thus, the phenomenon responsible for creating high-energy emissions from GRBs and other astrophysical sources is accepted to be the SSC mechanism. The SSC mechanism, while complex, uses a simple power-law function to explain the injected electron spectrum. The SSC spectrum can be described precisely as carrying out a complicated seed photon spectrum convolution and electron energy distribution. In certain circumstances, the GRB spectrum can be modelled as an SSC component at very high energy $\sim$10 MeV (Sari et al. 1996).

III. Thermal Components

In equilibrium, a black body must radiate as much energy as it absorbs, and thus it emits radiation at maximum energy for a given proper temperature. Black body radiation is emitted in an omnidirectional manner, and is defined in terms of intensity as a function of temperature. In spite of the success of the phenomenological Band function (Band et al., 1993) in describing a majority of GRB spectra, this model faces some difficulties, the main problem being when considering the emission source. It is known that GRB spectra are non-thermal and produced by synchrotron emission; however, about $\sim$ one-third of GRBs show low-energy slopes that are hard to constrain using this model (see, Oganesyan et al. 2017). In the late 1990s, several studies suggested that at least some of the observed sources could be not be entirely synchrotron-based, but contained a "thermal component"; an investigation of the occurrences of the thermal component was conducted by Ryde (2004), where using a sample of just a few GRBs they were able to show a thermal temperature evolution resulting in hard spectra. Another study by Ryde & Pe'Er (2009) was subsequently carried out but with a larger LGRB sample for spectral analysis. It was suggested that $\sim$ 30% to $>$ 50% of the energy released in the prompt emission phase (in the observed 25–1900 keV energy band) was through thermal photons.

In fact, the thermal component found in the prompt emission is in agreement with the predicted theoretical model of photon emission produced in the photosphere. Therefore, studying thermal emission has led to a better characterization of the photosphere radius. In general, the majority of the flux from a GRB that is produced in the internal shock region is predicted to be emitted as thermal emission (Goodman 1986; Paczynski 1986).

The thermal component is initially black body in nature and can also be emitted when the internal shock emission is thermalized, whilst the outflow is still optically thick and emitted as a black body at the photosphere, and is formed as black body radiation in the fireball regime. The thermal component is emitted when the jet becomes optically thin at a radius equivalent to the photosphere shell.

1.3 GRBs Observational Properties

1.3.1 Prompt Emission

In spite of the early discovery of GRB prompt emission and their intense investigation over several decades, evidence of the origins of GRB prompt emission are still the subject of considerable debate. This is due to their very small variability in timescale, with a typical duration of only a few seconds without repetition (Pe'er & Casella, 2009). The source of the confusion around GRB prompt emissions is related to the understanding of the particle radiation mechanism, the energy dissipation mechanism, and the particle acceleration mechanism. The broadband high-energy observations from *Fermi* have opened a new window to solving some of the currently unanswered questions in these areas. *Fermi* LAT, for example, has allowed for intense theoretical investigations that have helped to understand the origins of GRB prompt emission. The prompt emission most likely originates from internal dissipation of energy in the fast outflow, which can take place effectively by internal shock and magnetic dissipation. It is believed to be the direct emission outflow ejected from the central engine, as per the "fireball" model, which deposits its gravitational energy into a thermal explosion (Goodman 1986; Paczynski 1986). In other words, the prompt emission occurs when the kinetic energy from a catastrophic explosion event, such as massive star core collapse or the merger of two compact stars, is converted into electromagnetic radiation due to the internal shocks that result from collisions between shells of ejecta (Rees & Mészáros, 1994b). The result is that the fireball expands due to the effects of thermal pressure and is then accelerated to relativistic speeds, where the thermal energy is ultimately released in the form of photons at the photosphere. In the internal shock case, the dissipation happens inside the ejecta, where the ejecta is decelerated by the surrounding medium and this deceleration happens after the internal shock phase (internal dissipations are expected to happen without the deceleration). The deceleration by the surrounding medium causes the external shocks and afterglow. In particular, the origin of the bursts associated with the two phases,

namely the prompt emission and afterglow (gamma-ray and optical), respectively, produce two different emission mechanisms. The GRB fireball is believed to be dominated by matter, the basis for which is that GRB are phenomenologically dominated by electromagnetic (EM) radiation. A few baryons are injected from the central engine. The central engine emits a few baryons, thus there is a very high ratio of either Poynting flux and matter flux or comoving magnetic energy density and rest mass energy density, where these ratios are known as σ, which should be very high at the deceleration radius $(10^5 - 10^6)$ (Giannios et al. 2008; Zhang & Yan 2011b). Thus $\sigma > \Gamma^2 - 1$ (the sub-Alfvenic condition, when magnetic field-dominated flow can be highly relativistic) is satisfied, where Γ is the Lorentz Factor. In this scenario, there are two kinds of fireball/jet models: conventional baryonic jet model and Poynting-flux dominated (magnetised) jet model. In the former case, the fireball is initially radiation dominated and it includes a small number of baryons. As the fireball expands due to the thermal pressure, the thermal/radiation energy is converted to the kinetic energy of the baryons. In this model, the sigma parameter is zero in the prompt gamma-ray and afterglow phase. However, if the jet is magnetized (the latter model), the sigma parameter can be high in the prompt gamma-ray and afterglow phase. Magnetic reconnections might play a role in the production of prompt gamma-rays. If $\sigma > 0.1$ at the deceleration radius, the magnetic pressure is likely to suppress the formation of a reverse shock and optical flash. How high the σ parameter is in the GRB emission region is dependent on the radius R_{GRB} (where R is the distance from the centre of explosion where the magnetic energy is being dissipated), but from which it is very difficult to estimate the GRB location. The radius R_{GRB} and the value of σ are dependent parameters. The various observed aspects of GRB prompt emission, such as GRB light curves, characterization of GRB spectra and peak energy E_{peak}, need to be successfully interpreted to classify a model as an appropriate description of the associated physical reality. These characteristics can be listed as follows.

• GRB light curves vary on each occasion in length, shape and quantity of episodes. These light curves can be very simple, for instance with only one smooth spike, as is the case for most SGRBs. Others show highly complicated structures such as long multiple episodes separated with lags, and that are usually seen in long bursts. Indeed, some light curves are composed of both types, i.e., fast and slow components.

• GRB spectra can be well-described by the "Band function" for both their time-resolved and time-integrated spectra. A Band function is a smoothly-joined broken power law defined by three parameters, the low energy α, high energy β, and peak energy E_{peak}. *Fermi* (GBM and LAT) observations suggest that for most GRBs, the parameter components fit up to approximately 10^7 keV. However, the Band function for bright GRBs needs to have additional spectral components added to overcome any obstacles that might otherwise prevent this model being used to successfully account for such observations. These additional models could be the thermal component or the high-energy power-law component.

• The peak energy E_{peak} can take any of a range of energies, extending from very high energies of $\approx$ 15 MeV to lower energy bands of $\sim$ 10 keV. It behaves differently within the same GRB and shows different patterns, e.g., E_{peak} intensity tracking and hard-to-soft evolution.
The spectral sharpness suggested that there are more emission mechanisms than synchrotron emission alone in which the single-electron synchrotron power is unable to explain a large fraction of the GRB prompt spectrum observed (Yu et al., 2015). Therefore, a broader spectrum is observed when there is the possibility of adding additional synchrotron spectra. Thus, other emission mechanisms are required to explain the spectral peak or break in the prompt emission phase.

I. Spectral Properties

Describing GRBs' prompt emission spectra is not an easy task, so furthering our understanding of their properties is important. Since the launch of the Burst and Transient Source Experiment (BATSE) on board the Compton Gamma Ray Observatory (CGRO) satellite, a number of studies have been completed using the large GRB sample, as collected over 10 years, to study spectral properties. The observed spectra are very sensitive to the chosen method of analysis; indeed, it is essential to describe the analysis method properly before studying the spectra. One way to characterize GRB prompt emission spectra is to use the flux integrated over the total burst duration, namely the time-integrated spectrum, which has a sufficient photon count to allow for spectral analysis. This applies mostly to the weak bursts that have low photon counts. In contrast, for bright GRBs more careful analysis can be conducted to investigate spectral behaviour in considerable depth within a small time interval (e.g., analysing each pulse along the light curve individually); in this case, the spectra are best described as time-resolved, where this can overcome some of the time-integrated drawbacks, such as variability between individual pulses, that may carry important information about spectra which could possibly allow clearer theoretical explanation.

Next is the analysis method. There is only one method used for GRB spectral analysis due to the nonlinearity of the detector (and which cannot be reversed); it is called the forward folding method, and can be summarized as follows. First, one should choose a model that is folded with the detector response (containing information about the detector), after which the model is compared to the detected spectrum counts. Finally, the spectrum model parameters are searched to determine a best fit while minimizing the differences between the observed spectrum (data) and the model. A review of each model used in the analysis is given below:

• Simple Power-law Model (PL)

The power-law model is the simplest model that can be used to describe a GRB spectrum (e.g., Fishman & Meegan 1995). This model consists of two parameters: the low-energy photon index α and the normalization A. With these two parameters, the power-law model can fit the spectra of most GRBs if they are applicable to such a burst. This model is suitable when the signal-to-noise

ratio of the fitting spectrum is very low and in the case when the signal is weak and if the break energy cannot be determined due to the break energy of the broken power-law spectrum lying outside the energy band of such a detector (e.g., Cabrera et al. 2007). The power-law model is described by the equation below:

$$f_{PL}(E) = A(\frac{E}{E_{piv}})^{\alpha} \tag{1.1}$$

Where A is the normalization, which is the flux density of the spectrum at the E_{piv} energy in $\mathrm{ph}^{-1}\ \mathrm{cm}^{-2}\ \mathrm{keV}^{-1}$. α is the low-energy photon index (dimensionless). E_{piv} is the pivot energy, which is kept constant at 100 keV.

• Band function (Band)

The empirical model "Band function" (Band et al., 1993) has been successfully fitted to the majority of bright GRBs that are seen in BATSE and later observatories. This model is known as a smoothly-joined, broken power law, as defined below:

$$f_{Band}(E) = A \begin{cases} \left(\frac{E}{E_0}\right)^{\alpha}\ exp\ \left(\frac{-E}{E_0}\right), & if\ \ E < E_c \\ (\alpha-\beta)^{\alpha-\beta}\ \ exp\,(\beta-\alpha)\left(\frac{E}{E_0}\right)^{(\beta)}, & if\ \ E \geq E_c \end{cases} \tag{1.2}$$

Where,

$$E_c = (\alpha-\beta)\frac{E_{peak}}{2+\alpha} = (\alpha-\beta)E_0.$$

This model thus has four free parameters: A is the normalization in $\mathrm{ph}^{-1}\ \mathrm{s}^{-1}\ \mathrm{cm}^{-2}\ \mathrm{keV}^{-1}$, α is the spectral photon index at low-energy, β is the spectral photon index at high energy and a νF_ν peak energy E_{peak} in keV. Basically, νF_ν is the photon energy, $f(E)$, as integrated twice over all energies $(E^2 f(E))$, which represents the total energy flux for each energy band as described in the above equation. E_c is the Band characteristic energy, which is the energy scale of the power-law region in keV and E_0 is the e-folding energy.

The Band function that resembles a "broken power law" is able to provide a good fit for many GRB spectra, whether for time-integrated or time-resolved analysis (see for example, Kaneko et al. 2006; Nava et al. 2011). Particularly, this function has typical features such as in the high-energy index limit, $\beta \to -\infty$, where the spectrum reaches the cut-off power-law model (CPL), but when $\alpha \to \beta$, the spectrum reaches a PL.

However, this model in some complex GRB spectra is inadequate to allow for a complete description with only four free parameters, because this limited number of parameters can lead to an incorrect interpretation of the spectra. Therefore, alternative models are used, e.g., the broken power law (BPL) (Schaefer et al., 1992) and smoothly broken power law (SBPL) (Preece et al., 1996), lognormal (Pendleton et al., 1994) and the optically thin bremsstrahlung spectrum with a PL. Oganesyan et al. (2017) have studied the characterization of prompt emission spectra extending down into the soft X-ray region for a joint-fit spectral analysis of the GRB sample

observed via *Swift* (BAT+XRT) and *Fermi* (GBM) using a Band model with a high-energy cut-off (BandCut); this model consists of six parameters, the usual four Band parameters plus two extra parameters from the high-energy cut-off model, namely the high energy E_c and the e-folding energy E_0.

Additional spectral models have been suggested in the literature, e.g., the black body (BB) with power law (Pe'er, 2008), BB with Band function (Guiriec et al., 2011) and two BBs with power law (Basak & Rao, 2013b). The purpose of suggesting these models was to allow for a reasonable fit when the spectrum in question apparently contained different components, for instance, thermal and non-thermal, and which was thus intended to help explain the physics behind spectra that could not otherwise be usefully analysed with the standard models.

• Cut-off Power-Law Model (CPL)

The first-order correction to the PL model is referred to as the cut-off power law (CPL). This model is a low-energy power law with an exponential high-energy cut-off. It is well suited to the analysis of prompt spectra in many of the bursts detected via *Swift* and *Fermi* (Sakamoto et al. 2005; Sakamoto et al. 2008a; Paciesas et al. 2012). This is mainly because of the low-energy detectors used in these experiments; in the low-energy domain, it is hard to constrain the high-energy photon index, or when there is no high-energy tail that can be determined. This model has frequently been applied to *Fermi* GRBs, especially when the e-folding energy $E_0 = E_{peak}/2 + \alpha$ approaches $\sim$1 MeV, or in cases where Band model is undetermined. There are three parameters in this model; the normalization A, the low-energy photon index α and a vF_v peak energy E_{peak}. The CPL can be expressed as:

$$f_{CPL}(E) = A\ exp\left(\frac{-E(2+\alpha)}{E_{peak}}\right)\left(\frac{E}{E_{piv}}\right)^{\alpha} \tag{1.3}$$

Where E_{piv} is the pivot energy used for minimizing the correlation between the fitted parameters, which is usually fixed at 100 keV .

II. Spectral Evolution

Bright GRBs spectral analysis using time-resolved spectra has revealed important spectral evolution properties: it is been found there are two types of GRB pulse behaviour depending on the relation between E_{peak} and the energy flux. The first is the so-called "hard-to-soft" (e.g, Pendleton et al. 1994; Bhat et al. 1994; Ford et al. 1995; Liang & Kargatis 1996; Kocevski & Liang 2003; Hakkila et al. 2008; Hakkila & Preece 2014) evolution that occurs when E_{peak} decreases during the first rising part of the pulse (Norris et al., 1986); the second when the hardness of the spectra shows tracking behaviour with flux intensity, such as when E_{peak} increases during the first rising part of the pulse (Golenetskii et al., 1983). Both types of spectral evolution can potentially be seen within the same GRB (Lu et al. 2010 and Lu et al. 2012). Most, but not all GRBs follow hard-to-soft evolution behaviour (Hakkila & Preece 2011).

The hard-to-soft and intensity tracking evolution of E_{peak} is discussed in the literature by Lu et al. (2012) for a sample of 62 GRBs. Similarly, another example of spectral evolution is presented in Yu et al. (2016)'s catalogue, who reported spectral evolutionary trends for E_{peak} for a sample of 81 bright GRBs for time-resolved spectra, see, for example, Ford et al. (1995).

III. Energy Cutoff

An energy cut-off is expected to be seen at the tail end of the very high energy of the GRB prompt emission in the fireball shock model, which is believed to be caused by gamma-gamma "$\gamma\ \gamma$" absorption or by the high energy cut-off in the electron distribution. It is known that GRBs are produced via relativistic jets, with the bulk Lorentz factors Γ for most GRB jets constrained at $\Gamma > 100$, as, for example, obtained from the Compton/EGRET satellite. EGRET could detect GRBs at 100 MeV - 5 GeV (Dingus, 1995); at this high an energy, the GRB emission region should expand to become ultra-relativistic in order to allow the more energetic photons to escape and avoid $\gamma\ \gamma \rightarrow e^{\pm}$ absorption (e.g., Lithwick & Sari 2001). Only a few GRBs were detected via EGRET due to its low sensitivity and small field of view. In the *Fermi* (LAT) era, searching for such high energy spectral cut-offs has become more straightforward. LAT has detected a large number of GRBs, providing high-quality data with much greater sensitivity, covering the approximate energy range of 100 MeV – 300 GeV for the brightest GRBs.

For decades, the spectral cut-off at very high energy has the subject of intense discussion, which has encouraged numerous research groups to investigate the evidence behind the high energy spectra associated with GRB prompt emission. Basically, understanding the energy cut-off and the situations under which it occurs are amongst the most vital pieces of understanding required to allow a better description of the constraints on GRB jet properties. For instance, LAT has detected numerous bright GRBs at energies $>$ GeV with no energy cut-off detection, allowing estimates of $\gamma\ \gamma$ absorption by detecting photons with energies that are more energetic than the ones generally detected by LAT.

Most LAT GRB jets are considered to have a value of Γ that are larger than those suggested by EGRET. The larger values have allowed for the re-evaluation of Γ found in some bright GRBs (e.g., GRB 080916C, Γ = 900, GRB 090510, Γ = 1200, and GRB 090902B, Γ = 1000) (Granot et al., 2010). The highest cut-off measured to date is for GRB 090926A (Ackermann et al., 2011), where E_c = 1.4 GeV with Γ = 200 - 700. Another, GRB 100724B, has been reported to have a high-energy cut-off or break, see the *Fermi* (LAT) GRB catalogue in Ackermann et al. (2013).

IV. Temporal Properties

Spectral properties depend on the detector energy bandpass. For the same GRB, a low-energy detector can measure a longer T_{90}, while a highly sensitive detector can also measure a longer T_{90} due to its large collection area. Furthermore, T_{90} can be underestimated in some GRB light curves that are separated by long quiescent lags between pulses. Naturally, T_{90} obtained from

such emission may consist of emission from different GRB sites, e.g., internal or external shocks. Interestingly, for most GRBs, the emission within T_{90} is likely to appear to be consistent with the internal shock phase. Some of the associated temporal properties can be given as:

• T_{90} duration ranges approximately between a few milliseconds to 1000 s. The standard GRB classification scheme was determined from the temporal distribution seen by BATSE, which shows two lognormal components with a dip between the two distributions at about 2 s in the 25-350 keV energy band (Kouveliotou et al., 1993).

• T_{90} peaks at 20 - 30 s and 0.2 - 0.3 s in the LGRBs and SGRBs, respectively. It was found that GRBs' classification distribution showed that, statistically, the LGRB group is softer than the SGRB, where this distribution is based on a dependent energy band. This means that when comparing the ratio between photon counts in the different detector energy bands (high and low), the hard-to-soft ratio for (soft) LGRBs is smaller than for (harder) SGRBs.

• GRB light curves show a variety of shapes and structures which are classified in terms of their underlying pulse structure. Some GRB light curves are simple with only a single pulse, whilst others are complex with smoothly overlapping pulses separated by lags or with very rapid variabilities; see Figure 1.2. This complexity is generally the result of there being a large number of spikes that ultimately give a spectrum with very little structure. Other types of GRB light curve structures include Fast Rise Exponential Decay "FRED" (Kocevski et al., 2003), or the exponential pulse model (Norris et al., 2005) and Lognormal distribution (Bhat et al., 2012). A number of GRBs show softer and weaker precursors that are found to be around 10 s - 100 s separated from the main burst. Lazzati (2005), Burlon et al. (2008), Burlon et al. (2009) and Hu et al. (2014) have suggested that in some GRBs the precursor emission is independent of the character of the main episode, even though similar behaviour is observed in both the precursor and the main episode. Figure 1.3 shows the distribution of GRB duration (long and short) separated by 2 s, where the SGRBs duration range between 0.01 s - 2 s, while LGRBs last for more than 2 s and with a larger population than the short ones.

• LGRBs have been linked to rapid star formation in the brightest regions of galaxies, or in many cases to core collapse supernovae, associating LGRBs with the intense emission of radiation that is believed to be a signature of the death of massive stars (20 - 40 times the mass of the Sun)The brightness of a typical LGRB in the optical/infrared has been found by *Swift* to be approximately 18^{th} magnitude at a redshift $z > 5$ (Gehrels & Mészáros, 2012).

• The majority of GRBs can be categorized as LGRBs. It is generally believed that LGRB prompt emission is due to processing in the internal shock (see, for example, Belczynski et al. 2016), LGRBs are believed to have a supernova (SN-*Ic*) connection (Galama et al. 1998; Hjorth et al. 2003; Stanek et al. 2003; Woosley & Bloom 2006). Practically, the peak energy E_{peak} and the isotropic luminosity L_{iso} of an LGRB have magnitudes of $\sim$ 200 keV and 10^{50} erg s^{-1}, respectively, although E_{peak} can cover energies ranging from a few keV to $\sim$1 MeV.

• At the time of *Swift's* launch, little evidence existed as to the nature of short duration and

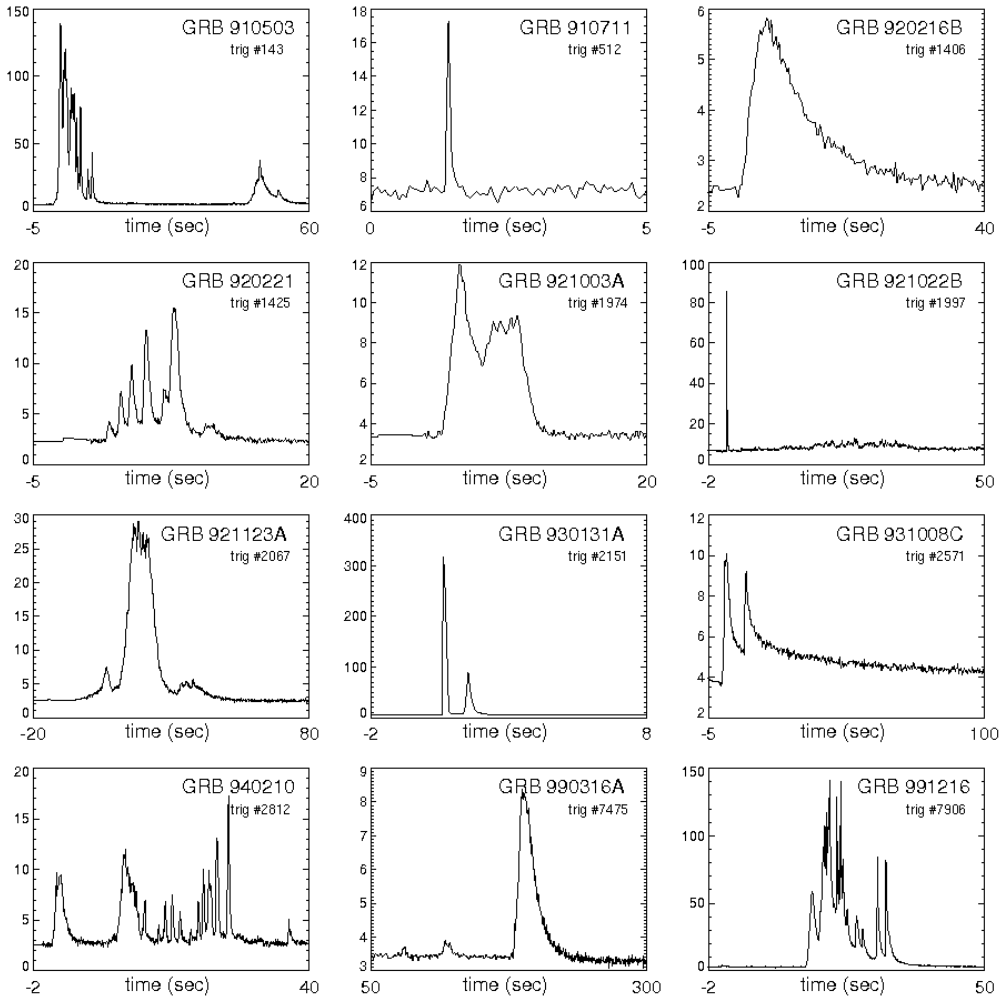

Figure 1.2: Light curves of 12 bright gamma ray bursts detected by BATSE. Taken from the public BATSE data archive.

http://gamma raymsfc.nasa.gov/batse/grb/catalog/

hard spectrum SGRBs. It had been suspected (on theoretical grounds) that SGRBs were the result of the binary merger of two compact objects (NS-NS or NS-BH) (Paczynski 1986; Fryer et al. 1999; Rosswog et al. 2003; Belczynski et al. 2006; Chapman et al. 2007). SGRBs have a very short lifetime (a few tens of milliseconds) (Bhat et al., 1992) and are fainter than LGRBs, and thus have lower detection rates (see, for example, Berger 2014). Generally, SGRBs display a hard spectral evolution that is even harder than their long counterparts, and which indicates there is a correlation between duration and spectral hardness, though with a highly complex variability (Dezalay et al., 1996). The peak energy E_{peak} is higher by 400 keV with a shallower spectral photon index and thus lower isotropic luminosity than LGRBs. The support for compact binary mergers as the origin of SGRBs was seen in GRB 130603B, which was possibly a "kilonova" signature (detected via *Swift* (BAT) and Konus-Wind) (Tanvir et al., 2013). More recently, the LIGO gravitational wave detection of GW 170817 and GRB 170817A was also detected via

Fermi (GBM), which is the best evidence to date (Goldstein et al. 2017; Lipunov et al. 2018; Cai et al. 2018; Green et al. 2018; Fargion et al. 2018; Creminelli & Vernizzi 2017; Salafia et al. 2017). This emission was formed by the decay of the transient caused by radioactive decay as a result of the merger of r-process nuclei (Li & Paczyński, 1998). It is believed that SGRBs

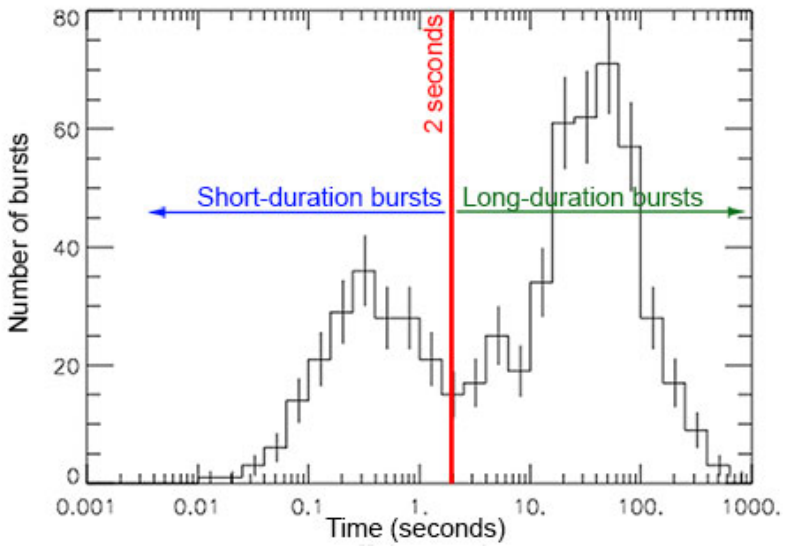

Figure 1.3: The GRB classification (long and short) distribution.

https://imagine.gsfc.nasa.gov/science/objects/bursts1.html

have different origins to LGRBs, as indicated by the varieties of their spectral and temporal phenomena as host types. These SGRBs are observed in a number of host galaxies and are frequently observed in star formation regions (e.g., Gehrels & Swift Team 2005). One of the occasional features of SGRBs is an associated Extended Emission (EE) that lasts for $>$ 10 s after the trigger, and is typically characterized by a relatively low flux compared to the prompt emission phase LGRB, and thus the two features can have a comparable fluence (Perley et al., 2009). Only about one-fifth to one-quarter of SGRBs are EEs.

• Over the years, a few GRBs that have shown ultra-long duration $T_{90} > 500$s have been observed by BATSE, e.g., GRB 970315 which shows a typical $T_{90} \geq 3000$ s (e.g., Tikhomirova & Stern 2005), the ultra-long duration being caused by the tail of the emission for extremely bright GRBs when decaying rapidly in the form of FRED, for example, GRB 971208 (Giblin et al., 2002). Other observatories have detected a number of ultra-long GRBs, though they are rare events. The capability to detect such events is based on detector phenomena such as the detection sensitivity or the quality of the trigger algorithms. Recently, GRB 130925A, one of the typically very long bursts that were detected via *Swift* (BAT), lasted about 20 kiloseconds, a duration consistent with the proposed category of ultra-long GRBs (Savchenko et al., 2013). More ultra-long GRBs with durations of kiloseconds have been observed by Gendre et al. (2013), Stratta et al. (2013) and Levan et al. (2014). Some other ultra-long categories of GRBs are

considered to be associated with blue supergiant progenitors (e.g., Gendre et al. 2013; Levan et al. 2014). The duration of ultra-long GRB activity periods has been observed to be longer than *Swift's* orbit, which is $\sim$ 90 minutes. Due to this, and the fact that flux levels are low, GRB activity can be missed and therefore only a very limited number of such have been detected to date. As is currently known, one of the defining features of GRBs is their high variability timescale, making it impractical to estimate "lost" fluence during orbital gaps. This is crucial since the fluence is dominated here by the lower luminosity integration rather than the bright peaks because the latter are generally missing in ultra-long bursts (Levan et al., 2014).

• X-ray Flashes (XRFs) are one of GRBs transient subclasses that are still the subject of intense debate (Heise & in't Zand 2003; Barraud et al. 2003; Sakamoto et al. 2005). It has been suggested that XRFs and GRBs are similar, related phenomena. Understanding the physical mechanisms of XRFs and GRBs leads to important insights into their nature. XRFs were first observed via the *BeppoSAX* Wide Field Camera (WFC) at a rate of four per year. One of the properties of XRFs (Heise & in 't Zand, 2001) is that their high-energy fluence is reduced in the GRB bands and increased in the X-ray bands, at 30 to 400 keV and 2 to 30 keV, respectively. However, XRFs have lower peak energies compared to GRB populations. They are believed to be an extension of the GRB's peak energy distribution, which shows the consistency between XRFs and GRBs (Sakamoto et al., 2004). In practice, these XRFs can be interpreted by spindown-powered emissions that are generated from long-lived neutron stars (NSs) (Ciolfi, 2016), or from some form of connection to a supernova (SN) shock breakout. To date, only a handful of XRFs have been localized and studied, even though a number of such show links with SN (Siegel & Ciolfi, 2016).

V. Correlations

Over the past decade, a number of GRBs have been detected and their calculated luminosities recorded in order to investigate spectral/temporal correlations. Several of these temporal relations can be obtained from the associated light curves such as the lag-luminosity (Norris et al., 2000) or the variability relations (Fenimore & Ramirez-Ruiz, 2000). Other relations were obtained from spectra, such as the Amati relation (Amati et al. 2002; Amati 2006; Amati et al. 2008; Amati et al. 2009), the Ghirlanda relation (Ghirlanda et al. 2004a; Yonetoku et al. 2004; Ghirlanda et al. 2010a), and the Liang-Zhang relation (Liang & Zhang, 2005). All of these relations have implications not only for the physics behind GRBs, but also for all cosmology. Below is a detailed description of these spectral relations.

• Amati and Yonetoku Relations

The Amati relation is one of the intrinsic GRB properties that broadens our general understanding of a number of the prompt emission properties that help to determine how GRBs can be categorized. Since the launch of the *Fermi* (GBM and LAT) instruments, a number of GRBs

observed in the high-energy domain have led to more accurate measurements of E_{peak}. In the meantime, the precise localization, as determined by *Swift* (BAT), assists us in gaining a better understanding of GRB properties by increasing the number of GRBs with known redshifts. This is required in order to study the correlation between E_{peak} and the vF_v spectrum in the source rest frame and the equivalent isotropic energy, E_{iso}.

Since 1997, the ability to measure redshifts has improved considerably, with more than 200 events to date providing a systematic basis by which to study GRB spectral properties. The key importance to investigating this correlation is to enlarge the sample with known redshifts and to examine the impact of instrumental selection effects. This enhances, and further improves, the extension of correlation analysis. For instance, in time-integrated spectra, spectral fitting shows a positive correlation between E_{peak} and E_{iso} (Amati et al. 2002; Wei & Gao 2003). This correlation is not usually assisted by GRBs and rather is only detected via *Swift*,(15-150 keV) due to the inability to use the data to estimate E_{peak}, see; Butler et al. (2007). More details about these relations are discussed in Chapter 3.

$$\frac{E_{peak,rest}}{100\ keV} \sim 4.8 \left(\frac{E_{iso,\gamma}}{10^{51} erg} \right)^{0.7} \tag{1.4}$$

Similarly, the Yonetoku relation shows a positive correlation between the ($E_{peak,rest} - L_{iso,\gamma}$) of GRBs at the peak flux (Wei & Gao 2003; Yonetoku et al. 2004). This correlation was adapted from the original relation:

$$\frac{E_{peak,rest}}{100\ keV} \sim 1.8 \left(\frac{L_{iso,\gamma}}{10^{52} erg\ s^{-1}} \right)^{0.52} \tag{1.5}$$

The nature of this correlation is described when pulses decay as the prompt emission softens, and where the flux decreases. It can also be applied to SGRBs which show extensive scattering for time-resolved spectra. The Amati and Yonetoku correlations are different, and can be seen in different types of LGRB or SGRB. In practice, the Amati relation can generally only be successfully applied to LGRBs. In contrast, isotropic luminosity seems to be more related to E_{peak}, which is satisfied for both LGRB and SGRBs in the Yonetoku correlation (Tsutsui et al., 2013). This suggests that LGRBs and SGRBs are produced in the same emission processes (Zhang et al. 2009b; Ghirlanda et al. 2009; Guiriec et al. 2013; Tsutsui et al. 2013).

• Ghirlanda Relation

This correlation, as originally noted by Ghirlanda et al. (2004a), is between E_{peak} and the collimation-corrected energy with a measured jet opening angle. If one has a sample of GRBs with known redshifts and E_{peak}, estimating the jet opening angle becomes possible from the achromatic break of their afterglow light curve, hence allowing the collimation-corrected energy of the bursts E_γ to be driven. Bursts with same E_γ and E_{peak} have different jet opening angles (Sari, 1999).

The Ghirlanda relation $E_{peak,z} - E_\gamma$ can be expressed as below:

$$E_{\gamma,app} = (1 - cos(\theta))\ E_{iso} \sim \left(\frac{\theta^2}{2}\right)\ E_{iso} \tag{1.6}$$

or in its original form (Ghirlanda et al., 2004b) as:

$$\frac{E_{peak,rest}}{100\ keV} \sim 4.8\ \left(\frac{E_\gamma}{10^{51} erg}\right)^{0.7} \tag{1.7}$$

where θ is the jet's half-opening angle and E_γ, app is the apparent collimation (geometrically)-corrected GRB energy. The Ghirlanda relation claimed to have a tighter correlation than the one completed by Amati. In the review by Frail et al. (2001), a sample of 15 GRBs with known redshifts and θ were thought to show a good correlation with $E_\gamma \sim 5 \times 10^{50}$ ergs; this was also independently investigated by Panaitescu & Kumar (2001). A larger sample of 24 GRBs was later studied by Bloom et al. (2003), which showed a distribution of $E_\gamma \sim 1.3 \times 10^{51}$ ergs, resulting in a universal energy even with the varying E_{iso} range.

• Lag Luminosity

The differences in arrival times between the high (100 - 300 keV) and the low (25 - 50 keV) energy photons (or the delay time lag, τ) are known to be common features of GRBs (Cheng et al. 1995; Norris et al. 1996; Band 1997). Analysing the spectral lag in different energy ranges provides temporal and spectral evidence by which to improve the GRB photon models (Lu et al. 2006; Shen et al. 2005; Qin et al. 2004; Schaefer 2004; Ioka & Nakamura 2001; Salmonson 2000). It has been suggested that the relationship between spectral lag and isotropic peak luminosity could be used as an indicator of redshift (Murakami et al. 2003; Band et al. 2004). This correlation is known as $L_{iso} - \tau$, that is, the Norris correlation (Norris et al., 2000), which is the anti-correlation of the GRB isotropic peak luminosity L_{iso} and spectral lag. The anti-correlation may be caused by the diversity in the line-of-sight velocity of different bursts (Salmonson, 2000). The assumption of a proportionality between the spectral-lag and the pulse width needs to be satisfied for the individual pulses.

• Variability-Luminosity

The correlation between the burst luminosity and the variability of GRB light curves, defined as "spikiness", has been extensively discussed by Fenimore & RamirezRuiz (2000) and Reichart et al. (2001). In general, the variability of GRB light curves was thought to be related to the background subtraction complexities for different GRB light curves' behaviour. It has been found that there are positive correlations with large outliers ($L_{\gamma,peak,iso} - V$), which leads to GRBs having a luminosity that is a function of redshift. Regardless of this relation, a range of values with a slope m = 3.3:1.1 have been obtained by Reichart et al. (2001) and Guidorzi et al. (2005).

1.3.2 Afterglow

The longer-lived afterglow provides important insights into the nature of GRBs, e.g., the measurement of redshift (Metzger, 1997) and the connection between GRB and supernova events (Hjorth et al., 2003). Afterglows had been proposed theoretically before their actual discovery in 1997 (Paczynski & Rhoads 1993; Katz 1994; Mészáros & Rees 1997b) and follow the prompt emission phase and emit low-energy radiation such as X-ray, UV, optical, infrared, microwave and radio frequencies. Afterglows are suggested to occur in two different environments: interstellar medium (ISM)-like environments, in which the surrounding material density is effectively constant, or wind-like (wind of a Wolf-Rayet star, for example) environments where the density varies with distance.

Not all GRBs are followed by an afterglow, possibly because of different density ranges. A high ISM density environment should result in brighter afterglows. A faint afterglow is produced either due to a very low ISM density, or where the intrinsic absorption is very high (Piran & Sari, 1998).

The first afterglow detected was for GRB 970228 with *BeppoSAX* (Costa et al. 1997; van Paradijs et al. 1997), after which a number of follow-up observations were conducted. These afterglow observations dramatically increased in number when precise localization was provided by *Swift*. The follow-up observation by *Swift* starts initially ~ 1 min after the burst trigger. Afterglows are usually detected for at least several hours after the burst trigger by other observatories.

A second golden era of GRB afterglow observations began with the launch of *Fermi* in 2008, which has given considerable insight into the discovery of extended high-energy (GeV) afterglows for many bright bursts (Kumar & Zhang, 2015).

1.3.3 The Bulk Lorentz Factor

It is known that the GRB jet moves at relativistic velocities with Lorentz factors $\Gamma \gg 1$, and which is believed to be constrained by attenuation of high-energy spectral observations; accordingly, this has to be extremely large, with $\Gamma \geq 10^2$. The GRB emission properties, such as the timescales and typical frequencies, that are measured in the observer frame appear different to those in the comoving frame of the fluid.

The only possible method to understand the emission region properties is by estimating Γ, though this can be very difficult to constrain purely from observations. However, where it can be determined, such information can help to subsequently determine, for example, the dissipation region location, emitted photon frequencies, and the ejecta mass. Different theoretical mechanistic features are subject to large uncertainties.

Thus, a good estimation of Γ can result in a good understanding of the nature of the central engine and the radiation processes. Moreover, it is essential to overcome the compactness problem and to understand the photons' short timescale variability (Ruderman 1975; Krolik &

Pier 1991; Fenimore et al. 1993a; Piran 1995; Baring & Harding 1997). The smallest number measured for Γ is believed to be in the case when observed high-energy photons on the $\gg$ MeV scale escape absorption without undergoing pair production ($\gamma\ \gamma$) absorption. This is possible if the very high-energy plasma expands with a bulk Lorentz factor of Γ=100 - 1000 (e.g., Piran 1999).

The afterglow observations of GRB 970508 in 1997 provided a breakthrough in the field by verifying the existence of relativistic GRB outflows and provided the first radio-frequency afterglow ever observed (Frail et al., 1997). Since the launch of *Swift* and the associated afterglow follow-up observations, an increasing number of GRBs have been detected and studied, and more in-depth research into Γ has been conducted, all of which was due to *Swift*'s high sensitivity and its additional instrumentation, coupled with information from *Fermi*. The information that has been obtained from studying Γ has helped to evaluate the properties of GRBs in the comoving frame, and has allowed for better estimations of timescale variabilities from studies that focussed primarily on individual GRBs.

The first recorded detection of Γ_0 was in the early afterglow peaks of GRB 060418 and GRB 060607A (Molinari et al., 2007). The initial constant Lorentz factor Γ_0 can be estimated from the ejecta in the fireball scenario when an optically thick acceleration takes place, which happens before deceleration due to interactions with the external material. In the last few decades, *Swift* afterglow follow-up observations suggest Γ_0 estimation to be possible. Ghirlanda et al. (2012) concluded that Γ_0 distributions can be differentiated depending on the circumburst medium density. They found there is a significant correlation between Γ_0^2 and L_{iso} compared to E_{iso}, and further found a linear correlation between Γ_0 and E_{peak}. These correlations provide a clear explanation for the Amati and Yonetoku relations, such that L_{iso} and E_{peak} become larger as Γ becomes larger. Ghirlanda et al. (2018) recently found 67 GRBs with peak features in their GeV light curves or in the optical band at a time t_p. Therefore, measuring t_p can provide the Γ_0 of the fireball before deceleration. They also found that t_p is expected to be the result of the fireball deceleration dynamics and is unrelated to the synchrotron spectrum over the optical band; further details can be found in Chapter 5.

1.4 Other GRB Research

This thesis focusses on the prompt emission of GRBs from a phenomenological perspective. This research is just one part of a large field of GRB research. Taking advantage of the facilities offered by the *Swift* and *Fermi* satellites is important to the study of spectral analysis of prompt emission before the end of their useful lifetimes. Some more important studies into the science of GRBs are listed below:

• The connection between prompt emission and afterglow, and the associated mechanism(s); the excellent quality of the data provided by *Swift* and *Fermi* is enabling scientists to realistically

explore the extensive phenomena related to prompt emission. This also leads to the joint-fit of *Swift* (XRT) and *Swift* (BAT), which provides an associated study of the prompt emission and the afterglow. Moreover, analysing the associated time-resolved spectra allows scientists to investigate any physical mechanism found in the small time bins of the light curve.

• The fact that LGRBs appear to be associated with massive star formation allows this process to be studied in the Universe through the features of the bursts' host galaxies. GRBs have become a means to trace back to the very distant Universe, assisting scientists in the determination of the history of star formation.

• SGRBs are considered to be the main source by which to examine electromagnetic radiation associated with gravitational waves (GWs), as recently discovered by the LIGO observatory.

1.5 Objective and Thesis Overview

The aim of this thesis is to further our understanding of the spectral properties that can be obtained from different observatories, namely *Fermi* (GBM+LLE) and *Swift* (BAT), for a sample of bright and LGRBs. These two observatories provide valuable data that helps to understand GRB spectra at different energies (in the range of 10 keV to a few hundred GeV). Throughout this project, attempts are made to use different spectral models (PL, CPL, Band and BandCut) to determine and test the best-fit model for these data.

Moreover, from a statistical perspective, it also attempts to use different statistical tests to search for the best fit according to most appropriate statistical test for such data; for instance, by testing both the "PGstat" and "Cstat" statistics in the case of the joint GBM and BAT data, it was found that the Cstat provided better statistical fits. Also, attempts are made to compare the Chi-squared χ^2 and Cstat statistics in order to determine if they could provide an improved fit to the data, but in this instance after rebinning in the form required to be described by such statistics.

Furthermore, attempts are also made to choose between different spectral fitting software, starting with a comparison of the "Rmfit" and the "XSPEC" software in order to check if both software could fit the data equally well; it was concluded that both pieces of software show few differences in the values of the spectral parameters so fitted, regardless of the different fitting methods offered by each. We ultimately chose to use XSPEC to fit the GRB spectra throughout the remainder of this thesis.

By providing the above key recipes, the following questions needed to be answered to properly present the investigation conducted herein to provide the a full overview of the concept of GRB spectral properties.

• Does the spectral joint-fit (GBM+BAT) provide an improvement in the values of the spectral parameters in a practical or statistical sense?

• Do different spectral models provide different quality fits?

• Do the Amati and Yonetoku relations agree with those determined in this study?

• What are the trends of the spectral E_{peak} evolution?

• Is it possible to detect a spectral high-energy cut-off and estimate the Lorentz factor in the high energy *Fermi* LLE?

Below, we provide a brief overview of the thesis's chapters.

Chapter 1 contains a brief introduction to GRBs, starting from an overview of GRBs through to the associated theoretical models, along with a discussion of the radiative processes that lead to certain observational properties.

Chapter 2 presents the observatory facilities that can justifiably be described as the most important GRB observatories over the period since the CGRO was launched in 1991 to the launch of *Fermi* in 2008, with a focus on the observatory technique used and the sensitivity of each observatory to the detection of bursts, along with a full description of the detectors used from a scientific perspective.

Chapter 3 addresses the joint GBM+BAT fitting for the time-integrated spectra and considers the spectral properties of a GRB sample detected coincidentally (i.e., simultaneously) via *Swift* (BAT) and *Fermi* (GBM). This chapter provides a comparative study of the two main fitting models (CPL and Band) in order to justify our choice of the best-fit model in these two cases, namely the joint-fit and the GBM-only. Additionally, other analyses, as obtained from other studies in the literature, will be considered for comparative purposes. Finally, this chapter also discusses the Amati and Yonetoku relations and examines the relevance of these two relations to the data in this study.

Chapter 4 addresses the joint GBM+BAT fitting for time-resolved spectra. Studying the spectral properties of a single sample, but in terms of its individual pulses, was achieved by slicing the time interval into small pulses. This chapter investigates E_{peak} evolution with both time and peak flux, which can only be obtained from the spectral joint-fit model. Once again, the time-resolved Amati and Yonetoku relations are examined and compared with this study for the individual pulses.

Chapter 5 systematically searches for such spectral high-energy cut-off detection features and estimates a Lorentz factor Γ from a sample of GRBs detected coincidentally via *Fermi* (GBM and LLE) at the high-energy end of GRB prompt emission.

Chapter 6 gives a summary of potential future work and a number of concluding remarks, which are then followed by the appendices.

Chapter 2

Observation Facilities

2.1 Observations Facilities

2.1.1 *Swift* and *Fermi* Era

In the early 1960s, the *Vela* satellites (Klebesadel et al. 1973b; Strong & Klebesadel 1974; Strong et al. 1974; Strong 1975) were the first to observe the phenomenon of GRBs. This discovery was not possible from the ground due to atmospheric absorption of high-energy photons. *Vela* was a nuclear test detection project run by the U.S. Department of Defense and the U.S. Atomic Energy Commission, and was launched on May 23, 1969, into a circular orbit at a distance of 118,000 km and with a period lasting $\sim$112 hours. In the *Vela* era, 73 GRBs were detected over a period of less than ten years.

Since the launch of *Swift* and *Fermi*, great milestones in GRB research have been achieved. They have played a significant role in a large number of astrophysical discoveries relating to numerous cosmological objects ranging from GRBs to Blazars. *Swift* is a NASA-led mission, run in collaboration with Italy and the UK, whereas *Fermi* is the result of a collaboration between NASA and the US Department of Energy along with other international partners including Italy and Germany. The key science in the *Swift* mission is to investigate four phenomena; GRB progenitors, the different physical processes underlying different GRB class observations, the interaction between the blastwave and its surroundings, and the early Universe through GRBs; *Swift* also investigates other non-GRB-related science.

Swift and *Fermi* detect more than 30 triggers in common per year. Indeed, orbiting these two satellites at the same time has provided high-quality data that has further helped scientists to investigate any systematic biases that may occur in each instrument. In previous decades, other satellites, such as COMPTEL, Compton/EGRET and *BeppoSAX*, have also played a significant role in providing the fundamental studies that have allowed for the exploration of complex interpretations of GRB events. The common science between *Swift* and *Fermi* allows for the study of their data in a spectral joint-fit that allows both for their cross-calibration and the ability for either GRB spectral or a temporal fitting to be investigated (Stamatikos, 2009). Figure 2.1 shows the effective energy region for *Swift* (BAT XRT UVOT) and *Fermi* (GBM-LAT); it also shows

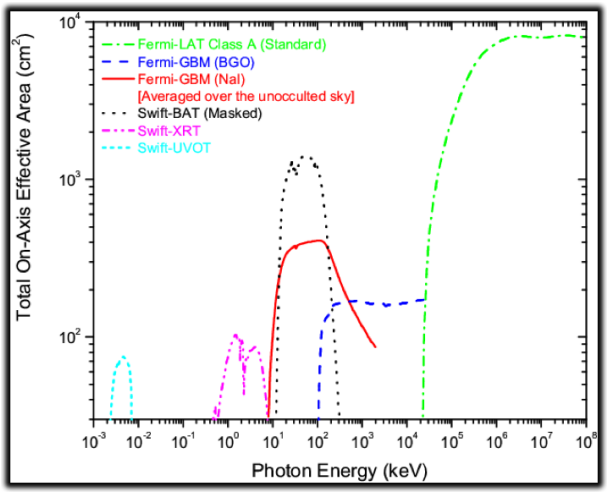

Figure 2.1: Effective energy regions for *Swift* (BAT, XRT, and UVOT) and *Fermi*-GBM/LAT.

http://inspirehep.net/record/826060/plots

how GBM and BAT share some of their effective energy range. The effective extent of the low-energy region ($\sim$ 20-100 keV) for masked BAT compared with GBM NaI is about a factor of three greater.

Swift and *Fermi* are still in orbit, providing data on a daily basis, allowing researchers to take advantage of the analysis of their data and to enhance the understanding of GRB phenomena before their useful lifetimes come to an end.

2.1.2 *Swift* (BAT)

The rapid response of *Swift* to the detection of GRB sources has revealed various pieces of evidence that have helped in solving the GRB mystery. The information provided promptly by *Swift* allows both ground and space telescopes to respond quickly. *Swift* is a multi-wavelength observatory, observing from the gamma-ray region, through the X-ray and UV down to the optical. The average detection rate of GRBs via *Swift* is $\sim$ 90 bursts per year with accurate localization. To date, *Swift* has discovered many distinct GRBs , including several at very high redshift, e.g., GRB 090423 (Tanvir et al., 2009) with a measured redshift of z = 8.2, and GRB 090429B (Cucchiara et al., 2011) with a redshift of z $\sim$ 9.4.

Figure 2.2 shows *Swift*, which consists of three main instruments: the Burst Alert Telescope (BAT) (Barthelmy et al., 2005), the X-Ray Telescope (XRT) (Burrows et al., 2005) and the UV Optical Telescope (UVOT) (Roming et al., 2005). All detectors can be simultaneously pointed at the source within 20-70 seconds after the beginning of a trigger for follow-up observation (Barthelmy et al., 2005).

BAT is the primary detector and is designed to perform a uniform hard X-ray all-sky survey while also monitoring for hard X-ray transients. The BAT field of view FOV (half coded) is 1.4

sr to detect bright bursts, with a two-dimensional coded aperture mask system and a large area, solid-state detector array for weak GRB detection (Barthelmy et al., 2005). It covers the energy range 15-150 keV with an energy resolution of about 7 keV and provides an approximate ~ 3 arcminute accuracy of burst location. The BAT detector is made of a 5200 cm^2 array of 4 x 4 mm^2 CdZnTe detectors grouped into 128 detector elements.

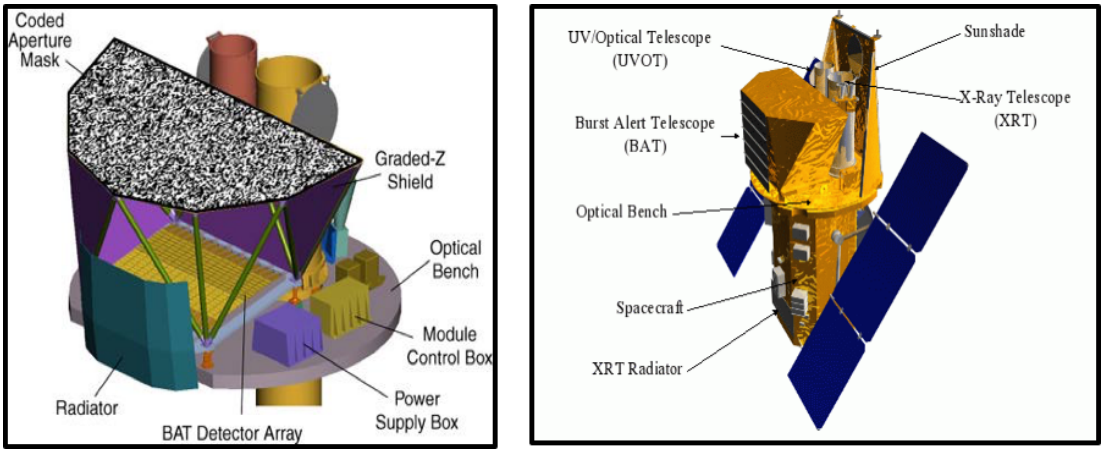

Figure 2.2: Right: the *Swift* telescope showing the three instruments: BAT, XRT and the UVOT (Gehrels & Swift, 2004). Left: the BAT detector description (Barthelmy et al., 2005).

http://www.swift.ac.uk/about/instruments.php

The use of a coded aperture technique is crucial for the capture of spectral images, which means that BAT can afford to lose individual pixels or modules without losing the entire information content associated with each event. The BAT coded aperture mask contains 52,000 lead tiles mounted above the CZT detector plane. BAT has two modes of operation: the first is the burst mode, which allows for burst localization, and the second is the survey mode, which allows for hard X-ray survey data. In the survey mode, the count rate collection in the instrument gives an approximate 5-minute time bin for 18 channels. Because of the varieties of burst phenomena, BAT currently provides the best dynamical range and trigger capability available for this service. Since its launch, it has detected a large number of bursts with observed afterglows, and for which redshifts have been determined (Gehrels & Razzaque, 2013).

The burst trigger algorithm counts any residuals in the detector count rate that appear in the source above the background rate. The algorithms provide a number of criteria that categorise the interval of the pre-burst background, the test interval of the GRB emission duration, the order of the estimated background level, the detector energy band, and the detector plane illuminated region. The BAT processor simultaneously aims to track a large numbers of these criteria.The imaging capability of BAT burst detection is one of BAT's most important features. In the on-board software burst-trigger, the software can check automatically for any unwanted sources such as the bright galactic sources and magnetospheric particle events and exclude them only when the trigger is pointed at the source. After the burst has been detected, the sky location

and intensity are immediately sent to the ground and distributed via the Gamma-ray Coordinate Network (GCN).

BAT can perform all-sky hard X-ray surveys whilst simultaneously searching for bursts. For on-board transient detection in four energy bands, the detector plane count rate maps of 1-minute and 5-minute accumulations with a 30-minute average map. A comparison between these images and on-board source catalogues are checked. Importantly, any burst that is undetected by the burst trigger algorithm, as a subclass of long smooth bursts, must be canceled during this processes.

2.1.3 *Swift* (XRT)

XRT is a sensitive X-ray imaging spectrometer that covers an energy range of $\sim$ 0.3 - 10 keV with a FOV 23.6 $\times$ 23.6 arcminutes. The XRT spectral resolution is 140 eV at 6 keV. With an angular resolution of 7 arcseconds and a detector sensitivity of 2 $\times 10^{-14}$ erg s^{-1} cm^{-2} in 10^4 s, the XRT is designed to measure fluxes, spectra, and light curves. Its read-out modes enable it to cover a wide dynamic range and rapid variability afterglow, and it also has the ability to change between read-out modes automatically. The XRT can localize a burst to an accuracy of less than 3-5 arcseconds in just a few minutes. This precision localization enables ground-based telescopes to make precise observations very quickly.

The XRT operation uses three main observation modes: image mode (IM), windowing-time (WT) and the photon counting mode (PC). XRT provides coverage of the gap between the prompt emission and the late afterglow phase; ideally, it allows for the complete study of these transitions (Zhang, 2005). The X-ray counterpart can last anything from a few minutes to days or weeks.

2.1.4 *Swift* (UVOT)

The onboard ultra-violet optical telescope (UVOT) allows *Swift* to be a true multi-wavelength facility. A technical description of the UVOT instrument is presented in Roming et al. (2005). Some of its properties are as follows: the UVOT is a 30 cm modified Ritchey-Chretien UV/optical telescope co-aligned with the X-ray Telescope and mounted on the telescope platform common to all instruments. Photons register on a microchannel plate-intensified CCD (MIC).

The UVOT has multiple filters, including a clear white light filter, and UV and optical prisms providing low-resolution spectra, a magnifier and a blocked filter. With its wavelength range of 170-600 nm, the UVOT provides an excellent combination with the XRT to localize bursts and make the appropriate follow-up observations (Lien et al., 2016). If a GRB is detected by the UVOT, its location can be determined within an accuracy of few tenths of an arcsecond.

When the UVOT observes a new GRB, it quickly processes through an established program that deals with filter combination and exposure times. Captured images are transferred to the ground and compared with archival observations to detect any optical counterparts. Finding chart images that take 100 s exposures through filters are sent via the Tracking and Data Relay Satellite

System (TDRSS) (Poza 1979) and the Gamma-Ray Coordinates Network (GCN) (Barthelmy et al., 1994).

2.1.5 *Fermi* (GBM)

Fermi has enabled scientists to explore the Universe in ways that were not previously possible. This unlocks the mystery of gamma rays and allows scientists to advance their theories of GRB emission mechanisms, and enables the study of objects such as massive black holes, neutron stars, and hot gases that move close to the speed of light (Atwood et al. 2009a; Meegan et al. 2009). Of the two instruments on board *Fermi*, the primary instrument is the Large Area Telescope (LAT) covering the energy band from 20 MeV to 300 GeV, which is designed to perform all-sky surveys to study astrophysical and cosmological phenomena. The secondary instrument is the Gamma-ray Burst Monitor (GBM), which provides high-quality data at lower energies (10 keV- 40 MeV) (Meegan et al., 2009). The GBM is specifically designed to measure the localization and duration of GRBs.

The GBM focusses on several goals, which include combining the analysis of the spectra and time histories of GRBs observed by both the GBM and LAT (Meegan et al., 2009). One of the interesting goals of *Fermi* is the attempt to understand why the energy spectra are extended toward higher energies. One of its principal capabilities is to provide data to study the spectral cut-off energy (Meegan et al., 2009).

The *Fermi* GBM uses scintillators to transform the gamma rays into optical signals, which are then measured by a Photon Multiplier Tube (PMT). The GBM contains different types of scintillation detectors, namely 12 thallium-activated sodium iodide [NaI (Tl)] and two bismuth germanates (BGO) detectors, as shown in Figure 2.3. The NaI detectors measure the low-energy spectrum (10 keV - 1 MeV) and are also used to determine the direction of the GRBs. The BGO detectors have an energy range of 300 keV - 40 MeV, and are mounted onto the spacecraft such that each view the sky in a different direction. The arrangement of the scintillation detectors offers a wide FOV of 8.6 Sr, allowing the straightforward determination of the arrival direction, although with much less accuracy than from *Swift*.

The signals from the twelve NaI and two BGO detectors are fed into a digital processing unit (DPU) which performs a pulse height analysis (*pha*). The DPU monitors all GBM instruments and generates three types of data: CTIME, CSPEC, and TTE (Time–Tagged Events) which are controlled by the GBM flight software. The CTIME is a count that is accumulated every 0.064 to 1.024 s in multiples of 0.064 s with a default value of 0.256 s in eight energy channels for each of the fourteen detectors. CSPEC is a count that is accumulated every 8.192 s in multiples of 1.024 s with a default value of 4.096 seconds in 128 energy channels for each of the fourteen detectors.

All of the information about the background and other related information is included in the trigger data TTE and TRIGDAT (TRIGger DATa). An increase in the count rate of the DPU

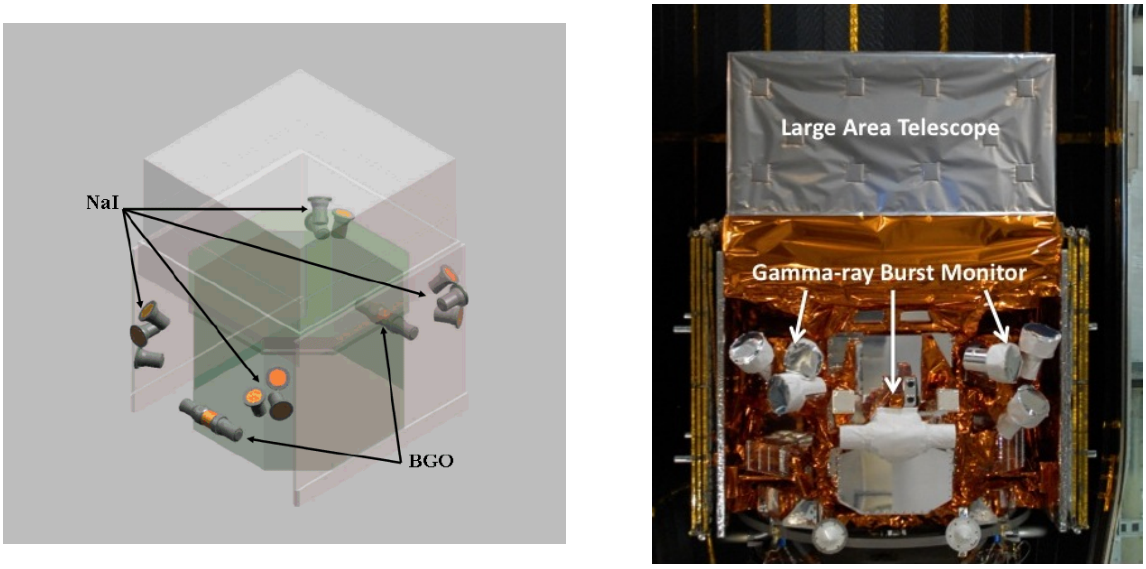

Figure 2.3: Right: the *Fermi* telescope carries two scientific instruments, the Large Area Telescope (LAT) and the Gamma-ray Burst Monitor (GBM). Left: the GBM instrument consists of 12 NaIs detectors located in different places on the instrument (determining location and low energy spectrum), and 2 BGO detectors located on opposite sides of the instrument (determining the mid-energy spectrum).

http://www.swift.ac.uk/about/instruments.php
https://fermi.gsfc.nasa.gov/ssc

digitized pulse height events from all GBM detectors should detect to 4.5 sigmas or greater to pass the trigger algorithm. TTE data is collected in two-microsecond time tag bursts for 300 s after receiving a trigger. The effective areas of the GBM (NaI and BGO) as a function of energy are shown in Figure 2.4.

2.1.6 *Fermi* LAT (LLE)

As mentioned above, the principal scientific instrument on board *Fermi* is LAT, with an energy band ranging from $\sim$ 20 MeV to more than 300 GeV, and sometimes extending to 20 GeV - 1 TeV. Its very large FOV covers about 20% of the sky at any given time (Atwood et al., 2009a).

LAT consists of four interconnected subsystems that allow for the detection of gamma rays, while other cosmic rays are rejected by filtering. The observatory is pointed toward a trigger and can slew autonomously when detecting bright GRBs, see Figure 2.5.

LAT has a sensitivity that is $\sim$ 30 times greater than any other equivalent or analogous observatory, and is able to detect thousands of astrophysical and cosmological phenomena such as pulsars, active galaxy nuclei (AGN), globular clusters, supernova remnants, compact binaries and, furthermore, the Sun, Moon and the Earth, in its operational lifetime.

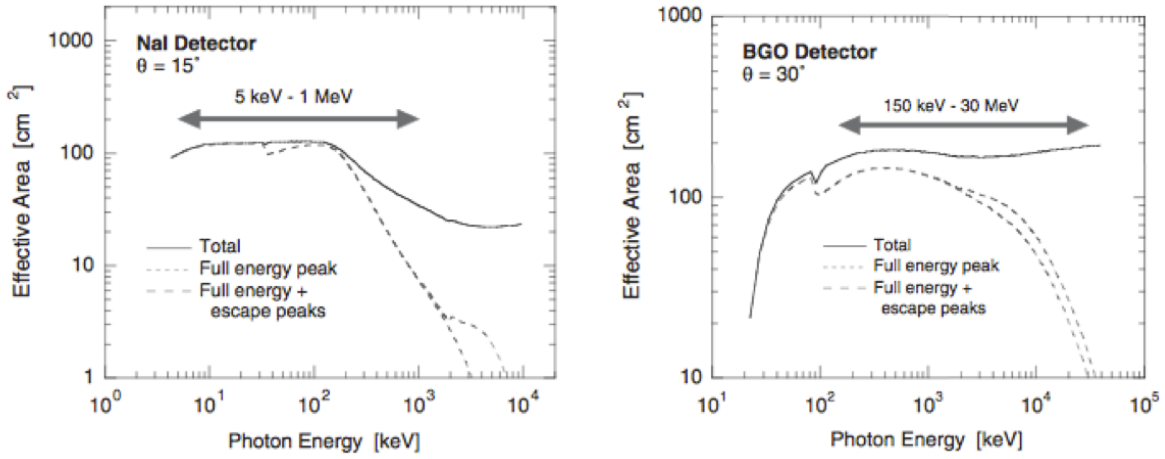

Figure 2.4: GBM (NaI and BGO) effective regions as a function of energy (Lichti et al., 2004).

The so-called LAT Low Energy (LLE) data cover an energy range of $\sim$ 30 - 130 MeV. These data, combined with a particularly large effective area with large off-axis angles, mean the LLE can provide excellent statistics with which to study the temporal and spectral properties of GRBs despite its higher background fluctuations. Therefore, LLE data can help to fill the gap between GBM and LAT and provide additional spectral cutoffs that would not otherwise be detected through the standard analysis of LAT. More details of the LLE data are provided in Chapter 5.

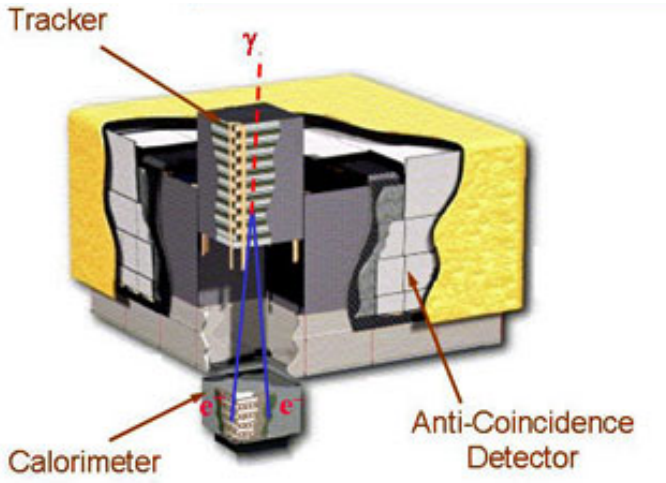

Figure 2.5: Cutoff of the *Fermi*(LAT) instrument shows the procedure of detecting Gamma-ray.

http://www.guidetothecosmos.com/radio/radio$_s how_0$950.*html*

2.1.7 Other Missions

The Compton Gamma-Ray Observatory (CGRO) allowed GRB data to be collected by three different experiments, namely the Burst and Transient Source Experiment (BATSE), the Energetic Gamma-Ray Experiment Telescope (EGRET), and the Imaging Compton Telescope (COMPTEL). The CGRO was launched on 5 April 1991, with the satellite itself being built in the early 1980s with four instruments to detect and study gamma rays, X-rays, and other astronomical objects. CGRO is considered to be one of the most important missions in terms of GRBs; it detected thousands of GRBs, as well as many other high-energy transient phenomena. BATSE observations allowed for the increased understanding of many of the characteristic features of GRBs at energies up to 1 MeV. However, the information available for higher energies was sparse, in spite of the observations made by COMPTEL and EGRET. Since EGRET detected very few GRBs, the characteristics of high-energy emission range was poorly understood before the launch of Fermi.

The BeppoSax observations investigated GRBs, observing targets ranging in energy from 0.1 to 300 keV; BeppoSax discovered numerous GRBs and other galactic objects. Providing a localization that ground-based telescopes can follow-up on, this enabled the first optical afterglow to be discovered by van Paradijs et al. (1997), and the first redshift by Metzger (1997). It also demonstrated that GRBs are cosmological objects. This satellite likewise detects the fading in X-rays (afterglow) after a long delay of about 4-6 hours. This satellite ended its mission on 30 April 2003. BeppoSax was most noted for its success in measuring redshifts and confirming that gamma rays originate from cosmological distances (Mészáros, 2006b).

Konus-Wind (Aptekar et al., 1995) a joint Russian-American experiment launched in 1994 on board the Global Geospace Science satellite (GGS-Wind), covering the energy range 10 keV - 10 MeV. The detection average of Konus-Wind 100 bursts per year. Two primary detectors are mounted on the telescope with another two detectors aligned inside the body of the telescope. It provides good coverage of the whole sky in an energy range covering gamma rays and hard X-rays, and also allows for soft gamma repeaters (SGRs) and solar flares to be monitored. It can generate light curves in three energy bands (10 - 50 keV, 50 - 200 keV, 200 - 750 keV, and above 10 MeV), with a time resolution of $\sim$ 64 ms. Since its launch, the era of the Konus-Wind observations has found a large number of GRBs.

Chapter 3

Joint GBM+BAT Fitting: Time-integrated Spectral Analysis

3.1 Introduction

Most of the important high-energy emission budget of GRBs is supposedly emitted during the prompt emission phase within the description offered by the internal shock model, which can be above GeV energies (Pe'Er et al., 2006). However, the discovery of early afterglow X-ray flares, as detected via *Swift*, also suggested the possibility of strong GeV emission from the external shocks (Wang et al. 2006; Fan & Piran 2006). Moreover, (Willingale et al. 2007) discussed the isotropic afterglow energy versus the isotropic prompt energy, which showed that the isotropic prompt emission energy is released about 10^{53} while the isotropic afterglow energy is released about 10^{51}. In most cases of GRB, the total energy released in X-rays from the afterglow showed a significant comparison with the γ and X-ray energy released from the prompt component (Willingale et al., 2007). Thus, studying GRBs' prompt emissions is very important to understand their natural mechanisms. Studying the spectral properties of GRB prompt emissions should lead to a greater understanding of the burst properties. To examine GRB properties, it is important to study their spectra in different energy domains in order to distinguish the varieties of spectra detected via different detectors. The most important high energy emission component is believed to be emitted from the prompt phase.

The spectral properties of prompt emission were first studied using BATSE data almost 30 years ago. With its wide energy range of 20 keV to 1 – 2 MeV, BATSE allowed the study of spectral phenomena related to both LGRBs and SGRBs. The integrated spectra over the burst duration of the prompt emission can be described by the peak in the vF_v spectrum, where E_{peak} represents the energy where the most intense emission occurs, regardless of the photon model used.

BATSE found a very narrow E_{peak} distribution across only a few hundred keV in the observer frame, with a distribution of one order of magnitude (Preece et al., 2000). The narrowing of the E_{peak} distribution in BATSE is due to its reduced sensitivity to harder bursts that emit in the MeV range. This is might be related to the jet structure of GRBs, though this matter is still under

debate. It has been suggested that there is potentially an instrumental sensitivity limitation that can interpreted as resulting in this narrower E_{peak} distribution, e.g., (Piran, 2005) as the E_{peak} shows a strong correlation with the fluence (or the peak flux) as shown by Nava et al. (2010) when comparing the E_{peak} from BATSE and *Fermi*, see Figure 3.1.

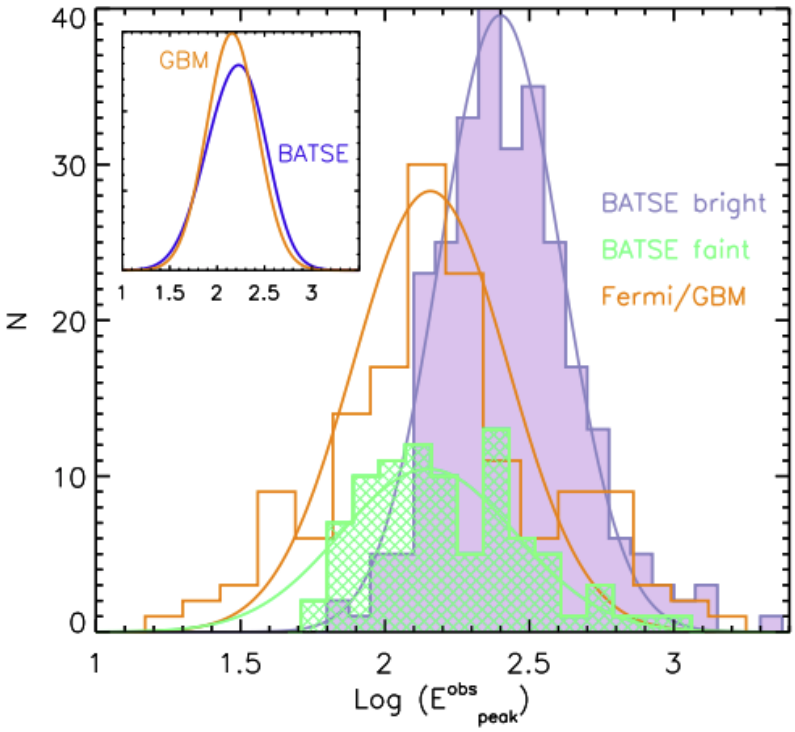

Figure 3.1: The E_{peak} distributions for BATSE bright bursts adapted from Nava et al. (2010) (filled histogram, from K06), BATSE faint bursts (shaded histogram, from Nava et al. (2008)) and *Fermi*(GBM) bursts (empty histogram). The insert compares the E_{obs}^{peak} distribution for the entire BATSE sample with that for Fermi(GBM) bursts.

http://heasarc.gsfc.nasa.gov/W3Browse/cgro/batsegrbsp.html

In the BATSE era, the data recorded allowed GRBs to be classified as LGRBs or SGRBs, as dependent on spectral/temporal properties. The spectral properties are different for these two classes due to the hardness ratio (HR) that characterizes each spectrum (Kouveliotou et al., 1993), where most GRB spectra vary in shape and their light curves can be either simple (smooth with a single pulse) or complex (constructed shape with a number of pulses separated by a timescale of the order of $\sim$ 10 milliseconds). Despite the diversity of burst spectra, correlations between the various spectral parameters have been determined for different burst properties. Hence, the HR of most SGRBs are hard, and thus exhibit a large E_{peak} in the observer frame. In the literature, Nava et al. (2008) and Ghirlanda et al. (2009) claimed that there is a relationship between E_{peak} and peak flux, while another study found there is a correlation between E_{peak} and fluence; therefore, different distributions based on these relations apply for both GRB classes.

Beside the Ghirlanda and Nava relations, a variety of empirical relations have been studied, (e.g., Amati et al. 2002; Amati 2003; Sakamoto et al. 2004; Sakamoto et al. 2006; Ghirlanda et al. 2004a; Liang & Zhang 2005; Yonetoku et al. 2004). Most of the *Swift* GRBs do not have a well-determined E_{peak}; a number of investigations have been undertaken to allow for the estimation of E_{peak} based on the observational quantities available. Re-examining the Amati $E_{peak,rest} - E_{iso,\gamma}$ and the Yonetoku $E_{peak,rest} - L_{iso,\gamma}$ relations for the joint-fit sample can help determine the

consistency of the original Amati and Yonetoku relation applied only for one instrument, e.g., GBM only. These two correlations are widely addressed in the literature and help to interpret and constrain the physical models as cosmological probes (e.g., Band & Preece 2005; Piran 2005; Kocevski 2012).

Since the launch of *Fermi* in 2008, a set of very interesting GRBs has been detected and recorded via both the *Fermi* (GBM/NaI+BGO) with its broad energy range (10 keV-40 MeV) and *Swift* (BAT), with its narrow energy range (15 - 150 keV). Thus, a spectral joint-fit of GBM+BAT is important for the *Swift* science in order to provide information about prompt emissions, e.g., E_{peak}. This is due to BAT having a narrower energy range, such that the peak of the spectrum in most cases is out of the observable energy range (Sakamoto et al., 2009), so adding GBM should enhance the spectral analysis in terms of allowing a better understanding of the E_{peak}. The higher effective area of the BAT should enhance the data quality at lower energies. In the joint-fit spectral analysis, the data are fit both jointly and separately to search for any significant improvements and to determine the spectral parameters in an unbiased manner.

This chapter is structured as follows. Section § 3.2 gives a description of the data reduction. The sample selection is given in section § 3.3. The spectral models are described in section § 3.4. The time-integrated spectra are analysed and interpreted in § 3.5. The results and discussion are presented in section § 3.6. The conclusions are finally given in § 3.7.

3.2 Data Reduction

The GBM data were downloaded from NASA's HEASARC website [1]. As mentioned in Chapter 2, *Fermi* has two detectors; 12 NaIs and two BGOs scintillators. In this analysis, it is important to choose the most illuminated GBM-NaI detectors, with detector angles < 60 degrees, and where these detectors should not be blocked by either the LAT detector or any other solar sources that could disturb the viewing angle (Goldstein et al. 2012; Gruber et al. 2014; von Kienlin et al. 2014). In total, two NaIs and one BGO GBM detectors are used. Here, only one of the BGO scintillators located near to the NaI detectors was chosen, unless there was only one bright NaI detector. The GBM energy bands range from 10 keV to 40 MeV (NaI: 10 keV-1 MeV and BGO: 200 keV-40 MeV).

Using the GBM CSPEC data (discussed in Chapter 2) for the purpose of the background subtraction procedure, this data type provides a high spectral resolution of 128 energy channels with a temporal resolution of 1024 ms. Subtracting the GBM background spectra is necessary for the spectral fitting analysis (more detail in this regard will be given the following section). The other data type is the Time Tagged Event (TTE); with a time resolution of 64 s, TTE data can record detection rates from 30 to 300 s in the pre-trigger and post-trigger intervals, while CSPEC data can extend the detection recording to about 8,000 s. Thus, CSPEC is more flexible

[1] http://fermi.gsfc.nasa.gov/

when subtracting the background to include as long a background interval as possible. The GBM tools, e.g., *gtbin* was used to generate light curves and spectra from an event data file; *gtbindef* is required by *gtbin* to create the input file in order to produce a modified energy and appropriate time binning [2]. The BAT data were downloaded from the UK *Swift* Science Data Centre (UKSSDC) archive [3]. BAT data were processed using the HEAsoft tools (NASA's Software packages, version v6.17) [4], specifically *batgrbproduct*, which generates typical *Swift*-BAT products, and *batbinevt* to produce time-sliced spectra. The BAT spectra were mask-weighted (also known as ray tracing; this is the operation required to perform the background subtraction), and created using *batupdatephakw* and *batphasyserr*. The *batdrmgen* tool was then used to create the response matrix.

3.3 Sample Selection

A number of GRBs ($\sim$ 80) were detected simultaneously with *Fermi* (GBM) and *Swift* (BAT) during the period between September 2008 and July 2017. The GRB sampling in this study was conducted from September 2008 to October 2015. The sample criteria are as follows: i) only LGRBs ($T_{90} > 2$s), ii) bright GRBs which had a peak flux in BAT > 2.6 ph cm^{-2} s^{-1} (as defined by Yu et al. (2016) were chosen, and iii) it is further required to bin with a signal-to-noise ratio, S/N > 30 in each time bin in order to have at least five counts bins for the source light curve, which was also adapted from the official GBM catalogue [5] (the GBM threshold is currently S/N per bin = 1.5). GRBs with spectroscopically confirmed redshift measurements were required for this study (with a redshift ranging from z = 0.49 - 2.73).

GRBs that were either detected by only one of the GBM detectors, or that did not satisfy the detector-to-source zenith angle of < 60 degrees (Paciesas et al., 2012) - that is, GRB 110213, GRB 120811, GRB 121128, GRB 130907, GRB 150314 and GRB 150821 - or if the spectra were faint and not well-constrained to the model - that is, GRB 141004 - were excluded from the analysis. By specifying these criteria, we ended up with high-quality data for a sample of 16 GRBs. Table 3.1 lists the population of the GRB sample and the associated redshifts.

3.3.1 Selection effects and biases

Figure 3.2 shows the data sample that is representative of the entire LGRB BAT catalogue by plotting 1-sec photon flux versus T_{90}. The data sample of LGRB with high photon fluxes shows the selection effect of our data is dependent on the availability of the coincident GRBs that were detected via *Swift* (BAT) and *Fermi* (GBM). Faint GRBs are hard to analyse because low photon

[2] https://fermi.gsfc.nasa.gov/ssc/data/p6v11/analysis/scitools/gbm_grb_analysis.html
[3] http://www.swift.ac.uk/swift_portal/
[4] https://heasarc.nasa.gov/lheasoft/
[5] https://heasarc.gsfc.nasa.gov/W3Browse/fermi/fermigbrst.html

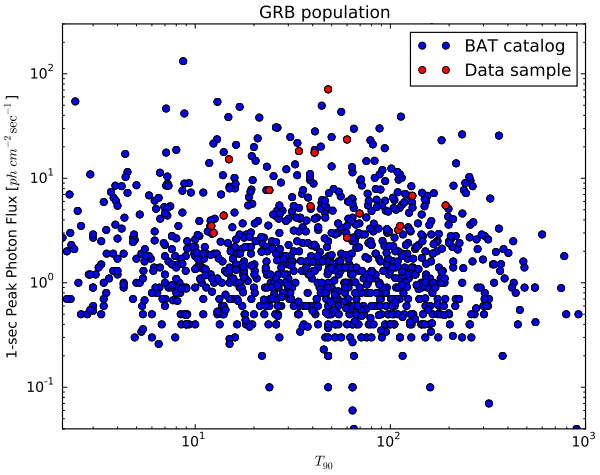

Figure 3.2: LGRBs distribution showing our data compared to the BAT catalogue 1-sec photon flux (ph cm^{-2} s^{-1}) verses T_{90} (sec).

counts are excluded. *Fermi* (GBM) and *Swift* (BAT) provide good GRB spectral coverage, which is essential to derive the spectral parameters of a prompt emission that includes different spectral models. Thus, choosing a data sample among the entire LGRB population is challenging in terms of ensuring that the data sample is not biased. The scope of the sample selection is purely that of focussing on a sample that satisfies our criteria, which is to limit the sample to providing only high-quality data that provides a reliable joint spectral analysis, especially in the case of time-resolved spectral analysis.

Table 3.1: The redshifts of the GRBs used in this analysis with their redshift references.

GRB	z	References
080916A	0.689	(Fynbo et al., 2008) GCN8254
081121A	2.512	(Berger & Rauch, 2008) GCN8542
081221A	2.26	(Hoversten et al., 2008)
081222A	2.77	(Cucchiara et al., 2008) GCN8713
090424A	0.544	(Chornock et al., 2009), (Jin et al., 2013), and (Wiersema et al., 2009) GCN9243
090926B	1.24	(Fynbo et al., 2009) GCN9947
091208B	1.063	(Wiersema et al., 2009) GCN10263
100615A	1.398	(Kruehler et al., 2013) GCN14264
100728B	2.106	(Flores et al., 2010) GCN11317
120326A	1.798	(Tello et al., 2012) GCN13118
120624B	2.1974	(Gruber, 2012) GCN13383
131105A	1.686	(Xu et al., 2013) GCN15450
140213A	1.2076	(Schulze et al., 2014) GCN15831
150301A	1.5169	(Lien et al., 2016)
150403A	2.06	(Pugliese et al., 2015) GCN17672
151027A	0.81	(Perley, 2015) GCN18487

3.3.2 Data statistics

In probability theory, the two main distribution types are the Gaussian (or normal) (equation 3.1) and Poisson distributions (equation 3.2). These two distributions provide a statistical test for data analysis that allows one to choose a best fit when using different models.

The *Cstat* data statics are used in this thesis, which are the favourite statistics for GBM data as they generally show low photon counts in the high energy bands (10 keV-40 MeV), which makes it inappropriate to use χ^2 (see equation 3.3), for example. In contrast, BAT data favours the use of χ as these data show high photon counts in the low energy bands (15 keV - 150 keV) which is an appropriate statistical method for this type of data. χ^2 is a statistical hypothesis test whereby the sampling has a χ^2 distribution only if the null hypothesis is true, which can be used to determine whether the fit is significantly different between the expected and the observed data when comparing the minimized χ^2. This is known as a minimum χ^2 estimation, which is a method used to estimate the expected data based on the observed data. The estimation of a minimum χ^2 can be calculated by dividing a statistic that is used over a number of degrees of freedom for each parameter estimated by this method. Other tests were used in this analysis, e.g,. the KS-test (the Kolmogorov–Smirnov test, see equation 3.4), which is a non-parametric test of the continuous equality known as a one-dimensional probability distribution. The KS-test is used where the distribution of a quantity is needed to determine if the two samples are driven from the same population via two parameters, the D-statistic (the absolute maximum distance between the CDFs, "the integrated PDF", of the two samples) and the P-value (the rejection of the null-hypothesis which shows that the two samples, for example, are drawn from the same distribution).

Here, it is essential to distinguish between the two different statistical tests that are used in this analysis. *Cstat*, which are known as Cash-statistics (Cash 1979; see equation 3.5), is essentially similar to the χ^2 statistic for counts/bins greater than about 10, which is not the same as when the counts/bins are in the order of 1. The differences between these two statistics are that χ^2 statistics are always scattered at 1.0, while the Cash-statistics can be extend to a large value at 1.2 for counts/bin = 1. Additionally, the slope of the scatter plots between χ^2 and Cash-statistics appears to change from gradients of < 1 for small counts to unity at large counts. However, unlike χ^2, the *Cstat* might be applied depending on the number of counts in each bin. Moreover, its magnitude depends on the number of bins included in the spectral fit and, indeed, the data values themselves.

$$P(x) = \frac{1}{\sigma\sqrt{2\pi}} e^{-(x-\mu)^2 \big/ 2\sigma^2} \tag{3.1}$$

$$P\left(x\right) = \frac{e^{-\lambda}\lambda^x}{x!} \tag{3.2}$$

$$\tilde{\chi}^2 = \frac{1}{d}\sum_{k=1}^{n}\frac{(O_k - E_k)^2}{E_k} \tag{3.3}$$

$$K_n = \sup_x |(F_n - F)(x)| \tag{3.4}$$

$$C = -2\sum_{i=1}^{9} In(1 - \sqrt{[(x_0 - x_i)^2 + (y_0 - y_i)^2]} + b) \quad (3.5)$$

3.4 Spectral Models

As mentioned in Chapter 1, GRBs can be described by the empirical "Band function" (Band et al., 1993) or by the exponential high-energy cut-off power law (hereafter referred to as CPL; see equation 1.3). The Band model is a unique function of two power laws joined smoothly at a so-called break energy (Band et al. 1993; Preece et al. 2000; see equation 1.2). This model is widely used for high-energy GRBs and is characterized by three parameters, the low- and high-energy photon indices (α and β, respectively) and the peak energy (E_{peak}, in keV). The CPL model is widely used to fit spectra when the Band model fails to constrain the high-energy index β; for the majority of cases the high-energy cut-off clearly needs to be constrained, and CPL is thus preferred over the Band model due to the lower number of free parameters available to allow a fit to be determined.

3.5 Spectral Analysis

In the following, a detailed description of the spectral analysis performed in this study is given, first through a discussion of the joint-fit method, then by introducing the criteria adapted for choosing the best-fit model and, finally, by defining the multiplicative factors determined through the joint-fit analysis to account for the inter-calibration uncertainties between different instruments. Combining time-integrated spectra (one spectrum for each GRB) from different GRB observatories leads to their characteristics being shared in a one-step "joint" analysis, such as the BAT large field-of-view "FOV" $\sim$ 1.4 sr and its high detection sensitivity, together with the high-energy GBM (10 keV - 1 MeV).

In practice, for some complex GRBs spectral backgrounds it is hard to obtain a perfect background subtraction using the *gtbin* tools, so in this case the use of the *Fermi* science tools, RMfit (V4.3.2)[6], was required to manually account for any possible background time evolution instead. Extracting the background is achieved by selecting a time interval before and after the burst, avoiding any part of the background close to the source in order to avoid contamination by the burst. In the *gtbin* tools, the software *GTburst* assumes (automatically) the background so determined is applicable to the chosen time interval.

[6]The software developed to process GBM spectral fitting and run as a virtual machine in the IDL environment

In this analysis, the most updated GBM response matrix was used, as released on the 6th September 2017 (*rsp2*) and which contains multiple matrices for the updated detector information corresponding to each time the detector is slewed 5 degrees across different regions. Simultaneously, the GBM *pha2* and BAT *pha* spectra files are read in XSPEC (v12.7.1) in order to be fitted with the desired model (Band and CPL) over the entire burst spectra and desired energy range. Excluding the GBM/NaI energy ranges between 30-40 keV is necessary to avoid the so called "Iodine K-edge" (Meegan et al., 2009); in this energy range, fewer photons are detected, and their systematic residuals are visible due to calibration issues (Guiriec et al., 2010).

For the BAT fit analysis, a new weighted response matrix was created when the satellite is slewed to account for the movement for each 5 degrees, which was then applied to the total spectrum (Lien et al., 2016). Due to the narrower energy range of the BAT (15 - 150 keV), the peak energy E_{peak} in most cases is not detected (Lien et al., 2016). For each burst, the spectrum is integrated over the T_{90}, which is the time during which 90% of the burst fluence is accumulated. This is required to ensure that the bright source alone is covered. In this analysis, the BAT trigger time is considered to be the reference trigger time.

Statistically, because the photons observed that constitute the BAT data are distributed in a Gaussian manner, the traditional χ^2 statistic was applied, which provides a certain "goodness-of-fit", and the GBM background subtraction was fitted using Gaussian statistics. However, the favourite GBM statistic is the $Cstat$, which contains Poisson errors and is used to estimate the 1σ asymmetric error.

Applying a constant of a normalization factor for GBMs (e.g., fixed at 1) and allowing the BAT to vary, the calibration will then be between 10 - 20%. This will clearly decrease the $Cstat$ for the majority of bright bursts due to the correction to the detector normalization. A large $Cstat$ can be due to a large calibration offset between the different detectors, and thus such a free factor is essential to overcome any systematic issues could affect the fit, especially when there are small errors in the data.

3.6 Results and Discussion

This section presents the results of the analysis for the time-integrated joint-fit spectra and the GBM-only using two models, namely the CPL and the Band models. Table 3.2 reports the results of the time-integrated joint-fit, where the spectra have been fitted using the CPL model. This table is ordered as follows: the time intervals (in Δt) over the duration of the T_{90} (column 2), the low-energy index α (column 3), the E_{peak} (column 4) in units of keV, and the normalization factor "offset" (column 5). The equivalent isotropic energy E_{iso} obtained from calculating the flux by integrating the best-fit model over the energy range 10 keV-1 MeV (in units of ergs) is listed (column 6), and finally the $Cstat$ is given (column 7).

In this section, a comparison of the spectral parameters found for the two cases considered (GBM-only and joint-fit) is discussed below, as follows: 1) a comparison of the low-energy photon indices; 2) a comparison of peak energies; and 3) a comparison of the E_{peak} and the low-energy indices α, in order to investigate any improvement in one compared to the other. Figure 3.3 shows the relationship between the CPL model parameters; the peak energy E_{peak}, as obtained from the analysis of GBM-only and joint-fit data fitted with the CPL model. Obviously, this correlation shows that when adding BAT data, the E_{peak} becomes high, and the red line (the regression line) diverges from the black line (the equality line) with a slope of 1.23 [0.03] (this slope is taken from the best-fit of the regression line), which indicates there are some significant differences in spectral behaviour between the BAT and the GBM spectral fitting. However, the two high $E'_{peak}s$ data points on the upper right can cause a bias, but cannot be ignored. Despite large error bars, the errors on the fit lines are sufficiently small that the lines have gradients that are not equal to unity. Similarly, the photon index α for the GBM-only versus the joint-fit shows a few deviations in the softer indices with a slope of 0.83 [0.04] when comparing the equality line and the best fit (red dashed line). Here, also as stated above, the large error bars cannot prevent the role of BAT data to get softer α, where the test statistics support this claim through a comparison of the value of the best-fit (regression line) although with the positive α located on the upper right in Figure 3.4. This positive value of α was obtained from the GBM-only that was fitted with the CPL model for the brightest burst in the sample "GRB 090926B", which has a hard low-energy spectral index α = 0.09 [+0.33, -0.29].

Here, also as stated above, the large error bars cannot prevent the role of BAT data to get softer α, where the test statistics support this claim through a comparison of the value of the best-fit (regression line) although with the positive α located on the upper right in Figure 3.4. This positive value of α was obtained from the GBM-only that was fitted with the CPL model for the brightest burst in the sample 'GRB 090926B', which has a hard low-energy spectral index α = 0.09 [+0.33, -0.29].

Figure 3.4 shows the spectral joint-fit analysis using the Band model for eight GRBs, where from the E_{peak} it is difficult to tell if the correlations are in agreement or otherwise, as seen in the plot of the best-fit line which deviates from the equality line in the higher and lower E_{peak} ranges, and intercepts it in the middle, with a gradient of 1.24 [0.04]. These eight GRBs that were best fitted with the Band model are listed in Table 3.3 for the joint-fit. The E_{peak} and the high-energy index β are listed in columns 4 and 5, respectively, with the $Cstat$ resulting from the fit and the associated *dof* (column 8). In these GRBs, the high-energy β were well constrained, which were preferred over the CPL with their slightly similar $Cstats$. The remaining GRBs were not well fitted by the Band model, with error bars that were sufficiently large that β could be $<$ -2 due to its high-energy tail being associated with a low photon count.

In contrast, the low-energy index α shows increased scattering that behaves differently to the spectral analysis obtained using the CPL model; these deviations may indicate the effect of

Table 3.2: The upper table is the time-integrated spectra for the GRB sample of this study fitted with the CPL model (joint-fit). The lower table is adapted from V12 of a sample of GRB fitted either with the CPL or Band models. The spectra in both studies were fitted in BAT energy bands (15 - 150 keV) and GBM energy bands (10 keV-1 MeV); the uncertainty adopted here was the 90% confidence interval.

GRB	Model	Δt [s]	α	E_{peak} [keV]	offset	E_{iso} [erg]	$Cstat(dof)$
			This study				
080916A	CPL	89.15	$-1.17^{+0.14}_{-0.15}$	116^{+32}_{-61}	0.82	$50.32^{+0.13}_{-0.28}$	322.1(417)
081121A	CPL	22.397	$-0.94^{+0.13}_{-0.14}$	341^{+89}_{-138}	0.76	$52.6^{+0.15}_{-0.39}$	269.7(294)
081221A	CPL	55.296	$-0.83^{+0.04}_{-0.05}$	82^{+4}_{-5}	0.8	$52.35^{+0.05}_{-0.06}$	483.9(299)
081222A	CPL	65.534	$-1.09^{+0.11}_{-0.12}$	153^{+38}_{-64}	0.8	$52.08^{+0.11}_{-0.2}$	287.4(418)
090424A	CPL	20.48	$-1.04^{+0.02}_{-0.02}$	178^{+10}_{-11}	0.87	$51.46^{+0.03}_{-0.04}$	644.1(417)
090926B	CPL	116.156	$-0.19^{+0.19}_{-0.2}$	76^{+10}_{-13}	0.83	$50.88^{+0.16}_{-0.54}$	236.6(299)
091208B	CPL	18.176	$-1.36^{+0.13}_{-0.14}$	114^{+34}_{-66}	0.94	$51.33^{+0.12}_{-0.24}$	435.7(416)
100615A	CPL	43.583	$-1.27^{+0.1}_{-0.1}$	73^{+13}_{-18}	0.81	$51.41^{+0.09}_{-0.16}$	308.9(299)
100728	CPL	287.748	$-0.91^{+0.03}_{-0.03}$	372^{+34}_{-39}	0.87	$52.22^{+0.04}_{-0.05}$	234.7(419)
120326A	CPL	23.613	$-1.14^{+0.16}_{-0.17}$	47^{+8}_{-12}	0.78	$51.56^{+0.13}_{-0.32}$	303.34(298)
120624B	CPL	204.803	$-.94^{+0.02}_{-0.02}$	819^{+77}_{-89}	0.83	$52.66^{+0.04}_{-0.04}$	477.09(419)
131105A[a]	CPL	127.548	$-1.3^{+0.07}_{-0.07}$	242^{+61}_{-103}	0.66	$51.63^{+0.08}_{-0.11}$	286.6(300)
140213A	CPL	90.045	$-1.25^{+0.1}_{-0.1}$	82^{+14}_{-21}	0.88	$51.3^{+0.09}_{-0.15}$	306.0(417)
150301A	CPL	26.303	$-1.28^{+0.15}_{-0.18}$	217^{+100}_{-337}	0.94	$51.45^{+0.15}_{-0.35}$	285.9(299)
150403A	CPL	48.704	$-1.0^{+0.02}_{-0.02}$	606^{+55}_{-63}	0.91	$52.76^{+0.03}_{-0.04}$	599.4(417)
151027A	CPL	168.704	$-1.44^{+0.08}_{-0.1}$	323^{+140}_{-382}	0.78	$50.69^{+0.10}_{-0.15}$	349.1(421)
GRB	Model	Δt [s]	α	E_{peak} [keV]	β	E_{iso} [erg]	$\chi^2(dof)$
			V12				
080916A	CPL	69.633	1.24 ± 0.1	134^{+3}_{-23}	-	-	402(410)
081121A	Band	21.501	$0.53^{+0.16}_{-0.18}$	175^{+31}_{-25}	$2.16^{+0.19}_{-0.14}$	-	398(391)
081221A	Band	39.422	0.86 ± 0.06	81 ± 3	$3.14^{+0.6}_{-0.28}$	-	568(410)
081222A	Band	14.336	$0.85^{+0.07}_{-0.08}$	140^{+14}_{-13}	$2.39^{+0.33}_{-0.2}$	-	460(371)
090113A	CPL	12.288	$1.29^{+0.19}_{-0.23}$	138^{+100}_{-39}		-	346(348)
090424A	Band	19.710	0.95 ± 0.02	155 ± 5	$2.89^{+0.26}_{-0.17}$	-	844(525)
090926B	CPL	64.513	$0.20^{+0.14}_{-0.15}$	83 ± 4	-	-	520(529)
091020A	CPL	28.672	1.36 ± 0.08	266^{+97}_{-59}	-	-	382(412)
091208B	CPL	13.312	1.36 ± 0.09	118^{+22}_{-15}	-	-	486(375)
100615A	Band	40.574	$0.91^{+0.29}_{-0.03}$	50^{+15}_{-10}	$2.07^{+0.20}_{-0.09}$	-	437(410)
100728A	CPL	191.487	0.80 ± 0.03	313^{+19}_{-17}	-	-	538(411)
100906A	Band	121.347	$1.44^{+0.11}_{-0.59}$	106^{+35}_{-64}	$1.99^{+0.23}_{-0.2}$	-	589(526)
120326A	CPL	16.924	1.21 ± 0.08	55^{+2}_{-61}	-	-	654(490)

[a]GRB 131105A shows a smaller offset (0.06) compared with the other GRBs which seems to be out of GBM and BAT calibration (10 - 20%) for unknown reason.

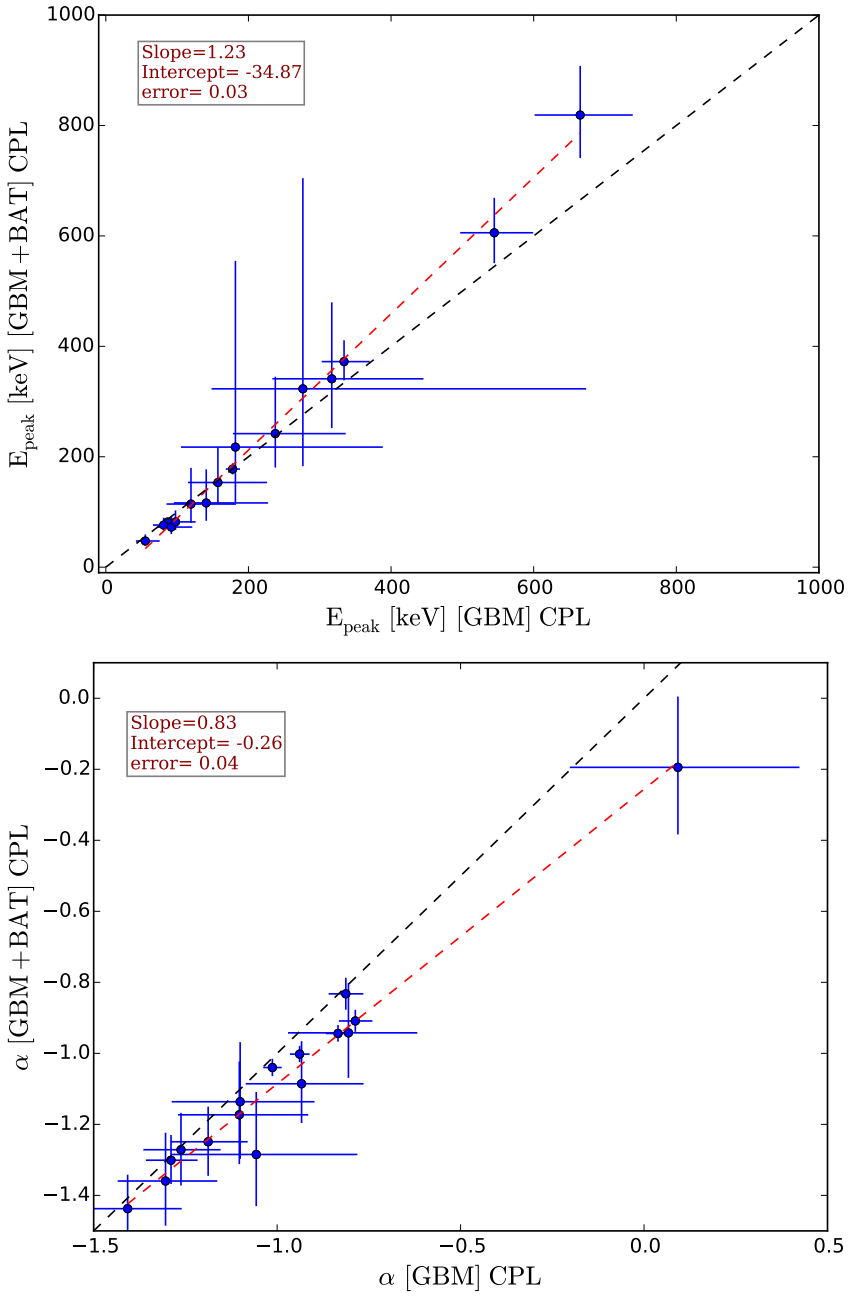

Figure 3.3: The upper panel is the E_{peak} correlation obtained from the joint-fit and GBM-only. The bottom panel is the α correlation obtained from the joint-fit and GBM-only. Fitted with CPL model, in both panels, the red dashed line is the regression best fit, whilst the black dashed line is the equality line.

the high-energy index β, which is unconstrained, with large parameter uncertainties in the high-energy band in certain GRBs. Generally, if the CPL model is sufficient to fit the data then there is no need to use the Band model; however, here we are only showing how these two models behave with regards to their best fits, as it has been suggested that models with fewer model parameters are usually preferred over more complicated models, at least in some cases. Interestingly, rather than β, which in principle controls the high-energy curvature, α in the CPL model, for both the low- and high-energy curvatures.

The upper panel in Figure 3.5 shows the $Cstat$ histogram of the two models (CPL and Band) in order to verify the improvements in the statistics between these two models. As can be seen, there are no noticeable (and significant) improvements, with both models showing a good fit to a number of GRBs. However, the Band model is generally favoured over the CPL model for most GBM-only spectral analyses. The lower two panels show the distribution of the E_{peak} and the α for GBM-only and the joint-fit, where the joint-fit is labelled in grey and GBM-only is labelled in red. The KS-test was applied to compare and study the distribution of the two samples with a reference probability distribution; the joint-fit and the GBM-only (statistic and P-values are labelled in the small boxes) for the E_{peak} and α distributions showed that the sample distributions were very likely drawn from the same population, with P-values of 0.912 and 0.633, respectively, whereas the $Cstat$ distribution shows a P-value of around 0.023, i.e., less than 2σ, which simply shows that this distribution is drawn from the same population but is not significant.

The majority of GRBs have an E_{peak} value ranging between 158 - 631 keV in both models. The low-energy index α distributions are similar in both cases (the joint-fit and the GBM-only), where the range of index values is between -1.5 and -0.9. For almost all GRBs in the sample, the GBM/BGO detector showed low photon counts in the high-energy tail (40 MeV). However, including the data gathered from this detector is important in terms of obtaining an upper limit to the high-energy side and to revealing the effective high-energy tail of the GBM data.

To summarize, the comparison between the two models (Band versus CPL) shows that they are not significantly different in some cases, and this fact can be clearly seen in the histograms, where the majority of the samples were fitted with the CPL model. Moreover, the distribution of E_{peak} and α for the GBM-only and the joint-fit models are consistent with each other. Furthermore, the spectral analyses of the joint-fit provided here are in agreement with those found in Yu et al. (2016). As can be seen, there is a slight, systematic difference in the best-fit parameters compared to GBM-only, which can be summarized as follows:

i) spectra are found to be somewhat softer when BAT is included. ii) the detected peak energies E_{peak} are systematically higher at high energies and lower at low energies when including the BAT data. Generally, there is a correlation between GBM-only and the joint-fit that can be noticed within the regression best-fit line (in red), though there is a deviation between this line and the equality line, which may be caused by normalization differences between the detectors.

Table 3.3: The time-integrated spectra for the eight GRBs that best fitted with Band model for the joint-fit. The spectra were fitted in the energy range for GBMs (10 KeV-1 MeV); the uncertainties adapted here are 90% confident levels.

GRB	Δt [s]	α	β	E_{peak} [keV]	offset	E_{iso} [erg]	$Cstat(dof)$
081121A	22.397	$-0.60^{+0.35}_{-0.50}$	$-2.00^{+0.56}_{-0.15}$	181^{+94}_{-233}	0.72	$52.86^{+0.38}_{-0.13}$	266.90(293)
081221A	55.296	$-0.77^{+0.07}_{-0.06}$	$-2.91^{+0.09}_{-0.23}$	78^{+6}_{-8}	0.81	$52.40^{+0.89}_{-0.88}$	479.43(298)
081222A	65.534	$-0.98^{+0.14}_{-0.17}$	$-2.13^{+0.72}_{-0.24}$	127^{+38}_{-58}	0.80	$52.34^{+0.64}_{-0.43}$	282.53(417)
090424A	20.48	$-0.98^{+0.03}_{-0.35}$	$-2.54^{+0.19}_{-0.13}$	157^{+12}_{-14}	0.87	$51.55^{+0.12}_{-0.13}$	627.13(416)
100615A	43.583	$-0.74^{+0.32}_{-0.39}$	$-2.05^{+0.15}_{-0.08}$	46^{+16}_{-31}	0.81	$51.73^{+0.27}_{-0.22}$	286.29(298)
120326A	23.613	$-0.64^{+0.36}_{-0.49}$	$-2.41^{+0.25}_{-0.15}$	39^{+13}_{-19}	0.78	$51.68^{+0.25}_{-0.35}$	295.18(297)
140213A	90.045	$-0.64^{+0.30}_{-0.34}$	$-2.02^{+0.09}_{-0.06}$	49^{+13}_{-21}	0.88	$51.65^{+0.34}_{-0.26}$	271.95(416)
150403A	48.704	$-0.98^{+0.03}_{-0.03}$	$-2.46^{+0.48}_{-0.23}$	563^{+65}_{-71}	0.90	$52.87^{+1.46}_{-1.41}$	589.30(416)

3.6.1 Spectral Analysis in The Literature

The spectral joint-fit has been extensively discussed in the literature (e.g., Ghirlanda et al. 2010b; Rao et al. 2011; Page et al. 2011; Bissaldi et al. 2011; Basak & Rao 2012b; Virgili et al. 2012). In this section, the comparison between this and previous studies is divided into two sections:

1. The Joint-fit

Virgili et al. (2012) (hereafter referred to as V12) have analysed a sample of 75 short/long bursts detected by *Swift* (BAT) and *Fermi* (GBM), which they fit individually and jointly with the PL, CPL and Band models. Table 3.2 reports the GRBs in common with this study fitted with the best-fit model (CPL or Band), as adapted from V12 with nine GRBs that are in common with this study.

To compare, in this analysis we found that there is considerable consistency between both analyses (this study and V12) as fitted with the CPL model. For example, GRB 080916A shows α values of -1.17 [+0.14, -0.15] and -1.24 [$\pm$0.10], measured E_{peak} values of 116 [+32, -61] and 134 [+31, -19], respectively. GRB 090926A recorded α values of 0.19 [+0.19, -0.2], 0.20 [+0.14, -0.15] and E_{peak} of 76 [+11, -10] and 83 [$\pm$4], respectively. In these two examples, it was found that the E_{peak} are smaller and α are harder compared to V12, but nevertheless lie within their uncertainties. GRB 091208B recorded an E_{peak} value of 114 [+34, -66] and 118 [+22, -15], while α was -1.36 [+0.14, -0.13] and -1.36 [$\pm$0.09], respectively. Again, in GRB 100728A, the E_{peak} in this study was higher at 372 [+34, -39] than found in V12 of 313 [+19, -17], whilst similar α values were found, at 0.91 [$\pm$0.03] and 0.8 [$\pm$0.03]. No significant differences were found between these two studies, however, and the few differences in the results may be due to the use of different analysis methods. Positive α signs in V12 are considered to be negative signs for

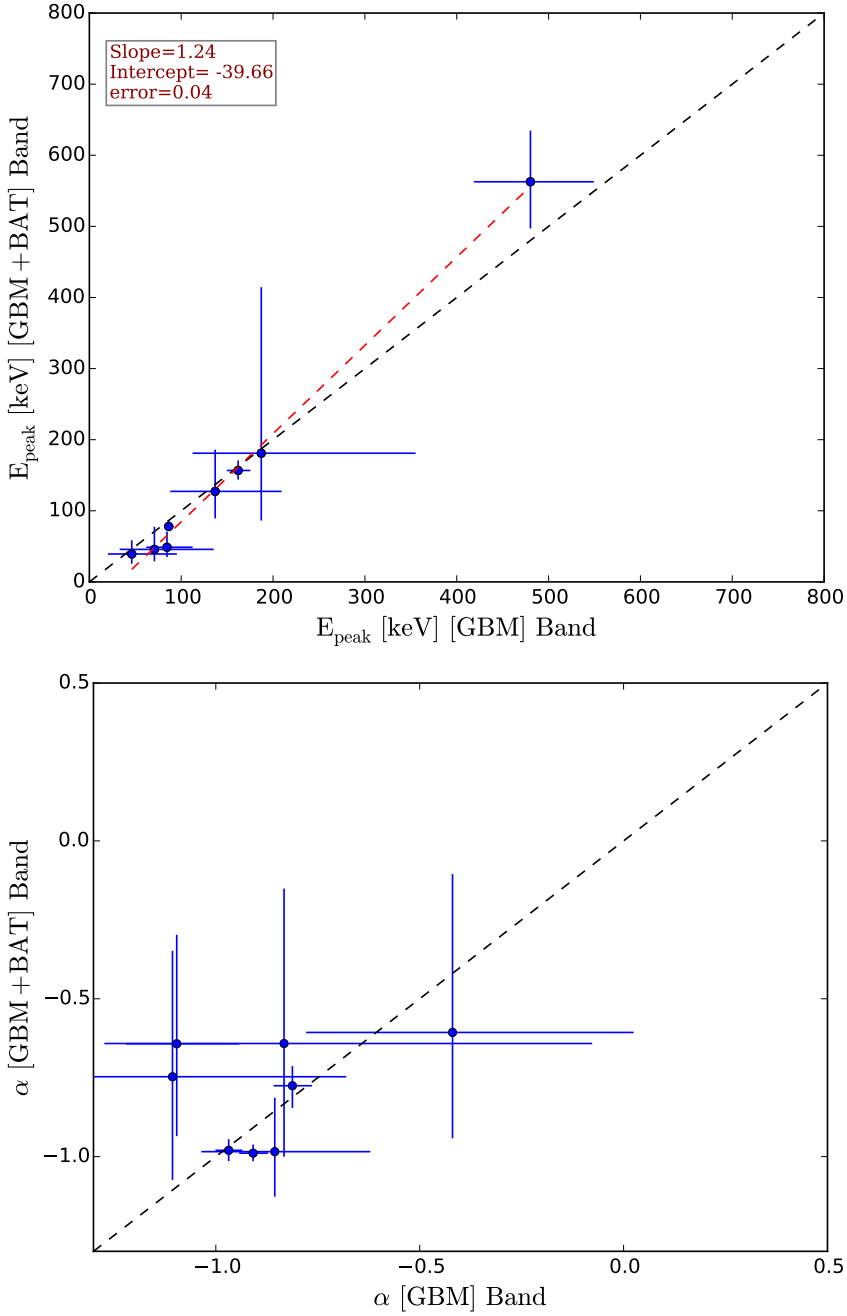

Figure 3.4: The upper panel is the correlation of E_{peak} for GBM-only vs. the joint-fit (the red dashed is the regression best-fit line and the black dashed line is the equality line.). The bottom panel is the correlation of the low-energy index α for GBM-only vs. the joint-fit, both fitted with the Band model (including only the GRBs that were best fit with the Band model).

clarity, which depends on the convention of the model.

2. GBM-only

Table 3.4 and Table 3.5 show the GRB spectral analyses for GBM-only (all samples) fitted with CPL and Band (only 10 GRBs), respectively. These two tables are provided to allow for comparison with the two GBM spectral analysis studies, namely Nava et al. (2011) (hereafter referred to as N11) and Bissaldi et al. (2011) (hereafter referred to as B11).

Table 3.6 shows the spectral fitting adapted from N11, the GCN archive, B11, and this study. In N11, a large sample of 323 *Fermi* (GBM) GRBs, as recorded up to March 2010, were analysed using either the CPL or Band models. It shows that the spectral joint-fit adapted from N11 and the GCN (for individual GRBs) are generally consistent within the associated parameter uncertainties in this work. There are a few deviations between N11, the GCN and this study that can be noticed when comparing the relevant parameters. For clarity, only a few of the GRBs that are in common with this study are reported in this table for comparative purposes.

Moreover, the spectral analysis results for two GRBs, namely GRB 081121A and GRB 090424A, are included (the same GRBs in this study sample), as adapted from B11. For instance, B11 found the E_{peak} values for GRB 081121 and GRB 090424 are smaller than those found by N11, while in this study were found to be much larger, but still consistent within the (large) error range reported in N11. Different spectral models can result in different values for the spectral parameters, but the values obtained from different studies using different models show roughly consistent parameter values within their error bars.

There is no significant difference between the α values obtained from N11, B11 and this study, whilst for GRB 081121A the α obtained from this study takes a larger value than those reported in N11 and B11. However, the time-intervals are different in these studies, yet the results are nevertheless somewhat consistent within the associated parameter uncertainties, as shown in Table 3.6. These few deviations between the spectral parameters obtained from this study and the previous studies (N11, B11 and V12) occur for the following reasons: i) different procedures used for extracting data and the choice of different time intervals for the GBM background subtraction; ii) different time intervals chosen for the burst; iii) different GBM detectors were chosen; or iv) different statistics were used, either χ^2 or $Cstat$.

Indeed, using different statistics might increase the possible deviations, but choosing appropriate statistics for different data is essential to the reduction of any systematic errors that might occur. For the joint-ft spectral analysis, in choosing the best-fit model by calculating the differences as $\Delta Cstat$, it was found that the best-fit model is that which provides the lowest $Cstat$.

Table 3.4: The spectral parameters for the time-integrated spectra (GBM-only) in this work. The spectra were fitted with CPL in the GBM energy range (10 keV - 1 MeV); the uncertainties adapted here are 90% confidence levels.

GRB	Δt[s]	α	E_{peak} [keV]	E_{iso} [erg]	$Cstat(dof)$
080916A	89.15	$-1.10^{+0.19}_{-0.17}$	141^{+45}_{-87}	$50.36^{+0.22}_{-0.24}$	263.07(360)
081121A	22.4	$-0.81^{+0.19}_{-0.16}$	317^{+83}_{-129}	$52.58^{+0.27}_{-0.31}$	211.37(237)
081221A	55.3	$-0.81^{+0.05}_{-0.05}$	86^{+5}_{-6}	$52.36^{+0.06}_{-0.06}$	353.98(242)
081222A	65.53	$-0.93^{+0.17}_{-0.15}$	157^{+42}_{-69}	$52.09^{+0.20}_{-0.22}$	226.83(361)
090424A	20.48	$-1.01^{+0.03}_{-0.02}$	178 ± 10	$51.46^{+0.03}_{-0.03}$	501.10(360)
090926B	116.16	$0.09^{+0.33}_{-0.29}$	81^{+15}_{-20}	$50.88^{+0.38}_{-0.43}$	160.82(242)
091208B	18.18	$-1.30^{+0.14}_{-0.13}$	119^{+34}_{-63}	$51.33^{+0.16}_{-0.18}$	374.50(359)
100615A	43.58	$-1.26^{+0.11}_{-0.10}$	92^{+19}_{-29}	$51.45^{+0.12}_{-0.13}$	234.65(242)
100728B	287.75	$-0.79^{+0.05}_{-0.04}$	334^{+31}_{-36}	$52.20^{+0.07}_{-0.07}$	172.74(362)
120326A	23.61	$-1.10^{+0.20}_{-0.19}$	55^{+13}_{-20}	$51.58^{+0.21}_{-0.23}$	247.17(241)
120624B	204.8	$-0.83^{+0.03}_{-0.03}$	665^{+64}_{-74}	$52.61^{+0.06}_{-0.06}$	376.33(362)
131105A	127.55	$-1.29^{+0.07}_{-0.07}$	238^{+60}_{-99}	$51.63^{+0.09}_{-0.10}$	206.19(243)
140213A	90.05	$-1.19^{+0.11}_{-0.10}$	98^{+20}_{-28}	$51.33^{+0.12}_{-0.13}$	207.51(360)
150301A	26.30	$-1.06^{+0.28}_{-0.23}$	182^{+76}_{-207}	$51.41^{+0.32}_{-0.38}$	223.26(242)
150403A	48.70	$-0.94^{+0.03}_{-0.03}$	545^{+48}_{-55}	$52.74^{+0.04}_{-0.04}$	451.46(360)
151027A	168.7	$-1.41^{+0.15}_{-0.12}$	276^{+128}_{-397}	$50.66^{+0.17}_{-0.20}$	291.46(364)

A comparison of the results obtained in this study with the latest GBM catalogue (Gruber et al., 2014) is important. This catalogue presents a complete sample of 943 GRBs detected via GBM during four years of operation. A time-integrated spectral analysis and a peak flux analysis were applied in this catalogue. Different photon models were used in order to allow comparison and to choose the most statistically preferred model for each GRB, resulting in more than 7500 spectral fits. The time-integrated spectral distributions can be characterized generally from their emission properties, without the need to consider any spectral evolution. For a typical GRB, the low-energy indices are distributed at -1.1, where up to 17% of the best low-energy indices exceed $\alpha = -2/3$ (violation from synchrotron "line-of-death"), whereas 18% of α are $< -3/2$ (violation from synchrotron cooling limit). The high-energy indices can peak at $\beta = -2.1$ and extend to a long tail at steeper indices. The catalogue also provides a comparison between the time-integrated low- and high-energy spectral indices $\Delta S = (\alpha - \beta)$, where this quantity is useful with regards to the synchrotron shock model (SSM), which can be used to predict this value in such cases (Preece et al., 2002). A consistent result for ΔS can be found in the time-resolved results in Preece et al. (2002) and the time-integrated results found in Kaneko et al. (2006). The E_{peak} distribution is generally a peak around 150 - 200 keV, which covers two orders of magnitude, and where the E_{peak} distribution is similar to that found in BATSE. Significantly, the E_{peak} value can affect the low-energy spectrum index, where spectra with smaller E_{peak} values

Table 3.5: The spectral parameters for the time-integrated spectra (GBM-only) in this work for only 10 GRBs that are best fitted with the Band model. The spectra were fitted in the energy range for BAT (15 - 150 keV) and for GBM (10 keV - 1 MeV); the uncertainties adapted here are 90% confidence levels.

GRB	Δt [s]	α	E_{peak} [keV]	β	$Cstat(dof)$
081121A	22.397	$-0.42^{+0.44}_{-0.36}$	187^{+168}_{-75}	$-2.08^{+0.13}_{-0.42}$	206.65(236)
081222A	65.534	$-0.86^{+0.23}_{-0.18}$	137^{+72}_{-49}	$-2.43^{-2.43}_{-0.41}$	224.42(360)
090424A	20.48	-0.97 ± 0.03	162^{+13}_{-12}	$-2.68^{+0.16}_{-0.25}$	490.97/359
091208B	18.176	-1.29 ± 0.14	116^{+66}_{-34}	$-2.97^{-2.97}_{-0.71}$	374.66(358)
100615A	43.583	$-1.11^{+0.43}_{-0.23}$	71^{+65}_{-38}	$-2.22^{-2.22}_{-0.23}$	235.07(241)
120326A	23.613	$-0.83^{+0.76}_{-0.44}$	46^{+49}_{-26}	$-2.57^{-2.57}_{-0.34}$	248.67(240)
120624B	204.803	-0.79 ± 0.04	572^{+77}_{-65}	$-2.33^{+0.17}_{-0.31}$	374.2(361)
140213A	90.045	$-1.10^{+0.15}_{-0.12}$	85^{+28}_{-23}	$-2.38^{+0.23}_{-0.48}$	202.86(359)
150403A	48.704	$-0.91^{+0.04}_{-0.03}$	480^{+69}_{-62}	$-2.32^{+0.17}_{-0.31}$	434.25(359)
151027A	168.704	$-1.35^{+0.26}_{-0.17}$	211^{+493}_{-132}	$-2.21^{-2.21}_{-0.36}$	291.39(363)

tend to have smaller α values due to the fact that the E_{peak} is close to the instrument's lower energy sensitivity limit. Smaller E_{peak} values contribute to the increase in the α measurement, which is due to the fact that a spectrum with a low E_{peak} can carry most of the curvature close to the lower end of the instrument's energy bands.

3.6.2 Case Study: GRB 090424A

GRB 090424A is one of the brightest GRBs ever detected via *Fermi* (GBM) or *Swift*/BAT, XRT and UVOT on 24th April 2009 at GBM:14:12:08.67 UT, and BAT:14:12:09.33 UT. The time difference in the GBM and BAT trigger times was $\sim$ -0.665 s. The T_{90} for GBM and BAT at 8 keV-1 MeV and 15-350 keV were 52 s and 48 $\pm$ 3 s, respectively. This bright GRB was used as an individual example with which to demonstrate a number of spectral properties. The GBM and BAT light curves showed an intense, multi-pulse and extended GRB with a total emission lasting about 60 s. This GRB light curve contained four main pulses lasting a total of about 6 s, which continue to a small pulse until about 20 s after trigger time; see Figure 3.6. In GBM, the time-averaged spectrum of the peak starts at T_0-1.024 s and lasts until T_0+19.456 s. The fluence (10 keV - 1 MeV) over the entire event at -0.3 s to 59 s was 5.2 $\pm$ 0.1 1×10^{-5} erg cm^{-2}. The 0.128-sec peak photon flux was 137 $\pm$ 5 ph cm^{-2} s^{-1} measured at 1.4 s in the 8-1 MeV range (see Cannizzo et al. 2009; Wiersema et al. 2009 Jin et al. 2013; GCN 9223). This GRB has a relatively low redshift of 0.544 [Gemini-South, GCN 9243 (Chornock et al., 2009)], [WHT ISIS, GCN 9250, (Wiersema et al., 2009)]. This burst showed a strong deviation of 1.6 σ in the time-integrated spectrum, which was due to an irregular spectral characteristic near E_{peak} (Tierney et al., 2013), which is known to cause deviations in time-integrated spectra (Abdo et al.

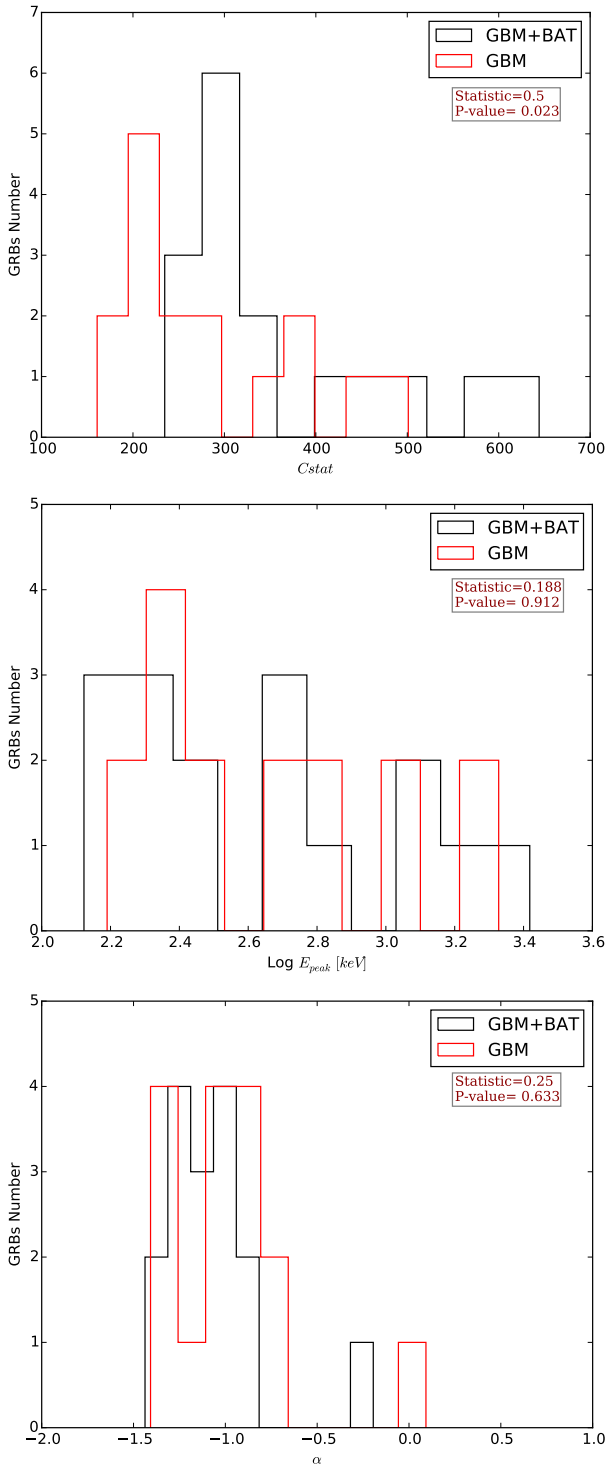

Figure 3.5: The upper panel is the distribution of Cstat statistics for all GRBs that were fitted with the CPL, where the GBM is shown in red and the GBM+BAT shown in black. The middle panel is the distribution of E_{peak} values, whilst the last panel is the distribution of α values for GBM and GBM+BAT fitted with the CPL model. The small boxes on the right-hand side show the KS-tests for each distribution.

2009a; Zhang et al. 2011). The peak flux for this burst was extremely high at 110 ph cm^{-2} s^{-1} (Paciesas et al., 2012).

The comparison of the spectral joint-fit of GRB 090424A in this study and the one in V12 is presented in Tables 3.2. Generally, there is reasonable consistency within the parameter uncertainties, even considering the different models used in this study and in V12, e.g., E_{peak} = 177.69 [+9.7, -10.52], α = -1.04 [+0.02, -0.02], were obtained from this study as fitted with CPL, whilst V12, as fitted with Band, gave values of E_{peak} = 155 [+5, -5] and α = -0.95 [+0.02, -0.02]. As discussed below, different statistics were applied in each analysis, which makes any comparison inaccurate. The observed spectra are shown in Figure 3.7, where the joint-fit spectra plot shows the GBM/NaI (n8, nb) and BGO (b1) and BAT, jointly fitted with the CPL and Band models in the 10 keV-1 MeV and 1 - 150 keV regions, respectively. All other GRB spectra are shown in Appendix A.1. The wavelength radio afterglow instruments, such as the Very Large Array (VLA), have also detected this GRB at a frequency of 8.46 GHz. GRB 090424A was one of the brightest radio afterglows detected at the UVOT position (Cannizzo et al. 2009 GCN 9223), where the radio flux density measured for this burst was 673 $\pm$39 uJy (Chandra & Frail 2009 GCN 9260). The Suzaku Wide-band All-sky Monitor (WAM) detected this same GRB at 14:12:09.216 UT in the 50 keV - 5 MeV energy band. The duration of this burst was T_{90}= 4.18 s, the fluence was 1.36 [-0.10,+0.28] $\times 10^{-5}$ erg cm^{-2} s^{-1}, and the 1-sec peak flux measured was 12.6 [-0.9,+1.6] photons cm^{-2} s^{-1} in the 100 keV - 1 MeV energy band. The time-averaged spectrum fitted with the CPL model from T_0 = 1 to T_0= 12 was for the E_{peak}= 250 [-83,+41] keV and α = 0.92 [-0.77,+0.66] (Hanabata et al. 2009 GCN 9270).

Table 3.6: Comparison of the spectral parameters (GBM-only) adapted from N11 and the GCN for some common GRBs in this study. Two repeated GRBs (GRB 081121A and GRB 090424A) were added, as adapted from B11.

GRB	Model	Δt [s]	α	β	$E_{peak}[keV]$	$Cstat(dof)$
			N11			
080916A	CPL	60.42	-0.99 ± 0.05	-	123 ± 7	583.16 (482)
081121A	Band	26.62	-0.46 ± 0.08	-2.19 ± 0.07	178 ± 11	411.3 (353)
081221A	Band	39.42	-0.82 ± 0.01	-3.73 ± 0.20	86 ± 0.74	999.8 (600)
081222A	Band	21.5	-0.90 ± 0.03	-2.33 ± 0.10	167 ± 8	744.6 (604)
090424A	Band	34.05	-1.02 ± 0.01	-3.26 ± 0.18	162 ± 2	1179 (718)
090926B	CPL	65.54	-0.19 ± 0.06	–	94 ± 2	934.8 (472)
091208B	CPL	13.31	-1.29 ± 0.04	–	119 ± 8	411.9 (348)
100615A	CPL	39.55	-1.34 ± 0.04	–	106^{+8}_{-6}	989.3 (606)
100728A	CPL	199.68	-0.76 ± 0.01	–	354 ± 7	3540 (727)
120326A	Band	17.41	-0.98 ± 0.14	-2.53 ± 0.15	46 ± 4	653.1 (489)
			The GCN			
120624B	Band	292.5	-0.85 ± 0.01	-2.36 ± 0.08	566 ± 20	–
131105A	Band	124	-1.2 ± 0.1	-1.8 ± 0.1	204 ± 31	–
140213A	Band	19	-1.01 ± 0.03	-2.41 ± 0.04	80 ± 2	–
150301B	CPL	11.26	-1.2 ± 0.1	–	256 ± 32	–
150403A	Band	22.3	-0.72 ± 0.02	$-1.85 \pm 0.0.3$	311 ± 14	–
151027A	CPL	135	-1 ± 0.04	–	340 ± 63	–
			B11			
081121A	Band	-	$-0.47^{+0.14}_{-0.12}$	$-1.94^{+0.06}_{-0.07}$	158^{+18}_{-17}	456(356)
090424A	Band	-	-0.86 ± 0.02	-0.76 ± 0.08	146 ± 3	843(478)
			This study			
081121A	CPL	22.4	$-0.81^{+0.19}_{-0.16}$	–	317^{+84}_{-129}	211.37(237)
090424A	CPL	20.48	$-1.01^{+0.03}_{-0.02}$	–	178 ± 10	501.10(360)

3.6.3 The inclusion of *Swift* (BAT) data

The consequences determined from this analysis through the inclusion of the BAT data in the joint-fit spectral analysis can be summarized as follows. The inclusion of BAT data resulted in changes in the model's parameters as the linear regression best-fit line (red dashed line) shown in Figure 3.3, for example, shows the E_{peak} has a gradient of 1.23[0.03], which can be significant. The plot itself shows that the inclusion of the BAT data shifted the E_{peak} to a higher value at higher energy bands and reduces the errors on low energy E_{peak} values. The importance of inclusion of the BAT data is to add more photons with more reliable good statistics and widen the useful energy band (10 keV - 40 MeV). A spectral joint-fit, in general, can provide better spectral fitting due to the joining of two instruments, which can overcome the obstacles that can be encountered when using only one instrument in isolation.

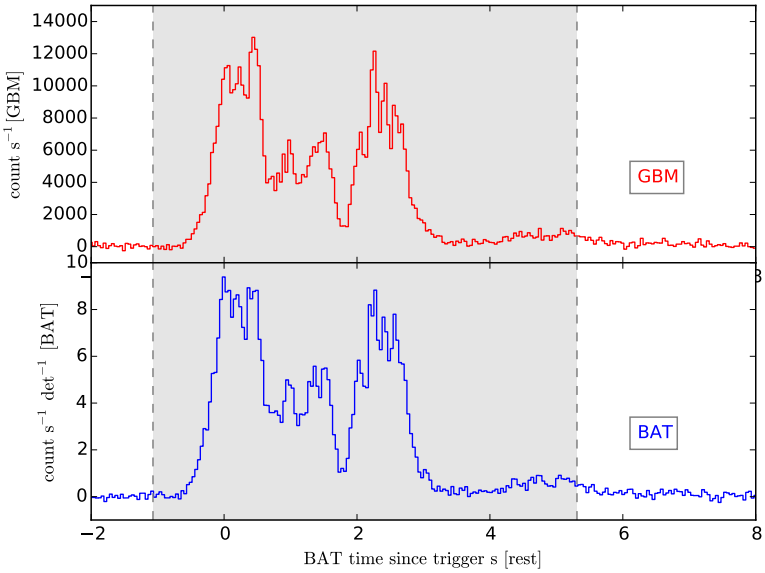

Figure 3.6: The light curves for GBM and BAT using the BAT time trigger in the rest frame. The shaded vertical dashed lines show the time interval selected for the time average T_{100}. BAT spectra are plotted in black, GBM spectra are plotted in red (n8), green (nb) and blue (b1).

With regards to the low-energy photon index α, it has been found that there is a lower shift to the softer α than was found without the inclusion of BAT. The significant differences found in this case were confirmed by the linear regression best-fit line which has a gradient of 0.38 [0.04] compared to the equality line (black dashed line). To link these features of the joint-fit (GBM+BAT) back to the physics described in Chapter 1, it is essential to note some of the advantages of including BAT, including the fact that BAT can provide good statistics, and BAT detector sensitivity can also allow for more accurate fitting. Together with the GBM high-energy band, it becomes possible to calculate E_{peak}, which is otherwise impossible.

3.6.4 Amati and Yonetoku Relations

The Amati and Yonetoku relations are applied when an observable (E_{peak}) and an unobservable can be correlated with either E_{iso} or L_{iso} quantities. Which these two quantities can be describe as the measuring of the maximum energy in an individual photon (the E_{peak}) and the total emitted energy that indicates the amount of energy released (E_{iso}). The E_{peak} physically has a larger and harder amount of energy, where most of the emission is radiated. High isotropic energy E_{iso} can lead to a high E_{peak}, and high isotropic luminosity L_{iso}, in which the rate at which energy can be released leads to a more energetic burst.

Furthermore, it is important to note that the Amati relation refers to the time-integrated spectral properties of GRBs, and is a reliable means of determining both the E_{peak} and the spectral

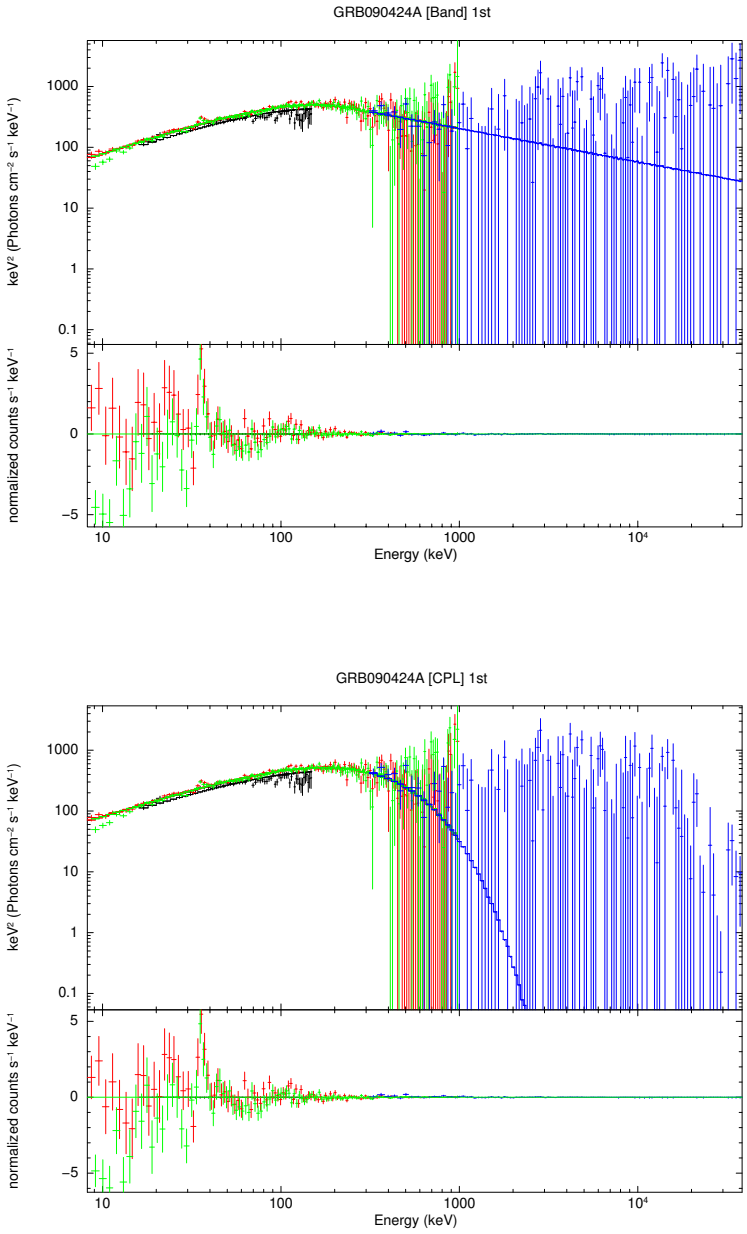

Figure 3.7: The upper panel shows the time-integrated spectra (joint-fit) of GRB 090424A fitted with Band. The bottom panel is the CPL model. The upper part of both panels shows the unfolded νF_ν spectra and the bottom part shows the residuals. BAT spectra are plotted in black, GBM spectra in red (n8), green (nb) and blue (b1).

indices that are needed to calculate the rest frame isotropic energy, E_{iso}.

However, in Chapter 4 time-resolved spectral analyses are presented to re-examine these relations, which demonstrates that GRB spectra show time evolution during the prompt emission phase (e.g., Ford et al. 1995; Preece et al. 2000; Ghirlanda et al. 2002). The spectral evolution is clearly different for each GRB (e.g., Ford et al. 1995), and is also clearly not related to other GRB properties such as peak flux, pulses or duration. This is may due to the time variation in the parameters caused by the GRB radiative processes (e.g., Liang & Kargatis 1996) or due to the relativistic outflow jet (e.g., Ryde & Petrosian 2002).

To understand such a correlation, it is essential to determine if these correlations are revealing the overall energetic characteristics or are dominated by time-resolved spectral properties. If these correlations are dominated by emission processes, one of the possibilities that arises is to compare the peak energy and the peak luminosity, which is what the Yonetoku relation does (Yonetoku et al., 2004).

Since the launch of the *Fermi* instruments, a number of GRBs with redshifts measured in the high-energy domain have allowed an accurate measurement of the peak energy, $E_{peak,rest}$. In the meantime, the precise localization achieved by the *Swift* instrument has indeed allowed for a better understanding of GRB properties with known redshifts in the study of the correlation between the peak energy in the vF_v spectrum in the source rest-frame and the equivalent isotropic energy, E_{iso}, in the 1 keV-10 MeV range. However, a fraction of the GRBs detected via *Swift* (BAT) were not useful to this relation, where $< 20\%$ of E_{peak} could only be estimated due to their relatively narrow energy band (15 - 150 keV); see Butler et al. (2007).

Since 1997, the possibility of being able to measure the redshifts of *Swift* GRBs (which total more than 200 events to date) has allowed for a systematic analysis of the study of GRB spectral properties. In order to calculate E_{iso} and L_γ, the $\wedge CDM$ cosmological standard model must be used, where H_0 = 70 km s^{-1} Mpc^{-1} is the Hubble constant is the unit of measurement used to describe the expansion of the universe [7], Ω m = 0.27, and $\Omega\wedge$ = 0.73 (which are density parameters for matter and dark energy, respectively) (Freedman et al., 2001). In this correlation study, the K-correction is also required (the correction of the energy bands between the observed source frame and observed rest frame). To calculate $E_{iso,rest}$ using its well-known formula:

$$E_{iso,rest} = 4\pi\, d_L^2\, F\, K_{corr} \frac{\Delta t}{(1+z)} \tag{3.6}$$

where Δt is the time interval over the spectral fit obtained, F is the averaged flux over time interval Δt, K is the K-correction, d_L is the luminosity distance, and the factor $(1+z)$ is the cosmological time dilation correction.

[7] The rate of expansion of the Universe is anisotropic; for instance, the nearby universe as measured by the Hubble Space Telescope and Gaia space telescope give a Hubble constant of $\sim$ 70 km s^{-1} Mpc^{-1}, whereas the more distant background universe, which has been measured by the Planck telescope, shows a smaller Hubble constant of $\sim$ 67 km s^{-1} Mpc^{-1})(Planck Collaboration et al., 2018), however in Riess et al. (2019) they used $\sim$ 73 km s^{-1} Mpc^{-1}, we used 70 as a value in between these two estimates

Table 3.7: The Amati and Yonetoku relations taken from this study and from N11. One of the samples provided in Nava's paper, which is the 'complete sample' of 46 GRBs, are reported showing the gradients, the normalizations and the number of GRBs in the sample.

Correlation	No. GRB	Slope	offset
		N11	
Amati	46	0.61 ±0.04	-29.60±2.23
		This study	
	16	0.46 ±0.09	-21.55±2.43
		N11	
Yonetoku	46	0.53±0.06	-25.33±3.26
		This study	
	16	0.45±0.13	-20.49±2.45

It was found that when using the Amati gradients and intercepts adapted from Nava et al. (2011), the Amati relation obtained from this work shows a certain consistency with the original Amati relation. Only LGRBs were found to follow the Amati relation, which was due to the lack of measured redshifts for the SGRBs and also due to their high energies, e.g., $E_{iso} \sim 10^{51} - 10^{55}$ ergs, while $E_{peak,rest}$ is between $10^2 - 10^4$ keV (Amati et al. 2008; Zhang et al. 2009c; Ghirlanda et al. 2009; Amati 2010; see, e.g., Norris & Bonnell 2006 & Zhang et al. 2009c). Similarly, the Yonetoku relation is the correlation between the equivalent isotropic energy and the isotropic luminosity at 1-sec peak flux ($E_{peak,rest} - L_{iso,\gamma}$) (Wei & Gao 2003;Yonetoku et al. 2004).

The nature of this relation describes the circumstance where pulses decay as the prompt emission softens, and thus flux decreases. Examining this correlation within this study shows some offsets around the equality line with a noticeable deviation shifted up to a high E_{peak}. Table 3.7 reports the gradients of the Amati and Yonetoku relations adapted from Nava et al. (2012); three samples were discussed in this paper, namely the total, the complete and the complementary samples. In Nava et al. (2012), the gradient and the normalization of the complete sample of 46 GRBs were chosen to test these two relations. The gradients for the complete sample for both Amati and Yonetoku are 0.61 [+0.04, -0.04] and 0.53 [+0.06, -0.06], respectively.

Generally, Figure 3.8 shows the Amati relation in this study are in agreement with Nava's best-fit line (90% of data errors and 3σ for the slope range). Almost all GRBs are inside their range within about 3σ. However, one GRB showed some slight deviation from the 3σ limit at an $E_{peak} \sim 500$ keV. In general, this is in agreement with the original Amati relation (Amati et al. 2002; Wei & Gao 2003).

The Yonetoku relation (Figure 3.8) shows a greater offset than the Amati relation due to the average luminosity seemingly being unaffected by $E_{peak,rest}$ compared to $E_{iso,\gamma}$, which shows a better correlation than L_{iso}. These offsets may due to the Yonetoku relation being used with 1-sec peak flux. The Yonetoku relation can be applied for both LGRBs and SGRBs, while the Amati

relation is only applicable for LGRBs, which might be produced by the same emission processes (Zhang et al. 2009b; Ghirlanda et al. 2009; Guiriec et al. 2013; Tsutsui et al. 2013).

3.7 Conclusions

To conclude, a joint-fit spectral analysis was applied to 16 bright LGRBs, all of which were coincidentally detected via *Swift* (BAT) and *Fermi* (GBM) during the period between September 2008 and October 2015. Procedures for analysing the spectra of GRBs were explained in detail, from the initial data collection to the results of the spectral fitting.

The joint-fit did, in general, show substantially different values for the spectral parameters compared to the GBM-only analysis, and adding BAT data was found to improve the fitting quality, reducing the systematic errors in some cases. Two spectral models (CPL and Band) were applied in this study. Regardless of the best-fit model, from a practical perspective both models were used for the purposes of joint-fit comparisons, but only the eight GRBs that were well fitted with Band were reported in this analysis. In fact, there is only one study to have provided a large joint-fit (GBM+ BAT) sample in the literature (V12), with data collected over the period from June 2008 to May 2011. It was necessary to choose sample criteria in this study that focussed only on the bright and LGRBs whose redshifts had been previously measured in order to investigate the behaviour of the special evolution in detail. The joint-fit spectral analyses were compared for the two parts, first for the joint-fits reported in this study and in V12, and second for GBM-only with the joint-fit reported in this study for both the CPL and Band models.

To compare this study with V12, it is very important to note that a number of comparative spectral analysis methods have been used in both studies that need to be considered. First, in this study, only bright and LGRBs were included, while V12 also included faint and SGRBs. Second, the time intervals in V12 were slightly different from the ones chosen for this study; in this analysis, the BAT trigger times were chosen as the reference trigger times, where the analogous reference was not otherwise mentioned in V12.

Third, it was important to examine the appropriate statistics and test the data fitting, which in this study was the use of χ^2 statistics for the BAT data and $Cstat$ for the GBM data, whilst it was considered that calculating $\Delta\ Cstat$ was the only way in which to find the goodness-of-fit because there is no standard probability distribution for the likelihood of $Cstat$. V12 used χ^2, which could only have been possible if the authors of this study rebinned the GBM spectra. In this case, the reduced χ^2 (~ 1) was determined to test the best fit. Therefore, a comparison of the statistics here would not necessarily represent an exact result. But, in general, the spectral joint-fit analysis showed good agreement with the results reported in V12, ignoring any deviations that were found between the joint-fit obtained in this study and in other studies that occurred as a result of the different analysis methods being used. Here, one of the GRBs in the sample (GRB 090424A) was examined in detail by considering its own spectral analysis. All other

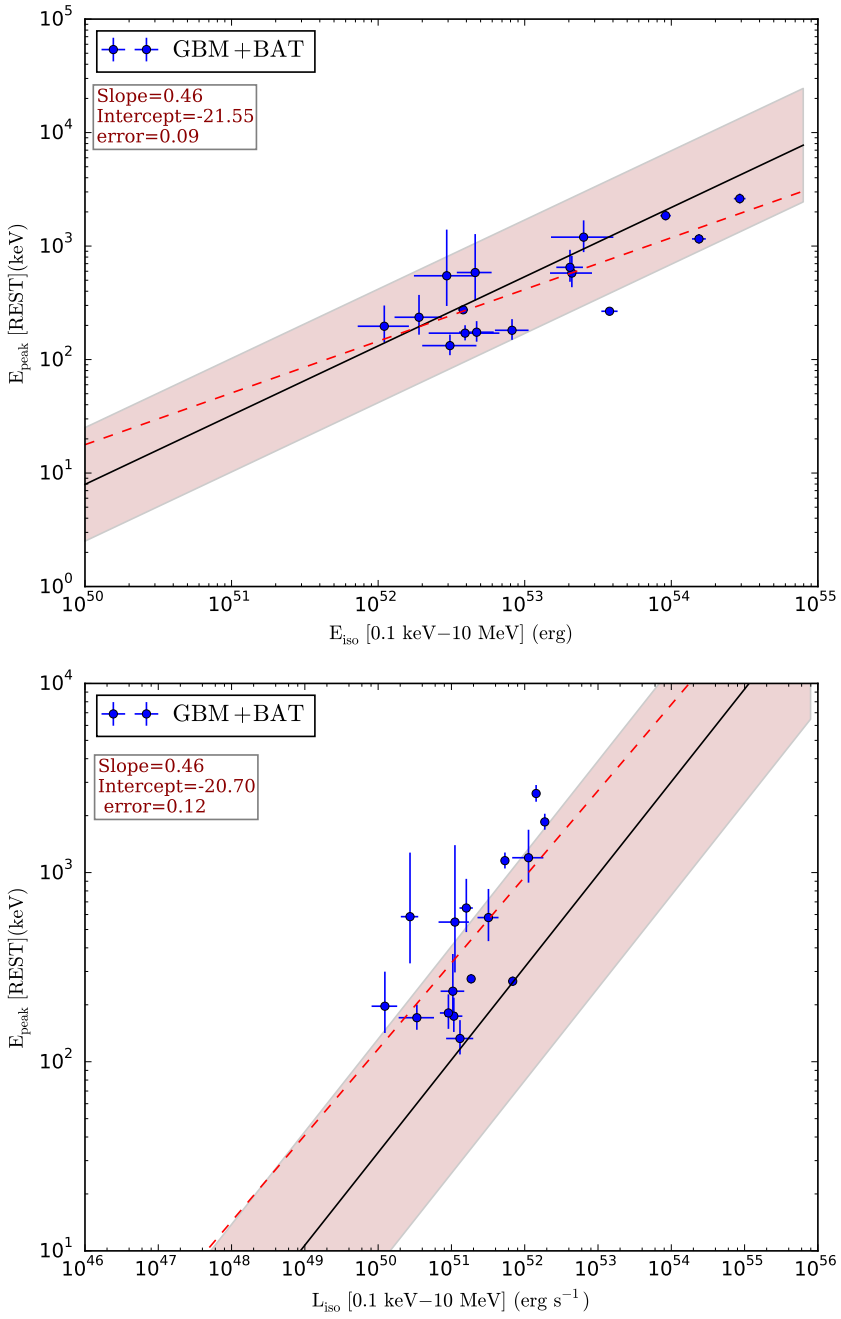

Figure 3.8: The upper panel is the Amati relation $E_{peak,rest}$-$E_{iso,\gamma}$ and the bottom panel is the Yonetoku relation $E_{peak,rest}$-$L_{iso,\gamma}$ for the time-integrated spectra in the rest frame for the joint-fit (GBM+BAT) fitted with the CPL model, as shown in blue. The pink shaded region represents the 3σ offset around the best-fit line adapted from Nava et al. (2008). The red dashed line is the best fit found in this study, as shown in both panels.

GRBs' spectral joint-fit analyses are listed in Appendix 1. With regards to independent GBM-only analyses in the literature, there are some studies that have analysed individual GRBs; for instance, N11 analysed 438 GRBs detected via GBM. In N11, there were 10 GRBs in common with this study, the comparisons of which were in good agreement with N11 and this study.

The Amati relation examined in this study showed a reasonable agreement with the original Amati. Including GRBs with measured redshifts in order to obtain the $E_{iso,rest}$ and $L_{iso,rest}$ was required to allow the examination of these relations. The gradient of the best fit (red dashed line) for this study was consistent within the bounds of its uncertainty with the original Amati (black solid line) reported in Table 3.7.

While the Yonetoku relation showed a deviation toward either higher E_{peak} or lower luminosity, this is may have been due to the different peak flux that was used in this study and the original Yonetoku relation, which the last used 1-sec peak flux, while the current study used the average flux. similarly, the gradient of the best fit (red dashed line) for this study was consistent, within its limits of uncertainty, with the original Yonetoku reported in Table 3.7.

Chapter 4

Joint GBM+BAT Fitting: Time-Resolved Spectral Analysis

4.1 Introduction

Time-resolved spectroscopy allows for a detailed interpretation of bright and LGRBs, giving a coherent physical picture of their spectra. Due to the long duration and high flux of long and bright GRBs, their data can provide better statistics for time-resolved spectral analysis, and also allow the systematic study of temporally extended emission (Zhang et al., 2016). For example, time-resolved spectral analysis can demonstrate the hard-to-soft spectral evolution seen in most GRBs (Ford et al. 1994; Ford et al. 1995; Band 1997). In theory, an understanding of bulk prompt emission phenomena can be improved if the emission is sliced into different time intervals (Zhang et al., 2012). Clearly, implementing some form of time-resolved spectral analysis is important.

The resolved spectral analysis for individual GRBs has been discussed in various studies for different X-ray and gamma ray instruments, e.g., BATSE (25 keV-2 MeV, Pendleton et al. 1994; Preece et al. 2000; Kaneko et al. 2006; Goldstein et al. 2013), *BeppoSAX* (40-700 keV, Frontera et al. 2009), *Swift*(XRT) (0.3-10 keV, Evans et al. 2009), *Swift* (BAT) (15-150 keV, Sakamoto et al. 2008b; Sakamoto et al. 2011), *Fermi* (LAT) (20 MeV-300 GeV, Ackermann et al. 2013), and *Fermi* (GBM) (time-integrated, 8 keV-40 MeV, Kaneko et al. 2006; Nava et al. 2011; Goldstein et al. 2012; Gruber et al. 2014; von Kienlin et al. 2014).

In particular, other researchers have studied time-resolved spectral analysis in significant detail in the attempt to provide a clear understanding of spectral properties and the manner of their evolution, e.g., Hakkila et al. (2008) studied the correlations of essential prompt emission features such as the pulse lag, luminosity and pulse duration. Another study by Hakkila & Giblin (2004) investigated the relationship between pulses and their structures in two GRBs (GRB 960530 and GRB 980125). In addition, Basak & Rao (2012a), Zhang (2012) and Page et al. (2011) analysed the spectral pulses of GRB 090618A in a time-resolved manner to allow for the spectral and temporal analysis of prompt emission. These studies have played an important role in clarifying the complex picture of the mechanism of prompt emission through the in-depth study of GRB spectra.

The aim of studying the spectral joint-fit analysis for time-resolved spectra analysis is to investigate spectral behaviour in different energy bands using different instruments' data and to account for such evolution in each time interval. A good S/N (e.g., > 30) ratio[1] is required to ensure significant counts per time bin (time slicing). The joint-fit time-resolved spectra analysis are a powerful tool with which to investigate, for example, the evolution of the peak energy, E_{peak}. Indeed, studying the spectral evolution of the parameters allows for certain advantages when considering evidence from GRBs. *Fermi* (GBM) and *Swift* (BAT) provide useful tools with which to simultaneously analyse spectral parameters and search for possible improvements to joint-fit time-resolved spectral analysis.

In this chapter, a time-resolved spectral analysis is performed with a sample of 16 GRBs and 189 spectra. Therefore, the technical joint-fit spectral analysis method and sample selection will not be discussed further here as they have already been described in Chapter 3. This chapter is structured as follows. In § 4.2, the spectral analysis and procedures, in order to further provide a perspective for the time-resolved spectra analysis, are discussed. The report of the spectral joint-fit results is discussed in § 4.3. The E_{peak} evolution is discussed in § 4.4. Amati and Yonetoku's time-resolved spectral relations are examined in § 4.5. The conclusions to this chapter are presented in § 4.6.

4.2 Spectral Analysis

The methodology for the joint-fit time-resolved spectra analysis used here was adapted from Ghirlanda et al. (2010b), and can be summarized and reintroduced (as mentioned in Chapter 3) as follows:

• Choosing a sample of 16 bright LGRBs observed coincidentally with *Fermi* (GBM) and *Swift* (BAT) between September 2008 and October 2015. The sample selection was based on a BAT peak flux of > 2.6 ph cm^{-2} s^{-1} with the time binned to an S/N ratio > 30 for each spectrum. Three of the *Fermi* (GBM) bright detectors (two NaI and one BGO) and *Swift*(BAT), in their desired energy bands, were chosen for each GRB.

• The delay times between GBM and BAT are always given due consideration; the telescope clock correction is applied, thus calculating the time differences between GBM and BAT using the UT trigger time for each in order to precisely account for the time differences between the two. There was a need to obtain the time differences in order to choose the exact time slice in the GBM and BAT light curves. Also, the MET trigger time was used to generate the BAT spectral files for each time slice, using the BAT tool *batbinevt*. Other differences in the GBM and BAT light curves were caused by the slewing of the telescope itself or often by the telescope being blocked by the Earth, leading to time gaps.

[1] S/N is used to group the time-resolved spectra analysis accumulated by the instrument.

• The criteria for selecting the time slices were met by covering the rising and the falling pulses individually. For some faint intervals, it was essential to consider the whole pulse in order to include as high a photon count as possible. The sample included only bright bursts, but in some cases the late time intervals of a burst have often faded, thus there would be insufficient counts to fit the associated spectra. To avoid any discrepancy in the time-resolved spectral analysis, any pulses occurring within the time intervals for one of the instruments that were not seen by the other were ignored.

• The software used to extract the GBM data and fit the background were RMfit, GTburst, and GTbin; whilst all these programs do almost the same job, it was found that GTbin can extract the data automatically by implementing the appropriate tools via a *Python* script run in XSPEC. Using GTbin, as provided by *Fermi* tools, helps to extract the relevant data and create *pha* files for each time slice, which is otherwise difficult to achieve manually. However, some of the GBM data backgrounds were extracted using RMfit (using CSPEC data, as mentioned in Chapter 3) and their backgrounds fit with an appropriate polynomial of an order ranging between 1-4. For most GBM data, GTburst was used, which is very useful due to its ability to subtract backgrounds and fit them with a model automatically, so here there was no need to try different polynomial orders to test the background best-fit model. With regards to BAT data, the data extraction was performed using the *Heasoft* tools (as mentioned in Chapter 3) and by adding BAT's *pha* to allow for a joint fit with GBM data in XSPEC.

• The statistics used in each instrument are $Cstat$ for GBM and a default χ^2 for BAT, where in this analysis the $Cstat$ test statistics were used for the joint-fit and the GBM-only spectral fitting, throughout both this and the previous chapter. The $\Delta Cstat$ obtained from the different models (CPL and Band) were compared in order to choose the best fit.

4.3 Results and Discussion

The presentation of the results of the joint-fit time-resolved spectral analysis is divided into two sections; first, a detailed discussion of the spectral analysis for one chosen example, GRB 090424A; and second, presenting the whole sample, applying the same method of analysis for all GRBs.

4.3.1 Case study: GRB 090424A

As mentioned in Chapter 3, this GRB is one of the brightest bursts detected via GBM and BAT, thus it is a very good example with which to study E_{peak} evolution and other spectral properties. The GRB 090424A light curve shows multiple and complex structures and contains three pulses groups. A significant low-energy deficit was detected in either the time-integrated or the time-resolved spectral analysis of this GRB. The first of these is a high pulse that consists of three

to four spikes which continued into a smooth decay, creating a smaller pulse cluster; then, the light curve rose again to another high pulse grouping of four pulses. The light curve was sliced into 35 time slices starting from -1.024 s and ending at +19.456 s; this selection of time interval was based on the rising and falling pulses on the light curve. Little spectral evolution was seen throughout this GRB. There was no specific criterion by which to choose the time interval, which was purely based on the duration of each pulse that appeared large enough to slice into small sequence time intervals, otherwise the whole pulse was chosen. This was determined by eye.

The upper panels in Figure 4.1 show the two light curves from GBM and BAT, where the blue light curve is BAT data (15 - 150 keV) and the red light curve is GBM data (10 keV - 1 MeV), assuming there are no significant background variations that could affect the burst light curve during the burst, which is consistent with the pre- and post-burst light curves shown in this Figure. The dashed grey lines are the T_{90} time intervals sliced into a number of main groups: the pre-burst, first pulse, second pulse, third pulse, and the quiescent regions. There was further time slicing between these groups of pulses (not shown in the plot).

Generally, in each time bin there were sufficient photon counts to allow for the spectral analysis fitting. Otherwise, if the time intervals of certain time slices had relatively low counts (a GRB is either weak or faint), for example when dividing the pulse into small time intervals, this would result in a bad fit so it was better to enlarge the time interval selection of a pulse since it is important to obtain sufficient counts. The lower two panels show, via black dots, the peak energy E_{peak} with its associated uncertainties and the low-energy index α plotted for each time slice. The E_{peak} shows different trend patterns; for instance, in the majority of time slices, E_{peak} is higher for bright pulses and low for faint pulses, where this behaviour can be described as an "intensity-tracking" evolution (E_{peak} evolution is discussed in the following section). The upper panel in Figure 4.2 shows the time-resolved joint-fit spectra fitted with CPL, whilst the lower panel shows the Band fit for the GBM detectors n6, n7 and b1 and BAT in the time interval [4.32 s: 4.43 s], whereas all the GRB spectra for each of the time slices are reported in Appendix A.2.

The time-resolved spectral analysis of GBM GRB 090424A presented by Tierney et al. (2013) is for only one time interval, [2.3 s: 3.3 s], for the CPL model, where the authors found E_{peak} = 169.50 [4.61, -4.40] keV, α = -0.87 $\pm$0.03 with $Cstat(dof)$ = 738.26 [596], whilst for Band fit the E_{peak} = 153 [+7.01, -7.33] keV, α = -0.80 $\pm$0.04 and β = 2.81 [+0.17, -0.23]. In this study, the same time interval [2.3 s: 3.3 s rest-frame] [4.32 s: 4.43 s observer-frame] was chosen and, using the CPL model, the following was obtained: E_{peak} = 168.15 [+25.85, -32.65] keV, α = -0.67 [+0.11, -0.12] and $Cstat(dof)$ = 261 (417). These two spectral parameters were consistent within their uncertainties; however, different GBM detectors were used for each of the analyses, as in this study the GBM detectors are n7, n8 and b1, while Tierney et al. (2013) used n6, n7, n8, nb and b1. Even though GRB 090424A, as used in this study, was fitted jointly with BAT, the results were in agreement with Tierney's analysis. Generally speaking, comparisons of the joint-fit and the GBM-only are usually consistent. For most GRBs, the BGO detector at

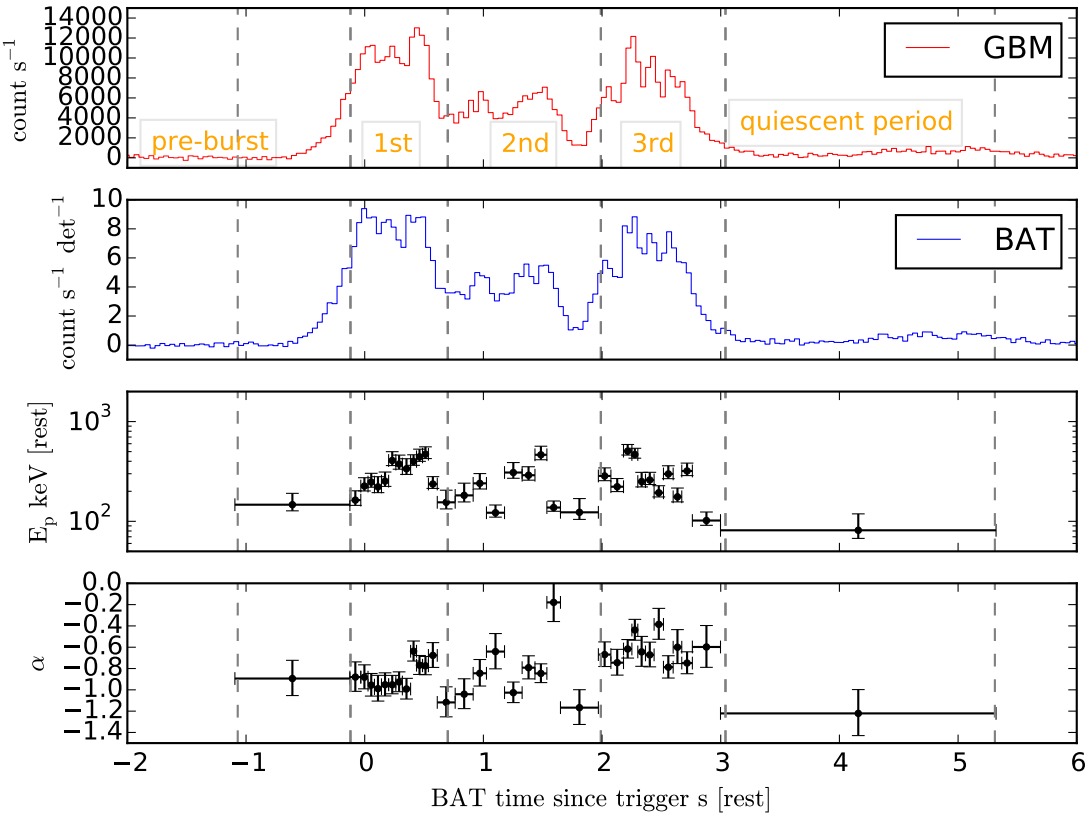

Figure 4.1: The GRB 090424A light curves for GBM and BAT refer to the BAT time trigger in the rest frame. The upper panel shows GBM [10 keV - 1 MeV] with the background subtracted light curve in red, whilst the second panel shows the background subtracted light curve for BAT [15 - 150 keV] in blue. The third panel shows E_{peak} plotted against time interval in black. The final panel shows low-energy index α plotted against time interval in black. The shaded vertical dashed lines show the time intervals where spectral analysis has been performed for the main three pulse groups, the pre-burst, and quiescent periods. The uncertainties adapted here are 90% confidence levels.

high energy (40 MeV) prevents the fitting from being constrained due to low photon counts in the BGO energy band.

4.3.2 Whole sample

The result of the joint-fit time-resolved spectra analysis for the sample are reported in Table 4.1. For each time slice fitted with the CPL model, the corresponding spectral parameters are given, from left to right, as the start time interval T_s, end time interval T_e, low-energy photon index α, E_{peak} in keV, and the calibration factor "offset" between the instruments which was set to 1 for all GBM detectors, and which is normally lower by 10-20% for BAT data.

For each time slice, CPL and Band were used to check the best-fit model, which indicated that the CPL model was more suitable for the majority of GRB time-resolved spectral analyses due

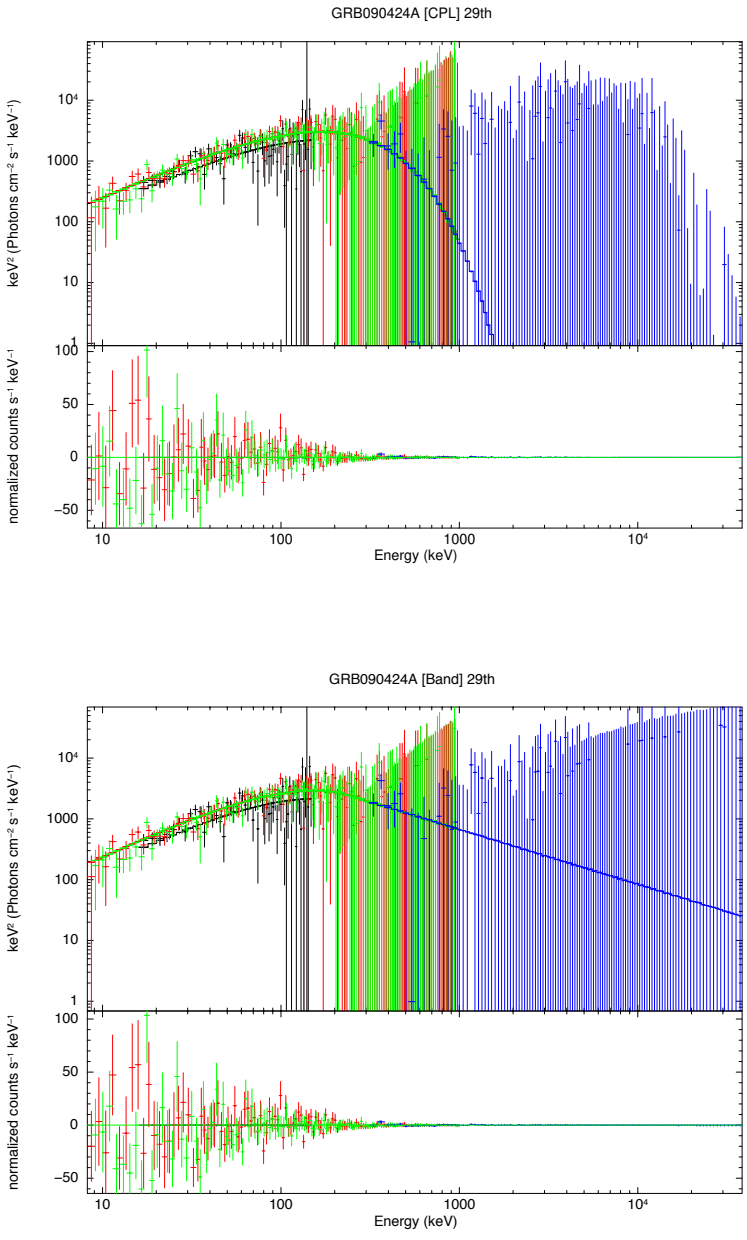

Figure 4.2: The upper panel shows the time-resolved spectra (joint-fit) of GRB 090424A fitted with CPL and the lower panel is the Band model for one time slice (4.32 s-4.43 s). The upper part of both panels shows the unfolded νF_ν spectra, whilst the lower part shows the fitting residuals.

to the small time bins required for each time slice; hence, the high-energy β is not constrained in most cases and its uncertainty is undefined because of the low photon counts at very high energy. In this section, two parts of the time-resolved spectral analysis, as discussed in the literature, are mentioned below.

• The Joint-fit

To date, there are no time-resolved spectral analysis studies that have been completed for a GRB sample using a joint-fit between BAT and GBM. The first discussion of the joint-fit (GBM+BAT) spectral analysis for the time-resolved spectral analysis of a GRB sample is, to the best of our knowledge, is that given in this study. This emphasizes the behaviour of the BAT data when added to the GBM data during the fitting process and how they affect the final spectral result. However, time-resolved spectral analysis of individual GRBs has been used in several studies, whether for spectral or temporal analysis. For example, Page et al. (2009) studied the energetic GRB 080810 observed by both *Fermi* (GBM) and *Swift* (BAT), wherein this detailed investigation of a multi-wavelength observation of the spectral evolution was discussed. Abdo et al. (2011) considered the time-resolved spectrum of GRB 100728A via *Fermi* (LAT) and *Swift* (BAT+XRT) for the purposes of detecting very high-energy (GeV) emissions during X-ray flare activity.

• GBM-only

For GBM-only, time-resolved spectral analysis has been presented by various authors. For instance, Basak & Rao (2012b) presented four bright GRBs (081221A, 080916C, 090902B and 090926A) fitted with Band, BBPL, mBBPL and 2BBPL. Basak & Rao (2012b) introduced a new method for pulse-wise time-resolved spectral analysis for two bright pulses in GRB 081221A using the BBPL (Band, black body with power-law), 2BBPL (2-black body with power-law) and mBBPL (black bodies with varying temperature with power-law) models. Burgess et al. (2014) analysed eight bright LGRBs observed with *Fermi* (GBM) that were dominated by a single emission pulse. The authors implemented a synchrotron model to fit the time-resolved spectral analysis, and also discussed E_{peak} evolution. Gruber et al. (2014) presented the fourth GBM catalogue but for time-integrated spectral analysis, as mentioned in Chapter 3. Ravasio et al. (2018) analysed GRB 160625B as observed via *Fermi* (GBM) and fitted with the SBPL (a Band model with broken power-law), SBPL+BB and 2SBPL models, and discussed the correlation between peak energy E_{peak} and break energy E_b.

Finally, Tierney et al. (2013) introduced time-integrated and time-resolved spectral analysis for a sample of the first two years of long and high-fluence bursts, including 45 GRBs detected via *Fermi* (GBM). This study was focussed on searching for low-energy spectral deviations with the result that, for 11% of the sample, significant deviations in the time-resolved spectral analysis were found, where these deviations were mostly present in high-fluence bursts due to their good data statistics, as compared to the faint bursts.

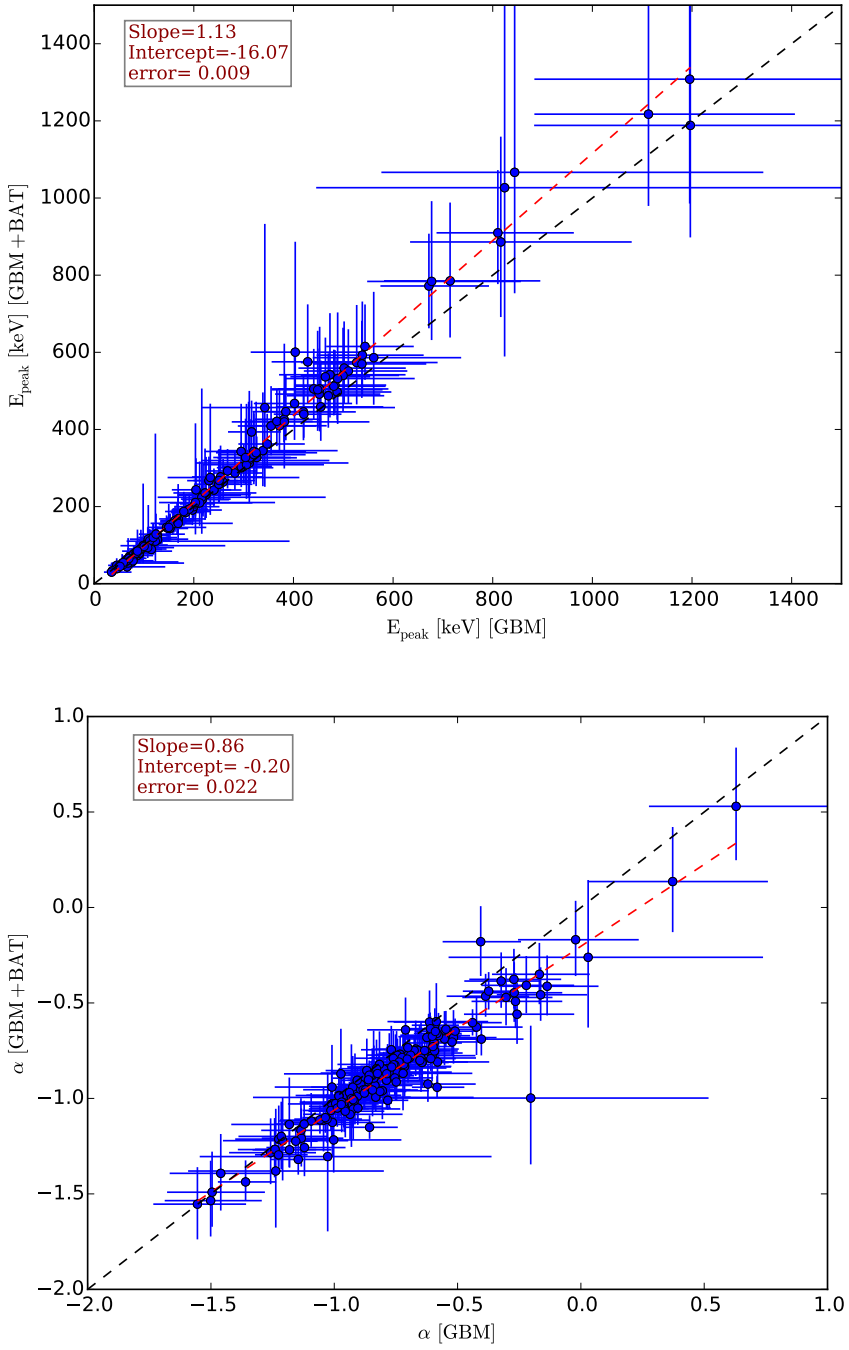

Figure 4.3: The upper panel shows the correlation of E_{peak} for GBM-only vs. joint-fit spectra. The lower panel is the correlation of the low-energy index α for GBM-only vs. joint-fit. Spectra are fitted with the CPL model. The red dashed line is the linear regression and the black dashed line is the equality line.

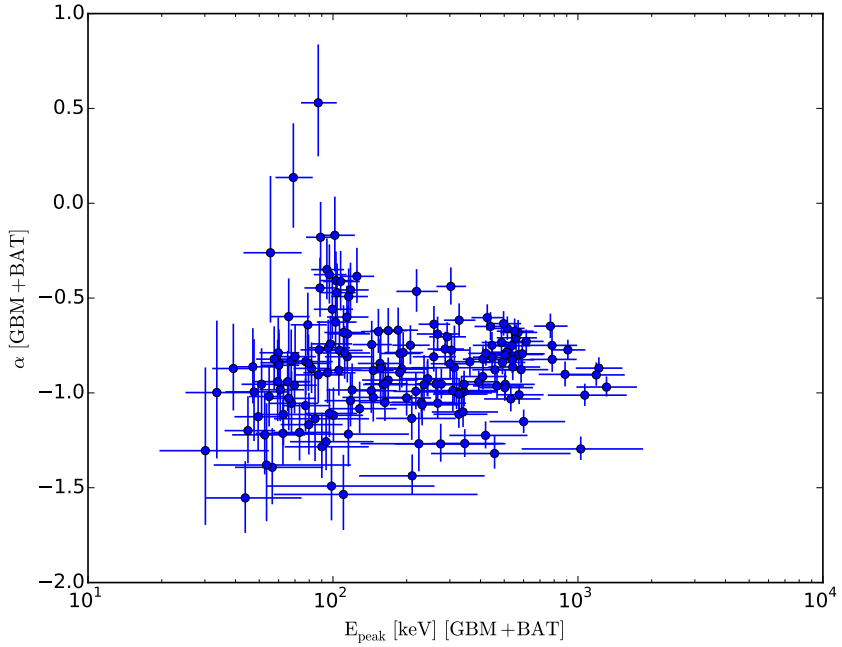

Figure 4.4: The peak energy E_{peak} vs. the low-energy index α for the joint-fit spectral fitted with the CPL model.

In this section, the comparisons are divided as follows: general comparisons for each model (CPL and Band), where the first comparisons are between the E_{peak} values obtained from the joint-fit and GBM-only using the CPL model. Then, the low-energy photon index α obtained from the joint-fit and GBM-only using the CPL model are compared. Here, the majority of the GRBs in the sample did not result in a good fit with the Band model except for a few isolated cases. Thus, Band was not found to be a good model for this time-resolved spectral analysis, and is only performed here for the purposes of comparison with the CPL model. The comparisons obtained from the time-resolved spectral analysis are as follows:

1) The correlations between the joint-fit (GBM+BAT) and GBM-only parameters, as fitted with the CPL model.

Figure 4.3 (upper panel) shows the E_{peak} correlation obtained from the joint-fit and GBM-only using the CPL model. The joint-fit results showed systematically higher E_{peak} values at higher energies, and a slight deviation at lower energies. The lower panel shows the correlation between α when plotting the joint-fit against the GBM-only, where a few deviations may be noted. The fact that the error bars are large does not prevent the significant differential between the joint-fit and the GBM-only from being noticeable, as can be determined by the statistical regression line of the slope/error.

Figure 4.4 shows the relationship between E_{peak} and α and the associated uncertainties, as obtained from the CPL model of the joint-fit. These two parameters show that there is no obvious

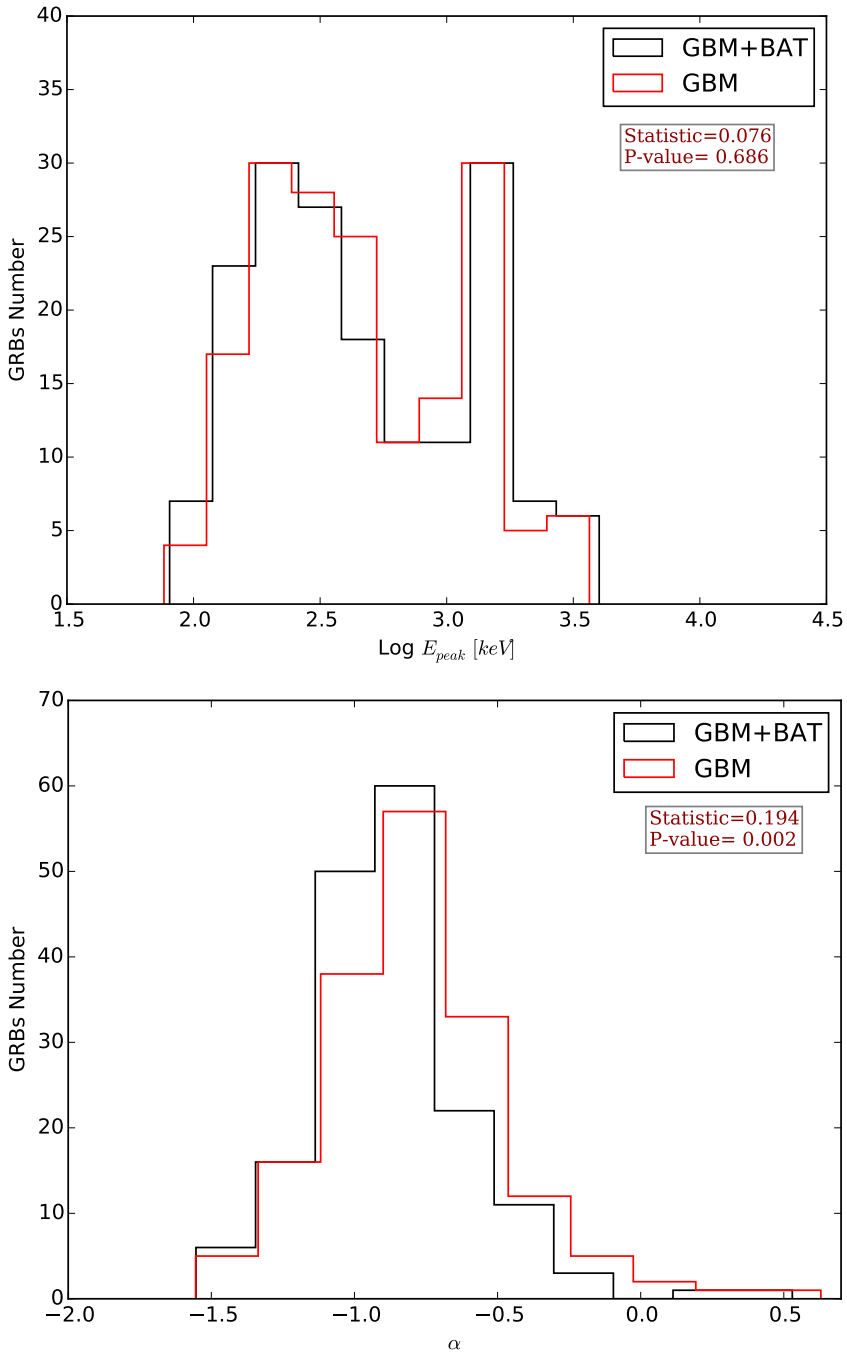

Figure 4.5: The upper panel is the peak energy E_{peak} distribution for GBM (in red) and GBM+BAT (in black). The lower panel is the low-energy α distribution for GBM (in red) and GBM+BAT (in black). Spectra are fitted with the CPL model. In both panels, the KS-tests are shown in the small boxes.

trend for individual GRBs.

Figure 4.5 shows that the E_{peak} distributions were in agreement regardless of whether the E_{peak} parameter was obtained from the GBM-only or the joint-fit, while the distribution of the low-energy α values showed different distributions between the joint-fit and GBM-only, where it appeared that the joint-fit was shifted towards softer indices. The KS-test was then applied to the joint-fit and GBM-only for the E_{peak} (statistics and P-values are labelled in the small boxes on left-hand side) which indicated that the distribution samples were very likely drawn from different populations and were inconsistent within 1 σ, with P-values of 0.686, whereas α had a P-value of 0.002, which was drawn from the various populations to less than 3 σ.

2) The correlation of the joint-fit and GBM-only parameters fitted with the Band model.

When fitting the GRBs in the sample with the Band model, it was found that there was considerably more data scatter than was found in the CPL model, with some undefined parameter uncertainties that might have been due to the high-energy tail that prevented the Band model from being constrained. In this case, the undefined parameters were excluded from Table 4.2, which ended up with only a few time slices for those GRBs whose parameters were relatively constrained and fit well with a Band model. In other words, only the GRBs that showed a good fit with the Band model were included.

Table 4.2 lists the GRBs fitted with the Band model with a constrained β for certain time-slices; for instance, GRB 081121A only has β defined in the middle pulse (second time interval of [7.85 s: 14.11 s]) while the first and last pulses, [-1.47 s: 7.85 s] and [14.11 s: 20.93 s], were best fitted with the CPL model. For GRB 081221, the Band model was suitable for fitting 12 out of 30 time slices. GRB 081222A seemed to fit only two parts of the initial time interval at [-2.18 s: 1.88 s] and the time interval at [5.47 s: 6.98 s]. For GRB 090424A, only six out of 32 time slices were fitted with the Band model which were spread over the entire time interval. GRB 100615A fit only one time slice at [-1.22 s: 2.83 s].

GRB 100728B, as fitted with the Band model, showed only two time slices that were constrained with this model (81.92 s: 83.97 s and 123.91 s: 128.00 s) out of 24 time-slices fitted with the CPL model. In GRB 120326A, only one time slice could be fitted with the Band model compared to three time slices with the CPL model. The Band model obtained a good fit for GRB 120624B with two time slices between [-270.34 s: -229.38 s], while 14 other time slices were best fit with the CPL model. The Band model for GRB 120624B was able to fit one time slice from [-245.76 s: -229.38 s] with a very high $Cstat$.

GRB 140213A showed nine time slices out of 15 for which no significant differences could be found when using either Band or CPL. One time slice for GRB 150301B was found to have a defined β with a consistent E_{peak} within its uncertainties at [-2.56 s: 3.59 s]. Lastly, in GRB 150403A, 13 out of 18 time slices were able to constrain β using the Band model. The Band and CPL models were consistently able to fit the spectra with no significant differences between

either, in terms of either the parameters so determined or their $Cstat$.

In Figure 4.6, the upper panel shows the E_{peak} correlation of the joint-fit and GBM-only fitted with the Band model, where in this case the E_{peak} was similar than those found for the spectra fitted with CPL, and with comparable uncertainties. There was a small offset between the two best-fit lines (dashed black line is the equality line and dashed red line is the regression line). However, the lower panel shows α behaves differently than the α obtained with CPL, as a greater amount of scatter was apparent due to the high-energy index β not being constrained in the GBM-only analyses.

Figure 4.7 shows the relationship between the E_{peak} and α fitted with the Band model where there is no obvious trend that can be noted. In this section, the comparisons between the spectral joint-fit and GBM-only were in agreement with the time-integrated spectra in Chapter 3, except for the fact that the time-resolved spectral analysis showed greater scattering due to the individual pulses being more sensitive to fitting than the time-integrated ones.

To conclude, when including BAT, the joint-fit spectral analysis fitted with CPL or Band showed a higher E_{peak} than when analysing GBM-only, while those fitted with Band show different correlations of α, and large amounts of scattering was found when using the Band model.

4.4 The Peak Energy Evolution, E_{peak}

It is known that studies of the GRB continuum spectra have allowed for the greatest understanding of GRB emission processes. However, the continuum GRB emission remains the subject of considerable debate, and thus the understanding of the physical emission process resulting in GRB spectra is complex. Importantly, investigating the dynamics of burst spectra might assist in resolving many of the issues related to GRB spectral properties that cannot currently be explained. In particular, time-resolved spectral analysis can be used to investigate the E_{peak} evolution, such as distinguishing between different fundamental behaviour trends in E_{peak}. In general, it has been found that GRB spectra can be mostly described by the empirical Band function, where this model, besides describing burst spectra, can quantify the evolution of E_{peak}, the energy at which the energy flux per energy band peaks. The peak energy of υF_υ E_{peak} can be obtained from one of several spectral models, such as the CPL model, using the relation $E_{peak} = E_c(2-\alpha)$, where E_c is the exponential cut-off power law, or the Band model which expresses E_{peak} as $E_{peak} = E_0(2+\alpha)$, where E_0 is the characteristic energy in keV.

E_{peak} is a function of the outflow luminosity, $L_{iso,\gamma}$, in all the prompt emission models. The E_{peak} in such cases behaves differently in each model, e.g., the outflow composition, the energy dissipation mechanism, particle acceleration processes. One possible feature that can join all these models is in instances where the emission stops suddenly due to the jet curvature, where the observed emission becomes high-latitude emission (e.g., Fenimore et al. 1996; Kumar & Panaitescu 2000; Dermer 2004; Liang & Zhang 2006; Qin et al. 2008; Zhang et al. 2009a).

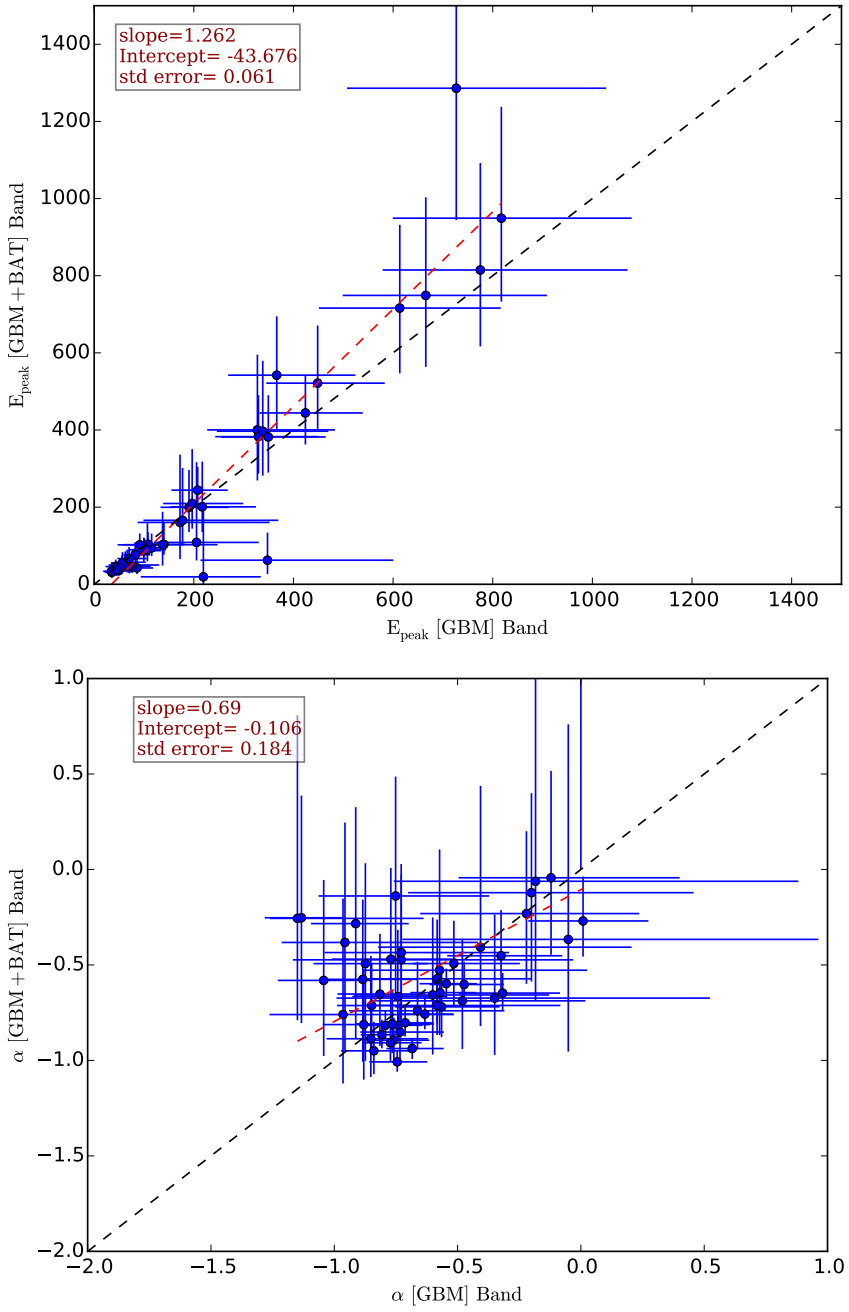

Figure 4.6: The upper panel shows the correlation of E_{peak} for GBM-only vs. joint-fit spectra. The lower panel is the correlation of the low-energy index α for GBM-only vs. joint-fit. For a few GRBs that were best fitted with the simple Band model, the red dashed line is the regression line and the black dashed line is the equality line.

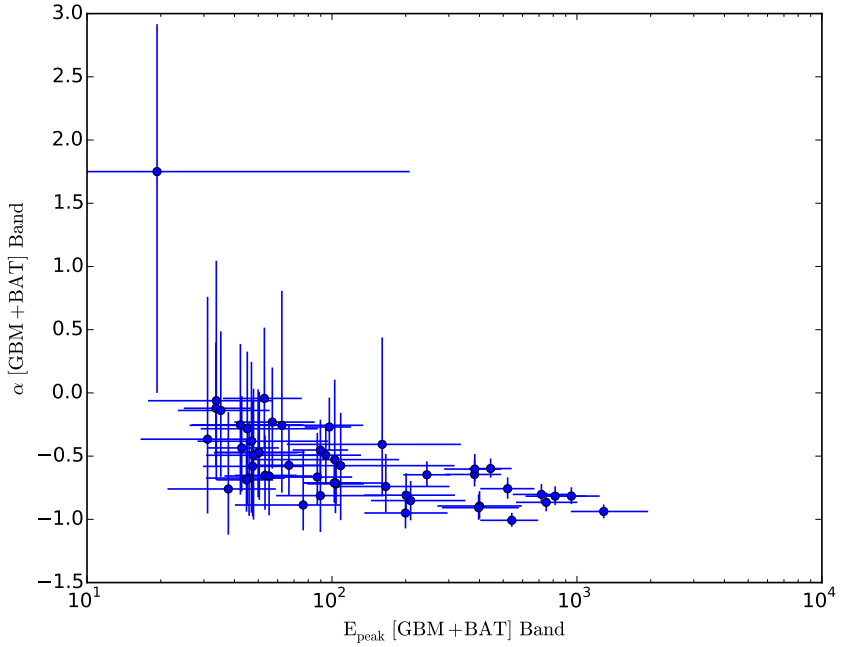

Figure 4.7: The peak energy E_{peak} vs. the low-energy index α for the joint-fit spectra fitted with the Band model.

Within the curvature effect, a possible intensity-tracking trend can be shown. As a result, the hard-to-soft and the intensity-tracking evolutions (as mentioned in Chapter 1), as characterized by decaying flux and hence a decreasing E_{peak}, can be explained by the so-called "curvature effect".

This could be concluded as the investigation of the prompt emission models can be explained by the E_{peak} evolution of the rising pulses. One of the challenges to distinguishing between different models is when both evolution trends can be seen in one burst, and which may be due to the jet composition and the viewing angle (Lu et al., 2010).

Substantial achievements derived from studying GRB spectra on the subject of GRB spectral evolution started with the BATSE observations. BATSE, for example, was the first to discover the global features of GRB continuum spectra that subsequently helped to clarify and interpret the obstacles to our understanding of GRB emission. Golenetskii et al. (1983) examined two-channel data over an energy range of 40 - 700 keV for five GRBs detected via the *Konus* experiment, the spectra for which could be described by an optically thin thermal bremsstrahlung (OTTB) model. A good correlation between luminosity and temperature T was noted, such that at a specific time, the spectral hardness was found to be dependent on the flux intensity.

Norris et al. (1986) investigated a small sample of GRBs using the hard-to-soft ratio and retested the relationship between hardness and intensity. They obtained a more complex relationship than found in Golenetskii et al. (1983). Their relation showed that for each intensity pulse (analysed individually) the intensity peaks after the hardness peaks. Kargatis et al. (1994)

studied the same relation and found that for a sample of GRBs there was no evidence of this relation and, thus, the trend of this relation appears not to be valid in some cases. Band et al. (1992) confirmed that the relationship is correct unless applied with a fine time resolution of time-averaged spectra. In contrast, Bhat et al. (1994) re-examined the relation using a single-pulse GRB observed via BATSE (LAD: Large Area Detector) that followed a FRED shape, and determining the spectral evolution of the hard-to-soft ratio via the hardness and the intensity relations. One of the spectral features obtained from Bhat's study is that of the time lag between the two quantities; the hardness ratio and the counting rate were found to be correlated with the counting rate rise time.

Looking at the E_{peak} distributions for a sample of bright BATSE GRBs, Preece et al. (2000) found that E_{peak} was grouped between 200-300 keV in the observer frame in the BATSE energy band. More generally, the E_{peak} distribution appeared to be spread over several keV to a few MeV (Kippen et al. 2000; Sakamoto et al. 2005), where the single distribution is evidence of the emission in GRBs having a common origin. E_{peak} has different energy ranges for different emission events, for instance, GRBs prompt emission have an E_{peak} larger than 50 keV, while E_{peak} for the low-energy X-ray emission ranges between 30-50 keV, and smaller than 30 keV in any XRFs (Sakamoto et al., 2009).

Gruber et al. (2011) again discussed the E_{peak} distribution of 32 GRBs detected via GBM. They found that the mean and the median of the E_{peak} distribution were 1.1 MeV and 750 keV, respectively, and also that for a sample of LGRBs the lognormal distribution peaked at $\sim$ 800 keV.

E_{peak} evolution behaviour was discussed in Lu et al. (2012) for 51 LGRBs, both in terms of the hard-to-soft ratio trend and intensity tracking that were classified for their sample. It was found there were five GRBs that followed the hard-to-soft ratio trend while three others followed the intensity tracking. The hard-to-soft ratio trend became asymmetric with the rising pulse tending to be steeper than the falling pulse, whereas the intensity tracking becomes more symmetric. In the rest of their sample, which had multiple pulses, E_{peak} became more complex.

Gruber et al. (2014) studied E_{peak} evolution but for a time-integrated spectrum, claiming that if a GRB evolves from hard-to-soft the peak photon flux was not always dependent on the highest E_{peak} value, e.g., Crider et al. (1999). This was only true when E_{peak} followed the intensity tracking, and its highest value corresponds to the peak photon flux. In fact, the time-integrated E_{peak} can be dependent on the ratio of peak photon flux to the average photon flux of the burst, for example, a larger ratio can result in a deviation of the average E_{peak} from the E_{peak} at peak flux.

E_{peak} evolution has also been discussed by Yu et al. (2016) for the time-resolved spectra analysis of a large sample of the brightest GRBs. In particular, E_{peak} evolution with either time or energy flux and photon flux was considered, with a comparison between these two correlations illustrated in Figure 6 in Yu et al. (2016). The authors noted two methods that are typically used

to distinguish E_{peak} evolution behavioural trends, namely the "machine test" (computer analysed) and the "human-eye test". They found that the human eye is more effective in visualizing any behavioural trends. 3.5% of their sample showed a hard-to-soft ratio trend, whilst 21% showed a mix of the two trends.

Following the previous studies, behavioural trends can be seen to fall into two categories, namely variations in the soft-to-hard ratio and in the flux intensity-tracking, e.g., Ford et al. (1995). Then, Norris et al. (1986) found that LGRB pulses show a hard-to-soft spectral evolution which does not appear to be caused by the time-variable spectral absorption below 100 keV in certain GRBs. The hard-to-soft evolution might only be seen in specific GRB classes with different behavioural evolution trends. Although there are a variety of behavioural trends, there are still a large number of different evolution types observed (Kargatis et al. 1994; Bhat et al. 1994; Ford et al. 1995). Studies of hard intensity correlation have been discussed extensively in the literature (e.g., Golenetskii et al. 1983; Paciesas et al. 1992; Kargatis et al. 1994). A number of GRBs' late time pulses appeared to follow intensity tracking, which is possible if this were due to the superposition of hard-to-soft pulses (Lu et al., 2012). The fact that all GRB correlated pulses can be interpreted using the hard-to-soft E_{peak} evolution, and intensity tracking may be caused by more than two hard-to-soft pulses' superposition was argued by Lu et al. (2012) and Hakkila & Preece (2014).

In this study, attempts have been made to consider the E_{peak} behavioural trends using the "human-eye test" to distinguish how E_{peak} evolves with time and/or energy flux. The E_{peak} evolution for the GRBs sample is illustrated in Figure 5.5, which excludes two bursts that have only two time slices, namely GRB 081221A and GRB 150301B, where the upper panel shows the GBM light curve plotted with the E_{peak} evolution (black-circles, right axis), and the bottom panel shows the correlation of the E_{peak} evolution with energy flux (black stars).

Here, the findings of the E_{peak} evolution are listed below for individual bursts:

- GRB 080916A had only three time slices that clearly followed a hard-to-soft trend.
- GRB 081221A showed a clear trend of intensity evolution in the beginning pulse.
- GRB 081222A showed a hard-to-soft trend that can be clearly seen but no clear evolution in intensity tracking could be found.
- GRB 090424A has three separate pulse groups that all showed evolution in intensity tracking even though the hard-to-soft trend appeared to be more complex.
- GRB 090926B is a single wide pulse that followed a clear evolution in intensity tracking.
- GRB 091208B has a first pulse that is unclear, while the later pulses followed evolution in intensity tracking.
- GRB 100615A had three pulses that followed evolution in intensity tracking.
- GRB 100728A showed a hard-to-soft trend in later pulses, and there was clear intensity tracking.

• GRB 120624B, the first pulses showed no clear trend, while the second pulses followed evolution in intensity tracking.

• GRB 131105A structured with five spikes pulses, which clearly showed an intensity-tracking behaviour.

• GRB 140213A showed a hard-to-soft trend in the first pulse, after which the second large pulse showed clear intensity tracking followed by a long quiescent region.

• GRB 150403A showed its first small pulses to have no trend but which were followed by a clear intensity tracking while the end tail again showed no evolution.

• GRB 151027A had two groups of pulses separated by a long quiescent region; the first group showed no clear trend, whereas the second showed a hard-to-soft trend. Most GRBs showed an intensity-tracking trend in at least some of their pulse groups. In these GRBs, the peak energy is high as the flux becomes high; only a few GRBs showed a hard-to-soft trend. For the others, it was difficult to follow their trends, and so they might better be described as being of "unknown trend". For comparative purposes with other studies, Figure 4.9 shows the E_{peak} evolution adopted from Yu et al. (2016) for some of the GRBs detected via *Fermi*(GBM). The plots can show different behavioural trends in E_{peak} evolution which was also plotted against energy flux (erg cm^{-2} s^{-1}).

4.5 Amati and Yonetoku Relations Time-Resolved Spectral Analysis

The Amati and Yonetoku relations have been extensively studied for time-integrated spectra, (e.g., Amati et al. 2002; Amati et al. 2008; Ghirlanda et al. 2009; Ghirlanda et al. 2010a; Amati 2010), in which a strong correlation has been confirmed between $E_{peak,rest} - E_{iso,\gamma}$. Basak & Rao (2012a) also found a correlation between the Amati time-resolved spectral analysis using the Ghirlanda et al. (2010a) sample of 12 GRBs, who claimed the reason for obtaining a poor correlation with the Amati time-resolved spectral analysis was due to the hard-to-soft evolution of the individual pulses. By definition, the hard-to-soft evolution is characterized by a high E_{peak}, even though the corresponding flux is low.

Basak & Rao (2012c) analysed a joint-fit (GBM+BAT) for GRB 090618 using an underlying pulse structure method to investigate the Amati and Yonetoku relations, concluding that these relations showed clear, strong correlations. Later, another study by Basak & Rao (2013a) studied and discussed the Amati relation "pulse-wise" for a sample containing 19 GRBs with 43 pulses. The authors concluded that the individual GRBs showed a strong Amati correlation, which was slightly better than when applied to the sample as a whole.

Here, an attempt was made to compare these relations for time-resolved spectral analysis. Figure 4.10 (upper panel) shows the Amati time-resolved spectral relation ($E_{peak,rest} - E_{iso,\gamma}$)

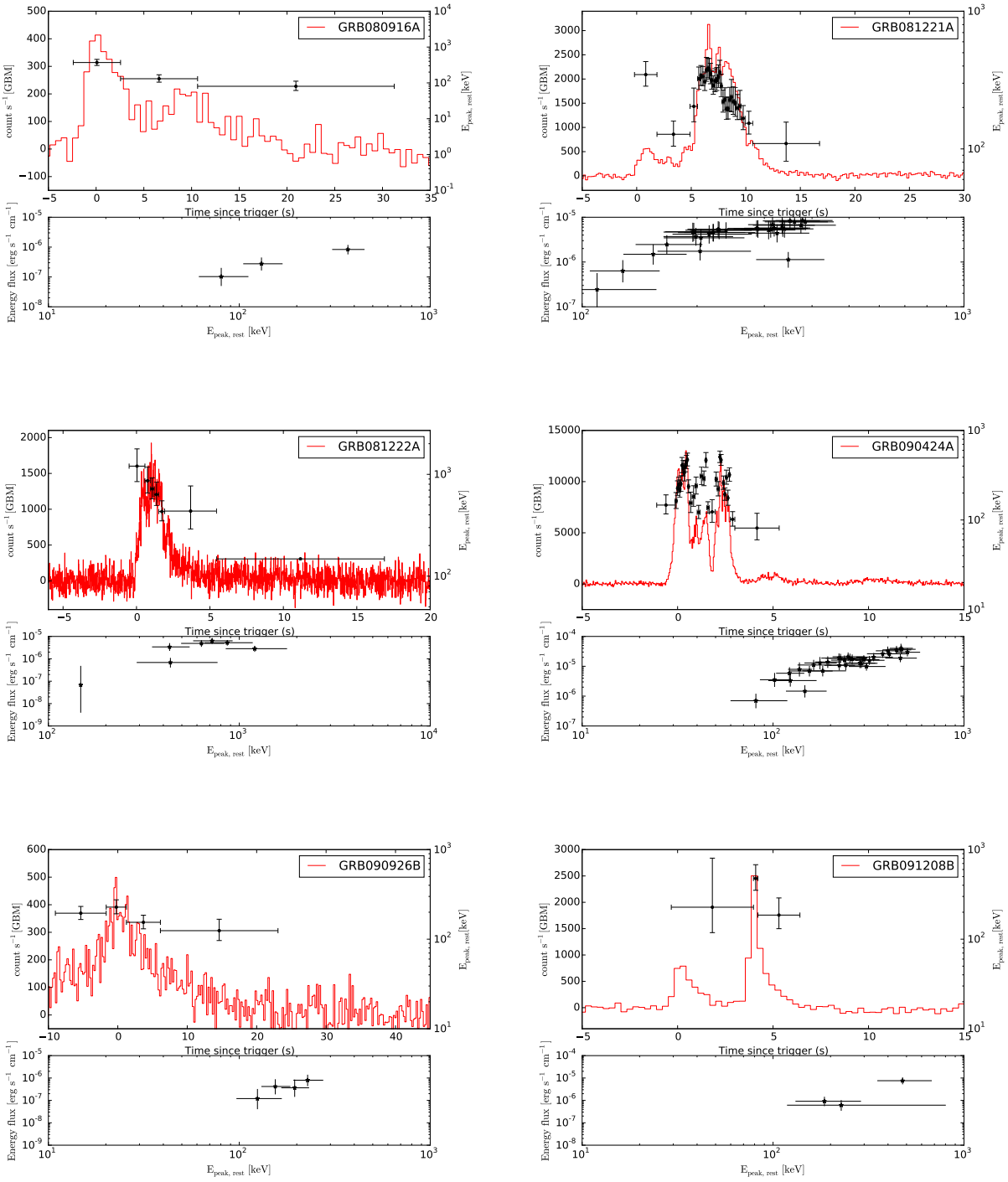

Figure 4.8: The peak energy E_{peak} evolution for 14 GRBs. The upper panel is the GBM light curve corresponding to the BAT trigger time, where black circles are the E_{peak}s, shown in terms of their evolution with time. The lower panel is the correlation of E_{peak} and the energy flux.

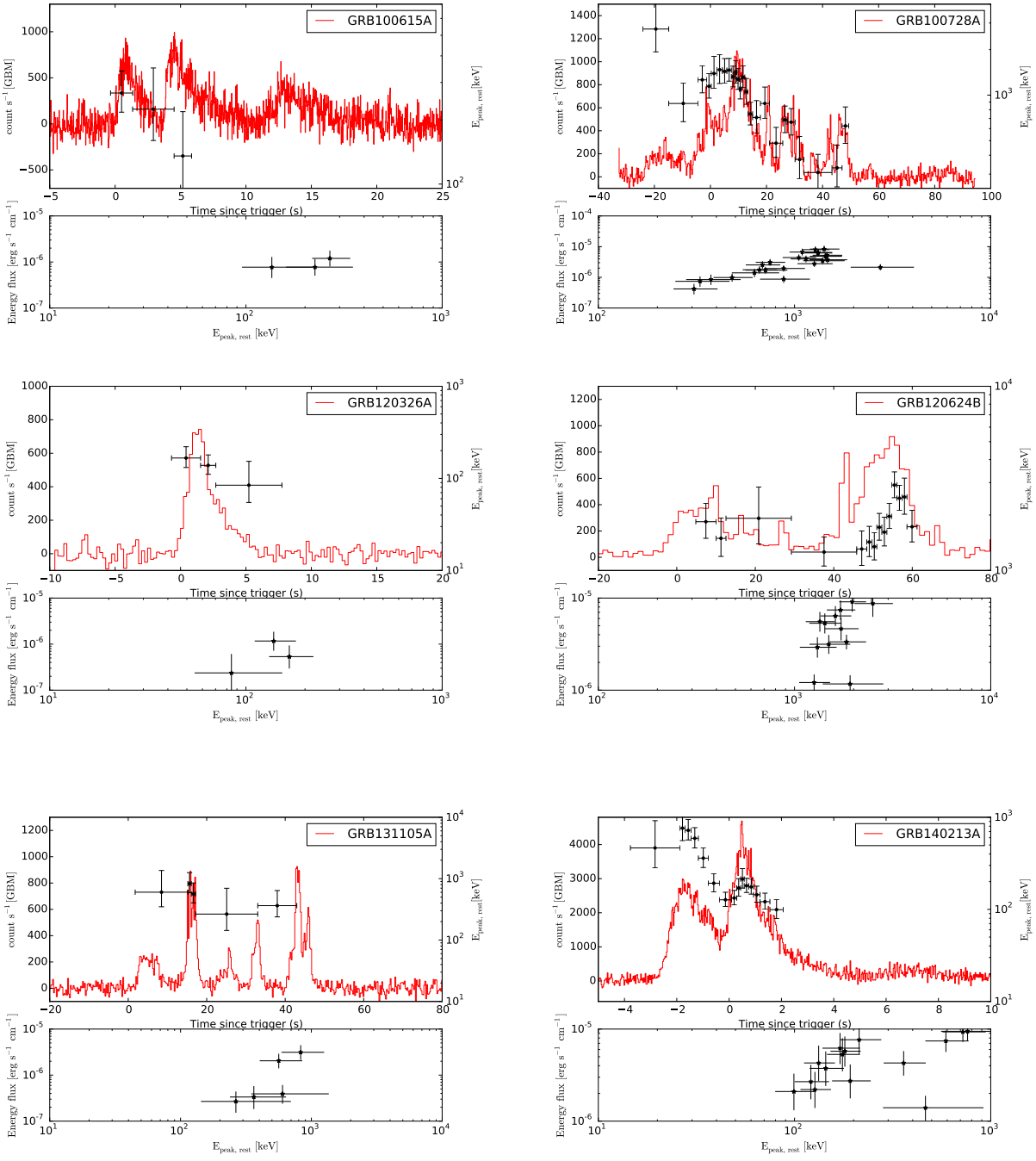

Figure 4.8: cont'd

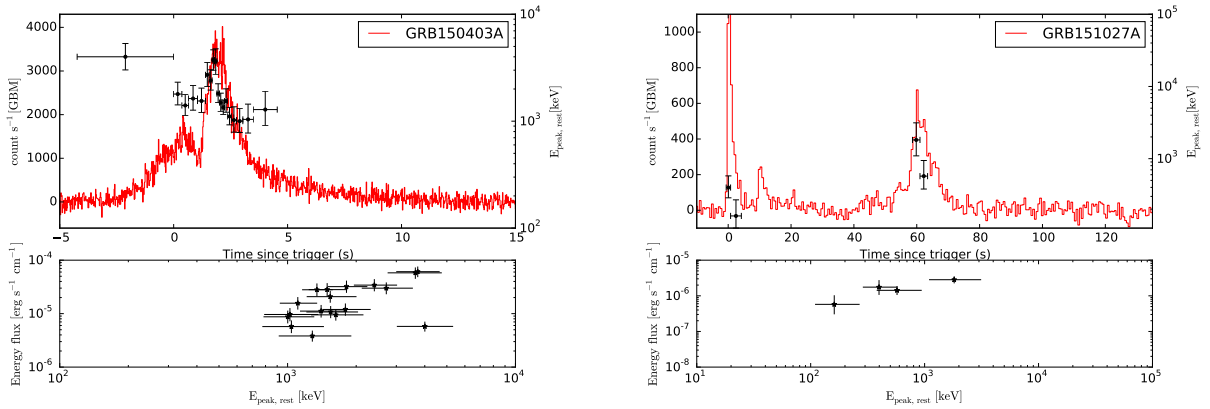

Figure 4.8: cont'd

for the joint-fit methods. This study data showed a similar degree of correlation, but with large deviations shifted above the original Amati best fit (solid black line, adapted from Nava et al. (2012), and mentioned in Chapter 3). These deviations outside the Amati limit (3 σ) are noticeable due to each GRB spectrum arising from individual pulses that affected the correlation consistency, as evidenced by the large offset from both fit lines (black solid and red dashed lines), where a slope of 0.47 [0.03] was obtained from this study; by comparison, a slope of 0.61 [0.04] was obtained from Nava's study. This was due to the fact that for each pulse from the individual GRBs, the E_{iso} dramatically changed and hence deviated from the original Amati best-fit line (obtained specifically from time-integrated spectra). The scattering of the Amati relation, however, may due to a data selection effect owing to a lack of GRBs at high energies (of about 10^{54} erg).

The lower panel shows a strong Yonetoku time-resolved spectra correlation ($E_{peak,rest} - L_{iso,\gamma}$) for the joint-fit within individual GRB pulses. Agreement in the correlation between the data obtained from this study (red dashed line) and the original best-fit Yonetoku relation (solid black line) can be seen, but with a few deviations above the Yonetoku best-fit lines of 0.53 [0.06] with a gradient of 0.45 [0.04]. The deviations accrued in this study were compared with the original Yonetoku study, and may have been due to the use of a different peak flux luminosity in each case, e.g., 1-sec peak flux, that was chosen for each GRB spectrum in the original Yonetoku, which would affect the luminosities of individual GRBs, while in this study an average peak flux was used. Moreover, the offset in this study above the best-fit line (Yonetoku) may due to the different integrated time bin chosen in either this study or in the original Yonetoku relation.

Generally, the Yonetoku relation, being a time-resolved spectrum quantity - as per the isotropic luminosity - might be more relevant to temporal fluctuations in the fireball scenario than an energetic representation. In fact, this claim is in agreement with the findings of Ghirlanda et al. (2010a), whilst in contrast with those of the original Yonetoku time-integrated relation. Ultimately, the results observed for the Amati and Yonetoku relations obtained in this study for the

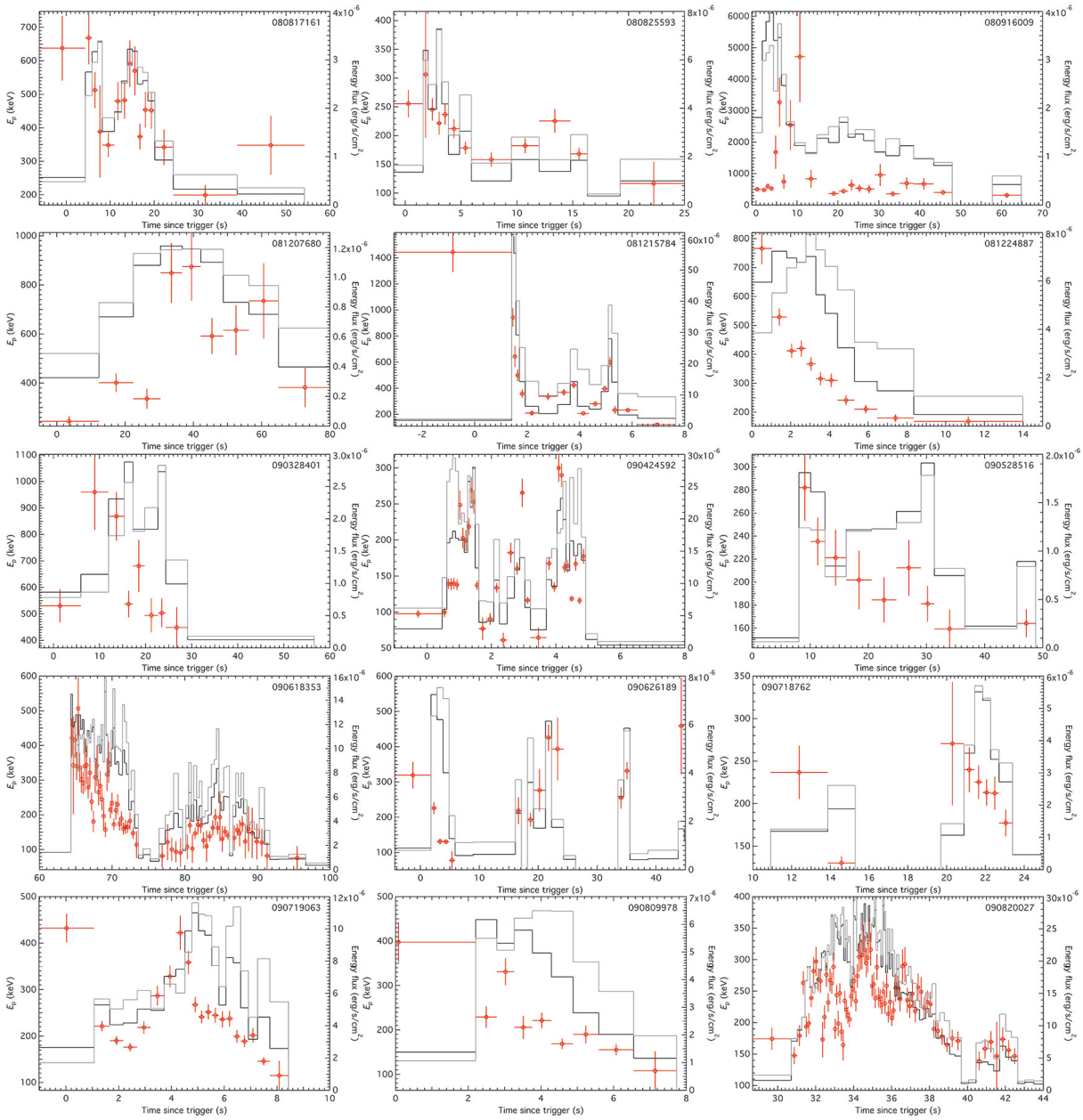

Figure 4.9: E_{peak} evolution (red data points on left axis), with the 10 keV1 MeV energy flux (black histograms on right axis) and the 10 keV 1 MeV photon flux (grey histograms, arbitrary units) overlaid. For a time-resolved spectral analysis adapted from Yu et al. 2016 for number of GBM bursts, this shows one GRB that was in our sample, namely "GRB 090424A".

joint-fit are consistent with the independent GBM analysis by Gruber et al. (2011).

It is important to re-examine the Amati relation, but this time with individual GRBs in order to compare the Amati correlation with the one completed earlier that examined the full sample to determine if there were any changes to this relation. Figure 4.11 shows the Amati relation applies for each GRB individually to verify how this relation behaves for individual GRBs. For example, GRB 080916A, GRB 081222A, GRB 120624B, and GRB 140213A showed a degree of correlation but tended to shift to high E_{peak}. GRB 081221A was not correlated, but was located inside the Amati best fit (within the 3 σ scatter). GRB 090926B, GRB 091208B, GRB 120326A, GRB 100615A, and GRB 131105A showed no clear correlations but were located within the Amati best-fit region. GRB 100728A was consistent with the Amati relation, but showed a few deviations when shifting towards higher E_{peak} from the Amati best fit within a 3 σ scatter. (The outliers of GRB 090424A and GRB 150403A showed steeper correlations than Amati best fit which were shifted to lower E_{iso} and away from the Amati best fit. GRB 090424A could be fitted using extra component power law as seen in other studies and could have resulted in a better fit. However, in this analysis we did not involve any extra component power law, which would not affect the time-resolved analysis regarding the small time slices that werer analysed individually). Finally, GRB 151027A followed a clear correlation but seemed to be outside the Amati best-fit region with a higher E_{peak} than the original Amati. This disagreed with the findings reported by Basak & Rao (2012a), wherein it was claimed that whilst the Amati relation was applied to individual GRBs, the Amati correlation seemed to be stronger than when applied to the complete sample.

To compare, the Amati time-integrated spectra, for instance, showed a strong correlation, whereas the time-resolved spectra showed more scattering around the Amati best-fit line due to the individual pulses that measured different E_{peak} values. This would indeed affect the strength of this relation because the individual pulses are treated separately. For instance, the E_{peak} values obtained from the time-integrated study were the average of the E_{peak}s obtained from the time-resolved spectral analysis study (this might be biased if some pulses are considerably brighter than others), while the E_{iso} values were basically the sums of the individual pulses. This can be noticed in the upper-left data, which is shifted by about a factor of two. In addition, obtaining few deviations from Amati best fit could be due to data selection effects resulting from a lack of GRBs with energies of $\sim 10^{54}$ erg.

In order to draw reasonable conclusions, it is important to enlarge the sample. However, the differences resulting from the Amati time-resolved spectra and the Amati time-integrated spectra best fits (red dashed lines in both cases) obtained from this study were insignificant. For example, the Amati time-resolved spectra had a gradient of 0.47 [0.03] when compared to the Amati time-integrated spectra, which had a gradient of 0.46 [0.09] when compared to the Amati best fit (solid black line). The scattered data found in the Amati time-resolved spectra data were due to the individual pulses being more sensitive than the Amati time-integrated pulses. Furthermore,

providing an individual Amati relation for individual bursts helped to distinguish between the Amati for the entire sample and the Amati for the individual GRBs, and to study the Amati relation in each case separately. For each GRB, it was found that there were different behaviours for the Amati relation. In contrast, the Yonetoku relation shows a strong correlation with the time-resolved spectra, which possibly reflects the associated effects on the flux luminosity, L_{iso}, for individual pulses that correlated well with E_{peak}, whilst the Yonetoku relation for the time-integrated seemed to show increasing scatter above the Yonetoku best fit (solid black line), it was found that the GRBs luminosity, L_{iso}, in this study was smaller than that found in the original Yonetoku relation.

4.6 Conclusions

The joint-fit time-resolved spectral analysis of 16 bright and LGRBs with known redshifts was performed. The data were collected for the period between September 2008 and October 2015, and were observed coincidentally via *Fermi* (GBM) and *Swift* (BAT). 189 spectra were obtained from 16 GRBs with high temporal resolution using a time-binning criterion of an S/N ratio > 30 for the GBM-NaI detector. Two spectral analyses, the joint-fit and GBM-only, were discussed. To distinguish the systematic effects of the GBM and BAT instruments, a comparison of the joint-fit analysis (GBM+BAT) versus the independent GBM analysis (GBM-only) was performed and interpreted. The spectra were fitted with two models, CPL and Band, in order to determine the best model by comparing the $\Delta Cstat$ obtained for each time interval. The majority of GRB spectra were found to achieve a best fit with the CPL model (the high-energy cut-off power-law model).

However, the Band model was able to fit a small number of GRBs, in this instance six out of 16 GRBs, due to poor count statistics at high energies preventing the model parameters from being constrained. The spectral model parameters, e.g., the peak energy E_{peak} and the low-energy index α obtained from the joint-fit and GBM-only and fitted with both the CPL and Band models, showed positive correlations. It was concluded that including BAT data in the GBM data when using the joint-fit changed the spectral fitting significantly, and did show a statistical improvement that could be noticed in some cases through the associated decrease in the parameter uncertainties.

The E_{peak} values that are measured from the joint-fit spectral analysis showed higher values when adding BAT data compared to the E_{peak} values that are measured from the GBM-only, which I conclude is not affected by the size of the errors bars. In contrast the low-energy index obtained from the joint-fit spectral analysis shows no new correlation (Figure 4.6).

Generally, some GRB time intervals showed that E_{peak} uncertainties could not be constrained due to the very small time bins used having insufficient counts to be able to properly define the parameter uncertainties.

In addition, the comparison of the GBM-only time-resolved spectra in this study with those in other studies was important, and thus comparisons were made with, e.g., Yu et al. (2016), who provided a time-resolved spectral analysis of large bright GBM sample bursts in their catalogue. By comparing with this catalogue, it was found that for the GBM-only spectral analysis, there was good consistency between the parameter values obtained for each (within the bounds of the associated uncertainties). Despite the spectral fitting processes being slightly different for each of the analyses, it was found that there were no significant differences between the spectral parameters thus determined. The joint-fit (GBM+BAT) time-resolved spectral analysis have, unfortunately, not previously been discussed in the literature, except for some GRBs that were fitted using time-resolved spectra analysis methods, but only for individual GRBs rather than a joint-fit.

The E_{peak} evolution obtained from the joint-fit time-resolved spectral analyses were examined using two evolution methods: the hard-to-soft ratio over time, and intensity tracking. Few GRBs showed a tendency to follow the hard-to-soft ratio, with the majority following the intensity-tracking method. However, other GRBs did not show any apparent evolution, which were defined as being of "unknown-trend".

The time-resolved Amati $E_{peak,rest}$-$E_{iso,\gamma}$ relation, as compared to this study, showed greater data scattering above the Amati best-fit that can be discussed further when plotting individual bursts to determine if Amati relation for each GRB is behave similarly. This relation, when applied to time-resolved data showed different behaviour to its time-integrated analogue due to the effect of the relative E_{iso} within the individual pulses, regardless of the time-interval scattering. The reason why the Amati relation was more likely to be close to the original Amati best fit in the time-integrated analysis was due to the higher E_{iso} values that are released over the entire time-integrated spectra while becomes less energetic if it is applied in individual bursts (time-resolved spectra) which generally moves down to the lower values of E_{iso}.

In particular, the Amati time-resolved relation was then re-examined with individual GRBs in order to compare to the Amati relation for the entire sample. For each GRB in the sample, it was found that the Amati relation could potentially show a different correlation than the original Amati relation; however, some GRBs did not show a clear Amati correlation. The GRB 090424A case study showed a large amount of scattering above the Amati best fit, which may have been due to the large T_{90} = 48 s with a complex light curve structure. Where fitting each pulse (35 time slices) individually resulted in different E_{peak} values and hence different amount of E_{iso} that is measured. This is can explain the differences between the time-integrated and time-resolved, which is, for example, the *Eiso* can release more energy for the whole burst but not likely to be as much energy as it was in the time-resolved spectra one due to the small time slices that are considered. Thus, Figure 4.11 allows us to visualise this scattering in GRB 090424A and other GRBs that show the same kind of behaviour. The average Amati relation points of the time-resolved spectra case were somewhere slightly inside Amati best fit region. This could

also explain the validity of Amati relation found in the time-integrated spectra rather than the time-resolved spectra because of the divergence of each pulse's spectral fitting and hence the divergence of the Amati relation.

In contrast, the time-resolved Yonetoku relation $E_{peak,rest}$-$L_{iso,\gamma}$ showed a strong correlation, whilst the time-integrated Yonetoku relation showed some correlation but nevertheless with a few outlying points above the Yonetoku best-fit line. This is may have been due to the sensitivity of the luminosity to the entire burst spectrum rather than to individual bursts. Generally, the scattering in the time-integrated Yonetoku relation may also have been due to the different measure of the flux used to calculate the luminosity L_{iso}, which was chosen to be a 1-sec peak flux, rather than average peak flux as used in this analysis. This showed a strong agreement with the original Yonetoku relation; moreover, a close Yonetoku relation in the time-resolved spectrum could also be interpreted, as in each individual pulse (time-sliced) the luminosity can carry sufficient flux that it can be observed in each pulse and hence the E_{peak} can also be effected in this matter. Thus, the Yonetoku relation can show good agreement for both quantities. It has been found that the time-resolved correlations within individual GRBs were consistent, and were similar to those found in the time-integrated spectral properties. This represented a strong argument with regards to the physical origin of these correlations due to the way that, for individual bursts, it was unlikely that the instrumental selection was effected, or indeed that other effects linked to the $E_{peak,rest}$, E_{iso} or L_{iso} played any role (Nava et al., 2012).

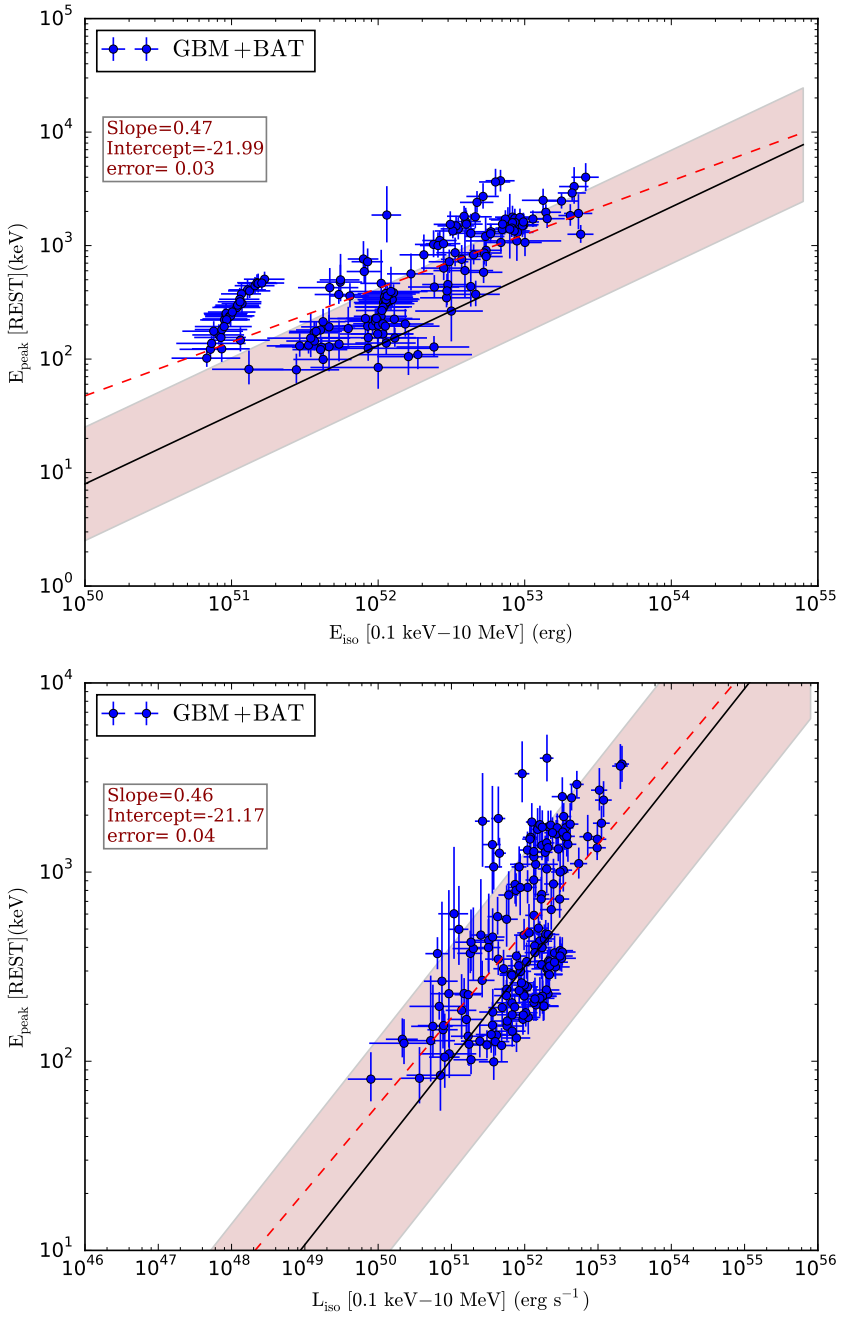

Figure 4.10: The upper panel is the E_{peak} vs. E_{iso} for the joint-fit in the rest frame. The lower panel is the E_{peak} vs. L_{iso} for the the joint-fit. The solid black line is the best fit with a gradient of 0.61 [0.04] for $E_{peak,rest} - E_{iso,\gamma}$ and 0.53 [0.06] for $E_{peak,rest} - L_{iso,\gamma}$, the pink shaded region represents the 3 σ scatter around the best-fit line adapted from the complete sample in Nava et al. (2012). The red dashed line is the best fit from this study in both panels with their gradients (the small left sided box). The uncertainty confidence level is 90% for the data while the Amati Yonetoku gradients is 3 σ.

This was as used in V12 as they considered two different uncertainty confident levels, 90% for the data and 3 σ on the correlation gradients.

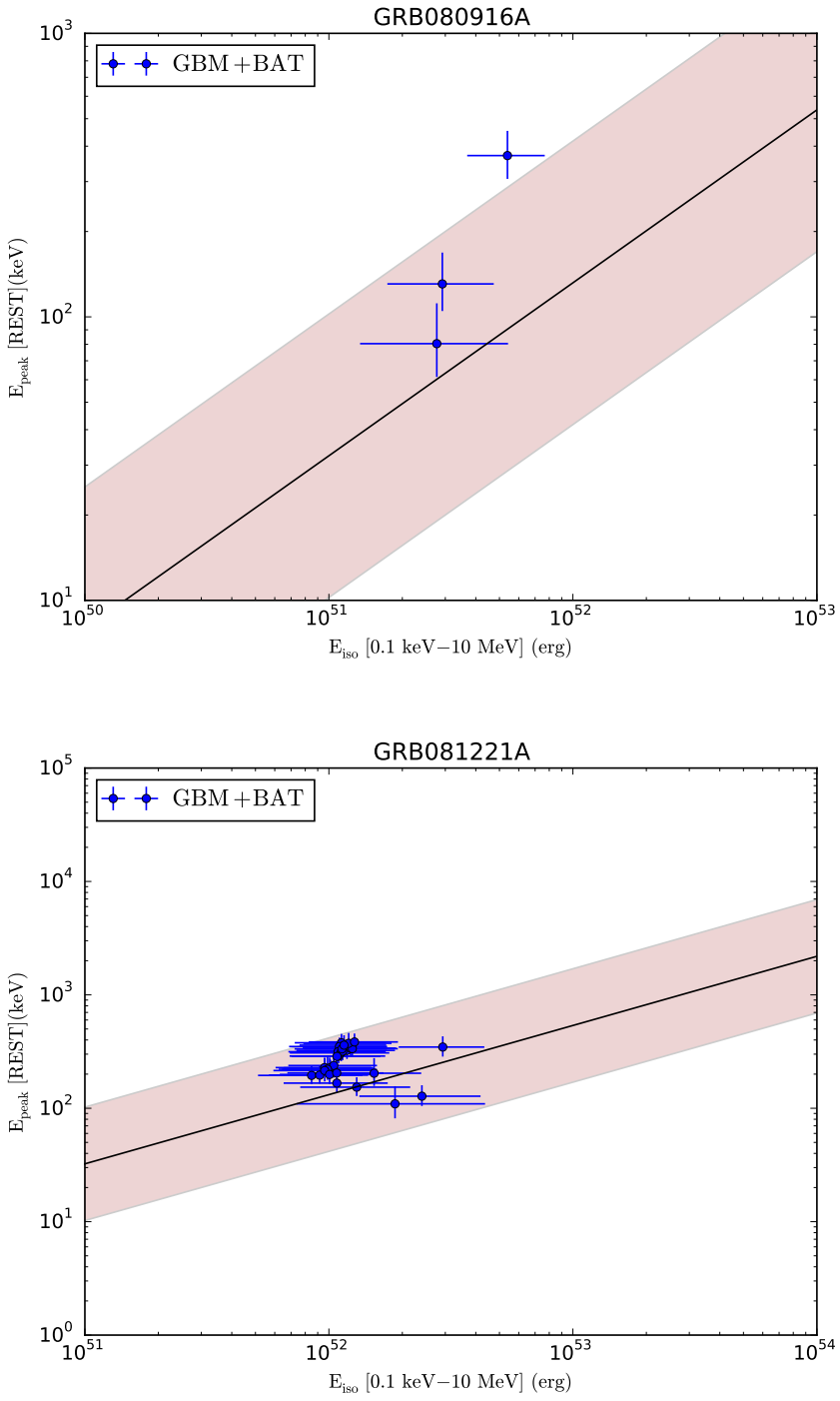

Figure 4.11: Amati relation for individual bursts (all GRBs are shown except GRB 081221A and GRB 150301B). The solid black line is the best fit with a slope of 0.61 $\pm$0.0.4 taken from the complete sample, and the pink shaded region represents the 3 σ scatter around the best-fit line adapted from Nava et al. (2012).

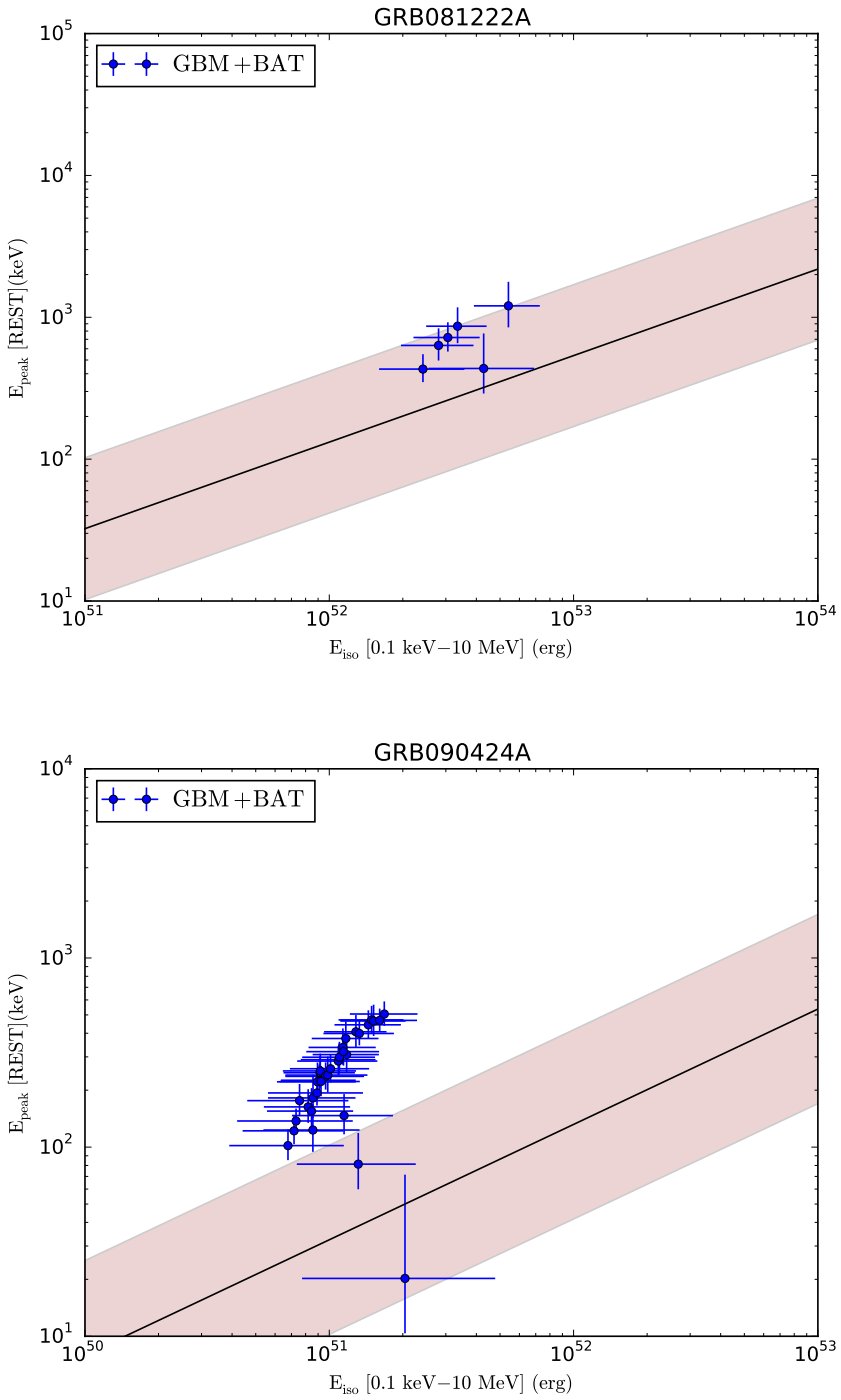

Figure 4.11: cont'd

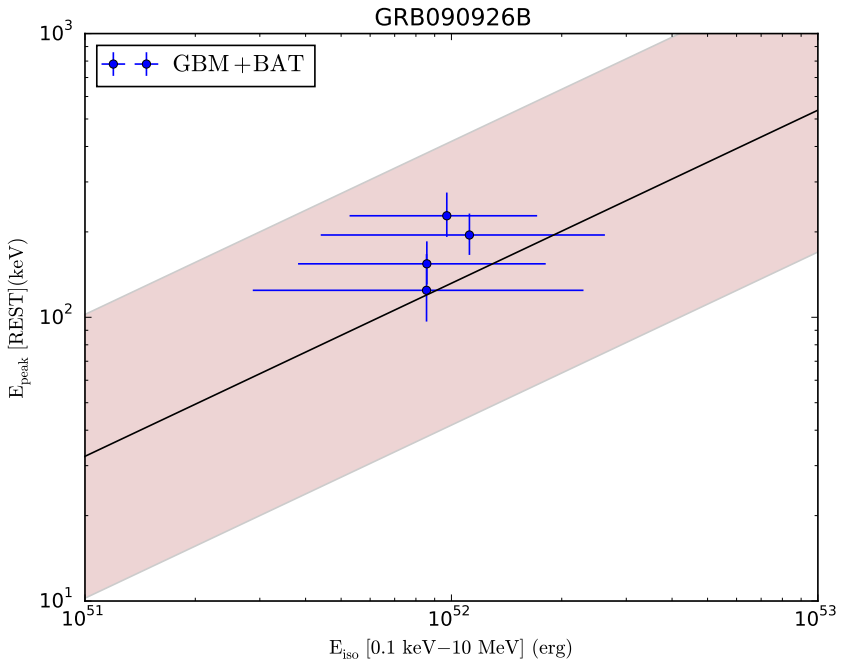

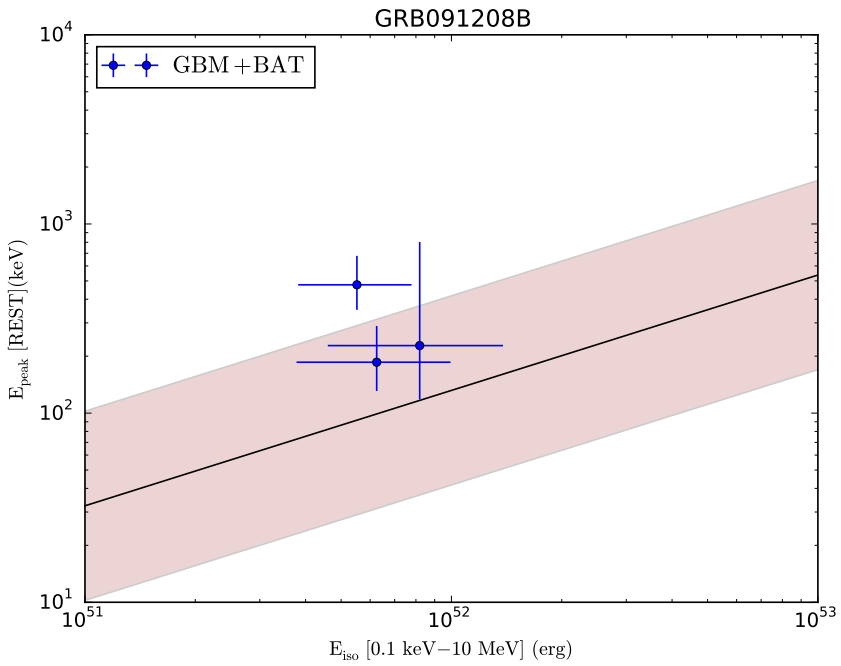

Figure 4.11: cont'd

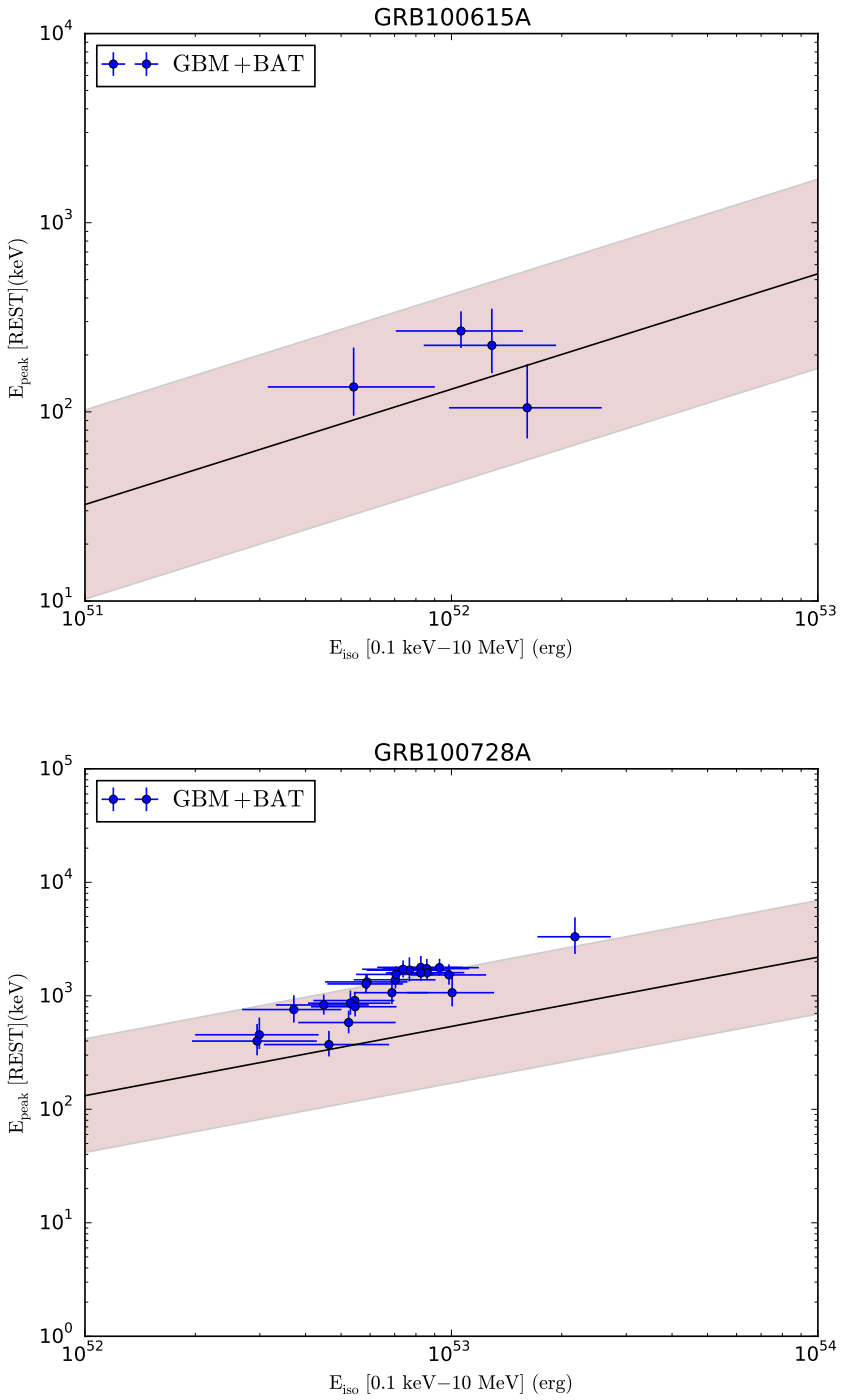

Figure 4.11: cont'd

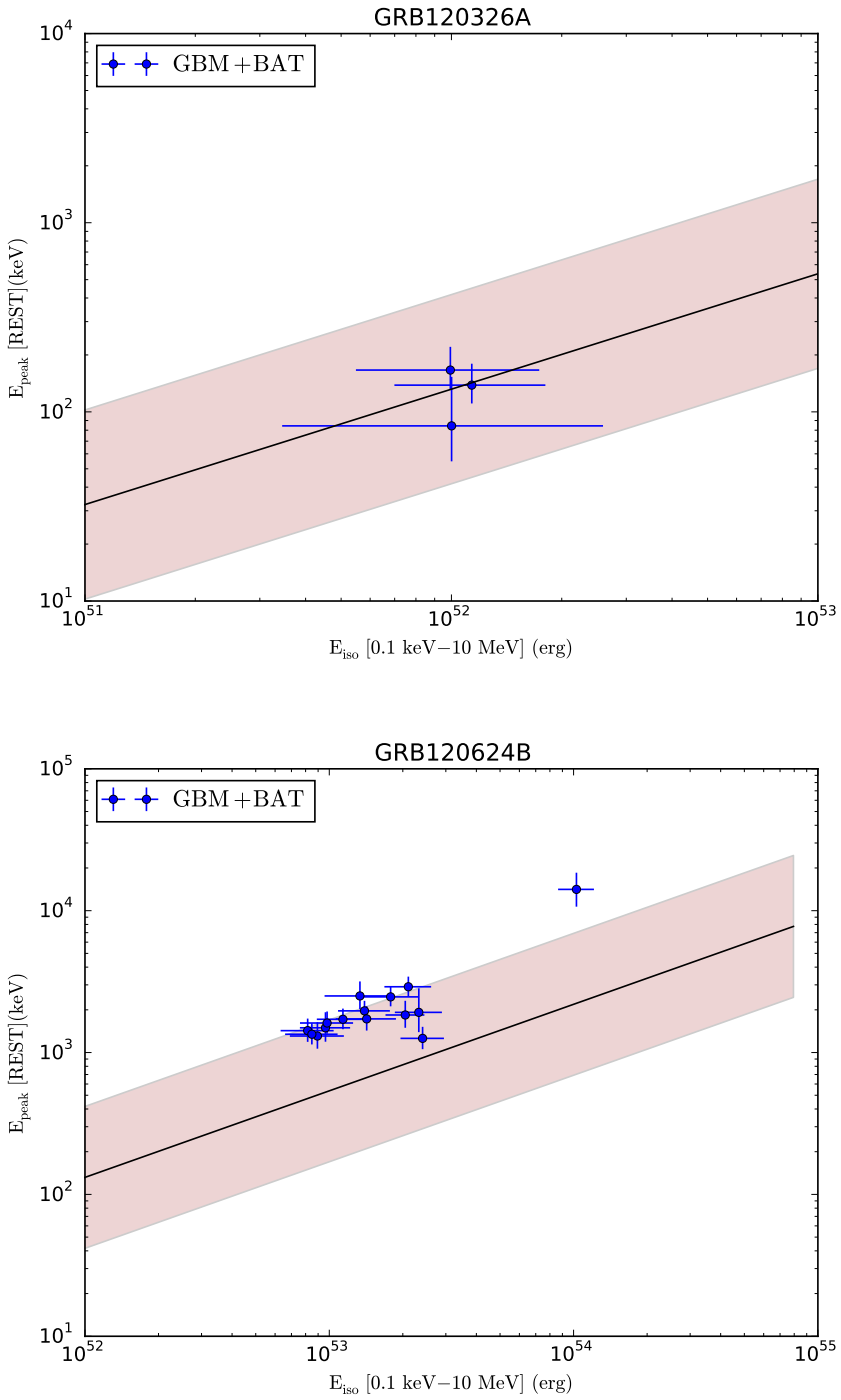

Figure 4.11: cont'd

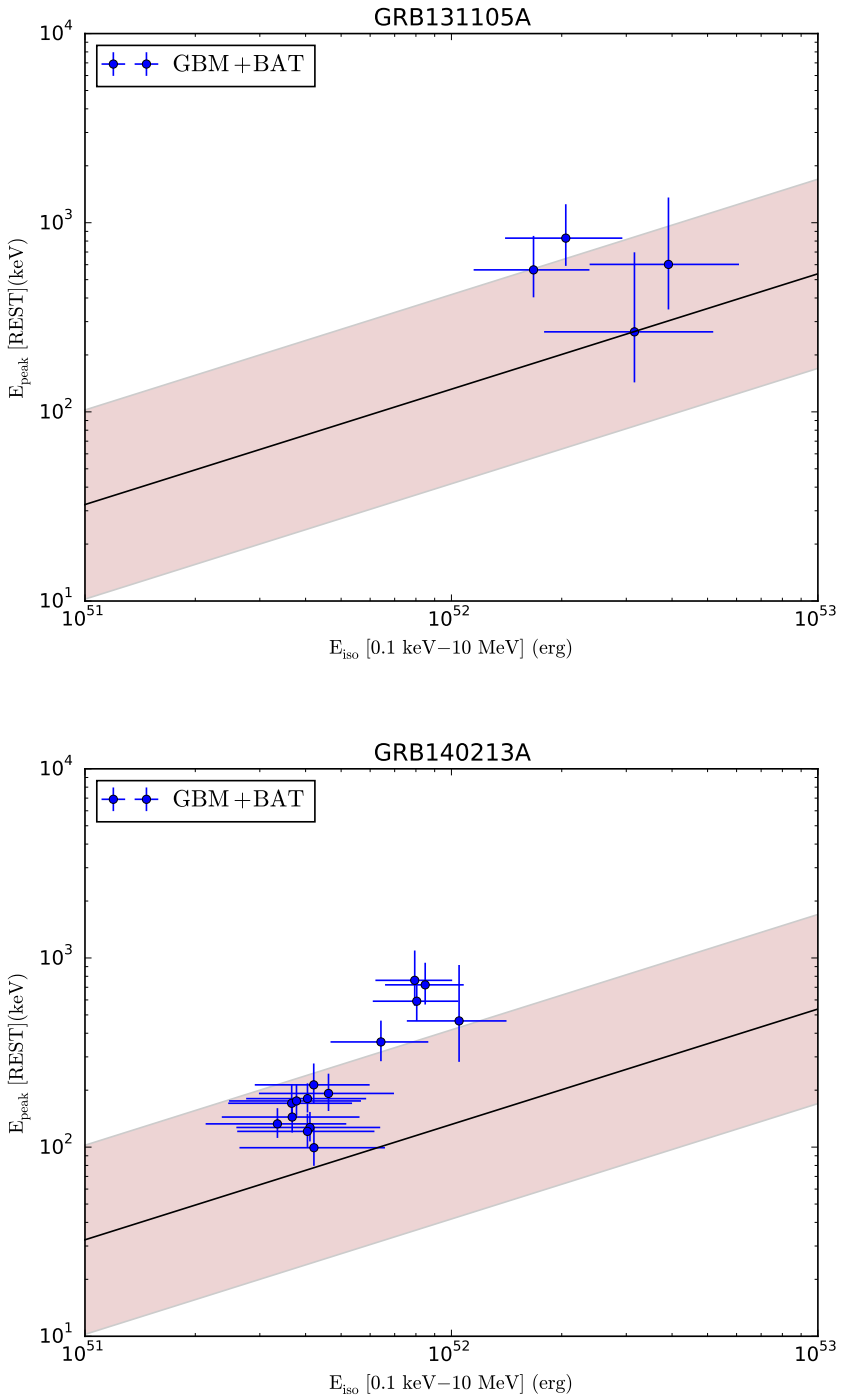

Figure 4.11: cont'd

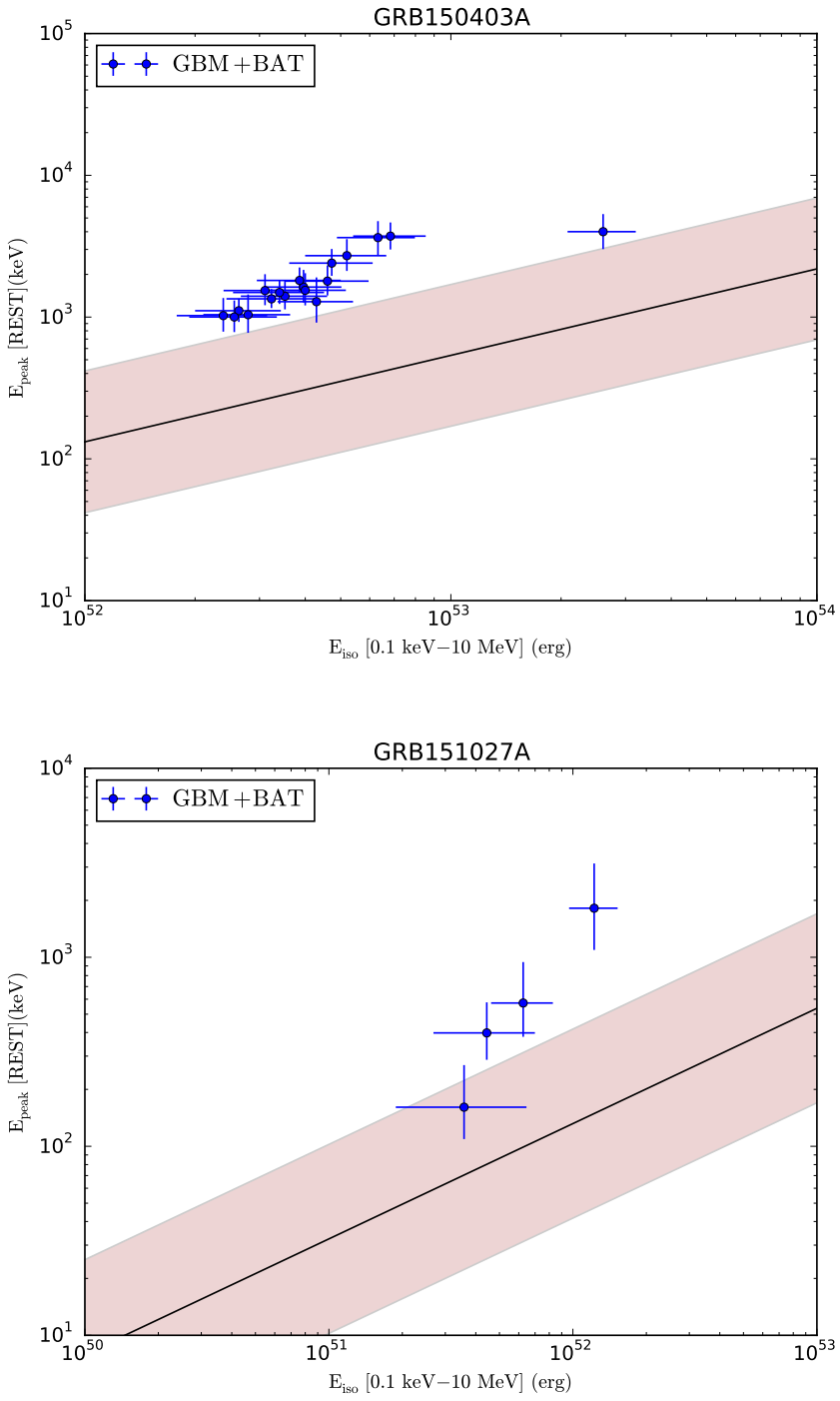

Figure 4.11: cont'd

Table 4.1: Time-resolved spectra for GRBs that were best fit with the CPL model. The spectra were fitted with the energy range for BAT (15-150 keV) and for GBM (10-1000 keV). The uncertainties adapted here are 90% confidence levels.

T_s[s]	T_e[s]	α	E_{peak} $[keV]$	offset	$Cstat$	dof	E_{iso} $[erg]$
GRB 080916A							
-2.37	6	$-0.46^{+0.11}_{-0.12}$	$219.41^{+37.93}_{-48.73}$	0.81	388	417	$51.04^{+0.12}_{-0.37}$
6	19.63	$-0.84^{+0.18}_{-0.19}$	$77.37^{+15.29}_{-22.42}$	0.75	390	417	$50.56^{+0.15}_{-0.41}$
19.63	54.42	$-0.99^{+0.26}_{-0.28}$	$47.62^{+11.27}_{-18.47}$	0.82	404	417	$50.13^{+0.18}_{-0.46}$
GRB 081121A							
7.85	14.11	$-0.87^{+0.19}_{-0.22}$	$313.08^{+104.2}_{-186.87}$	0.62	246	294	$52.70^{+0.19}_{-0.45}$
GRB 81221A							
-1.02	5.7	$-0.78^{+0.14}_{-0.14}$	$106.32^{+18.72}_{-25.85}$	0.84	266	299	$52.15^{+0.13}_{-0.38}$
5.7	15.56	$-0.87^{+0.22}_{-0.24}$	$39.20^{+7.07}_{-9.76}$	0.83	301	299	$51.90^{+0.16}_{-0.43}$
15.56	17.85	$-1.21^{+0.17}_{-0.18}$	$62.48^{+14.15}_{-22.42}$	0.84	266	299	$52.34^{+0.14}_{-0.40}$
17.85	18.54	$-0.56^{+0.16}_{-0.16}$	$99.37^{+15.85}_{-21.33}$	0.82	244	299	$52.74^{+0.14}_{-0.40}$
18.54	19.12	$-0.47^{+0.15}_{-0.15}$	$103.93^{+15.22}_{-19.81}$	0.82	242	299	$52.84^{+0.13}_{-0.39}$
19.12	19.69	$-0.41^{+0.15}_{-0.15}$	$102.85^{+14.46}_{-18.43}$	0.84	213	299	$52.86^{+0.14}_{-0.39}$
19.69	20.25	$-0.35^{+0.16}_{-0.16}$	$94.43^{+12.96}_{-16.56}$	0.87	233	299	$52.81^{+0.14}_{-0.40}$
20.25	20.72	$-0.69^{+0.14}_{-0.15}$	$114.74^{+19.66}_{-26.93}$	0.86	212	299	$52.92^{+0.13}_{-0.39}$
20.72	21.14	$-0.46^{+0.14}_{-0.14}$	$117.89^{+17.07}_{-22.04}$	0.8	282	299	$52.99^{+0.13}_{-0.39}$
21.14	21.49	$-0.49^{+0.14}_{-0.15}$	$115.92^{+17.54}_{-22.96}$	0.85	212	299	$53.03^{+0.13}_{-0.39}$
21.49	21.83	$-0.41^{+0.15}_{-0.16}$	$107.44^{+16.24}_{-21.26}$	0.8	231	299	$53.02^{+0.14}_{-0.40}$
21.83	22.25	$-0.38^{+0.15}_{-0.16}$	$96.69^{+13.24}_{-16.94}$	0.82	243	299	$52.93^{+0.14}_{-0.40}$
22.25	22.76	$-0.45^{+0.15}_{-0.16}$	$88.53^{+12.09}_{-15.40}$	0.85	249	299	$52.84^{+0.14}_{-0.40}$
22.76	23.31	$-0.76^{+0.14}_{-0.15}$	$95.64^{+15.92}_{-21.76}$	0.86	199	299	$52.83^{+0.13}_{-0.39}$
23.31	23.83	$-0.74^{+0.14}_{-0.15}$	$97.66^{+16.15}_{-21.93}$	0.83	192	299	$52.85^{+0.13}_{-0.39}$
23.83	24.27	$-0.63^{+0.15}_{-0.15}$	$102.46^{+16.57}_{-22.35}$	0.84	235	299	$52.92^{+0.13}_{-0.39}$
24.27	24.65	$-0.68^{+0.14}_{-0.14}$	$110.43^{+18.19}_{-24.61}$	0.86	212	299	$53.00^{+0.13}_{-0.39}$
24.65	25.15	$-0.77^{+0.14}_{-0.15}$	$87.89^{+14.26}_{-19.37}$	0.91	202	299	$52.85^{+0.13}_{-0.39}$
25.15	25.73	$-0.83^{+0.16}_{-0.17}$	$67.53^{+10.75}_{-14.52}$	0.83	196	299	$52.76^{+0.14}_{-0.40}$
25.73	26.22	$-0.81^{+0.16}_{-0.17}$	$70.05^{+11.26}_{-15.22}$	0.79	196	299	$52.81^{+0.14}_{-0.40}$
26.22	26.69	$-0.79^{+0.18}_{-0.19}$	$59.79^{+9.68}_{-13.06}$	0.79	212	299	$52.77^{+0.15}_{-0.41}$
26.69	27.19	$-0.84^{+0.17}_{-0.18}$	$60.13^{+9.54}_{-12.82}$	0.81	199	299	$52.77^{+0.14}_{-0.40}$
27.19	27.68	$-0.96^{+0.15}_{-0.16}$	$69.67^{+11.78}_{-16.26}$	0.82	216	299	$52.83^{+0.13}_{-0.39}$
27.68	28.21	$-1.21^{+0.15}_{-0.16}$	$73.04^{+15.89}_{-24.98}$	0.87	186	299	$52.81^{+0.13}_{-0.39}$
28.21	28.77	$-1.06^{+0.16}_{-0.17}$	$67.73^{+13.08}_{-19.38}$	0.8	221	299	$52.76^{+0.14}_{-0.40}$
28.77	29.37	$-1.03^{+0.17}_{-0.18}$	$65.98^{+13.08}_{-19.38}$	0.81	193	299	$52.72^{+0.14}_{-0.40}$
29.37	30.07	$-0.98^{+0.17}_{-0.17}$	$60.92^{+10.82}_{-15.32}$	0.84	183	299	$52.67^{+0.14}_{-0.40}$
30.07	30.88	$-1.11^{+0.16}_{-0.17}$	$62.78^{+12.61}_{-18.83}$	0.81	217	299	$52.64^{+0.14}_{-0.40}$
30.88	32.02	$-0.95^{+0.18}_{-0.19}$	$51.12^{+8.78}_{-12.23}$	0.83	224	299	$52.49^{+0.14}_{-0.41}$
32.02	34.29	$-0.86^{+0.19}_{-0.20}$	$47.09^{+7.76}_{-10.50}$	0.78	290	299	$52.27^{+0.15}_{-0.41}$

Table 4.1 cont'd

T_s[s]	T_e[s]	α	E_{peak} $[keV]$	offset	$Cstat$	dof	E_{iso} $[erg]$
34.29	54.27	$-1.00^{+0.35}_{-0.38}$	$33.57^{+8.56}_{-14.45}$	0.92	292	299	$51.48^{+0.21}_{-0.51}$
GRB 081222A							
-2.18	1.88	$-0.99^{+0.09}_{-0.10}$	$319.39^{+94.19}_{-152.44}$	0.84	382	418	$52.70^{+0.11}_{-0.35}$
1.88	3.24	$-1.05^{+0.09}_{-0.10}$	$229.52^{+55.23}_{-82.39}$	0.88	325	418	$52.97^{+0.10}_{-0.35}$
3.24	4.26	$-0.87^{+0.10}_{-0.11}$	$191.05^{+38.97}_{-53.61}$	0.81	308	418	$53.05^{+0.11}_{-0.35}$
4.26	5.47	$-0.93^{+0.11}_{-0.12}$	$167.99^{+36.47}_{-53.82}$	0.81	301	418	$52.94^{+0.11}_{-0.36}$
5.47	6.98	$-0.81^{+0.14}_{-0.14}$	$114.43^{+21.80}_{-31.33}$	0.78	335	418	$52.78^{+0.13}_{-0.38}$
6.98	20.25	$-1.22^{+0.17}_{-0.19}$	$115.58^{+38.62}_{-88.51}$	0.82	367	418	$52.09^{+0.15}_{-0.40}$
GRB 090424A							
-1.02	0.47	$-0.89^{+0.16}_{-0.17}$	$95.06^{+19.38}_{-28.50}$	0.87	322	417	$51.08^{+0.14}_{-0.40}$
0.47	0.61	$-0.88^{+0.13}_{-0.14}$	$105.68^{+18.67}_{-25.36}$	0.76	284	417	$51.95^{+0.13}_{-0.38}$
0.61	0.71	$-0.88^{+0.11}_{-0.12}$	$146.17^{+24.09}_{-31.07}$	0.85	236	417	$52.17^{+0.12}_{-0.37}$
0.71	0.79	$-0.96^{+0.10}_{-0.11}$	$160.12^{+27.43}_{-36.09}$	0.84	209	417	$52.23^{+0.11}_{-0.37}$
0.79	0.88	$-0.99^{+0.12}_{-0.12}$	$143.40^{+27.54}_{-38.06}$	0.71	291	417	$52.18^{+0.12}_{-0.37}$
0.88	0.98	$-0.95^{+0.11}_{-0.11}$	$163.73^{+28.87}_{-38.34}$	0.81	254	417	$52.18^{+0.11}_{-0.37}$
0.98	1.07	$-0.95^{+0.08}_{-0.09}$	$263.61^{+44.85}_{-59.68}$	0.89	244	417	$52.32^{+0.10}_{-0.36}$
1.07	1.16	$-0.93^{+0.09}_{-0.10}$	$243.03^{+41.98}_{-55.70}$	0.81	221	417	$52.33^{+0.11}_{-0.36}$
1.16	1.26	$-0.99^{+0.09}_{-0.10}$	$217.96^{+41.26}_{-56.82}$	0.79	242	417	$52.21^{+0.11}_{-0.36}$
1.26	1.34	$-0.64^{+0.09}_{-0.10}$	$258.30^{+34.64}_{-42.69}$	0.78	225	417	$52.42^{+0.11}_{-0.37}$
1.34	1.42	$-0.77^{+0.09}_{-0.09}$	$287.05^{+43.79}_{-55.59}$	0.81	229	417	$52.46^{+0.10}_{-0.36}$
1.42	1.49	$-0.77^{+0.08}_{-0.09}$	$304.82^{+44.78}_{-56.71}$	0.81	200	417	$52.48^{+0.10}_{-0.36}$
1.49	1.61	$-0.68^{+0.11}_{-0.12}$	$153.23^{+22.78}_{-28.48}$	0.81	210	417	$52.11^{+0.12}_{-0.38}$
1.61	1.84	$-1.12^{+0.14}_{-0.15}$	$100.43^{+21.94}_{-32.41}$	0.86	312	417	$51.75^{+0.13}_{-0.38}$
1.84	2.08	$-1.04^{+0.14}_{-0.14}$	$117.88^{+25.61}_{-38.38}$	0.81	248	417	$51.75^{+0.13}_{-0.38}$
2.08	2.25	$-0.84^{+0.12}_{-0.13}$	$155.67^{+29.42}_{-39.32}$	0.75	258	417	$51.94^{+0.12}_{-0.38}$
2.25	2.48	$-0.64^{+0.16}_{-0.17}$	$78.95^{+11.77}_{-15.45}$	0.77	311	417	$51.67^{+0.14}_{-0.41}$
2.48	2.71	$-1.03^{+0.09}_{-0.10}$	$199.79^{+38.33}_{-51.73}$	0.88	234	417	$51.90^{+0.11}_{-0.36}$
2.71	2.88	$-0.79^{+0.11}_{-0.11}$	$187.71^{+31.21}_{-40.61}$	0.9	278	417	$52.00^{+0.12}_{-0.37}$
2.88	3.04	$-0.85^{+0.09}_{-0.09}$	$300.78^{+50.27}_{-65.96}$	0.83	270	417	$52.18^{+0.10}_{-0.36}$
3.04	3.21	$-0.18^{+0.18}_{-0.19}$	$89.02^{+11.38}_{-14.52}$	0.6	385	417	$51.80^{+0.15}_{-0.42}$
3.21	3.71	$-1.17^{+0.16}_{-0.17}$	$79.74^{+18.60}_{-29.74}$	0.84	240	417	$51.43^{+0.14}_{-0.39}$
3.71	3.87	$-0.67^{+0.11}_{-0.12}$	$184.60^{+29.54}_{-37.78}$	0.79	221	417	$52.01^{+0.12}_{-0.38}$
3.87	4.03	$-0.75^{+0.12}_{-0.13}$	$143.96^{+23.65}_{-30.01}$	0.86	244	417	$51.94^{+0.12}_{-0.38}$
4.03	4.14	$-0.62^{+0.09}_{-0.09}$	$327.37^{+43.70}_{-54.27}$	0.88	235	417	$52.38^{+0.11}_{-0.37}$
4.14	4.22	$-0.44^{+0.10}_{-0.10}$	$302.88^{+38.26}_{-46.77}$	0.78	245	417	$52.51^{+0.12}_{-0.38}$
4.32	4.43	$-0.67^{+0.11}_{-0.12}$	$168.15^{+25.85}_{-32.65}$	0.74	261	417	$52.14^{+0.12}_{-0.38}$
4.43	4.55	$-0.39^{+0.14}_{-0.15}$	$125.26^{+17.81}_{-22.02}$	0.84	243	417	$52.05^{+0.14}_{-0.39}$
4.55	4.68	$-0.79^{+0.10}_{-0.11}$	$193.47^{+31.01}_{-40.08}$	0.81	297	417	$52.13^{+0.11}_{-0.37}$
4.68	4.79	$-0.60^{+0.15}_{-0.17}$	$114.03^{+19.48}_{-25.63}$	0.79	272	417	$52.02^{+0.14}_{-0.40}$
4.79	4.93	$-0.75^{+0.10}_{-0.11}$	$207.05^{+32.36}_{-41.32}$	0.87	239	417	$52.11^{+0.11}_{-0.37}$
4.93	5.29	$-0.60^{+0.19}_{-0.20}$	$65.97^{+10.68}_{-14.34}$	0.85	266	417	$51.46^{+0.15}_{-0.42}$

Table 4.1 cont'd

T_s[s]	T_e[s]	α	E_{peak} $[keV]$	offset	$Cstat$	dof	E_{iso} $[erg]$
5.29	8.88	$-1.22^{+0.21}_{-0.22}$	$52.65^{+13.88}_{-24.29}$	0.88	350	417	$50.75^{+0.16}_{-0.42}$
GRB 090926B							
-0.26	16.15	$0.53^{+0.28}_{-0.31}$	$87.07^{+13.00}_{-16.54}$	0.78	330	299	$51.18^{+0.21}_{-0.51}$
16.15	22.67	$-0.17^{+0.19}_{-0.20}$	$101.77^{+16.05}_{-21.08}$	0.84	326	299	$51.52^{+0.16}_{-0.43}$
22.67	33.64	$0.14^{+0.26}_{-0.29}$	$68.90^{+10.65}_{-13.78}$	0.77	293	299	$51.24^{+0.19}_{-0.48}$
33.64	71.57	$-0.26^{+0.37}_{-0.40}$	$55.57^{+12.45}_{-18.97}$	0.87	267	299	$50.70^{+0.22}_{-0.55}$
GRB 091208B							
-0.64	8.24	$-1.54^{+0.19}_{-0.21}$	$110.29^{+52.92}_{-279.0}$	0.91	399	416	$51.28^{+0.16}_{-0.41}$
8.24	8.72	$-1.06^{+0.11}_{-0.12}$	$231.15^{+60.76}_{-97.71}$	0.91	278	416	$52.37^{+0.12}_{-0.37}$
8.72	13.26	$-1.28^{+0.16}_{-0.18}$	$90.07^{+26.58}_{-49.90}$	0.9	370	416	$51.45^{+0.14}_{-0.40}$
GRB 100615A							
-1.22	2.83	$-0.79^{+0.14}_{-0.14}$	$111.64^{+20.91}_{-30.13}$	0.67	257	299	$51.80^{+0.13}_{-0.38}$
2.83	10.44	$-1.26^{+0.15}_{-0.16}$	$93.74^{+26.94}_{-52.64}$	0.68	337	299	$51.61^{+0.13}_{-0.38}$
10.44	13.64	$-1.39^{+0.19}_{-0.21}$	$56.51^{+16.68}_{-34.76}$	1.19	298	299	$51.61^{+0.15}_{-0.41}$
13.64	33.49	$-1.55^{+0.18}_{-0.19}$	$43.84^{+13.67}_{-30.59}$	0.86	294	299	$51.29^{+0.14}_{-0.40}$
GRB 100728A							
-4.1	19.46	$-1.01^{+0.06}_{-0.06}$	$1066.5^{+313.5}_{-515.37}$	0.91	363	419	$52.46^{+0.08}_{-0.34}$
19.46	46.08	$-0.99^{+0.08}_{-0.08}$	$342.97^{+83.05}_{-123.52}$	0.83	402	419	$52.07^{+0.10}_{-0.35}$
46.08	54.27	$-0.84^{+0.06}_{-0.07}$	$491.69^{+88.46}_{-118.02}$	0.85	429	419	$52.57^{+0.08}_{-0.35}$
54.27	58.37	$-0.75^{+0.07}_{-0.07}$	$445.55^{+73.50}_{-95.57}$	0.84	350	419	$52.73^{+0.09}_{-0.35}$
58.37	63.49	$-0.86^{+0.07}_{-0.07}$	$541.80^{+110.6}_{-159.68}$	0.86	406	419	$52.67^{+0.09}_{-0.35}$
63.49	68.61	$-0.80^{+0.07}_{-0.07}$	$573.51^{+108.5}_{-149.18}$	0.91	338	419	$52.70^{+0.09}_{-0.35}$
68.61	72.71	$-0.71^{+0.07}_{-0.07}$	$558.99^{+92.75}_{-121.07}$	0.79	376	419	$52.81^{+0.09}_{-0.35}$
72.71	76.8	$-0.68^{+0.06}_{-0.07}$	$569.85^{+88.07}_{-111.81}$	0.9	348	419	$52.85^{+0.09}_{-0.35}$
76.8	79.87	$-0.66^{+0.06}_{-0.06}$	$515.03^{+73.49}_{-90.78}$	0.86	388	419	$52.94^{+0.08}_{-0.35}$
79.87	81.92	$-0.67^{+0.06}_{-0.07}$	$551.51^{+85.09}_{-108.19}$	0.82	344	419	$53.05^{+0.09}_{-0.35}$
81.92	83.97	$-0.63^{+0.06}_{-0.07}$	$497.10^{+71.83}_{-89.26}$	0.84	373	419	$53.03^{+0.09}_{-0.35}$
83.97	86.02	$-0.60^{+0.07}_{-0.07}$	$426.41^{+59.03}_{-73.15}$	0.83	342	419	$52.95^{+0.09}_{-0.35}$
86.02	89.09	$-0.79^{+0.06}_{-0.06}$	$511.95^{+75.47}_{-94.91}$	0.81	379	419	$52.92^{+0.08}_{-0.34}$
89.09	92.16	$-0.82^{+0.06}_{-0.07}$	$409.61^{+70.75}_{-92.09}$	0.82	351	419	$52.77^{+0.08}_{-0.35}$
92.16	96.26	$-0.70^{+0.07}_{-0.08}$	$292.36^{+45.21}_{-56.85}$	0.79	389	419	$52.62^{+0.09}_{-0.35}$
96.26	103.43	$-0.95^{+0.08}_{-0.08}$	$276.92^{+57.95}_{-81.26}$	0.87	378	419	$52.36^{+0.09}_{-0.35}$
103.43	111.62	$-0.95^{+0.07}_{-0.07}$	$342.96^{+70.78}_{-97.35}$	0.87	378	419	$52.42^{+0.08}_{-0.34}$
111.62	123.91	$-0.89^{+0.10}_{-0.10}$	$187.24^{+36.71}_{-50.96}$	0.82	395	419	$52.12^{+0.10}_{-0.36}$
123.91	128	$-0.69^{+0.09}_{-0.09}$	$267.32^{+47.50}_{-62.22}$	0.83	416	419	$52.53^{+0.10}_{-0.35}$
128	135.17	$-0.81^{+0.08}_{-0.08}$	$257.89^{+46.03}_{-59.63}$	0.82	409	419	$52.37^{+0.09}_{-0.35}$
135.17	143.36	$-1.02^{+0.13}_{-0.14}$	$146.04^{+36.81}_{-61.03}$	0.89	350	419	$52.05^{+0.12}_{-0.37}$
143.36	168.96	$-0.98^{+0.13}_{-0.14}$	$119.73^{+25.63}_{-38.16}$	0.84	372	419	$51.75^{+0.13}_{-0.37}$
168.96	178.18	$-1.08^{+0.13}_{-0.14}$	$128.50^{+32.32}_{-53.17}$	0.93	433	419	$52.00^{+0.13}_{-0.37}$
178.18	184.32	$-0.92^{+0.09}_{-0.10}$	$243.53^{+56.74}_{-81.75}$	0.89	445	419	$52.27^{+0.11}_{-0.35}$
GRB 120326A							

Table 4.1 cont'd

T_s[s]	T_e[s]	α	E_{peak} $[keV]$	offset	$Cstat$	dof	E_{iso} $[erg]$
-4.16	2.06	$-0.94^{+0.21}_{-0.22}$	$59.45^{+12.56}_{-19.42}$	0.95	280	298	$51.65^{+0.16}_{-0.43}$
2.06	5.31	$-1.13^{+0.18}_{-0.19}$	$49.49^{+9.89}_{-14.75}$	0.7	263	298	$51.99^{+0.14}_{-0.40}$
5.31	19.45	$-1.30^{+0.39}_{-0.44}$	$30.14^{+10.57}_{-24.59}$	0.72	276	298	$51.30^{+0.22}_{-0.53}$
GRB 120624B							
-245.76	-229.38	$-1.01^{+0.05}_{-0.05}$	$575.32^{+107.8}_{-148.97}$	0.83	2866	419	$52.60^{+0.07}_{-0.33}$
-229.38	-221.19	$-0.96^{+0.06}_{-0.07}$	$467.34^{+94.54}_{-134.25}$	0.85	2774	419	$52.58^{+0.08}_{-0.35}$
-221.19	-167.94	$-1.15^{+0.06}_{-0.06}$	$600.38^{+164.8}_{-286.24}$	0.9	2656	419	$52.15^{+0.08}_{-0.34}$
-167.94	-114.69	$-0.94^{+0.06}_{-0.06}$	$393.64^{+63.22}_{-81.07}$	0.86	2714	419	$52.16^{+0.07}_{-0.34}$
-114.69	-106.5	$-0.91^{+0.07}_{-0.07}$	$409.00^{+76.05}_{-103.29}$	0.71	2756	419	$52.54^{+0.09}_{-0.35}$
-106.5	-102.4	$-0.81^{+0.07}_{-0.07}$	$446.18^{+74.18}_{-96.55}$	0.8	2909	419	$52.80^{+0.09}_{-0.35}$
-102.4	-98.31	$-0.79^{+0.06}_{-0.07}$	$420.96^{+64.19}_{-81.57}$	0.77	2897	419	$52.82^{+0.09}_{-0.35}$
-98.31	-94.21	$-0.75^{+0.06}_{-0.06}$	$536.47^{+79.77}_{-101.66}$	0.82	2978	419	$52.95^{+0.09}_{-0.35}$
-94.21	-90.11	$-0.80^{+0.06}_{-0.07}$	$505.11^{+80.15}_{-103.78}$	0.83	2977	419	$52.88^{+0.09}_{-0.35}$
-90.11	-86.02	$-0.73^{+0.06}_{-0.06}$	$615.18^{+86.71}_{-108.88}$	0.76	3236	419	$53.04^{+0.09}_{-0.35}$
-86.02	-81.92	$-0.77^{+0.05}_{-0.05}$	$909.76^{+132.9}_{-162.62}$	0.77	3745	419	$53.21^{+0.08}_{-0.34}$
-81.92	-77.83	$-0.65^{+0.06}_{-0.07}$	$771.95^{+109.7}_{-135.56}$	0.8	3564	419	$53.14^{+0.09}_{-0.35}$
-77.83	-73.73	$-0.75^{+0.08}_{-0.08}$	$783.76^{+152.0}_{-208.13}$	0.76	3265	419	$53.02^{+0.11}_{-0.36}$
-73.73	-65.54	$-0.82^{+0.07}_{-0.08}$	$540.00^{+93.23}_{-123.71}$	0.81	3009	419	$52.74^{+0.10}_{-0.35}$
GRB 131105A							
-3.97	32.08	$-1.27^{+0.15}_{-0.16}$	$224.17^{+94.64}_{-281.94}$	0.69	261	300	$51.46^{+0.14}_{-0.39}$
32.08	34.45	$-0.99^{+0.11}_{-0.12}$	$308.62^{+88.46}_{-157.70}$	0.65	255	300	$52.37^{+0.12}_{-0.37}$
34.45	37.4	$-1.13^{+0.11}_{-0.12}$	$209.72^{+59.59}_{-107.35}$	0.62	285	300	$52.18^{+0.12}_{-0.37}$
37.4	79.93	$-1.49^{+0.18}_{-0.21}$	$98.62^{+45.31}_{-161.06}$	0.71	251	300	$51.30^{+0.16}_{-0.39}$
113.53	123.58	$-1.40^{+0.11}_{-0.15}$	$1259.0^{+957.5}_{--1259.}$	0.79	319	300	$52.04^{+0.14}_{-0.34}$
GRB 140213A							
-2.94	1.22	$-1.44^{+0.10}_{-0.11}$	$210.51^{+82.60}_{-205.34}$	0.83	365	417	$51.75^{+0.11}_{-0.35}$
1.22	1.69	$-1.27^{+0.07}_{-0.08}$	$345.04^{+92.15}_{-150.95}$	0.84	294	417	$52.58^{+0.09}_{-0.34}$
1.69	2.19	$-1.11^{+0.07}_{-0.08}$	$326.57^{+69.61}_{-100.78}$	0.8	253	417	$52.57^{+0.09}_{-0.35}$
2.19	2.79	$-1.05^{+0.08}_{-0.09}$	$267.60^{+57.33}_{-81.69}$	0.84	321	417	$52.47^{+0.09}_{-0.35}$
2.79	3.62	$-1.05^{+0.10}_{-0.11}$	$162.98^{+34.04}_{-48.28}$	0.84	329	417	$52.23^{+0.10}_{-0.36}$
3.62	4.56	$-0.90^{+0.15}_{-0.16}$	$87.07^{+16.74}_{-23.67}$	0.74	347	417	$52.04^{+0.13}_{-0.39}$
4.56	5.6	$-0.82^{+0.16}_{-0.17}$	$57.54^{+8.99}_{-11.95}$	0.78	288	417	$51.94^{+0.14}_{-0.40}$
5.6	6.03	$-0.85^{+0.16}_{-0.17}$	$60.11^{+9.45}_{-12.65}$	0.8	259	417	$52.23^{+0.13}_{-0.40}$
6.03	6.36	$-1.07^{+0.14}_{-0.14}$	$77.26^{+14.43}_{-20.37}$	0.8	220	417	$52.39^{+0.12}_{-0.38}$
6.36	6.66	$-1.11^{+0.12}_{-0.13}$	$96.67^{+19.63}_{-28.70}$	0.78	269	417	$52.48^{+0.12}_{-0.37}$
6.66	7.05	$-0.87^{+0.13}_{-0.14}$	$81.75^{+12.68}_{-16.76}$	0.74	329	417	$52.36^{+0.12}_{-0.38}$
7.05	7.45	$-0.84^{+0.14}_{-0.15}$	$79.46^{+13.20}_{-17.97}$	0.75	242	417	$52.32^{+0.13}_{-0.39}$
7.45	7.99	$-0.94^{+0.16}_{-0.16}$	$65.32^{+11.25}_{-15.57}$	0.74	250	417	$52.17^{+0.13}_{-0.39}$
7.99	8.83	$-1.02^{+0.16}_{-0.17}$	$54.86^{+9.49}_{-13.05}$	0.78	282	417	$52.03^{+0.13}_{-0.39}$
8.83	9.95	$-1.20^{+0.17}_{-0.18}$	$44.97^{+8.88}_{-13.08}$	0.78	246	417	$51.92^{+0.14}_{-0.40}$
GRB 150301B							

Table 4.1 cont'd

T_s[s]	T_e[s]	α	E_{peak} $[keV]$	offset	$Cstat$	dof	E_{iso} $[erg]$
-2.56	3.59	$-0.87^{+0.19}_{-0.22}$	$156.58^{+50.56}_{-101.82}$	0.88	266	299	$51.70^{+0.17}_{-0.42}$
3.59	17.99	$-1.57^{+0.15}_{-0.19}$	$347.52^{+240.3}_{347.52}$	1.01	313	299	$51.45^{+0.15}_{-0.38}$
17.99	23.74	$-0.81^{+1.12}_{-1.95}$	$83.07^{+73.84}_{-83.07}$	0.69	283	299	$50.60^{+0.30}_{-1.44}$
GRB 150403A							
-7.1	5.86	$-0.97^{+0.05}_{-0.06}$	$1308.0^{+322.3}_{-432.93}$	0.9	446	417	$52.79^{+0.08}_{-0.33}$
5.86	6.96	$-0.88^{+0.07}_{-0.07}$	$586.08^{+121.9}_{-170.67}$	0.97	345	417	$53.11^{+0.09}_{-0.35}$
6.96	7.86	$-0.88^{+0.07}_{-0.08}$	$458.52^{+88.03}_{-120.08}$	0.84	343	417	$53.08^{+0.09}_{-0.35}$
7.86	9.06	$-1.03^{+0.07}_{-0.07}$	$531.97^{+117.7}_{-171.43}$	0.91	324	417	$53.00^{+0.09}_{-0.35}$
9.06	10.13	$-0.95^{+0.07}_{-0.08}$	$505.00^{+109.9}_{-161.15}$	0.89	302	417	$53.06^{+0.09}_{-0.35}$
10.13	10.63	$-0.90^{+0.06}_{-0.07}$	$886.07^{+194.6}_{-273.04}$	0.84	298	417	$53.50^{+0.09}_{-0.35}$
10.63	11.02	$-0.82^{+0.07}_{-0.07}$	$785.18^{+146.7}_{-203.04}$	0.83	284	417	$53.56^{+0.09}_{-0.35}$
11.02	11.35	$-0.87^{+0.05}_{-0.06}$	$1217.4^{+237.9}_{-302.03}$	0.87	315	417	$53.81^{+0.08}_{-0.34}$
11.35	11.66	$-0.91^{+0.06}_{-0.07}$	$1188.2^{+290.4}_{-364.22}$	0.9	276	417	$53.79^{+0.09}_{-0.33}$
11.66	12.01	$-0.79^{+0.07}_{-0.07}$	$592.57^{+102.4}_{-139.08}$	0.89	287	417	$53.53^{+0.09}_{-0.35}$
12.01	12.35	$-0.73^{+0.08}_{-0.08}$	$487.44^{+82.91}_{-109.97}$	0.88	266	417	$53.48^{+0.10}_{-0.36}$
12.35	12.68	$-0.65^{+0.07}_{-0.08}$	$439.52^{+61.18}_{-76.21}$	0.92	268	417	$53.47^{+0.10}_{-0.36}$
12.68	13.11	$-0.97^{+0.07}_{-0.07}$	$502.90^{+106.6}_{-152.86}$	0.89	266	417	$53.35^{+0.09}_{-0.35}$
13.11	13.6	$-0.84^{+0.07}_{-0.08}$	$362.28^{+60.26}_{-78.30}$	0.89	263	417	$53.22^{+0.09}_{-0.35}$
13.6	14.31	$-1.00^{+0.08}_{-0.09}$	$334.60^{+76.69}_{-110.93}$	0.86	341	417	$53.01^{+0.10}_{-0.35}$
14.31	15.15	$-1.01^{+0.08}_{-0.08}$	$327.28^{+71.13}_{-100.67}$	0.87	306	417	$52.97^{+0.10}_{-0.35}$
15.15	16.55	$-1.10^{+0.08}_{-0.09}$	$339.61^{+86.46}_{-132.25}$	0.89	326	417	$52.79^{+0.10}_{-0.35}$
16.55	19.77	$-1.22^{+0.07}_{-0.07}$	$419.64^{+120.8}_{-202.69}$	0.97	324	417	$52.61^{+0.09}_{-0.34}$
GRB 151027A							
-1.02	1.5	$-0.94^{+0.14}_{-0.16}$	$219.88^{+61.37}_{-99.19}$	0.81	323	421	$51.50^{+0.14}_{-0.39}$
1.5	7.71	$-1.18^{+0.22}_{-0.25}$	$88.96^{+28.62}_{-59.61}$	0.8	402	421	$51.02^{+0.17}_{-0.43}$
106.27	110.58	$-1.28^{+0.06}_{-0.06}$	$1004.2^{+400.0}_{-727.86}$	0.77	354	421	$51.71^{+0.08}_{-0.34}$
110.58	114.96	$-1.27^{+0.09}_{-0.10}$	$316.45^{+106.7}_{-204.67}$	0.73	358	421	$51.41^{+0.10}_{-0.35}$

Table 4.2: Time-resolved spectral analysis for GRBs fitted with the Band model and constraining β for some of the time slices of certain GRBs. The spectra were fitted with the energy range for BAT (15-150 keV) and for GBM (10-1000 keV). The uncertainties adapted here are 90% confidence levels. T_s and T_e are the start and stop time intervals, respectively. z is the redshift, and offset is the calibration factor between instruments.

T_s [s]	T_e [s]	α	E_{peak} [keV]	β	offset	$Cstat$	dof
GRB 081121A z=2.51							
7.85	14.11	$-0.41^{+0.41}_{-0.85}$	$160.3^{+94.98}_{-175.85}$	$-1.96^{+0.30}_{-0.16}$	0.59	237.97	293
GRB 081221A z=2.26							
5.70	15.56	$-0.121^{+0.74}_{-0.52}$	$33.59^{+8.75}_{-13.67}$	$-2.65^{+0.25}_{-9.16}$	0.82	284.54	298
21.49	21.83	$-0.26^{+0.19}_{-0.23}$	$97.54^{+20.18}_{-22.22}$	$-2.72^{+0.62}_{-0.37}$	0.80	229.78	298
23.83	24.27	$-0.45^{+0.21}_{-0.24}$	$89.68^{+20.64}_{-26.76}$	$-2.52^{+0.64}_{-0.29}$	0.84	231.93	298
24.27	24.65	-0.49 ± 0.22	$94.35^{+21.40}_{-37.02}$	$-2.48^{+2.32}_{-0.27}$	0.86	208.90	298
27.68	28.21	$-0.25^{+0.55}_{-0.64}$	$42.28^{+15.54}_{-34.22}$	$-2.13^{+0.15}_{-0.10}$	0.87	175.18	298
28.21	28.77	$-0.28^{+0.60}_{-0.61}$	$45.11^{+16.03}_{-42.48}$	$-2.22^{+0.29}_{-0.12}$	0.80	213.29	298
28.77	29.37	$-0.47^{+0.35}_{-0.50}$	$49.94^{+16.99}_{-22.32}$	$-2.35^{+0.22}_{-0.16}$	0.80	179.86	298
29.37	30.07	$-0.49^{+0.51}_{-0.53}$	$47.83^{+17.22}_{-42.06}$	$-2.38^{+0.77}_{-0.17}$	0.84	183.08	298
30.07	30.88	$-0.58^{+0.40}_{-0.53}$	$47.44^{+17.69}_{-29.32}$	$-2.35^{+0.30}_{-0.16}$	0.81	210.58	298
30.88	32.02	$-0.67^{+0.30}_{-0.44}$	$45.88^{+15.28}_{-18.26}$	$-2.68^{+0.53}_{-0.26}$	0.83	224.33	298
32.02	34.29	$-0.68^{+0.25}_{-0.32}$	$44.77^{+11.03}_{-12.72}$	$-3.02^{+0.98}_{-0.36}$	0.78	287.85	298
34.29	54.27	$-0.36^{+0.59}_{-1.13}$	$31.05^{+14.51}_{-17.96}$	$-2.76^{+0.44}_{-0.28}$	0.91	289.99	298
GRB 081222A z=2.77							
-2.18	1.88	$-0.74^{+0.20}_{-0.26}$	$165.8^{+65.07}_{-135.80}$	$-1.86^{+0.29}_{-0.14}$	0.80	377.29	417
5.47	6.98	$-0.71^{+0.16}_{0.19}$	$103.8^{+24.59}_{-31.27}$	$-2.52^{+0.82}_{-0.33}$	0.78	333.63	417
GRB 090424A z=0.54							
0.47	0.61	$-0.66^{+0.22}_{-0.35}$	$87.12^{+30.97}_{-33.81}$	$-2.60^{+0.61}_{-0.29}$	0.77	278.22	416
0.79	0.88	$-0.71^{+0.24}_{-0.22}$	$103.3^{+26.71}_{-57.44}$	$-2.38^{+0.50}_{-0.18}$	0.72	279.12	416
1.84	2.08	-0.81 ± 0.29	$89.70^{+30.59}_{-68.59}$	$-2.36^{+0.97}_{-0.21}$	0.80	249.68	416
3.21	3.71	$-0.38^{+0.57}_{-0.63}$	$46.91^{+18.67}_{-49.64}$	$-2.21^{+0.24}_{-0.12}$	0.85	233.85	416
4.93	5.29	$-0.04^{+0.40}_{-0.56}$	$52.95^{+17.08}_{-22.34}$	$-2.64^{+0.37}_{-0.22}$	0.85	264.27	416
5.29	8.88	$-0.06^{+0.63}_{-1.11}$	$33.71^{+15.96}_{-23.76}$	$-2.29^{+0.17}_{-0.13}$	0.87	329.93	416
GRB 100615A z=1.40							
-1.22	2.83	$-0.71^{+0.16}_{-0.20}$	$102.2^{+26.18}_{-29.66}$	$-2.42^{+0.72}_{-0.35}$	0.67	256.46	298
GRB 100728B z=2.10							
81.92	83.97	-0.59 ± 0.07	$444.1^{+81.82}_{-97.29}$	$-2.42^{+0.94}_{-0.31}$	0.83	374.38	418
123.91	128.00	$-0.64^{+0.09}_{-0.11}$	$244.05^{+48.70}_{-60.15}$	$-2.59^{+1.43}_{-0.38}$	0.82	414.95	418
GRB 120326A z=1.80							
2.06	5.31	$-0.13^{+0.53}_{-0.63}$	$35.16^{+11.67}_{-20.48}$	$-2.30^{+0.16}_{-0.11}$	0.70	243.45	297
GRB 120624B z=2.20							
-270.34	-245.76	$-0.93^{+0.05}_{-0.06}$	1286^{+342}_{-667}	$-1.66^{+0.12}_{-0.08}$	0.84	2989.39	418
-245.76	-229.38	$-1.00^{+0.05}_{-0.06}$	$542.1^{+139.2}_{-152.6}$	$-2.12^{+0.81}_{-0.28}$	0.83	2899.52	418
GRB 140213A z=1.21							

Table 4.2 cont'd

T_s[s]	T_e[s]	α	E_{peak} [keV]	β	offset	$Cstat$	dof
2.19	2.79	$-0.94^{+0.12}_{-0.15}$	$199.5^{+63.99}_{-96.82}$	$-2.18^{+0.51}_{-0.21}$	0.82	319.80	416
3.62	4.56	$-0.23^{+0.37}_{-0.37}$	$57.08^{+17.16}_{-27.96}$	$-2.23^{+0.19}_{-0.13}$	0.73	342.18	416
4.56	5.60	$-0.65^{+0.27}_{-0.27}$	$53.25^{+13.15}_{-18.37}$	$-2.90^{+3.38}_{-0.33}$	0.78	289.90	416
5.60	6.03	$-0.46^{+0.38}_{-0.48}$	$50.50^{+17.29}_{-26.85}$	$-2.63^{+0.66}_{-0.23}$	0.80	254.12	416
6.36	6.66	-0.88 ± 0.20	$76.30^{+36.16}_{-32.67}$	$-2.36^{+0.37}_{-0.26}$	0.78	263.61	416
7.05	7.45	$-0.57^{+0.23}_{-0.31}$	$66.71^{+18.98}_{-22.74}$	$-2.57^{+0.40}_{-0.23}$	0.75	235.05	416
7.45	7.99	$-0.65^{+0.31}_{-0.41}$	$55.37^{+18.98}_{-28}$	$-2.56^{+0.64}_{-0.24}$	0.74	249.27	416
7.99	8.83	$-0.43^{+0.34}_{-0.41}$	$42.80^{+11.95}_{-17.85}$	$-2.48^{+0.22}_{-0.15}$	0.78	273.16	416
8.83	9.95	$-0.75^{+0.36}_{-0.61}$	$37.75^{+16.45}_{-21.22}$	$-2.55^{+0.35}_{-0.20}$	0.78	239.43	416
			GRB 150301B z=1.52				
-2.56	3.59	$-0.52^{+0.34}_{-0.63}$	$102.61^{+54.35}_{-85.35}$	$-1.88^{+0.43}_{-0.20}$	0.89	262.75	298
			GRB 150403A z=2.06				
9.06	10.13	$-0.89^{+0.10}_{-0.12}$	$400.2^{+131.0}_{-195.20}$	$-2.19^{+0.96}_{-0.26}$	0.87	301.65	416
10.13	10.63	$-0.86^{+0.07}_{-0.08}$	$748.9^{+185.2}_{-254.3}$	$-2.35^{+0.66}_{-0.29}$	0.83	298.44	416
10.63	11.02	$-0.80^{+0.07}_{-0.08}$	$716.0^{+169.}_{-215.8}$	$-2.43^{+0.70}_{-0.31}$	0.82	286.35	416
11.02	11.35	$-0.81^{+0.06}_{-0.07}$	$949.1^{+216.4}_{-288.9}$	$-2.31^{+0.40}_{-0.23}$	0.86	310.85	416
11.35	11.66	$-0.81^{+0.07}_{-0.08}$	$814.8^{+198.1}_{-277.1}$	$-2.33^{+0.42}_{-0.24}$	0.88	268.38	416
11.66	12.01	$-0.75^{+0.08}_{-0.09}$	$521.3^{+118.4}_{-149.3}$	$-2.36^{+0.51}_{-0.26}$	0.88	287.11	416
12.01	12.35	$-0.64^{+0.09}_{-0.11}$	$381.9^{+92.42}_{-108.1}$	$-2.17^{+0.31}_{-0.19}$	0.86	262.21	416
12.35	12.68	$-0.60^{+0.10}_{-0.12}$	$382.7^{+95.72}_{-107.7}$	$-2.32^{+0.75}_{-0.26}$	0.91	272.06	416
12.68	13.11	-0.90 ± 0.10	$396.81^{+115.4}_{-182.5}$	$-2.28^{+1.30}_{-0.26}$	0.87	262.84	416
13.60	14.31	$-0.80^{+0.15}_{-0.17}$	$200.7^{+65.52}_{-117.1}$	$-2.02^{+0.30}_{-0.15}$	0.83	338.48	416
14.31	15.15	$-0.85^{+0.16}_{-0.16}$	$209.4^{+65.19}_{-140.8}$	$-2.01^{+0.42}_{-0.14}$	0.84	310.79	416
15.15	16.55	$-0.57^{+0.43}_{-0.42}$	$108.5^{+46.63}_{-207.6}$	$-1.76^{+0.21}_{-0.07}$	0.86	324.50	416
19.77	41.60	$-0.25^{+0.53}_{-1.06}$	$62.43^{+36.23}_{-71.64}$	$-1.73^{+0.10}_{-0.08}$	0.99	436.79	416

Chapter 5

Detection of The High-Energy Cut-offs of Bright *Fermi*(GBM and LAT/LLE) GRBs

5.1 Introduction

It has been determined that GRB prompt emission is powered by ultra-relativistic jets (see Chapter 1). Commonly, the minimum estimation of Γ can be gained if high energy photons can be observed, e.g., that is if ≥ 1 MeV photons can escape without suffering from the $\gamma\gamma$ absorption "pair production" effect (e.g., Krolik & Pier 1991; Fenimore et al. 1993b; Woods & Loeb 1995; Baring & Harding 1997, see also Chapter 1). Thus, if the high-energy spectral cut-off can be detected due to such absorption, the specific value of Γ can be obtained (Mészáros & Rees, 1994). A spectral cut-off that is caused by the absorption in the high energy tail can be expected to be seen within the fireball shock model, although this is only possible in practice if the detector is sensitive enough to detect such a cut-off and covers a wide energy that includes ≥ 1 MeV (more details in section 5.4).

A decade before the launch of *Fermi*, high-energy gamma ray emission was detected from GRBs using EGRET on board the Compton Gamma Ray Observatory (CGRO; 1991 – 2000), which covered an energy range from 30 MeV-30 GeV (Hughes et al. 1980; Kanbach et al. 1988; Thompson et al. 1993; Esposito et al. 1999). Another observatory that recently performed such a role was the Gamma Ray Imaging Detector (GRID) on board the Astro-rivelatore Gamma a Immagini Leggero spacecraft, which detects high-energy GRBs in the 50 MeV - 10 GeV range (AGILE; Giuliani et al. 2008; Tavani et al. 2008; Tavani et al. 2009).

Since the launch of *Fermi* (LAT), the Large Area Telescope (Atwood et al., 2009b), in June 2008 (see Chapter 2), numerous GRBs have been detected at high energies (≥ 30 MeV), despite its event reconstruction and classification being restricted to the high-energy domain ≥ 30 MeV. Together, GBM and LAT cover more than seven decades in energy, where the LAT-detectable energies range from 30 MeV to more than 300 GeV. The LAT Low Energy (LLE) covers an energy band from 30 MeV - 130 MeV, and has detected significant numbers of GBM GRBs to date. The use of the LLE technique improves the photon statistics > 130 MeV, and thus allows us to define GRB prompt emission spectral phenomena in an improved manner; in particular,

the GBM and LLE data have been jointly fitted to provide an understanding of the spectral properties beyond the high energy range > 30 MeV. In addition, the GBM and LLE joint-fit can provide further knowledge of the high-energy cut-off features of the high-energy bands in some GRBs. Thus, the very high energy at 30 MeV provided by the *Fermi* (LAT/LLE) technique has the potential for the detection of the high-energy spectral cut-off E_c in some GRBs above the GBM energy range, and hence an estimate of the bulk Lorentz factor Γ becomes more possible. There are three scenarios that can be used to estimate the bulk Lorentz factor, Γ: first, from the onset, peaks were observed in the afterglow light curve. Due to the interaction with the external medium in the fireball and after the optically thick acceleration phase, the ejecta decreases with a constant Γ_0. Within this dynamical process, the Γ_0 represents the ultimate value gained by the outflow, resulting in a direct Γ_0 estimation with the onset afterglow emission. This only became possible in the last decade, and the first estimate of Γ_0 was from the detection of an onset afterglow peak t_p 150 - 200 s of GRB 060418 and GRB 060607 (Molinari et al., 2007). More details about this scenario have been discussed in Ghirlanda et al. (2018).

Second, the thermal component scenario is believed to be the result of a matter-dominated fireball, which is possibly dominated by a small fraction of Poynting flux in the central engine (Gao & Zhang, 2015). Due to the GRB beaming effect and within $\theta \leq 1/\Gamma$ (where θ is the angle of the line-of-sight starting), the observed flux is emitted for an expanding black body sphere with a Lorentz factor Γ ($\Gamma \geq 1$), see Zou et al. (2015). By measuring the thermal component and the object redshift, Γ becomes a measurable quantity. There are some GRBs that are reported to include a thermal component in the prompt emission phase, e.g., GRB 060218 (Campana et al., 2006), GRB 090618 (Page et al., 2011), GRB 090902B (Pe'Er et al., 2012), GRB 100316D (Starling et al., 2011), GRB 100724B (Guiriec et al., 2011), GRB 120323A (Guiriec et al., 2013), and (Burgess et al., 2014). For a given $\Gamma \sim 100$, the observed temperature must be relatively low < 10 keV. If not, the thermal radiation will be massively high and cannot be avoided by the observation. This low temperature observed explains why there are few GRBs that have been determined to have a thermal component (Zou et al., 2015). In the thermal component scenario, this can used to estimate the Lorentz factor Γ which can be detected in some GRBs (e.g., Pe'er et al. 2007; Peng et al. 2014; Zou et al. 2015).

Third, the high energy spectral cut-off of the prompt GRB spectrum is because of deceleration of the fireball in the medium (e.g., Baring & Harding 1997; Lithwick & Sari 2001; Gupta & Zhang 2008), where this scenario was applied in this study to estimate the Lorentz factor Γ obtained from the joint GBM+LLE high-energy spectra. In practice, the Lorentz factor, Γ, is more likely to be estimated through the high-energy spectral cut-off absorption because it is less model-dependent.

Tang et al. (2015) (hereafter referred to as T15), have provided a joint-fit spectral analysis of a sample of 16 GRBs (short, long, with/without redshifts) via *Fermi* (LAT, LLE, and GBM) which have been fitted to three models; Band, BandPL (Band model multiplied with a power-law

component) and BandCut (Band model with high-energy spectral cut-off). They found that eight out of these 16 bursts have high-energy cut-off features. The correlation between the Lorentz factor Γ and E_{iso} / L_{iso} was also studied, from which the authors found a correlation between Γ-E_{iso} and Γ-L_{iso}; whilst they suggested enlarging the sample for a better understanding of these correlations, our study, however, did not discuss those relations. Following the spectral analysis provided by Tang et al. (2015), a joint-fit (GBM+LLE) spectral analysis was provided in this chapter but with a larger sample of 36 GRBs detected simultaneously via GBM and LLE for long and bright bursts only. Attempts have been made to constrain the high-energy cut-off achievable by observations using the BandCut model for those forms of GRB that are best fitted with this model. It was suggested that shape of the GRB spectrum in the high-energy spectral cut-off region was relevant to the cut-off region of the primary particles within the prompt emission (Romoli et al., 2017).

This chapter is organized as follows: in § 5.2, an overview of *Fermi* (LLE) is given. In § 5.3, the data analysis and associated procedure are reported. In § 5.4, the bulk Lorentz factor Γ is explained. In § 5.5, the overall results are discussed, and some concluding remarks are given in § 5.6.

5.2 Overview of *Fermi* (LAT/LLE)

The *Fermi* (LAT) is a pair-production telescope, which measures the track of electrons and positrons that are created when a gamma ray of an energy > 1 MeV is annihilated via the interaction with an electron in the form of pair production. In the LAT instrument calorimeter, the subsequent electromagnetic e^+ e^- is measured. The calorimeter is located under the trackers in order to acquire the energy produced via the incident gamma ray photon.

The non-standard (extended) LAT analysis is permitted to cover the energy range of the prompt emission from $\sim$ 30 MeV - 130 MeV. A new method was presented with this aim by Pelassa et al. (2010) which suggests combining the energies determined by each instrument and generating the so-called LAT Low-Energy (LLE). LLE appears to be a very promising means by which to improve the quality of the photon statistics covering energies above $\geq$ 30 MeV, and give a better understanding of the spectral properties associated with prompt emission.

There are some features of the LLE technique that are worth noting: 1) The LLE event class data requires a tracker signal, while a LAT event class requires a tracker and a calorimeter signal (Pelassa et al., 2010); 2) the LLE event contains all events that pass the gamma ray filter, which includes a reconstructed direction (Ackermann et al., 2012); 3) the LLE class is less restricted than other classes (Transient and Diffuse), and is characterized as having a larger effective area at lower energies below 130 MeV and larger off-axis angles above 60 degrees compared to a standard LAT; 4) an LLE event class has a wide Point Spread Function (PSF) at different energy ranges, e.g., with a 68% containment radius of 20° at 30 MeV, 13° at 50 MeV and 15° at 5100

MeV; 5) an LLE event class background is more complicated than the LAT background, which requires a background rate > 1 Hz in its entire FOV in order to provide a sufficiently high signal-to-background ratio (Ackermann et al., 2013), hereafter referred to as A13); and 6) the LLE event class has a sensitivity that can extend to large off-axis angles, $\theta \sim 90^{\circ}$. Three features of the LLE technique, namely soft spectra, high off-axis, and a significant large effective (below 130 MeV) area, are allowing scientists to analyse and examine GRBs in considerable detail through features that are not otherwise provided by other LAT classes (e.g., Transit class and Diffuse class). Particularly, and due to the decreased GRB energy flux, the LLE event class is a useful tool by which to study GRB temporal structure. For more information about the GBM instrument, see chapter 2.

5.3 Data Analysis and Procedure

5.3.1 Sample Selection and Data Reduction

Since the launch of *Fermi*, $\sim$ 350 GRBs are being detected per year with the GBM. *Fermi* can slew directly to a source if it is bright enough to process the burst location and hence can provide observations for individual bursts, enabling a search for bright GRBs that are detected via LLE and GBM in order to study their spectra and find their high energy cut-offs. The sample criteria for joint-fit spectral analysis are as follows: GRBs that were detected coincidentally via GBM and LLE from August 2008 to May 2017 are included, and only long GRBs $>$ 2 s, and bright GRBs with high-energy fluence $\geq 10^{-5}$ erg cm^{-2}, are chosen. Among the complete GBM+LLE catalogue, comprising 100 bursts that were triggered simultaneously, only 36 GRBs were chosen for joint analysis in this chapter, as per the sample criteria. The LLE and GBM data were downloaded from the GTburst software [1]. The joint-fit GBM+LLE spectral fitting was performed using Time-Tagged Event (TTE) data and by choosing GBM response matrix files (*rsp2*) that contained multiple files for each slew. The GBM and LLE data were extracted using the same method adapted from the GBM catalogue (Goldstein et al. 2012; Gruber et al. 2014; von Kienlin et al. 2014), as mentioned earlier in chapters 3 & 4.

5.3.2 Spectral Models

In this joint-fit analysis, two spectral models are used: simple Band, and BandCut. With regards to the aim of this study - the examination of the high-energy spectral cut-off features - the BandCut model (Band model with high-energy spectral cut-off) is required, whilst still applying the simple Band model for the remaining GRBs in the sample that do not require the BandCut model.

[1] https://fermi.gsfc.nasa.gov/ssc/data/analysis/scitools/gtburst.html

•BandCut Model

Spectral models such as the PL, CPL and Band models are usually used to describe GRB spectra. The BandCut model, however, is used to study the change of spectral slopes, where the model is a modified form of the simple Band model with an additional high-energy exponential cut-off component with two-break energy spectrum, as introduced in Zheng et al. (2012). The E_{peak} obtained from this model is located around the high-energy exponential cut-off. In some GRBs in the sample, the BandCut is not well defined at the high-energy cut-off but we instead find an energy peak E_{peak} with a break energy E_b which is located somewhere between the smooth connection of the two power laws' low-energy indices (Oganesyan et al., 2018). The BandCut model can simply be expressed as:

$$N_{BandCut}(E) = \begin{cases} E^{\alpha}\, e^{-\frac{E}{E_0}} & ,if \;\; E \leq E_b \\ \left(\frac{E_0\, E_c}{E_c - E_0}(\alpha - \beta)\right)^{\alpha-\beta}\, e^{\alpha-\beta}\, E^{\beta}\, e^{-\frac{E}{E_c}} & ,if \;\; E > E_b \end{cases} \tag{5.1}$$

Where,

$$E_b = \frac{E_0\, E_c}{E_c - E_0}(\alpha - \beta) \tag{5.2}$$

where E_0 is the characteristic Band energy and E_c characterizes the position of the cut-off energy. α_1 and β are the low-energy indices, above and below the break, respectively. The signs of α β are based on the spectral model convention, where in our case the spectral indices have a negative sign.

Statistically, the use of the GBM+LLE joint-fit analysis using the $Cstat$ statistic to compare between different models is necessary in order to account for the few photons detected in the GBM-LLE detectors' high-energy bands. Three spectral analysis criteria, as adapted from Tang et al. (2015), are: i) calculate the $Cstat$ differences ($\Delta Cstat$) between the two models, as the lower the $Cstat$ values, the better the fit (dof). Ackermann et al. (2011) claimed that significant changes were produced when a value of > 28 is obtained from $\Delta Cstat$; ii) have well-defined model parameter uncertainties; and iii) be able to verify the reliability of the residual structure.

5.3.3 Spectral Analysis

The same spectral analysis procedure discussed in chapters 3 & 4 is applied here. The T_{100} was chosen so as to integrate over the entire burst fluence; the T_{100} was taken from the *Fermi* GBM burst catalogue as deciding to cover the entire time interval, not only the 90%, to account for the total fluence [2]. For each detector, certain energy channels were excluded such as the GBM/NaI detector channels between 30 - 40 keV (the Iodine K-edge, see Meegan et al. (2009)), as were the GBM energy channels below 10 keV and above 1 MeV, and the LLE energy channels below 30 MeV and above 130 MeV. The desired time intervals were chosen. Then the GBM light

[2] https://heasarc.gsfc.nasa.gov/W3Browse/fermi/fermigbrst.html

curve backgrounds were subtracted and fitted with a polynomial of appropriate order (from 1-4) in an automated manner in GTburst. Indeed, the LLE background is dominated by the cosmic radiation CR component, where the background of the CR component depends on the satellite geomagnetic coordinates and the GRB direction in the detectors' coordinates (Ackermann et al., 2013). The LLE background was simultaneously estimated with the LLE data collected with each observation. The GBM and LLE background counts were statistically fit with a Gaussian curve, while their spectral counts were fitted with Poisson statistics.

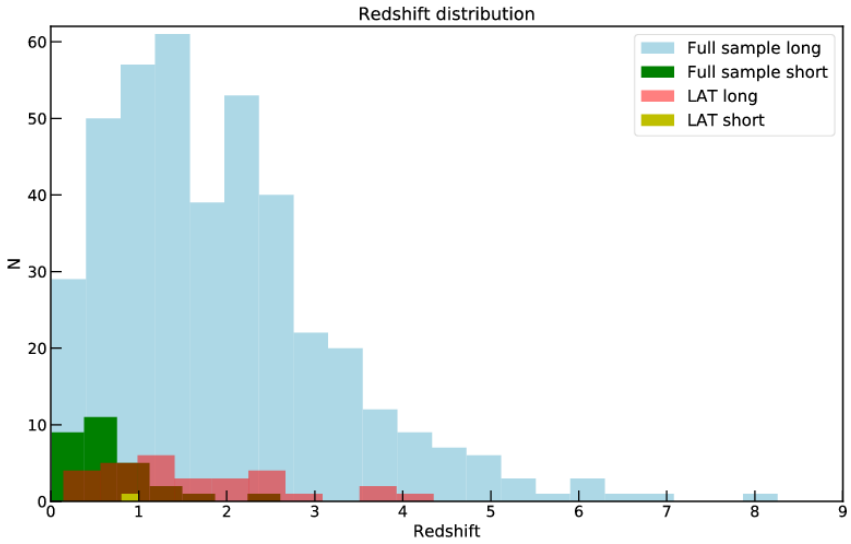

Figure 5.1: The redshift distribution of a GRB sample (LGRBs/SGRBs) detected via *Fermi* (LAT) up to December 2017. The pink histogram is the LAT LGRBs and the yellow histogram is the LAT SGRBs compared to the full sample (long/short), adapted from Nava (2018).

For each GRB, all spectra and response matrices obtained from the different detectors were loaded into XSPEC. The standard statistical procedure in this analysis is $Cstat$. Table 5.1 reports the GRB (LAT) sample properties, such as the off-axis angles θ, the declination (Dec), and the right ascension (RA) at the trigger times, and the detectors used in this analysis. Figure 5.1 illustrates the redshift distribution of LAT LGRBs and SGRBs up to December 2017, compared to the full sample. Table 5.2 reports the redshifts (for GRBs with no measured redshift, it was assumed that z = 1 [3] as suggested by Tang et al. (2015).

[3]Choosing z = 1 is just to calculate the cut-off and there is no real value of redshift that could be considered for those GRBs that do not have measured redshifts.

Table 5.1: *Fermi* (GBM and LLE) GRB properties observed in the period between September 2008 and April 2017.

GRB name	θ	Dec	RA	Detector	Ref [a]
080825C	10	-4.6	232.2	n9,na,b1, LLE	1
080916C	52	-61.3	121.8.88	n3,n4,b0, LLE	2
081224A	16	213.37	74.23	n0,n8,b1, LLE	3
090902B	51	27.33	264.0	n0,n1,n0, LLE	4
090217A	24	-8.4	204.9	n6,n9,b1,LLE	5
090227A	21	-43.1	3.2	n1,n2,b0,LLE	6
090323A	5	17.08	190.69	n9,nb,b1,LLE	7
090328A	57	41.95	90.87	n7,n8,b1,LLE	8
090926A	48.1	-66.34	353.56	n6,n7,b1,LLE	9
091031A	22	-57.5	71.7	n0,n9,b1 LLE	10
100116A	27	14.45	305.02	n3,n4,b0,LLE	11
100225A	24	-59.4	310.3	n0,n3,b0,LLE	12
100724B	44	76.55	119.89	n0,n1,b0.LLE	13
110328B	12	43.2	117.6	n0,n9,b1,LLE	14
110721A	0	-39.0	333.4	n6,n9,b1,LLE	15
120328B	6.7	25.29	229.03	n7,nb,b1,LLE	16
121225B	92	-34	308.91	n3,n5,b0,LLE	17
130305A	1	52	116.76	n6,n9,b1,LLE	18
130504C	51	3.846	91.71	n0,n1,b0,LLE	19
130518A	43	47.64	355.81	n3,n6,b0,LLE	20
130821A	37	-12	314.1	n6,n9,b1,LLE	21
131014A	71.9	-19.1	100.5	n9,n1,b1,LLE	22
131108A	54	9.90	156.47	n3,n6,b0,;LLE	23
131231A	40	-1.85	10.59	n3,n6,b0,LLE	24
140102A	47	1.36	211.9	n7,n9,b1,LLE	25
140206B	45	-8.51	315.26	n0,n1,b0,LLE	26
150403A	55	-62.76	311.79	n3,n4,b0,LLE	27
150510A	55	4.79	16.16	n1,n5,b0,LLE	28
150523A	26	-45.40	115.35	n0,n1,b0,LLE	29
150902A	38	-69.36	214.93	n0,n3,b0,LLE	30
160509A	32	76.1	311.3	n0,n3,b0,LLE	31
160816A	35	37.16	322.45	n6,n7,b1,LLE	32
160821A	17	42.3	171.3	n6,n7,b1,LLE	33
160905A	18	-50.88	162.02	n0,n9,b1,LLE	34
160910A	71	38.76	221.26	n1,n5,b0,LLE	35
170405A	53	-25.23	219.37	n6,n7,b1,LLE	36

[a] **Ref**: The first announcement of the GRB; 1. (Bouvier et al., 2008). 2. (Tajima et al., 2008). 3. (Wilson et al., 2008). 4. (de Palma et al., 2009). 5. (Ohno & Fermi LAT/GBM Collaboration, 2010). 6. (Bissaldi et al., 2009). 7. (Ohno et al., 2009). 8. (Cutini et al., 2009). 9. (Bissaldi et al., 2009). 10. (de Palma et al., 2009). 11. (McEnery et al., 2010). 12. (Piron et al., 2010). 13. (Tanaka et al., 2010). 14. (Vasileiou et al., 2011). 15. (Vasileiou et al., 2011). 16. (Vianello & Kocevski, 2012). 17. (Kocevski et al., 2012). 18. (Guiriec et al., 2013). 19. (Kocevski et al., 2013). 20. (Omodei & McEnery, 2013). 21. (Kocevski et al., 2013). 22. (Desiante et al., 2013). 23. (Vianello et al., 2013). 24. Sonbas et al. 2013; Jenke & Xiong 2014 . 25. Sonbas et al. 2014; Zhang & Bhat 2014. 26. Bissaldi et al. 2014; von Kienlin & Bhat 2014. 27. (Longo et al., 2015). 28. (Racusin et al., 2015). 29. (Bissaldi et al., 2015). 30. (Arimoto et al., 2015). 31. (Longo et al., 2016). 32. (Racusin & Kocevski, 2016a). 33. (Arimoto et al., 2016). 34. (McEnery et al., 2016). 35. (Racusin & Kocevski, 2016b) 36. (Vianello & Kocevski, 2017).

Table 5.2: The measured GRB redshifts; the remainder of the sample with no redshifts are assumed to have z = 1.

GRB name	z	Ref [a]
090902B	1.822	1
090323A	3.57	2
090328A	0.73	3
090926A	2.1062	4
130518A	2.488	5
131108A	2.4	6
131231A	0.642	7
150403A	2.06	8
170214A	2.53	9

[a] **Ref**: 1.(Cucchiara et al., 2009) (GCN 9873) 2. (Chornock et al., 2009) (GCN 9028) 3. (Cenko et al., 2009) (GCN 9053) 4. (Malesani et al., 2009) GCN 9942) 5. (Sanchez-Ramirez et al., 2013) (GCN 14685) 6. (de Ugarte Postigo et al., 2013) (GCN 15470) and (Xu et al., 2013) (GCN 15471) 7. (Sonbas et al., 2013) (GCN 15640) 8. (Pugliese et al., 2015) (GCN 17672) 9. (Kruehler et al., 2017) (GCN 20686)

5.4 The Bulk Lorentz Factor, Γ, Estimation

The spectral energy cut-off E_c can be interpreted when $\gamma\gamma$ absorption (only for photon energies that are larger than the highest photon energy in the LAT detections) takes place within the source; due to this, an estimation of the bulk Lorentz factor, Γ, of the emitting region is made possible by satisfying the condition $\tau_{\gamma\gamma}(E_c) = 1$, where τ is the optical depth. To compute the bulk Lorentz factor Γ, one assumes that all bursts are produced by synchrotron radiation and only consider the photons produced in a single region (e.g., the one-zone model where the photons are isotropic, uniform and time-independent in the comoving frame) (see; Abdo et al. 2009b). Yu et al. (2015) discussed the idea that the majority of time-resolved *Fermi* for eight energetic GRBs were consistent with a synchrotron model with good statistics.

The target photons must have an energy greater than $E_t = \Gamma^2(m_e c^2)^2/[E_c(1+z)^2]$, which removes the energy cut-off, E_c, photons. The derivation of the bulk Lorentz factor Γ has been given in Tang et al. (2015) and Zhao et al. (2011), and can be defined as:

$$\Gamma \sim \frac{E_c}{m_e c^2}(1+z) \tag{5.3}$$

where E_c is the high-energy spectral cut-off, z is the spectroscopic redshift and $m_e c^2$ is the rest mass of the electron (constant factor = 511 keV). Equation 5.3 is only applied for GRBs that have small E_c values. If the high-energy spectral cut-off E_c is large (> 130 MeV), which may caused by large Γ, for example $\Gamma > 10^3$, and this equation is not sufficient to model the observations; however, the estimated values of Γ for most GRBs are still not defined, with only lower limits to Γ generally being known.

It is known that the GRB Lorentz factor, Γ, is constrained by the attenuation of the spectral high-energy observations. Zhao et al. (2011), using the one-zone model (where all photons are produced from a single region) to measure $\gamma\gamma$ optical depth via applying a target photon

spectrum with a high-energy cut-off, found this model to be more appropriate for $\Gamma < 100$. Recently, it has been suggested by *Fermi* (LAT) with regards to GeV emission that there is a possibility that the high-energy emission $\geq$ MeV might offer some evidence as to how the emission occurs from different origins, and hence using the two-zone model where the high energy has a large radius, as compared to the MeV-range emission, can result in a very high $\Gamma \geq 1000$ being measured. They concluded that the high energy may be attenuated by the MeV-range emission and thus showed a steepening spectrum instead of an exponential spectral cut-off, which indicated that there was no sharp cut-off as a result of the attenuation by the $\gamma\gamma$, assuming the one-zone model.

5.5 Results

The GRB samples were fit with the simple Band model or the BandCut model deciding on the best-fit model by comparing the $\Delta Cstat$, as reported in Table 5.3 in order to choose which spectral model was most appropriate. Whilst others (not included in the table) showed very small $\Delta Cstat$ improvements whether using Band or BandCut. The purpose of using the BandCut model was to detect possible high-energy spectral cut-off features in the $\geq$ MeV energy range.

An attempt to constrain the high-energy spectral cut-off for all the GRBs in this sample ultimately found that seven out of 38 GRBs showed such features, but only three out of seven GRBs showed a high-energy cut-off The other four GRBs are examples where a low break energy E_b was found with a peak energy E_{peak} instead of a high-energy cut-off E_c.

5.5.1 GRBs fitted by BandCut Model

There are three GRBs that were fitted with the BandCut model that showed high-energy spectral cut-off features. The remainder of the sample (four GRBs) showed instances when the GRB spectral fit attempted to find the high-energy cut-off, but instead found a break that represented the peak energy obtained from the simple Band model. The two cases of using the BandCut model are explained below:

i) GRB with a constraining high-energy spectral cut-off, E_c

Table 5.4 reports the possible three GRBs joint spectral analysis that showed high-energy spectral cut-off E_c features and which are graphically represented in Figure 5.3. No obvious direct evidence for a high-energy spectral cut-off at energies $E_c < 1$ GeV was apparent until the detection of GRB 100724B (Ackermann et al., 2013), thus GRB 100724B was the first clear high-energy cut-off below the GeV energy threshold, where other GRBs detected via Fermi/LAT had similar $E_c \sim$ GeV to those found by Tang et al. (2015). As can be seen in certain GRBs, the prompt GRB spectrum is consistent with a Comptonized spectrum (power law with exponential

Table 5.3: The $\Delta Cstat$ between Band and BandCut models pure for GRBs that showed large $\Delta Cstat > 28$.

GRB name	Band-$Cstat$	BandCut-$Cstat$	$\Delta Cstat$
100724B	583.59	523.65	59.94
120328A	692.28	660.23	32.05
130821A	3444.36	3397.26	47.1
131014A	404.24	357.67	46.57
140206A	2739.76	2709.26	30.5
150403A	432.65	398.11	34.54
160509A	19952.25	19758.69	193.56
160821A	1855.68	1620.16	235.52

cut-off) though with very high typical $E_{peak} < 1$ MeV, and that cannot be considered a high-energy cut-off E_c as found in case (ii), which was believed to have most likely had a different physical origin.

From equation 5.1, the estimated Lorentz factors Γ were calculated, the values for which were 142.81 [+187.88,-115.51], 129.50 [+150.99,-111.97] and 279.52 [+894.03,-161.13], respectively. Generally, the values of Γ, which range from $\sim$ 100 to 300, present strong evidence that the GRB is powered by an ultra-relativistic outflow. GRB 100728B, GRB 160821A, and GRB 160910A are good examples of high-energy cut-offs E_c that are the result of the pair production when the νF_ν spectrum is rising-decaying and is then cut off with a proper estimation of Γ.

In Figure 5.3, the upper panels illustrate the light curves from the three detectors (GBM/NaI, GBM/BGO, and LLE). Using red for the GBM/NaI, green for the GBM/ BGO and blue for the LLE, where the vertical dashed lines are the time-integrated intervals (T_{100}), the bottom panels show the three GRBs that showed high-energy spectral cut-offs, where the red and black spectra are the GBM/NaI, the green is the GBM/BGO, and the blue spectrum is the LLE. These spectra show the cut-off feature in the high-energy LLE bands, where the fitting residual is shown in the lower bottom of the fitting spectra panel.

In general, the detection of the high-energy cut-off requires the large photon statistics that can only be found in bright sources, which themselves are not found in large numbers in the *Fermi* bursts (Romoli et al., 2017). The implication of this analysis can be summarised as follows: the high-energy spectral cut-off features found in only three GRBs ranged from only a few tens of to $\sim$ 80 MeV. It was found in this analysis that the cut-offs were obtained from the BandCut model at $\sim$ tens of MeV, and there is no evidence of cut-offs beyond 130 MeV. This is possibly due to the limited number of photons with energies above 130 MeV. Statistically, it is difficult to distinguish between Band and BandCut, such as in cases when the break is somehow located beyond 130 MeV. However, it is convenient to predict the cut-offs if there are additional hard components that help to include larger high-energy photon counts in some GRBs (see: Tang et al. 2015; Li & Li 2012).

ii) GRB spectra which show an energy peak E_{peak} instead of E_c

The second scenario is that of fitting spectra with the BandCut model which show no cut-off energies < 12 MeV. As mentioned above, the model cannot exceed the high energy beyond 130 MeV due to insufficient high-energy photon counts, therefore the BandCut model showed an energy peak E_{peak} (obtained from the simple Band model) instead of a cut-off. This case shows one curvature and a steeper break, which is in contrast with the spectra fitted with BandCut in the first case, which show two curvatures and a cut-off. The GRB νF_ν spectra show rises that then decayed, but with no cut-offs being found. For instance, GRB 110828B GRB 130504C, GRB 140206 and GRB 160509A showed "breaks". The fact that some GRBs do not show cut-offs is due to the spectrum having one curvature instead of two, similar to that seen in the simple Band model, and thus a lower-value Γ was estimated. It has been suggested that if there is no spectral cut-off detected, the assumption that the absorption optical depth $\tau_{\gamma\gamma} < 1$ for the highest energy photons is applied, where a lower-value Γ can be determined instead of the observed maximum energy photon (Krolik & Pier 1991; Fenimore et al. 1993b; Woods & Loeb 1995; Baring & Harding 1997; Hascoët et al. 2012).

Table 5.5 reports the four GRBs that show energy peaks E_{peak} instead of high-energy cut-offs E_c. In this case, the high energy is defined but it is actually the energy peak $_{peak}$ from the simple Band model which shows a break somewhere in the low-energy band. For example, if Band is applied instead of BandCut with no high-energy cut-off E_c, the high-energy index β will have a positive value and will continue to an infinite value, and the spectrum will look rather extended with no cut-off or curvature. The reason for not obtaining a high-energy cut-off E_c for those GRBs may due to the low-energy counts of the high energy being insufficient, thus showing E_{peak} in terms of the high-energy cut-off E_c and β. The energy peak E_{peak} in this case was calculated from $E_{peak} = E_c(2 + \beta)$.

Figure 5.4 illustrates GRB 110328B, GRB 130504C, GRB 140206B, and GRB 160509A, which show the energy break and the energy peaks. These can be an indication of the insufficient detection of the spectral cut-offs E_c beyond 130 MeV. In contrast with Table 5.4, which reports the high-energy cut-offs with an energy peak E_{peak} and β obtained from the BandCut model. However, in the case when there is no high-energy cut-off there is no need to estimate Γ as this is not due to electron annihilation.

These GRBs are a good example of when the break is found in the instance when the spectrum shows two rising phases (rising-rising) rather than a cut-off, which is important finding proposed in (Oganesyan et al. 2017, Oganesyan et al. 2018 and Ravasio et al. 2018), who noted that marginally fast cooling with a spectral break can be the solution to the synchrotron line-of-death problem.

For clarity, the reason why some GRBs show high-energy cut-offs and others do not can be explained by looking at Table 5.6 which reports the energy flux for the GRBs fitted with BandCut. The GRBs listed in this table showed that for higher energy flux GRBs the high energy cut-off

Table 5.4: The spectral joint-fit analysis LAT+LLE+GBM obtained from A13, T15, which showed the high energy spectral cut-off E_c detection and estimations of the Lorentz factor Γ for some GRBs. All errors are in the 90% confidence band.

GRB	Model	T_s [s]	T_e [s]	α	β	E_{peak} [keV]	E_c [MeV]	Γ	$Cstat\ (dof)$
				A13					
080825C	Band	-	-	-065 ± 0.02	$-2.40^{+0.03}_{-0.04}$	141 ± 5	-	-	1002.(821)
100116A	Band	-	-	-1.02 ± 0.01	$-3.00^{+0.10}_{-0.13}$	1133^{+91}_{-82}	-	-	381.2(356)
100724B	BandCut	-	-	$-0.73^{+0.01}_{-0.00}$	-2.00 ± 0.01	263 ± 4	40 ± 3	-	734.7(468)
				T15					
100724B	BandCut	-	-	-0.71 ± 0.01	-2.08 ± 0.01	354.5 ± 1.5	42.4 ± 4.0	165.9 ± 15.6	1202.3(389)
131014A	Band	-	-	-0.21 ± 0.01	-2.62 ± 0.02	308.5 ± 2.7	-		990(487)
131108A	Band	-	-	-0.88 ± 0.03	-2.16 ± 0.01	308.5 ± 14.6	-	-	440.9(388)
140102A	Band	-	-	-0.75 ± 0.02	-2.58 ± 0.04	182.1 ± 4.3	-	-	808(632)
				This study					
100724B	BandCut	-62.46	244.74	$-0.81 \pm 0.0.3$	-1.97 ± 0.07	$346.58^{+33.13}_{-30.26}$	$31.89^{+10.06}_{-6.10}$	$124.81^{+39.86}_{-24.36}$	523.65(354)
160821A	BandCut	-2.05	220.16	-1.01 ± 0.01	$-2.25^{+0.05}_{-0.05}$	$881.10^{+41.15}_{-39.79}$	$33.09^{+5.49}_{-4.48}$	$129.51^{+21.99}_{-18.04}$	1620.1(354)
160910A	BandCut	-1.02	77.82	$-0.81^{+0.05}_{-0.04}$	$-2.18^{+0.13}_{-0.11}$	$315.59^{+37.63}_{-35.55}$	$71.42^{+157.01}_{-30.25}$	$279.53^{+615.61}_{-119.49}$	432.7(355)

Table 5.5: The GBM+LLE joint-fit spectral analysis of the four GRBs that showed peak energies E_{peak} instead of cut-offs E_c. T_s is the start time-interval, T_e is the end time-interval, α is the low-energy index, β is the high-energy index, E_{peak} is the peak energy in keV, and E_b is the break energy in keV.

GRB name	T_s [s]	T_e [s]	α	β	E_{peak} [keV]	E_b [keV]	$Cstat\ (dof)$
110328B	-4.096	91.138	$1.13^{+0.03}_{-0.20}$	$-1.51^{+0.06}_{-0.08}$	$5.46E+02^{+8.93E+02}_{-1.12E+03}$	$26.50^{+3.64}_{-22.08}$	492.6(356)
130504C	-4.096	118.78	$-0.94^{+0..06}_{-0.05}$	-1.76 ± 0.08	$1.95E+03^{+6.97E+03}_{-6.15E+02}$	$275.0^{+33.17}_{-17.34}$	562.48(339)
140206A	-1.024	276.48	$0.43^{+0.33}_{-0.16}$	-1.58 ± 0.01	$4.73E+03^{+3.77E+02}_{-3.71E+02}$	$20.23^{+0.39}_{-1.61}$	2709.2(358)
160509A	-15.36	393.22	$-0.86^{+0.05}_{-0.07}$	-1.40 ± 0.02	$4.72E+03^{+2.17E+02}_{-1.78E+02}$	$115.44^{+11.13}_{-14.04}$	1758.(356)

E_c can be detected, as seen for GRB 110724B, GRB 160821A and GRB 160910A, while GRBs that have lower energy fluxes may prevent the high-energy cut-offs E_c from being detected, and detect a high E_{peak} and show a break instead.

5.5.2 GRBs fitted by the simple Band model

The remaining GRBs (29) are well described by the simple Band model, as reported in Table 5.7. The spectral parameters of the sample fitted with the simple Band model are as follows: the low-energy indices, α, were in the range of -0.46 to -1.36, with an average value of -0.89 and a standard deviation of 0.06. The high-energy indices, β, ranged between -2.13 to -3.43 with an average value of -2.58 and a standard deviation of 0.29. The peak energy E_{peak} values were between 180.41-1662.40 keV, with an average of 442.95 keV, and a standard deviation of 350.84, see Figure 5.5 (Appendix A.3 reports all GRBs fitted with the simple Band and BandCut models). To compare, another joint-fit (LAT and GBM) analysis (without LLE data) reported in (Zhang et al., 2011) shows that the average Band spectral parameters were: α = -0.9, β = -2.6, and E_{peak} $\sim$ 781 keV, respectively, which are roughly consistent with this study except for the E_{peak} which shows higher values. The latter is likely due to the inclusion of LAT data (> 300 GeV) in Zhang's

Table 5.6: The averaged energy fluxes measured for some GRBs that showed high-energy cut-offs E_c, and other GRBs that did not.

GRB	Flux [erg cm^{-2} s^{-1}]	E_c [MeV]
100724B	1.63E-06	31.89
110328B	2.36E-07	-
130504C	1.05E-06	-
140206A	1.56E-06	-
160509A	5.51E-07	-
160821A	5.44E-06	33.09
160910A	1.95E-06	71.42

joint-fit analysis. Furthermore, this study also shows a consistency, though with a higher E_{peak}, with the findings of the BATSE GRB sample (Preece et al., 2000).

5.5.3 GBM+LAT+LLE Spectral Analysis in the Literature

Table 5.4 shows the comparison of our spectral analyses with previous studies, such as A13, and T15, for the GRBs that were best fitted with the BandCut model and the simple Band model. The spectral fitting results obtained from this study were found to be consistent with only some of the GRBs (seven GRBs in common) presented in these two studies.

One GRB in A13 and T15 are in common with this study, namely GRB 100724B, which has a value of E_c = 42.4 [$\pm$4.0] MeV obtained from A13 and E_c = 40 $\pm$3 with a Lorentz factor Γ = 165.9 [$\pm$15.6] obtained from T15, respectively, while in this analysis roughly consistent results were found, i.e., E_c = 31.89 [+10.06,-60.98] MeV, and the Lorentz factor, Γ, was estimated to be 142.81 [+187.88,-115.51].

With regards to the simple Band model, it was found there were two GRBs that were common to A13. For instance, GRB 080825C, as obtained by A13, showed α and E_{peak} values of -0.65 [$\pm$0.02] keV and 141 [$\pm$5] keV, respectively, while in this study α and E_{peak} were found as -0.68 [$\pm$0.08] and 180.03 [+26.45,-22.39] keV, respectively. GRB 100116A showed α and E_{peak} values of -1.02 [$\pm$0.01] and 1133 [+91,-82] keV, respectively, while in this study α and E_{peak} were found as -1.04 [+0.09,-0.07] and 931.80 [+476.21,-291.34] keV, respectively. These two GRBs spectral analyses, in both A13 and this study, were consistent within the associated parameter uncertainties. In this analysis, three GRBs in common with T15 were fitted with the simple Band model, namely GRB 131014A, GRB 131108A, and GRB 140102A; see Table 5.4. The spectral parameters were consistent within their uncertainties as compared to T15.

Moreover, in recent work by Vianello et al. (2018), hereafter referred to as V18, the high-energy cut-offs E_c of two bright GRBs were measured, namely GRB 100724B and GRB 160509A, as observed by *Fermi*/GBM and LLE but for the time-resolved spectra. The outcomes of this paper can be compared with those already reported in this chapter, for instance GRB 100724B showed a sharp high-energy cut-off E_c at energies between $\sim$ 20 - 60 MeV, while GRB 160509A had energies E_c between $\sim$ 80 - 150 MeV. This was achieved by applying two spectral models:

1) a Band spectrum with $\tau_{\gamma\gamma}$ from the internal shock (Granot et al., 2008)), and the phosphoric model described by Gill & Thompson (2014). These two models each provided a good fit to the data with appropriate parameters which hence allowed for the estimation of the Lorentz factors Γ in the range of 100 - 400 on the lower limit of *Fermi*.

V18 also showed a larger E_c value (80 - 150 MeV) for GRB 100724B compared to that found in this study; even though this GRB showed a time-resolved spectrum, a similar Γ range was found in each analysis of $\sim$ 100 - 400. Generally speaking, the Lorentz factors Γ and the relatively high energy cut-off E_c ($\geq$ 100 MeV) found in both V18 and this analysis are lower than those obtained from the *Fermi*/LAT GRBs because they were extremely bright at $\geq$ MeV.

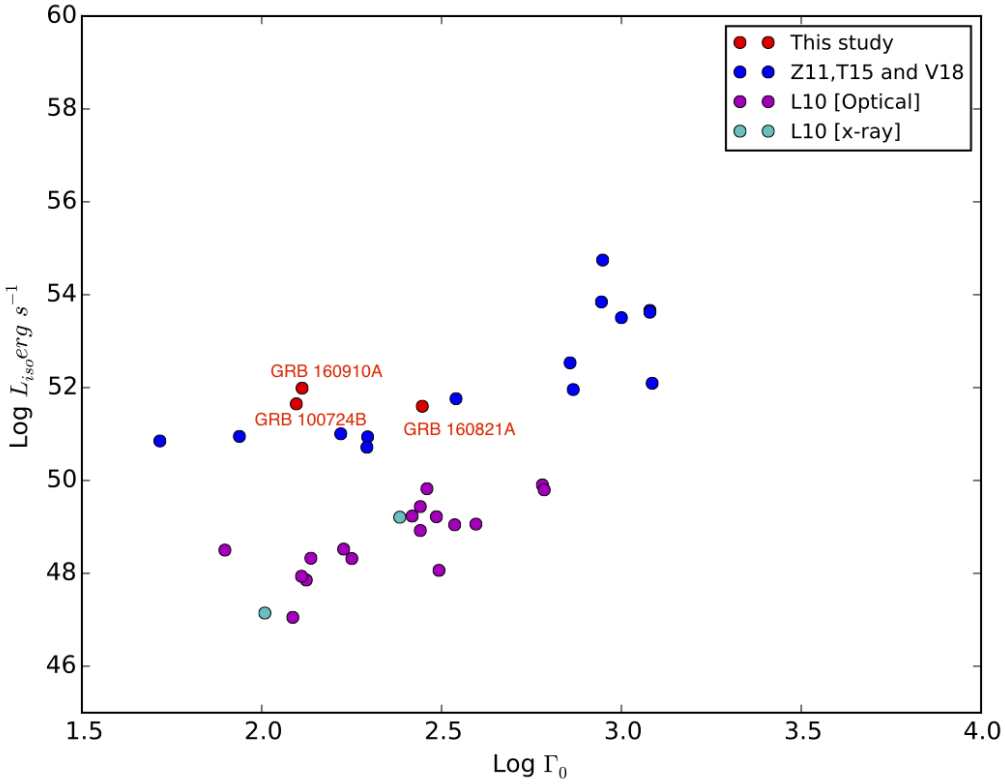

Figure 5.2: The distribution of Lorentz factor Γ_0 verses luminosity adapted from other studies (as shown on the plot), and the three GRBs from this study plotted in red.

Figure 5.2 shows the distribution of Γ_0 verses luminosity for a number of GRBs adapted from different studies (e.g., Liang et al. (2010), hereafter L10, optical and X-ray, Zou et al. (2011), hereafter Z11; Tang et al. (2015); Vianello et al. (2018), hereafter V18). This plot shows a trend in this study and other studies (Z11, T15 and V18 in blue), the afterglow onset (optical in purple and X-ray in crayon) also show a trend.

With regards to the afterglow onset method of estimating Γ_0 discussed in the literature, e.g., Liang et al. (2010), Γ_0 was estimated by applying the standard afterglow model in a constant density medium to obtain the initial Lorentz factor Γ_0 (Sari & Piran, 1999a).

$$\Gamma_0 = 2 \left[\frac{3E_{\gamma,iso}}{32\pi\, n\, m_p\, c^5\, \eta\, t_{p,z}^3} \right]^{1/8} \tag{5.4}$$

where $\eta = E_{\gamma,iso}/E_{K,iso}$ is the ratio between the isotropic energy and the isotropic blast wave kinetic energy, where, $n = 1$ cm^{-3}, η = 0.2 and $t_{p,z}$ is the fireball deceleration onset time. The typical result for Γ_0 is in the range of a few hundreds. Equation 5.4 shows that the Γ_0 was dependent on E_{iso} and $t_{p,z}$, which shows a tight correlation between tp,z and E_{iso}.

Other studies, e.g., Ghirlanda et al. (2012) have showed that the Γ_0 distribution extended to low Γ_0 values, and thus low Γ_0 GRBs must be found in the GRB population detected via sensitive detectors. These low Γ_0 GRBs have a late time afterglow onset, and therefore that the prompt emission was uncontaminated by the late time afterglow.

Furthermore, Ghirlanda et al. (2018) have reviewed and compared different methods to compute the bulk Lorentz factor Γ_0 from t_p (from onset afterglow), as proposed in different studies (e.g., Ghirlanda et al. 2012; Ghisellini et al. 2010; Molinari et al. 2007; Nappo et al. 2014; Nava et al. 2013; Sari & Piran 1999a).

These different methods deviated by a factor of two, thus the method used to compute Γ_0 must show a small fraction of systematic difference in the correlation constant normalization and values of an average Γ_0. In this review, they found average values of Γ_0 between 155 - 320 for the wind case and the homogeneous, respectively. In addition, regarding the correlation between Γ_0 and either E_{iso} (Amati et al., 2002) or L_{iso} (Yonetoku et al., 2004), they found the existence of correlations when comparing the two cases (wind case and homogeneous) in that the gradients ($E_{peak} - E_{iso}^{0.53}$, $E_{peak} - L_{iso}^{0.50}$ were consistent with these correlations of a sample of 151 GRBs, where consistent values of Γ_0 have been estimated in these different studies.

5.6 Conclusions

A joint-fit spectral analysis of GBM and LLE GRBs detected during the period between August 2008 to May 2017 was performed, and their spectral parameters were measured using the Band and BandCut models. The aim of this study was to constrain the high-energy spectral cut-off E_c, and to study the features of the high-energy prompt emission. Fitting the GRB spectra with the BandCut model allowed the high-energy spectral cut-off to be measured at the end of the high-energy LLE bands at up to 130 MeV. In total, there were only three GRBs that showed cut-off features that could be used to estimate their Lorentz factors Γ. The highest value of the cut-offs was found to be 71.42 MeV with a corresponding Γ of 279.52. In this analysis, the one-zone model for the MeV-GeV prompt emission region was assumed in order to compute the Lorentz factor Γ, which only can be estimated at a very high energy cut-off of $\sim$ 130 MeV in the LLE energy bands.

In particular, the low values of E_c might prevent *Fermi*/LAT detection, and this would result in biases in the Fermi/LAT GRB sample in comparison to GRBs observed with low Lorentz factors Γ, as well as short variability times compared to small emission radii. In fact, L_{iso} and Γ can be positively correlated, though this correlation is not necessarily strong for a single GRB time-resolved spectrum; this correlation has been introduced and discussed in the literature (e.g., Lu et al. (2012)).

Introducing and estimating Γ values from either prompt emission (the detection of high-energy cut-offs) or from the onset afterglow allows astronomers to derive the mass of the fireball for different bursts, as based on the assumption of a typical jet opening angle of 5°, which shows a consistency in the spatial distribution of the jet mass (10^8 and 10^4 $M_\odot$). Furthermore, computing the Γ_0 comoving frame properties allows us to understand their physics. The correlation between Γ and luminosity (erg s^{-1}) in Figure 5.2 can potentially show whether there is a trend, and the different estimated Γ_0 values are in the range of 300 - 1500 for different GRBs detected with different instruments, either from the prompt emission phase or from the onset of the afterglow.

The two values of Γ_0 estimated by Vianello et al. (2018) for the two brightest GRBs (100724B and 160509A) observed by *Fermi* at MeV energies have provided an estimation of Γ_0 as being in the range of 100 - 400. These values are low compared with other *Fermi*/ LAT GRBs, which is likely due to their high-energy cut-off E_c being low as their isotropic luminosity increases, which in fact requires a higher Γ_0. This could also be biased in the*Fermi*/LAT GRB sample against GRBs with low Γ_0 and short time variabilities, which tends to result in a low E_c that becomes more difficult to detect via *Fermi*/LAT. Thus, these two GRBs showed that there is important knowledge to be gained from the physics of the Γ_0 population.

Attempts were made to constrain the high-energy spectral cut-offs using the BandCut model for the remainder of the GRB sample, but no evidence of cut-offs was found. However, four GRBs showed E_{peak} showed break energies E_b instead of E_c, where the E_{peak} obtained from the BandCut was similar to the one obtained from the simple Band.

Moreover, to fit the remainder of the GRBs (29) that did not show a constrained high-energy spectral cut-off, the best fit was found via the simple Band model. Finally, comparisons were made with previous studies in the literature, i.e., T15 and A13, which showed consistent results for only one of the GRBs common to this study for the BandCut model. The simple Band model was consistent within the parameter uncertainties reported in studies A13 and T15, and in this study for five GRBs.

To summarize, two cases have been discussed: 1) fitting using the BandCut model, which results in two scenarios a) there are cases when E_c is constrained and Γ had to be estimated, and b) there are cases where the spectral breaks are found and it is important to study these break energies in order to understand certain other GRB properties; and 2) when fitting using the simple Band model, there are cases when the Band model fits spectra from 8 keV to 130 MeV, which indicates that Γ is large since E_c is above the LLE energy range.

Table 5.7: The GBM+LLE joint-fit spectral analysis of 29 GRBs that were best fitted with the simple Band model. T_s is the start time interval T_e is the end time interval, α is the low-energy index, β is the high-energy index, and E_{peak} is the peak energy in keV.

GRB name	T_s [s]	T_e [s]	α	β	$offset$	E_{peak} [keV]	$Cstat\ (dof)$
080825C	-1.02	31.74	-0.68 ± 0.08	$-2.40^{+0.06}_{-0.10}$	4.16E-02	$180.03^{+26.45}_{-22.39}$	271.26(354)
080916C	-4.10	87.04	$-1.01^{+0.04}_{-0.03}$	-2.20 ± 0.03	1.32E-02	$484.03^{+79.49}_{-66.50}$	361.98(356)
081224A	0	34.82	$-0.79^{+0.07}_{-0.06}$	$-2.92^{+0.20}_{-0.92}$	2.02E-02	$360.72^{+60.59}_{-50.86}$	308.75(353)
090902B	-1.02	55.3	-1.02 ± 0.01	-2.76 ± 0.03	4.36E-02	$1063.61^{+53.68}_{-50.69}$	1002.(359)
090217A	-1.02	72.7	$-0.71^{+0.08}_{-0.07}$	-2.45 ± 0.07	5.98E-03	$452.82^{+89.74}_{-75.13}$	838.29(357)
090227A	-3.01	0.9	$-0.46^{+0.17}_{-0.14}$	$-2.68^{+0.56}_{-0.24}$	5.38E-03	$1662.40^{+640.49}_{-499.43}$	206.55(359)
090323A	-3.07	245.76	-1.30 ± 0.02	$-2.40^{+0.06}_{-0.05}$	6.85E-03	$734.31^{+156.03}_{-122.77}$	2119.(355)
090328A	-4.1	78.85	$-1.09^{+0.05}_{-0.04}$	$-2.26^{+0.07}_{-0.06}$	8.44E-03	$573.11^{+129.91}_{-101.24}$	447.94/356
090926A	-7.17	51.2	-0.79 ± 0.02	-2.24 ± 0.02	5.69E-02	$278.91^{+15.38}_{-14.19}$	482.9(357)
091031A	-1.02	37.89	$-0.97^{+0.14}_{-0.11}$	$-2.32^{+0.11}_{-0.08}$	5.80E-03	$534.63^{+301.38}_{-183.05}$	321.64(355)
100116A	-2.05	107.52	$-1.04^{+0.09}_{-0.07}$	$-2.63^{+0.13}_{-0.18}$	3.53E-03	$931.80^{+476.21}_{-291.34}$	375.02(357)
100225A	-16.38	12.29	$-0.65^{+0.50}_{-0.31}$	$-2.19^{+0.11}_{-0.17}$	3.51E-03	$433.52^{+81.71}_{-65.81}$	242.5(357)
110721A	-1.02	53.25	-1.18 ± 0.04	$-2.36^{+0.07}_{-0.06}$	9.46E-03	$685.49^{+209.96}_{-144.45}$	441.80(353)
120328B	-1.02	56.32	-0.85 ± 0.04	$-2.27^{+0.06}_{-0.05}$	4.18E-02	$195.88^{+21.30}_{-18.72}$	692.28(350)
121225B	-2.05	104.45	-1.25 ± 0.03	$-2.95^{+2.95}_{-0.33}$	1.19E-02	$433.52^{+81.71}_{-65.81}$	917.49(359)
130305A	-12.29	57.35	-0.78 ± 0.03	$-2.67^{+0.11}_{-0.09}$	1.30E-02	$718.38^{+75.07}_{-66.41}$	2719.(357)
130518A	-12.29	92.16	-0.87 ± 0.04	$-2.75^{+0.19}_{-0.11}$	1.48E-02	$435.30^{+47.38}_{-41.63}$	523.45(353)
130821A	-21.5	149.5	-1.19 ± 0.05	$-2.87^{+0.80}_{-0.20}$	9.25E-03	$296.79^{+69.91}_{-48.44}$	3444.(354)
131014A	0	32.77	-0.47 ± 0.02	$-2.57^{+0.07}_{-0.06}$	0.120984	$320.57^{+12.21}_{-11.35}$	404.24(352)
131108A	-1.02	24.58	$-0.89^{+0.07}_{-0.06}$	-2.13 ± 0.02	2.30E-02	$322.62^{+61.99}_{-49.94}$	257.25(355)
131231A	-3.07	76.8	-1.36 ± 0.02	$-2.76^{+0.21}_{-0.11}$	3.81E-02	$242.96^{+17.59}_{-16.14}$	2564.(355)
140102A	-1.02	12.29	$-0.88^{+0.08}_{-0.07}$	$-2.46^{+0.17}_{-0.09}$	4.42E-02	$180.40^{+29.72}_{-24.94}$	381.71(352)
150403A	-2.05	37.89	-0.88 ± 0.03	$-2.63^{+0.09}_{-0.13}$	2.27E-02	$471.74^{+50.77}_{-45.36}$	432.65(352)
150523A	-1.02	82.94	$-0.83^{+0.08}_{-0.07}$	$-2.62^{+0.13}_{-0.09}$	5.11E-03	$607.38^{+137.76}_{-106.69}$	566.71(356)
150510A	0.00	76.80	-1.00 ± 0.02	$-3.70^{+0.31}_{-1.00}$	1.33E-02	$1604.^{+164.40}_{-158.39}$	561.81(356)
150902A	-2.05	31.74	-0.62 ± 0.03	$-2.66^{+0.07}_{-0.06}$	4.24E-02	$395.67^{+26.47}_{-24.27}$	483.72(357)
160816A	-1.02	15.36	-0.69 ± 0.05	$-2.63^{+0.15}_{-0.09}$	6.13E-02	$212.97^{+19.49}_{-17.65}$	286.91(356)
160905A	-3.07	97.28	$-0.97^{+0.05}_{-0.04}$	$-3.43^{+0.42}_{-0.21}$	1.16E-02	$983.26^{+192.57}_{-151.18}$	538.81(355)
170405A	-2.05	188.42	$-0.50^{+0.10}_{-0.08}$	$-2.39^{+0.06}_{-0.05}$	1.45E-02	$217.80^{+31.96}_{-30.85}$	2074.(356)

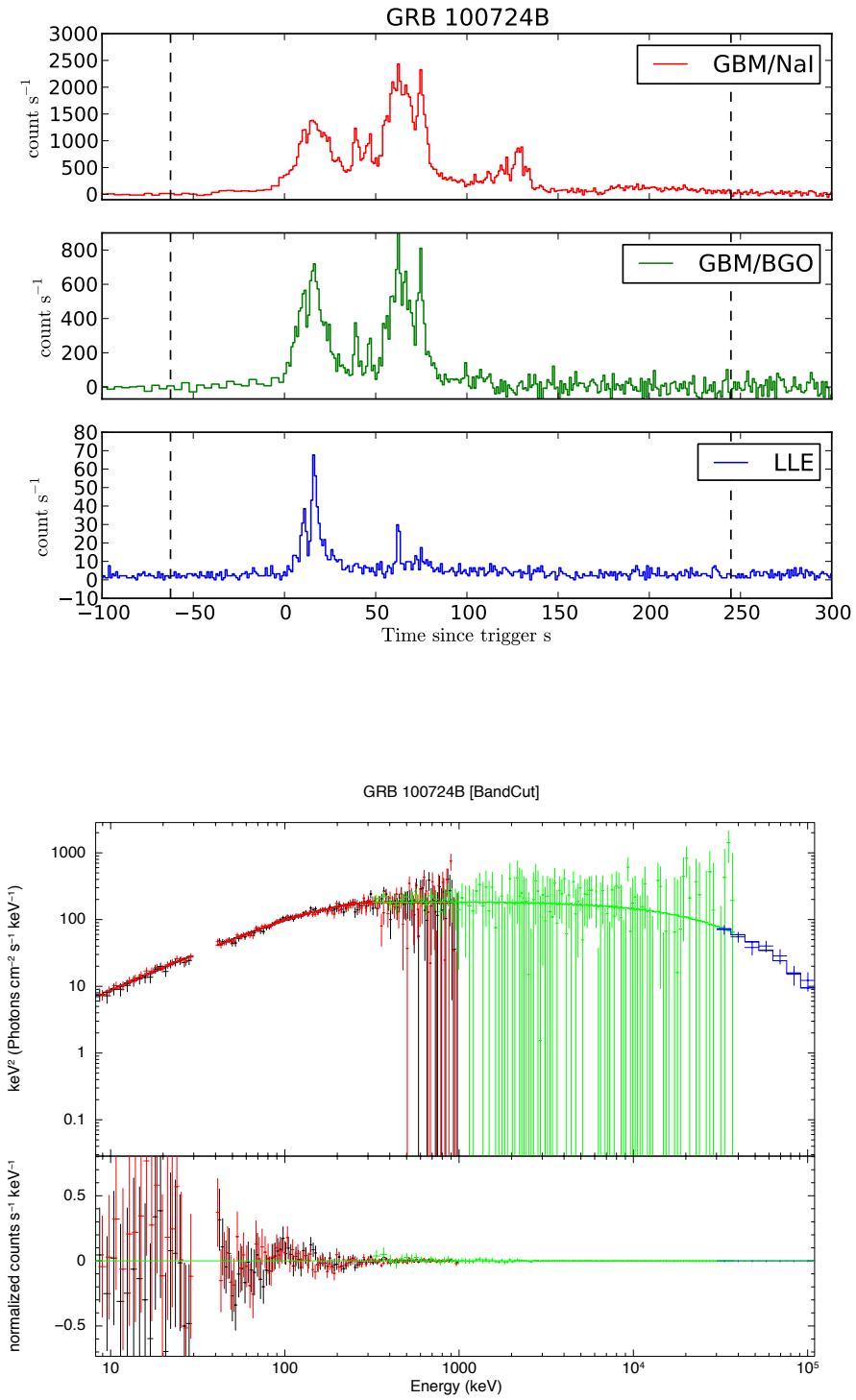

Figure 5.3: The upper panels are the GBM/NaI, GBM/BGO and LLE light curves. The lower panels are the spectral analysis showing the three best cases when E_c is measured and which is associated with the Γ detected via *Fermi* (LLE and GBM), as fitted with the BandCut model. The residuals are shown in the bottom panel. The GRBs from top to bottom are 100724B, 160821A, and 160910A.

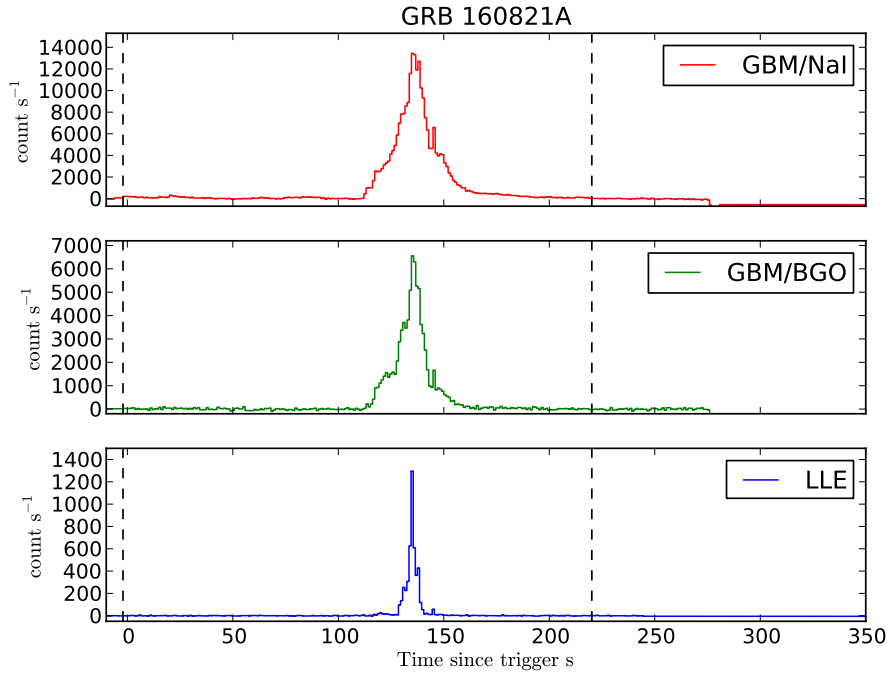

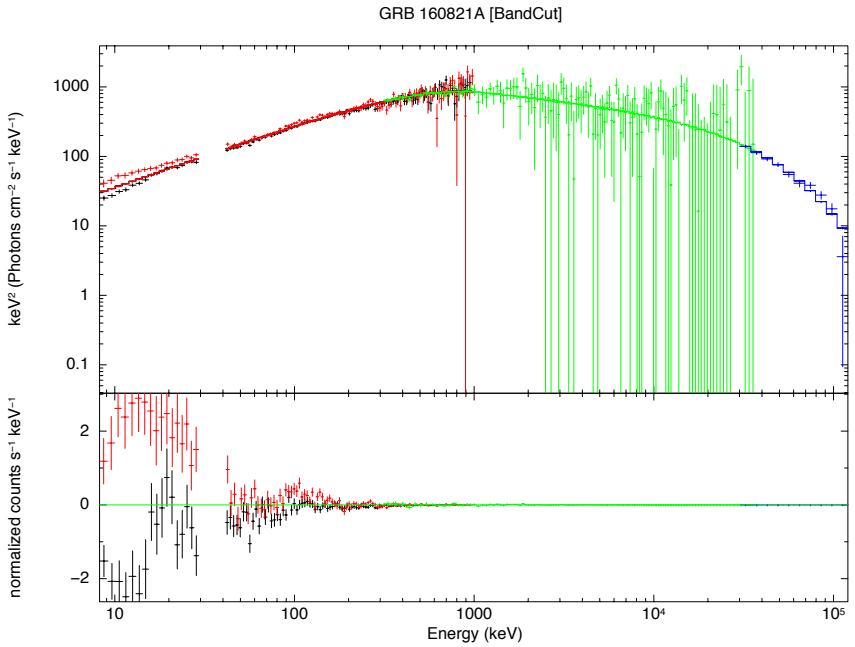

Figure 5.3: cont'd

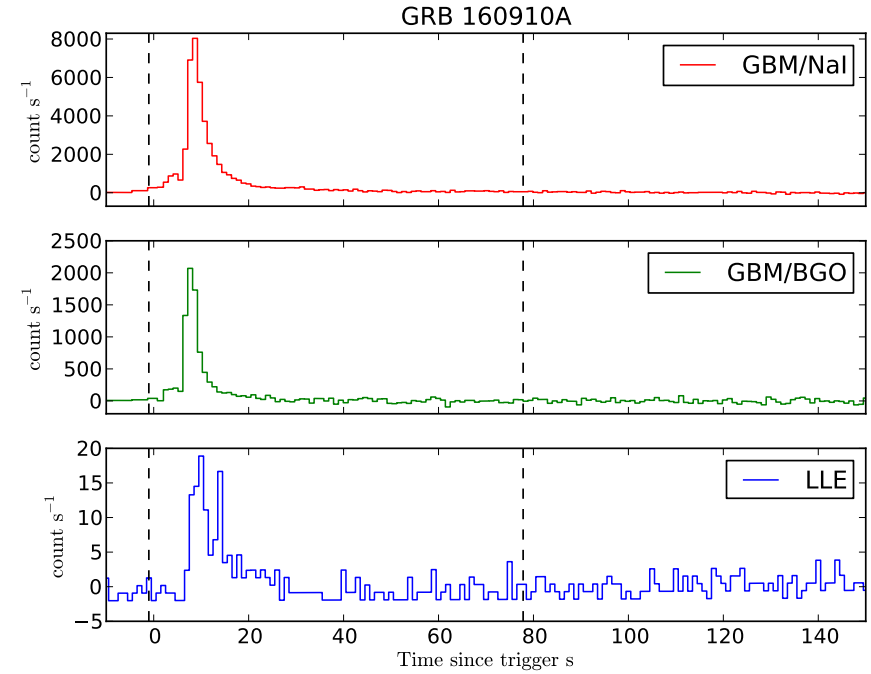

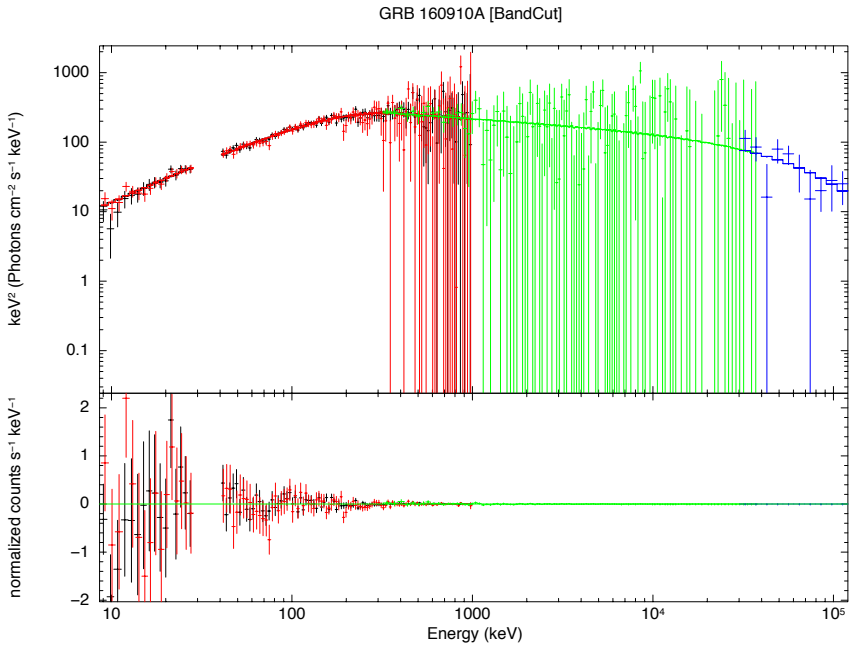

Figure 5.3: cont'd

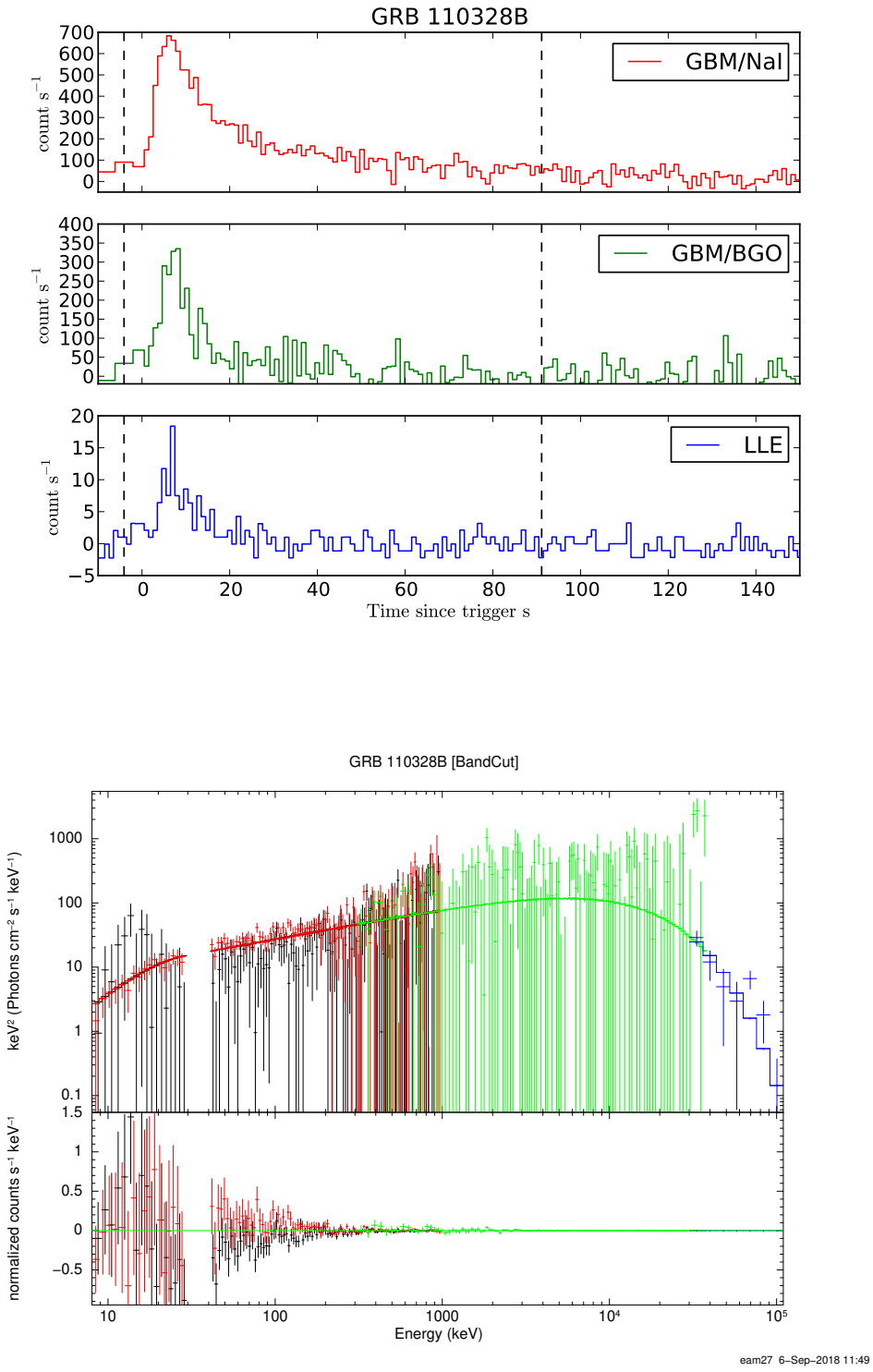

Figure 5.4: The upper panels are the light curves from GBM/NaI, GBM/BGO and LLE. The lower panels are the spectral analyses showing the case of detecting the break energy E_b of four GRBs detected via *Fermi* (LLE and GBM), as fitted with the BandCut model. The residuals are shown in the bottom panel. The GRBs from top to bottom are GRB 110328B, GRB 130504C, GRB 140206A, and GRB 160509A.

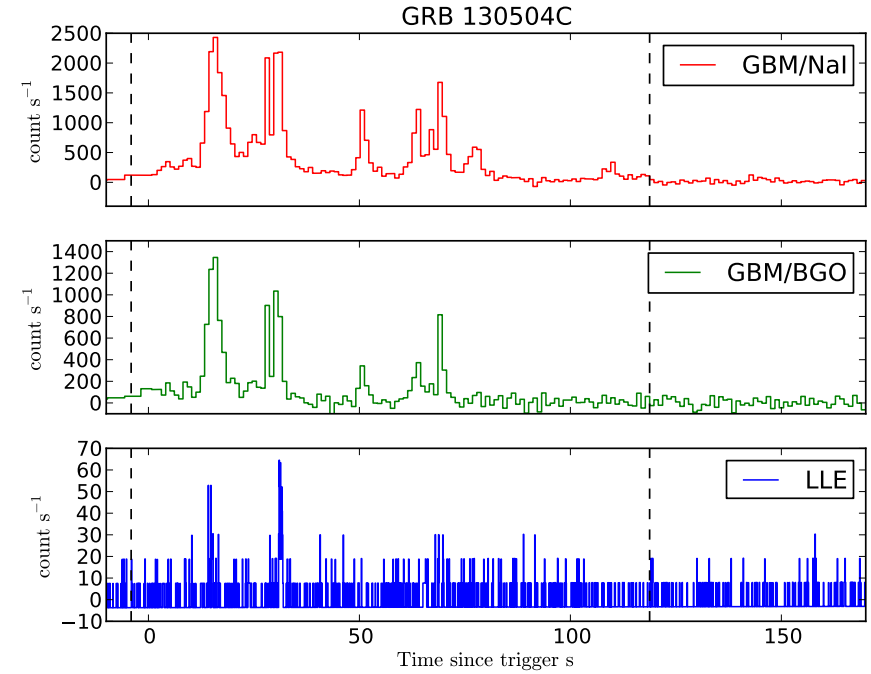

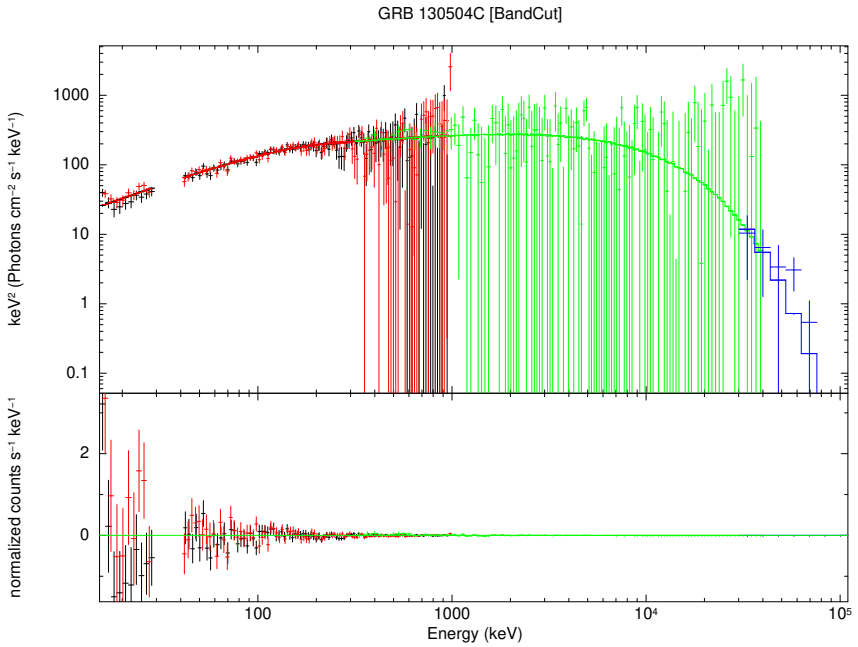

Figure 5.4: cont'd

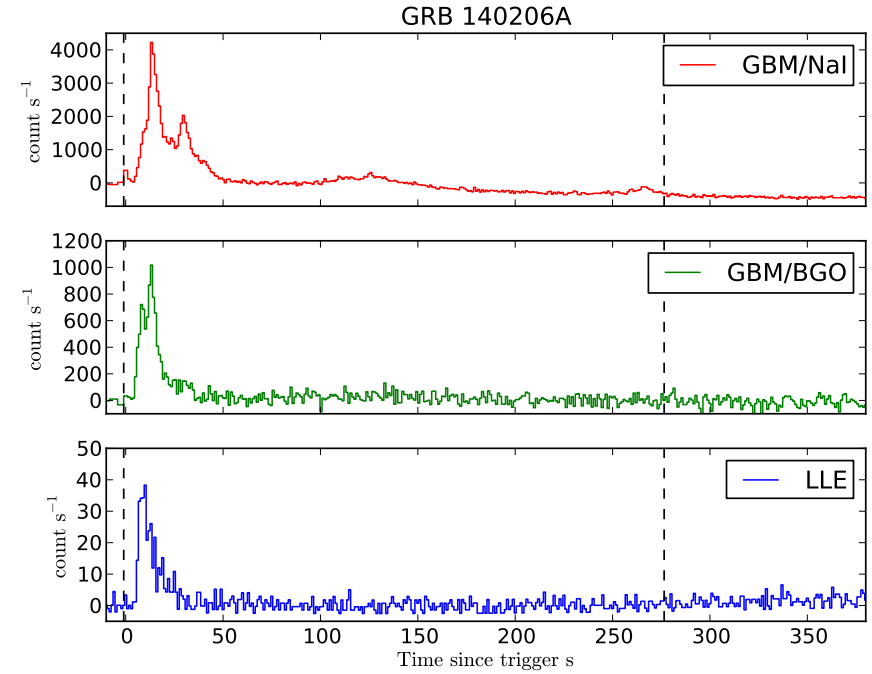

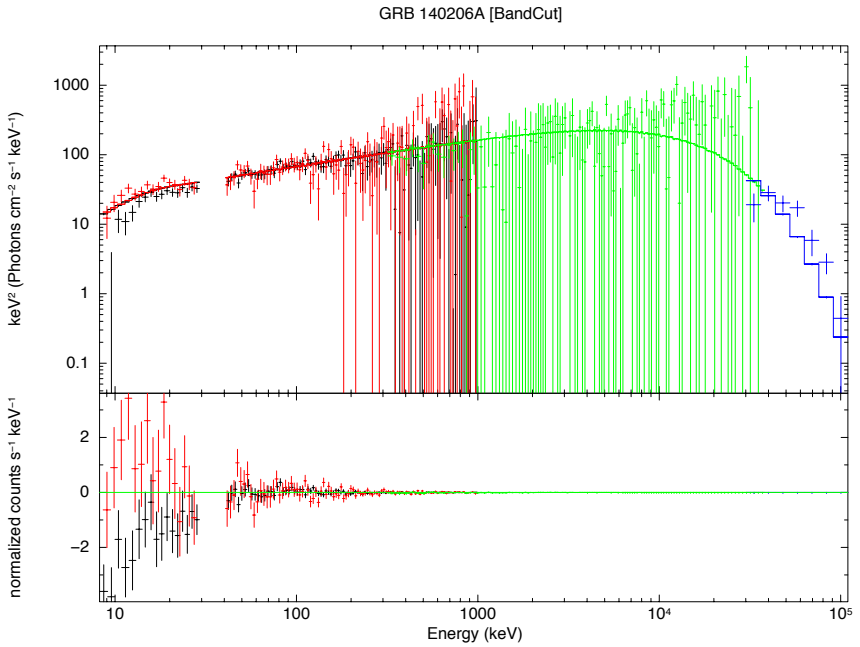

Figure 5.4: cont'd

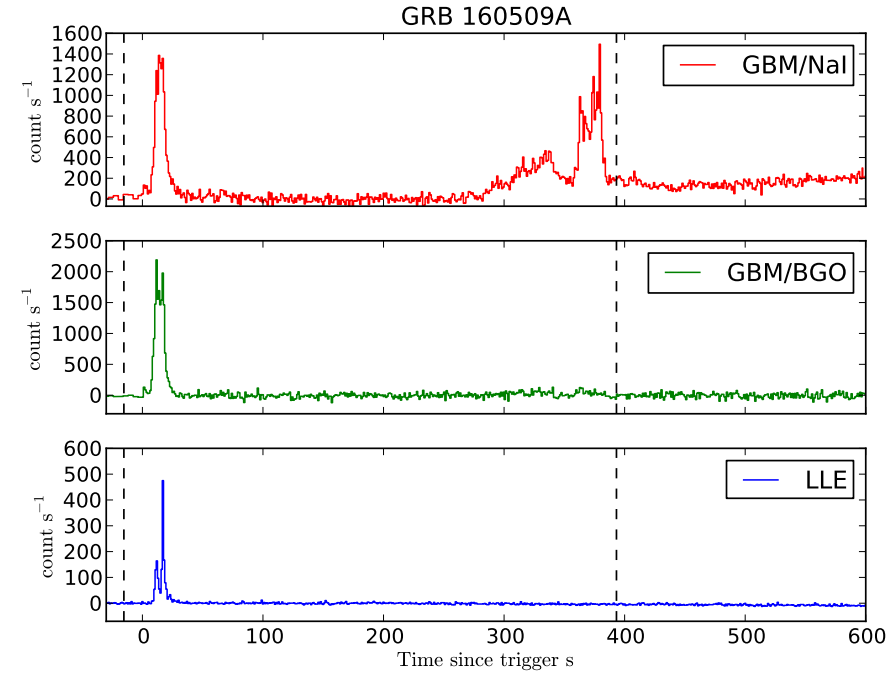

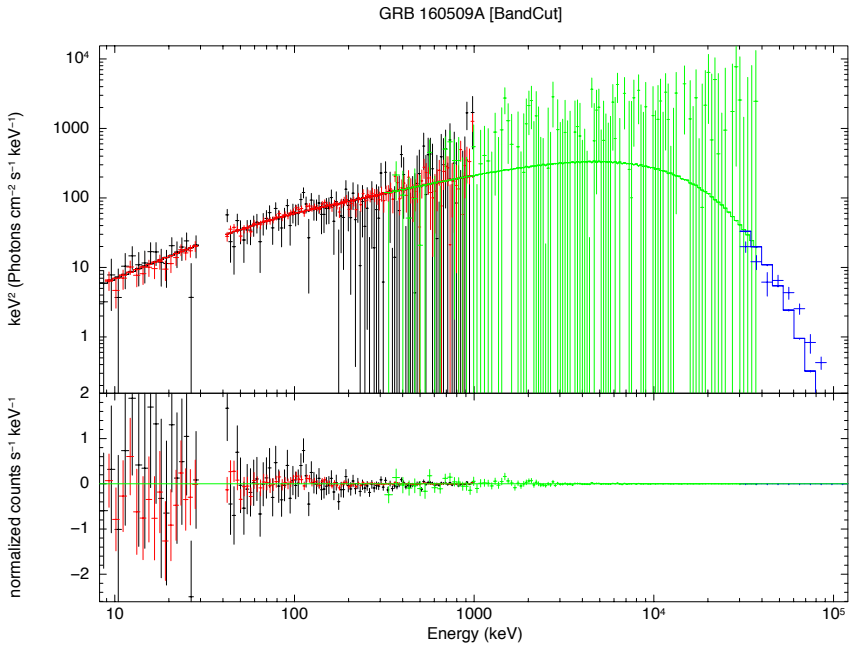

Figure 5.4: cont'd

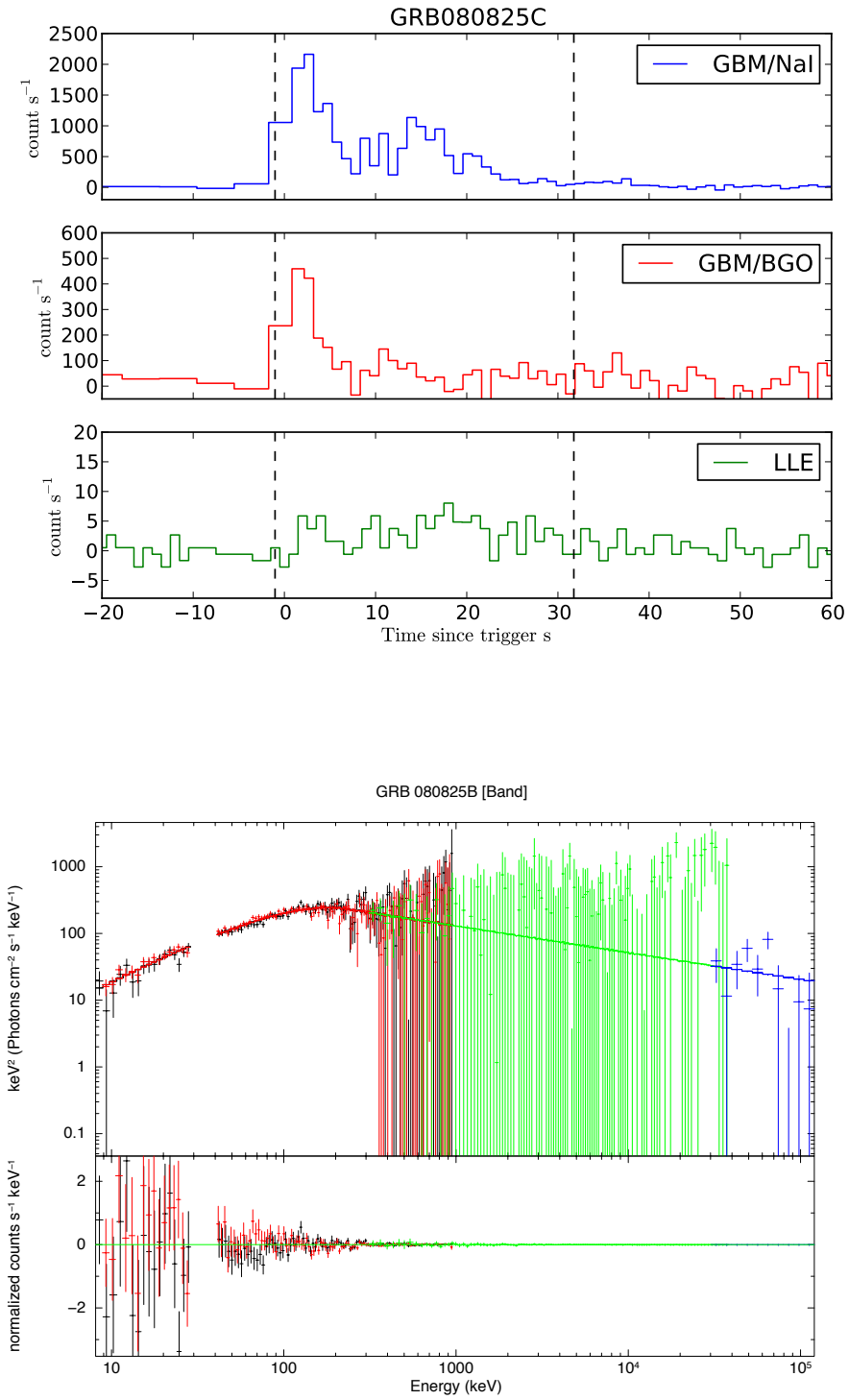

Figure 5.5: The upper panels are the light curves of GBM/NaI, GBM/BGO and LLE for GRB 080825C and GRB 080916A. The lower panels are the spectral analyses showing the high-energy peaks of these two GRBs detected via *Fermi* (LLE and GBM), as fitted with the simple Band model. The residuals are shown in the lower part of the bottom panel. The remainder of the sample is given in Appendix A.3.

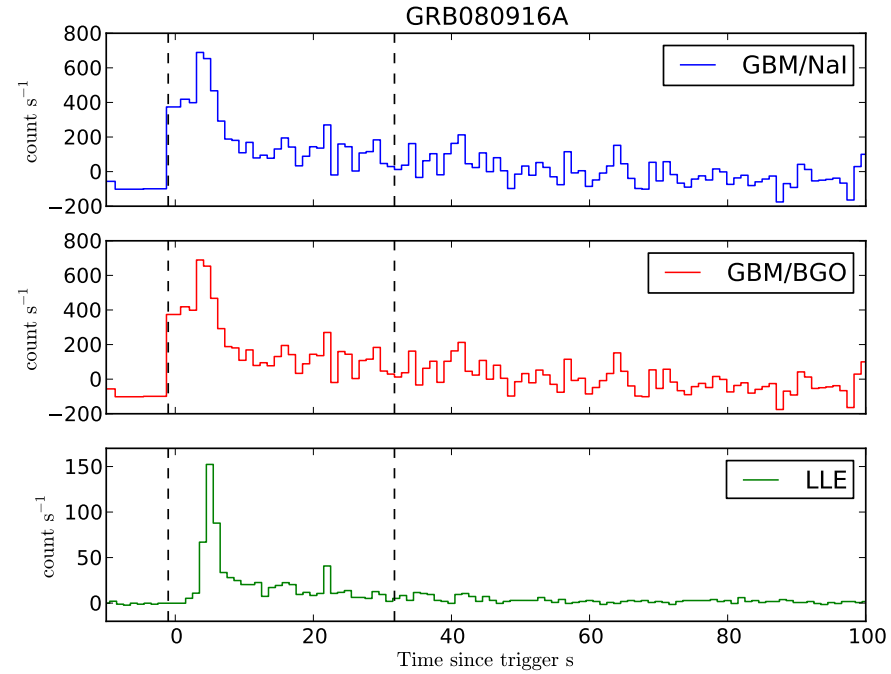

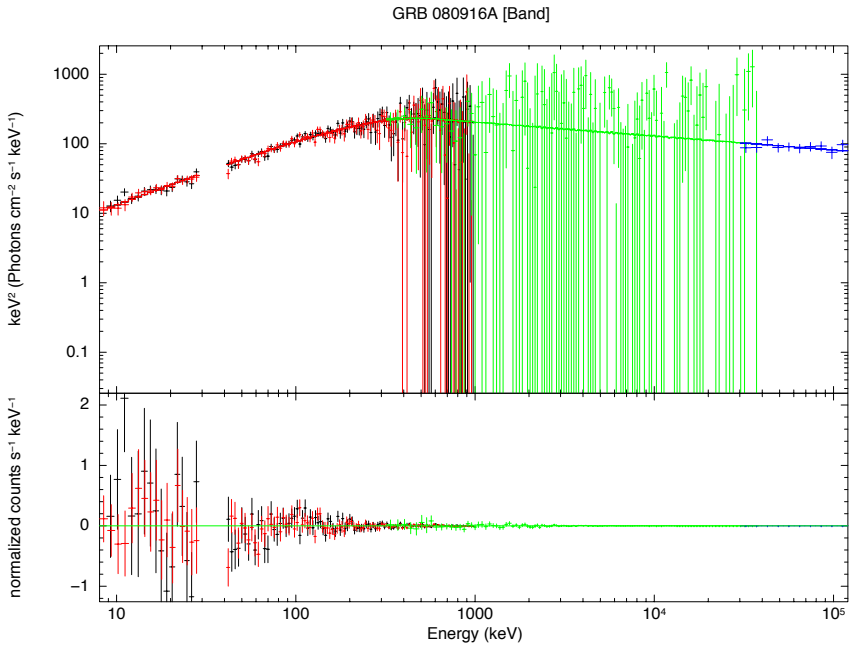

Figure 5.5: cont'd

Chapter 6

Summary and Future prospects

6.1 Key Conclusions

During this thesis, a joint-fit spectral analysis of a sample of GRBs using data obtained via *Fermi* and *Swift* have been considered. This chapter presents the main findings and gives a further summary of the analysis undertaken, as well as a study of spectral high-energy cut-off features and Lorentz factor estimation. Future work with regards to the continuing analysis of GRBs via GBM+BAT+XRT to examine other spectral properties could well be very promising with any new observatory in the context of future technology. Together, data that include LAT data could also be considered. In this chapter, a number of key conclusions can be made as follows:

• The joint-fit (GBM+BAT) spectral analysis for the time-integrated spectra were obtained. Significant differences were found when plotting the GBM-only versus the joint-fit, in that adding BAT (joint-fit) resulted in a higher E_{peak} than found for the E_{peak} obtained from GBM-only. The low-energy indices α seemed to be softer than when obtained from GBM-only. Regardless of the unconstrained GBM/BGO detectors used to observe the majority of GRBs, the joint-fit time-integrated spectra showed a certain consistency with the use of different spectral models, either the CPL model or the Band model, for certain GRBs that were best fit with the Band model, for example. Comparisons with other studies such as V12 for the joint-fit part generally showed there to be a degree of inconsistency in certain GRBs, where different spectral parameters are found. This may be due to the differences in the spectral analysis methods used by different users. The majority of GRBs where the CPL model was favoured over the Band model were due to the high-energy index β at the very high-energy end of the *Fermi*/GBM-BGO data being unconstrained. Again, a comparison of the GBM-only with other studies such as N11, B11, and GCN provided a few differences in the spectral parameters for certain GRBs due to the different analysis methods used by each of the associated authors, but in general there are consistencies within their uncertainties. The Amati relation was consistent with the literature for the analyses undertaken in this study. This $E_{peak} - E_{iso,rest}$ relation showed considerable agreement. The Amati best-fit gradient is similar to that found in this study within the respective uncertainties, whereas for the Yonetoku relation, $E_{peak} - L_{iso,rest}$, the data were correlated but lay above the Yonetoku best-fit line, as they were shifted to lower luminosity. These deviations were probably

due to the Yonetoku relation in the literature using a 1-sec peak flux, while in this study the average peak flux was instead considered.

• The joint-fit spectral analysis for the time-resolved spectra can enable a wide range of GRB spectral studies that can help to understand the physics behind individual pulses. Slicing the time interval can provide a clearer of GRB spectra in terms of their individual behaviours. The joint-fit was found to be significantly different than the GBM-only, in that it obtained a higher E_{peak} and a softer index α than otherwise obtained from GBM-only when comparing their statistical tests. The Band model can fit some of the GRBs time slices that have their β values constrained. Similarly, there are significant differences between the joint-fit and the GBM-only fitted with Band, although the low-energy α shows no clear correlation and has large uncertainties, which may have been due to the effectiveness of the unconstrained high-energy β. In general, the majority of GRB time slices can be well fitted with the CPL model. The trend in E_{peak} evolution could be categorized as being predominantly one of two ways: variability from a hard-to-soft intensity ratio, or intensity tracking. The majority of GRBs were found to evolve in an intensity-tracking manner, whilst only a few showed a hard-to-soft type. The Amati relation analysis using time-resolved methods did not show as strong a correlation as that found for the time-integrated spectra. It was believed that this may have been due to the effects of the individual pulses for each GRB whose E_{iso} were divided for each time slice. This resulted in some scattering above the original Amati best fit. However, the Amati best-fit gradient is consistent with Amati in this study, regardless of the best-fit Amati being drawn from a time-integrated analysis. Furthermore, plotting the Amati relation for individual bursts revealed there are different behaviours for each burst, and hence some of the scatter in the Amati correlation could be due to individual trends. It was found that there were different behaviours for each burst according to their Amati correlation, where for some GRBs it was noticed that the fewer time slices plotted the stronger the correlation, and vice versa. In contrast, the Yonetoku relation shows a much stronger correlation, which can be interpreted as this relation being less sensitive to the luminosity, L_{iso}, of the individual pulses compared to the E_{peak} values (dividing the data has less effect on Yonetoku). The Yonetoku gradient is consistent with the findings for the Yonetoku relation in this study, even though, the Yonetoku relation does not apply to the time-resolved spectra. The Amati and Yonetoku relations for the time-integrated and the time-resolved analyses showed consistent gradients within their respective uncertainties.

• Spectral high-energy cut-off features were investigated using a spectral analysis of a sample of 46 bright LGRBs detected via *Fermi* (GBM+LLE). Only three GRBs were shown to have spectral high-energy cut-offs, whereas the remainder of the sample did not show any evidence of cut-offs Within the observed band, which could have been due to the high-energy photon counts being insufficiently small in number to prevent the detection of the cut-off due to being above the LLE band. Another case of using the BandCut model was found to obtain a peak energy E_{peak} instead of the energy cut-off, E_c, which was found for only four GRBs. For the remaining GRBs

that are not well fit with the BandCut model, the simple Band model was otherwise used. For the GRBs that were well defined in terms of their cut-offs, it was found that the associated Lorentz factor, Γ, was in the range $\sim$ 30-300. The other scenario of estimating the Lorentz factor Γ_0 (e.g., afterglow onset) was discussed by comparing different Γ's as adopted from a number of studies.

6.2 Future Work

6.2.1 *Fermi* and *Swift* (GBM+BAT+XRT) Spectral Analysis

In this thesis, a joint spectral fit was analysed and studied for different spectra of the GBM+BAT type. Adding an extra instrument to the GBM+BAT joint-fit could be another approach to investigating the study of prompt emission by covering the very low-energy range of XRT spectra. The detection of prompt emission via the *Swift* (XRT) X-Ray Telescope provided a set of unique tools by which to study the prompt spectrum GRBs in the low-energy domain (0.3-10 keV) (Burrows et al., 2005).

The spectral joint-fit (GBM+BAT+XRT) could help to investigate outcomes that may be interesting, and could reveal, and thus help us to understand, the shape of spectra below the vF_v peak energy in this low-energy range. Extending the energy up to 10 MeV and down to 0.3 keV should help to broaden the study of prompt emission spectra and to allow models for the different behaviours seen in such cases to be proposed and developed. This can be undertaken by choosing *Swift* GRBs in which the XRT was observing the extended part of the prompt emission seen with BAT+GBM. Thus, in studying the prompt emission in these low-energy bands, previous work suggests that the observed spectral shape is different to that predicted by the synchrotron model (Oganesyan et al., 2017).

The number of GRBs being detected simultaneously via XRT and BAT is more than $\sim$80 since Jan 2017. In this analysis, the sample of 16 GRBs was conducted from the period of October 2008 to June 2017 via GBM (with two NaI and one BGO detectors), BAT and, XRT. The sample selection was made based on three criteria: 1) all GRBs had measured redshifts; 2) all GRBs were chosen so as to have a signal-to-noise ratio greater than 30; and 3) all GRBs were long and bright with photon fluxes $>$ 2.6 ph cm^{-2} s^{-1}. Most of the GRBs were detected coincidentally via GBM+BAT+XRT. If the XRT did not overlap well with GBM+BAT, those GRBs were excluded from the sample.

From the *Swift* Science Data Centre, as provided by the University of Leicester (Evans et al., 2009), the XRT light curves were retrieved from the *Swift* archive XRT event files. For the time-integrated spectra, the data were extracted from the automated XRT repository, excluding all channels below 0.5 keV from the spectral analysis. All energy channels were grouped in order to use χ^2 statistics via the *grbpha* tool for only 20 counts in each time bin. The joint analysis of (GBM+BAT+XRT) spectral data was not a straightforward task due to the necessity to model

the effect of galactic and intrinsic dust absorption, the pile-up of photons in the XRT detector, and the uncertainties in the intercalibration of the various different instruments involved. The following gives an indication of the initial results found. Several GRBs that overlapped with the three detectors (GBM+BAT+XRT) showed a degree consistency. Figure 6.1 shows examples of GRB light curves found by the three detectors.

There are some time intervals where the data could be divided into a number of time intervals for each burst, where each individual time interval could be analysed, allowing for normalization factors to deal with any calibration issues. Taking into account both galactic and intrinsic metal absorption, the spectra could be analysed via XSPEC using *tbabs* and *ztbabs*, respectively (Wilms et al., 2000).

Continuing to address this area of study is strongly recommended, as already published by Oganesyan et al. (2017), in order to provide a comparison study to determine any further spectral analysis properties by enlarging the sample provided in the previous study.

6.2.2 *Fermi* (LAT+LLE+GBM) Spectral Analysis

As well as going to lower energies, adding LAT data to the GBM and LLE can extend the band to higher energies, fitting them jointly in order to search for further spectral cut-off features. This may give the opportunity to measure more high-energy cut-offs and Lorentz factors, Γ. Adding the LAT data in the very high-energy range from 20 MeV to more than 300 GeV seems very promising in terms of either enlarging the number of cut-off energies or in terms of improving spectral analysis statistics (Ackermann et al., 2013). There would be relatively few GRBs with XRT, BAT, GBM and LAT data, but such an analysis would be important to further study the spectral properties of the brightest GRBs in the higher energy domain. The future Einstein Probe and the proposed *THESEUS* mission will also increase the number of prompt X-ray detections.

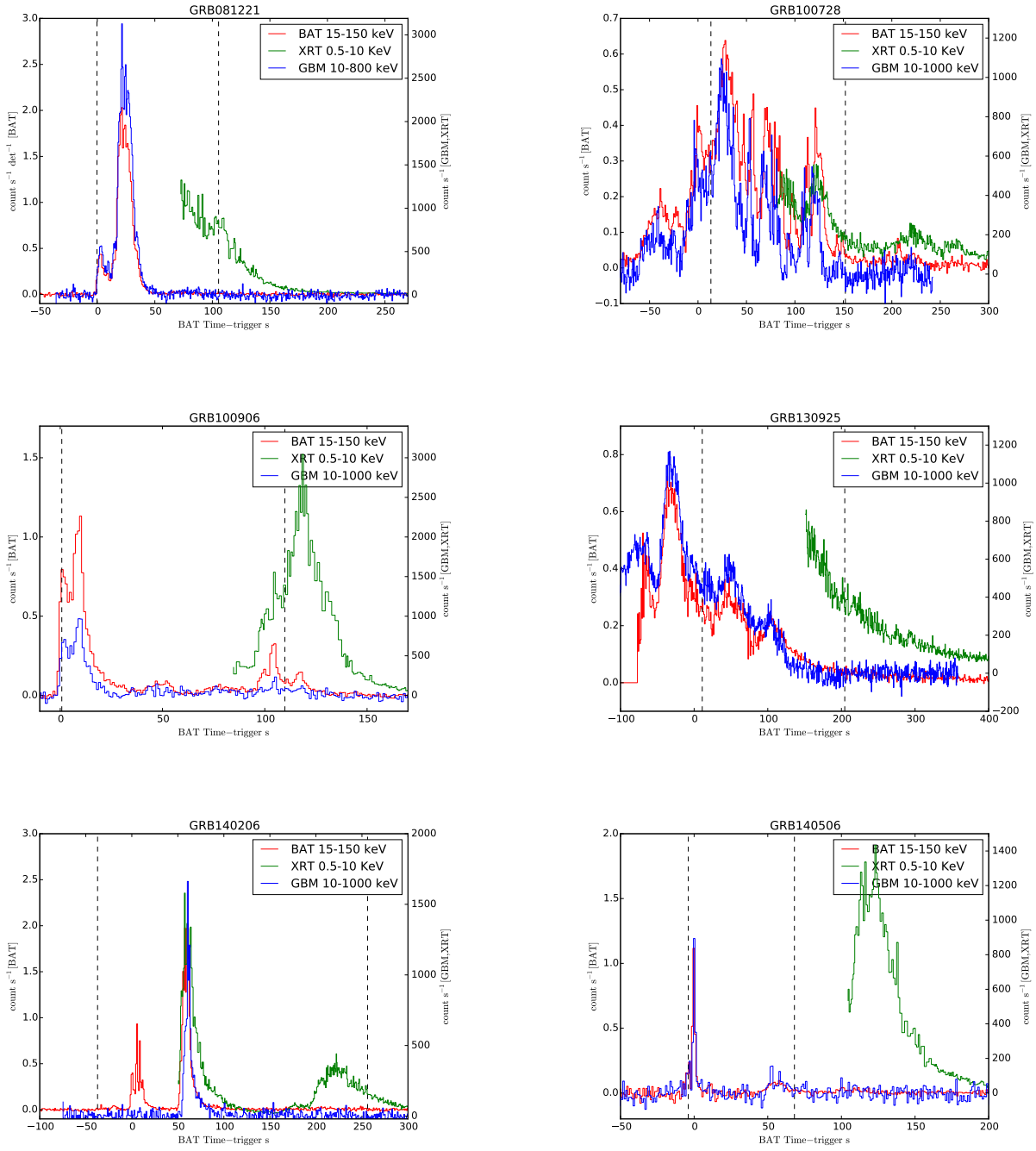

Figure 6.1: The temporal analysis of the joint-fit (GBM+BAT+XRT) of some GRBs. GBM (in blue), BAT (in red) and XRT (in green). The black dashed line shows the time interval chosen for the T_{90}.

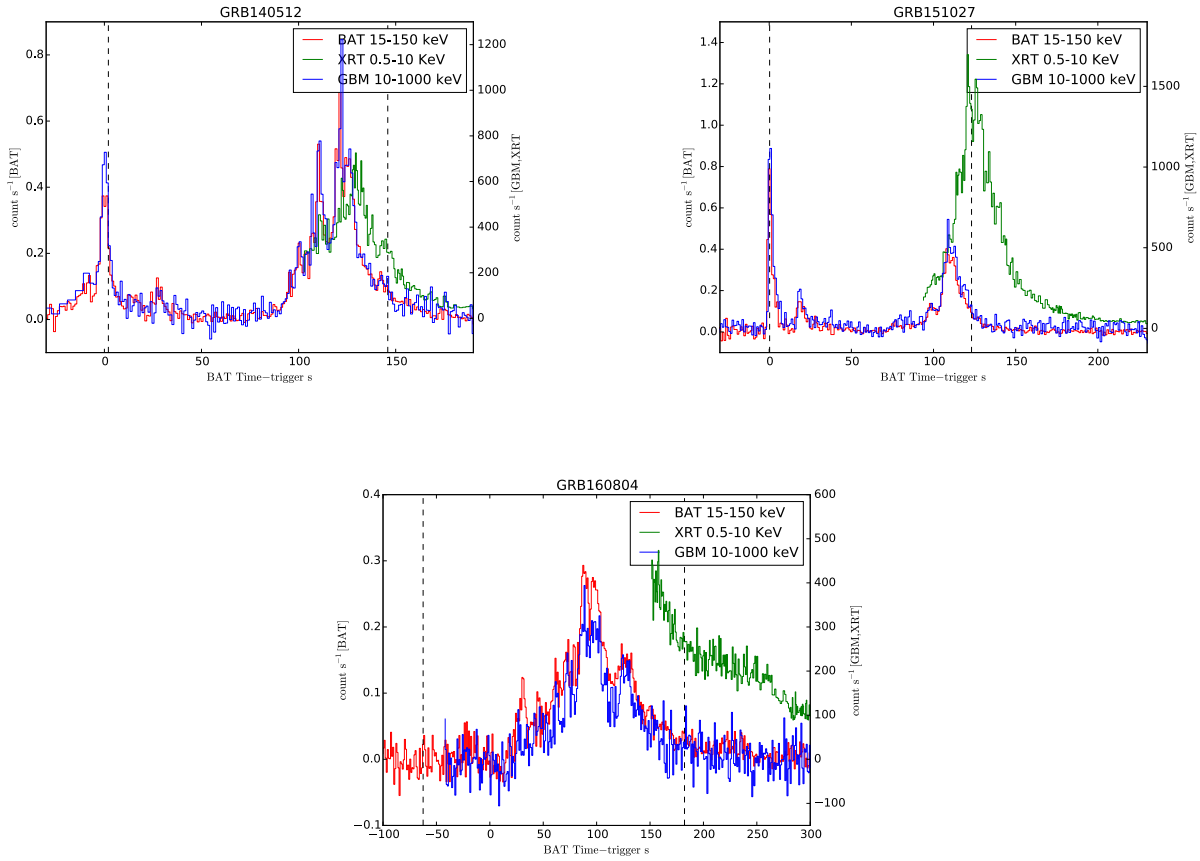

Figure 6.1: cont'd

Appendix A

A.1 The spectral analysis for the time-integrated spectra

Appendix A.1 shows the time-integrated spectral analysis for each GRB of the joint-fit (*Fermi*GBM /NaI & BGO and *Swift* BAT instruments).

A.2 The spectral analysis for the time-resolved spectra

Appendix A.2 shows the time-resolved spectral analysis for each GRB of the joint-fit (*Fermi*GBM /NaI & BGO and *Swift* BAT instruments).

A.3 The spectral analysis of *Fermi* (GBM+LLE)

Appendix A.3 shows all possible fitting for the whole sample for both models; the simple Band and the high energy cutoff BandCut. It also illustrated all the light curves (GBM and BAT) for the sample.

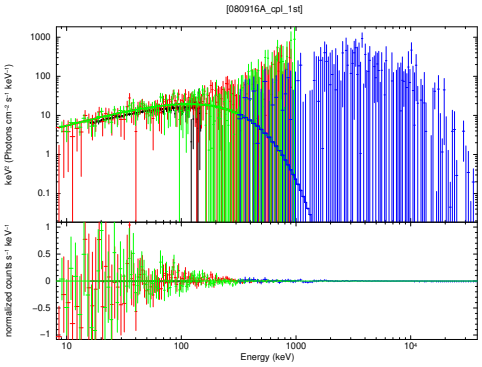
[080916A_cpl_1st]
keV² (Photons cm⁻² s⁻¹ keV⁻¹)
normalized counts s⁻¹ keV⁻¹
Energy (keV)

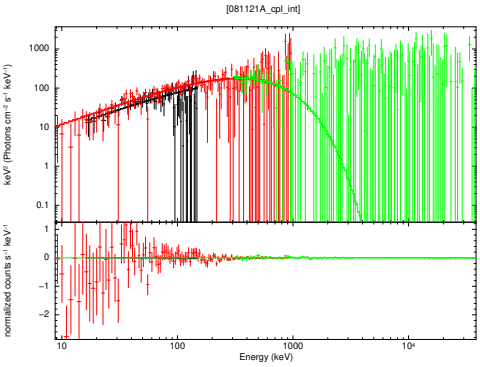
[081121A_cpl_int]
keV² (Photons cm⁻² s⁻¹ keV⁻¹)
normalized counts s⁻¹ keV⁻¹
Energy (keV)

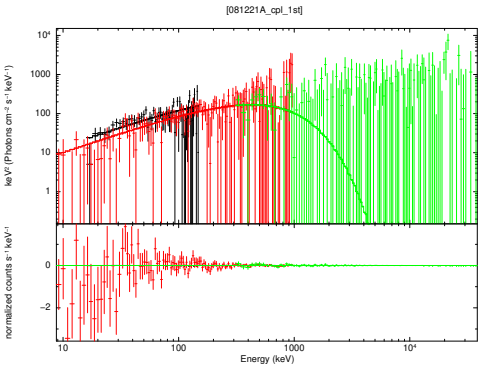
[081221A_cpl_1st]
keV² (Photons cm⁻² s⁻¹ keV⁻¹)
normalized counts s⁻¹ keV⁻¹
Energy (keV)

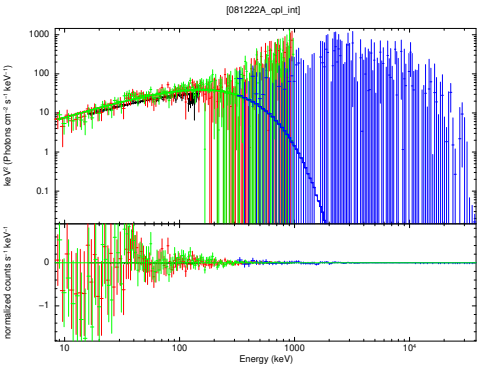
[081222A_cpl_int]
keV² (Photons cm⁻² s⁻¹ keV⁻¹)
normalized counts s⁻¹ keV⁻¹
Energy (keV)

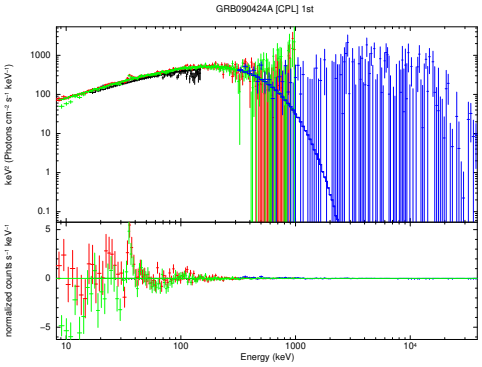
GRB090424A [CPL] 1st
keV² (Photons cm⁻² s⁻¹ keV⁻¹)
normalized counts s⁻¹ keV⁻¹
Energy (keV)

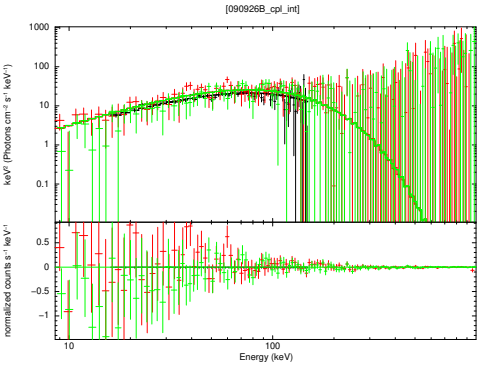
[090926B_cpl_int]
keV² (Photons cm⁻² s⁻¹ keV⁻¹)
normalized counts s⁻¹ keV⁻¹
Energy (keV)

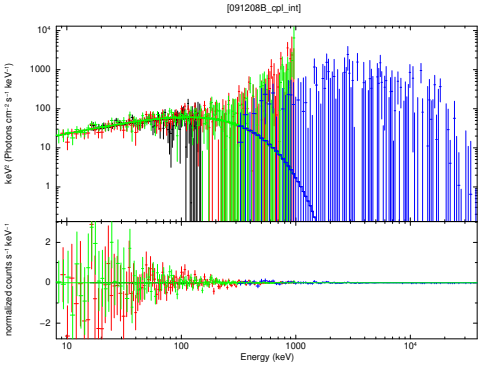
[091208B_cpl_int]
keV² (Photons cm⁻² s⁻¹ keV⁻¹)
normalized counts s⁻¹ keV⁻¹
Energy (keV)

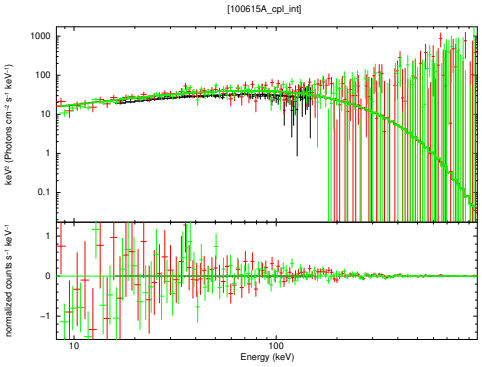
[100615A_cpl_int]
keV² (Photons cm⁻² s⁻¹ keV⁻¹)
normalized counts s⁻¹ keV⁻¹
Energy (keV)

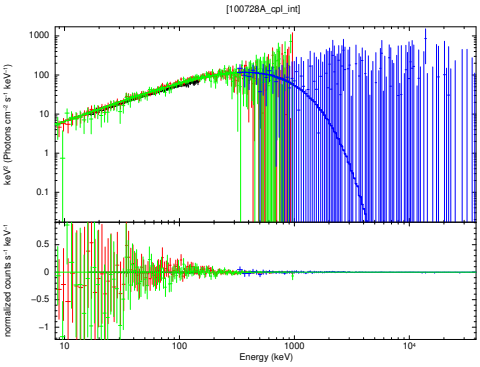
[100728A_cpl_int]
keV² (Photons cm⁻² s⁻¹ keV⁻¹)
normalized counts s⁻¹ keV⁻¹
Energy (keV)

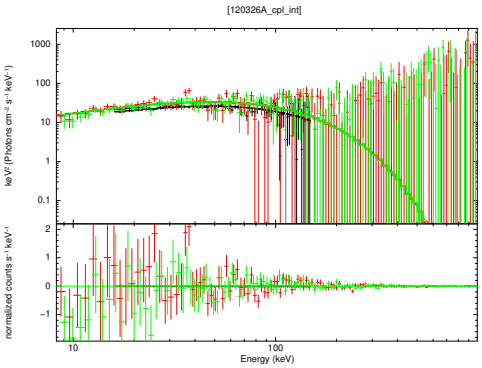
[120326A_cpl_int]
keV² (Photons cm⁻² s⁻¹ keV⁻¹)
normalized counts s⁻¹ keV⁻¹
Energy (keV)

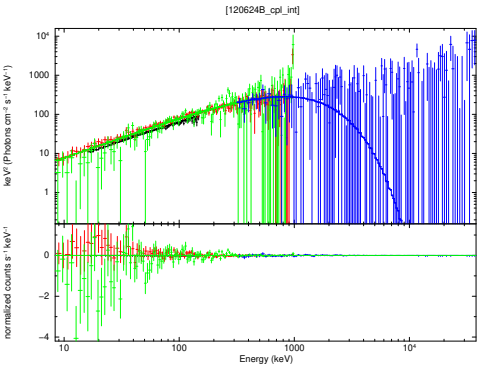
[120624B_cpl_int]
keV² (Photons cm⁻² s⁻¹ keV⁻¹)
normalized counts s⁻¹ keV⁻¹
Energy (keV)

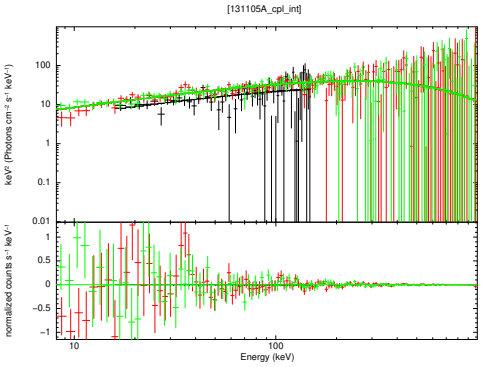
[131105A_cpl_int]
keV² (Photons cm⁻² s⁻¹ keV⁻¹)
normalized counts s⁻¹ keV⁻¹
Energy (keV)

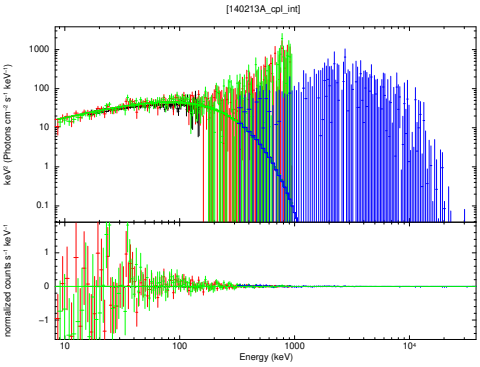
[140213A_cpl_int]
keV² (Photons cm⁻² s⁻¹ keV⁻¹)
normalized counts s⁻¹ keV⁻¹
Energy (keV)

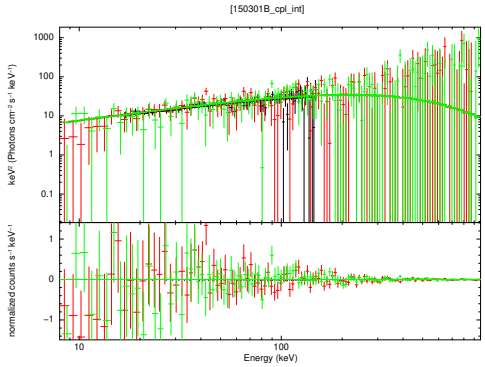
[150301B_cpl_int]
keV² (Photons cm⁻² s⁻¹ keV⁻¹)
normalized counts s⁻¹ keV⁻¹
Energy (keV)

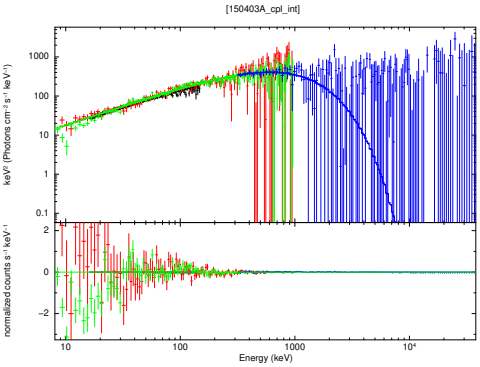
[150403A_cpl_int]
keV² (Photons cm⁻² s⁻¹ keV⁻¹)
normalized counts s⁻¹ keV⁻¹
Energy (keV)

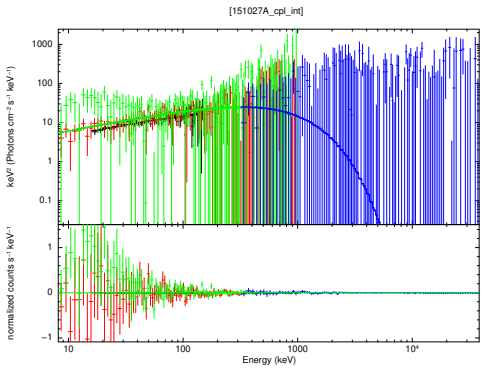

Figure A.1: The spectral analysis of the joint-fit (GBM+BAT) for the time-integrated spectra of the GRB sample.

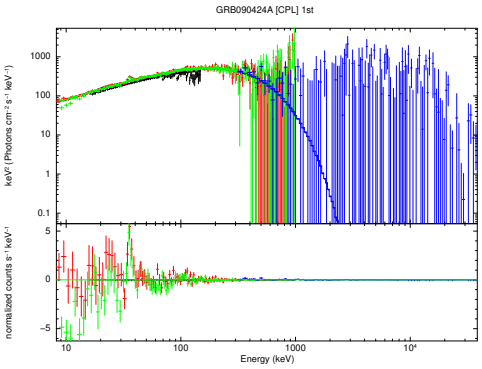
GRB090424A [CPL] 1st
keV² (Photons cm⁻² s⁻¹ keV⁻¹)
normalized counts s⁻¹ keV⁻¹
Energy (keV)

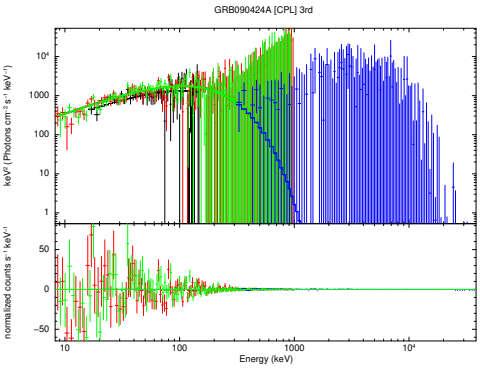
GRB090424A [CPL] 3rd
keV² (Photons cm⁻² s⁻¹ keV⁻¹)
normalized counts s⁻¹ keV⁻¹
Energy (keV)

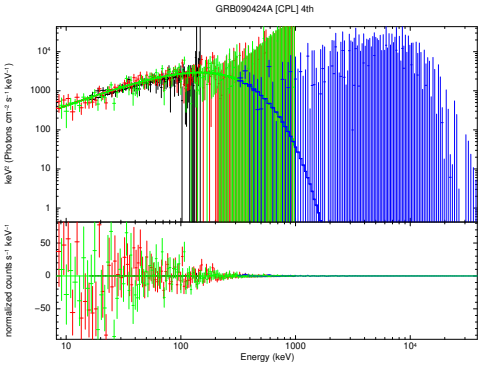
GRB090424A [CPL] 4th
keV² (Photons cm⁻² s⁻¹ keV⁻¹)
normalized counts s⁻¹ keV⁻¹
Energy (keV)

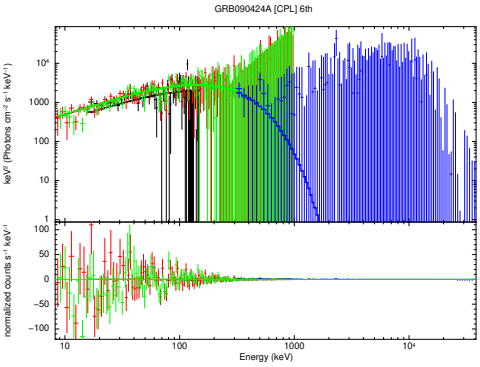
GRB090424A [CPL] 6th
keV² (Photons cm⁻² s⁻¹ keV⁻¹)
normalized counts s⁻¹ keV⁻¹
Energy (keV)

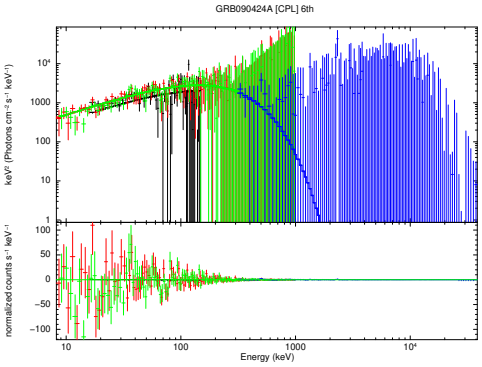
GRB090424A [CPL] 6th
keV² (Photons cm⁻² s⁻¹ keV⁻¹)
normalized counts s⁻¹ keV⁻¹
Energy (keV)

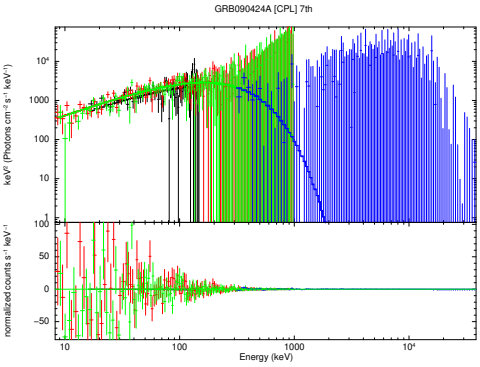
GRB090424A [CPL] 7th
keV² (Photons cm⁻² s⁻¹ keV⁻¹)
normalized counts s⁻¹ keV⁻¹
Energy (keV)

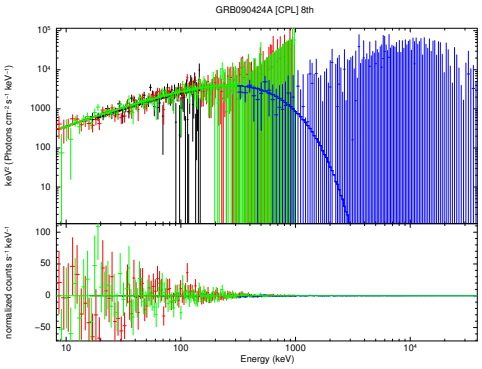
GRB090424A [CPL] 8th
keV² (Photons cm⁻² s⁻¹ keV⁻¹)
normalized counts s⁻¹ keV⁻¹
Energy (keV)

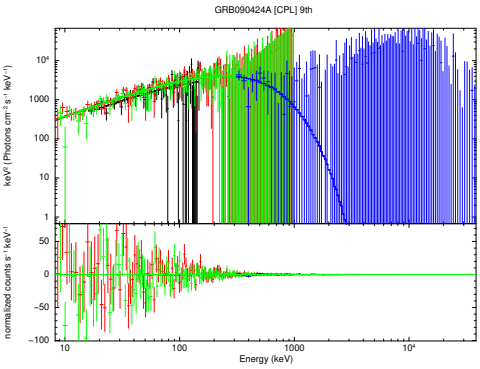
GRB090424A [CPL] 9th
keV² (Photons cm⁻² s⁻¹ keV⁻¹)
normalized counts s⁻¹ keV⁻¹
Energy (keV)

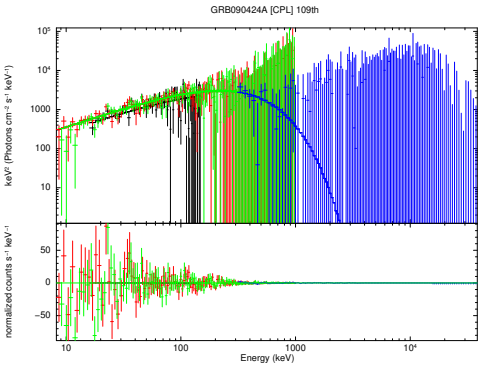
GRB090424A [CPL] 109th
keV² (Photons cm⁻² s⁻¹ keV⁻¹)
normalized counts s⁻¹ keV⁻¹
Energy (keV)

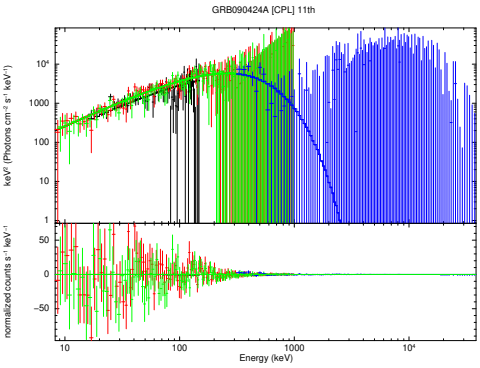
GRB090424A [CPL] 11th
keV² (Photons cm⁻² s⁻¹ keV⁻¹)
normalized counts s⁻¹ keV⁻¹
Energy (keV)

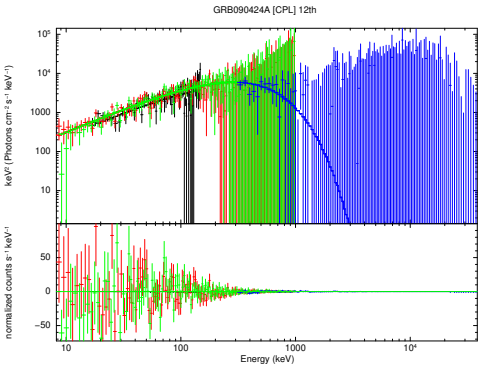
GRB090424A [CPL] 12th
keV² (Photons cm⁻² s⁻¹ keV⁻¹)
normalized counts s⁻¹ keV⁻¹
Energy (keV)

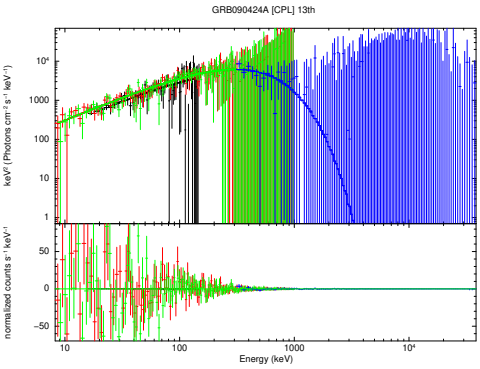
GRB090424A [CPL] 13th
keV² (Photons cm⁻² s⁻¹ keV⁻¹)
normalized counts s⁻¹ keV⁻¹
Energy (keV)

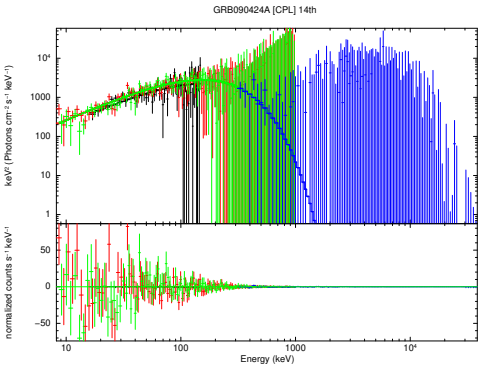
GRB090424A [CPL] 14th
keV² (Photons cm⁻² s⁻¹ keV⁻¹)
normalized counts s⁻¹ keV⁻¹
Energy (keV)

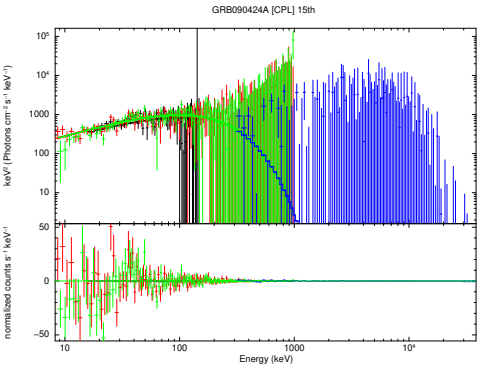
GRB090424A [CPL] 15th
keV² (Photons cm⁻² s⁻¹ keV⁻¹)
normalized counts s⁻¹ keV⁻¹
Energy (keV)

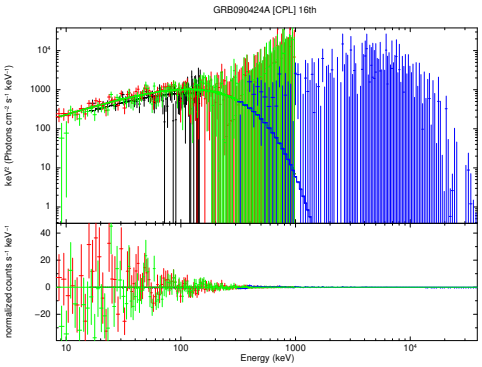
GRB090424A [CPL] 16th
keV² (Photons cm⁻² s⁻¹ keV⁻¹)
normalized counts s⁻¹ keV⁻¹
Energy (keV)

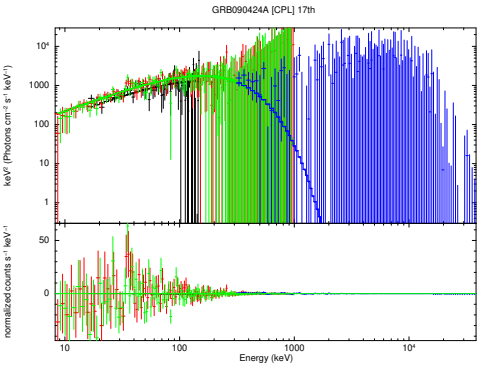
GRB090424A [CPL] 17th
keV² (Photons cm⁻² s⁻¹ keV⁻¹)
normalized counts s⁻¹ keV⁻¹
Energy (keV)

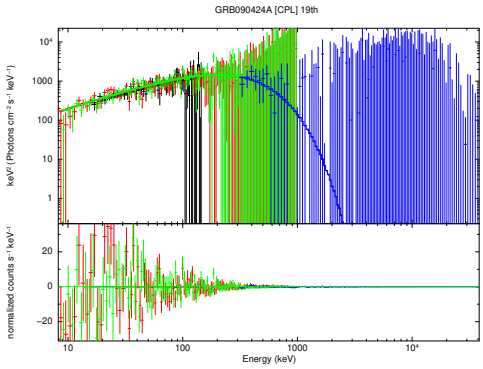
GRB090424A [CPL] 19th
keV² (Photons cm⁻² s⁻¹ keV⁻¹)
normalized counts s⁻¹ keV⁻¹
Energy (keV)

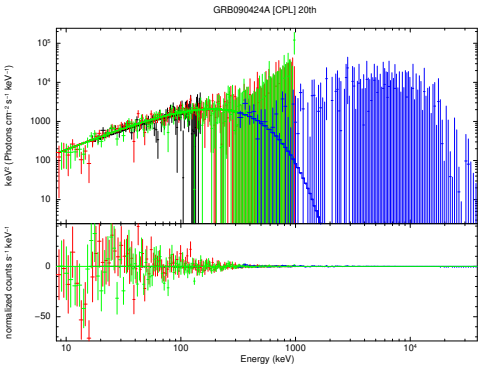
GRB090424A [CPL] 20th
keV² (Photons cm⁻² s⁻¹ keV⁻¹)
normalized counts s⁻¹ keV⁻¹
Energy (keV)

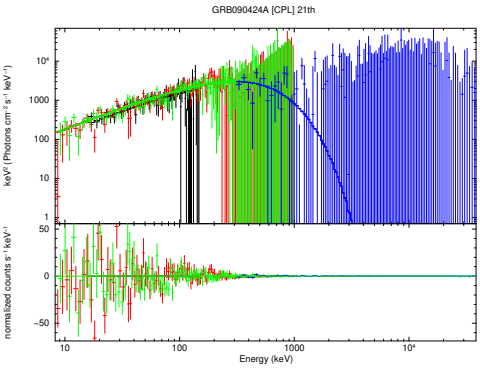
GRB090424A [CPL] 21th
keV² (Photons cm⁻² s⁻¹ keV⁻¹)
normalized counts s⁻¹ keV⁻¹
Energy (keV)

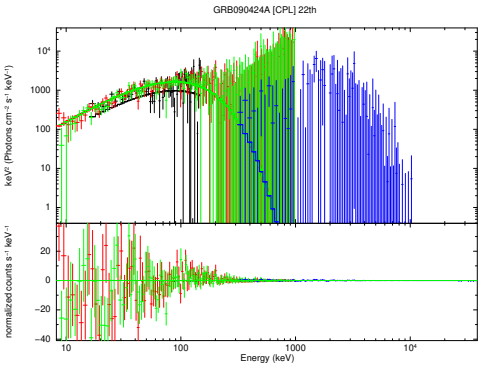
GRB090424A [CPL] 22th
keV² (Photons cm⁻² s⁻¹ keV⁻¹)
normalized counts s⁻¹ keV⁻¹
Energy (keV)

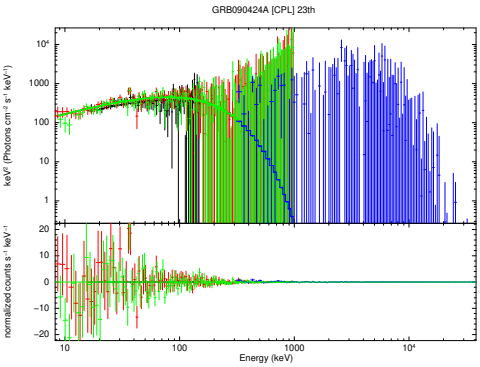
GRB090424A [CPL] 23th
keV² (Photons cm⁻² s⁻¹ keV⁻¹)
normalized counts s⁻¹ keV⁻¹
Energy (keV)

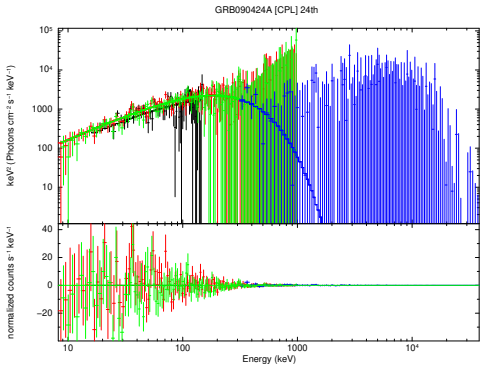
GRB090424A [CPL] 24th
keV² (Photons cm⁻² s⁻¹ keV⁻¹)
normalized counts s⁻¹ keV⁻¹
Energy (keV)

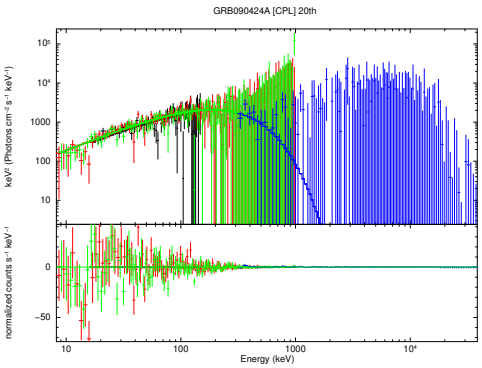
GRB090424A [CPL] 20th
keV² (Photons cm⁻² s⁻¹ keV⁻¹)
normalized counts s⁻¹ keV⁻¹
Energy (keV)

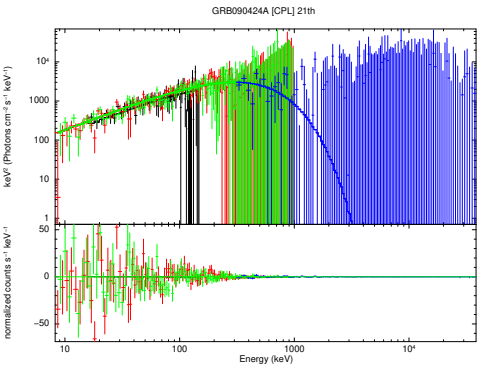
GRB090424A [CPL] 21th
keV² (Photons cm⁻² s⁻¹ keV⁻¹)
normalized counts s⁻¹ keV⁻¹
Energy (keV)

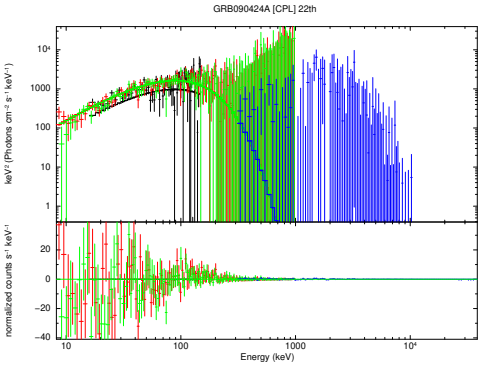
GRB090424A [CPL] 22th
keV² (Photons cm⁻² s⁻¹ keV⁻¹)
normalized counts s⁻¹ keV⁻¹
Energy (keV)

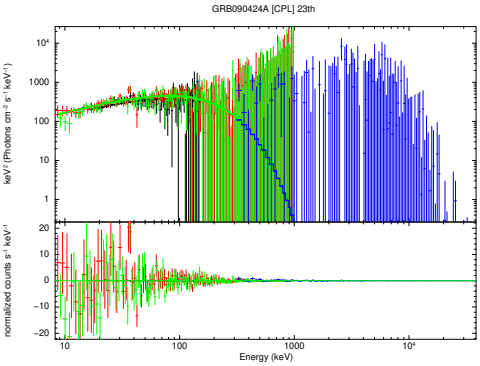
GRB090424A [CPL] 23th
keV² (Photons cm⁻² s⁻¹ keV⁻¹)
normalized counts s⁻¹ keV⁻¹
Energy (keV)

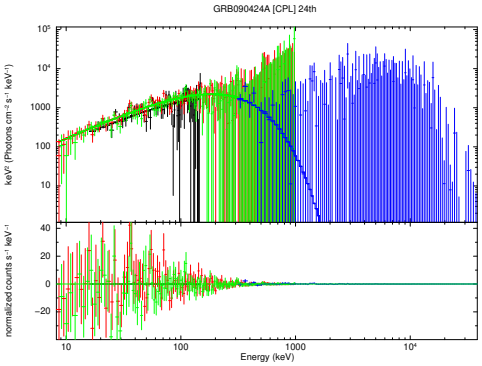
GRB090424A [CPL] 24th
keV² (Photons cm⁻² s⁻¹ keV⁻¹)
normalized counts s⁻¹ keV⁻¹
Energy (keV)

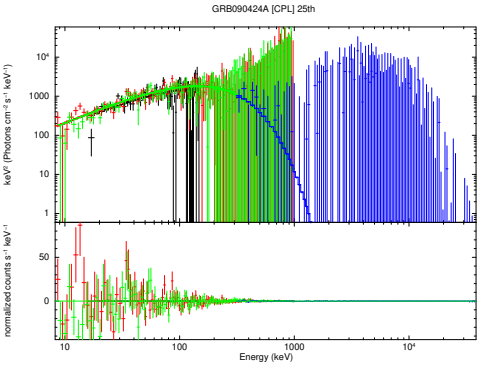
GRB090424A [CPL] 25th
keV² (Photons cm⁻² s⁻¹ keV⁻¹)
normalized counts s⁻¹ keV⁻¹
Energy (keV)

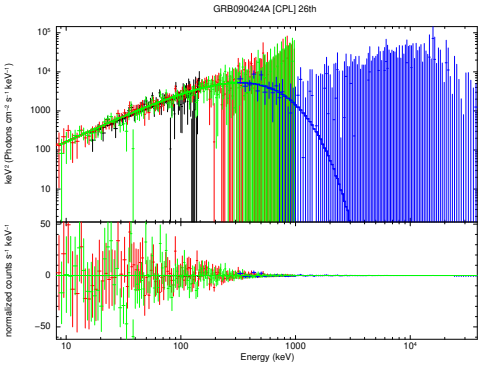
GRB090424A [CPL] 26th
keV² (Photons cm⁻² s⁻¹ keV⁻¹)
normalized counts s⁻¹ keV⁻¹
Energy (keV)

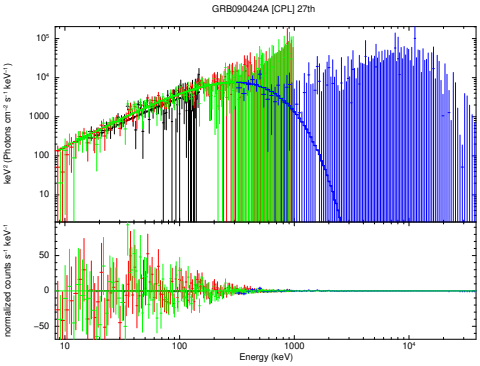
GRB090424A [CPL] 27th
keV² (Photons cm⁻² s⁻¹ keV⁻¹)
normalized counts s⁻¹ keV⁻¹
Energy (keV)

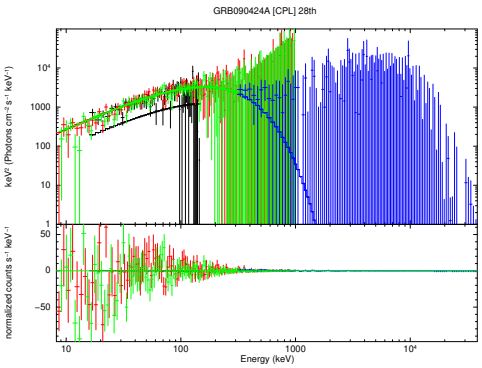
GRB090424A [CPL] 28th
keV² (Photons cm⁻² s⁻¹ keV⁻¹)
normalized counts s⁻¹ keV⁻¹
Energy (keV)

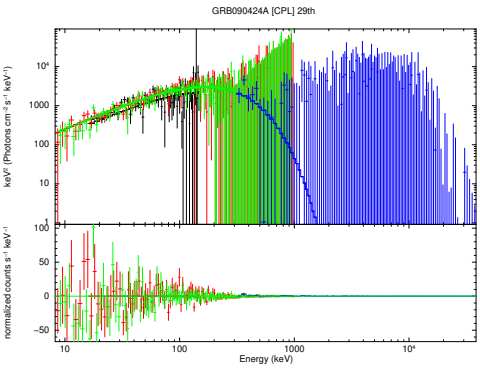
GRB090424A [CPL] 29th
keV² (Photons cm⁻² s⁻¹ keV⁻¹)
normalized counts s⁻¹ keV⁻¹
Energy (keV)

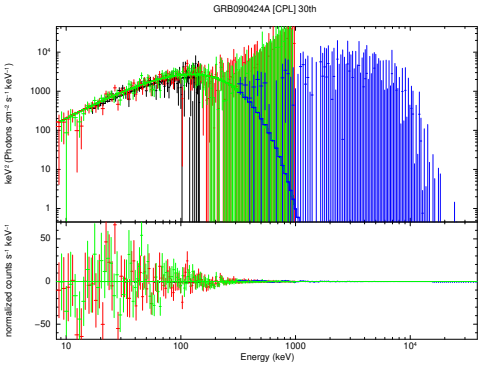
GRB090424A [CPL] 30th
keV² (Photons cm⁻² s⁻¹ keV⁻¹)
normalized counts s⁻¹ keV⁻¹
Energy (keV)

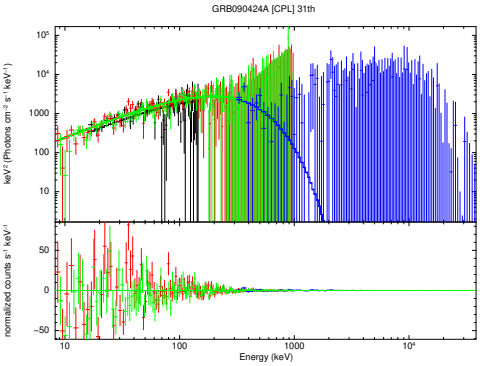
GRB090424A [CPL] 31th
keV² (Photons cm⁻² s⁻¹ keV⁻¹)
normalized counts s⁻¹ keV⁻¹
Energy (keV)

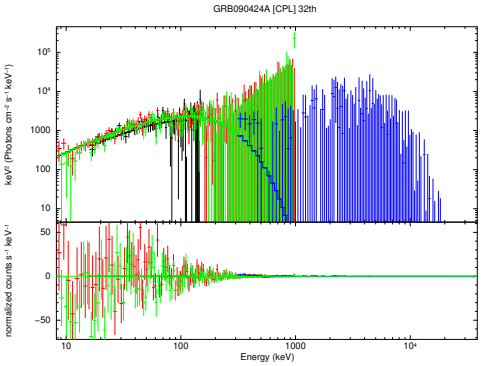
GRB090424A [CPL] 32th
keV² (Photons cm⁻² s⁻¹ keV⁻¹)
normalized counts s⁻¹ keV⁻¹
Energy (keV)

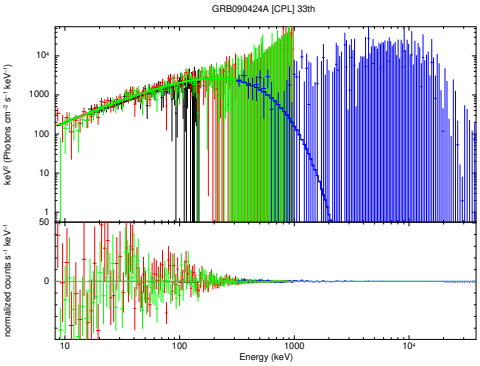
GRB090424A [CPL] 33th
keV² (Photons cm⁻² s⁻¹ keV⁻¹)
normalized counts s⁻¹ keV⁻¹
Energy (keV)

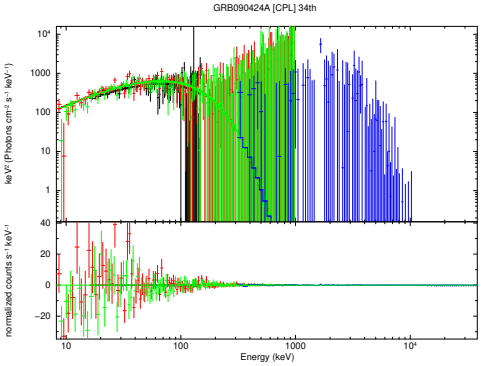
GRB090424A [CPL] 34th
keV² (Photons cm⁻² s⁻¹ keV⁻¹)
normalized counts s⁻¹ keV⁻¹
Energy (keV)

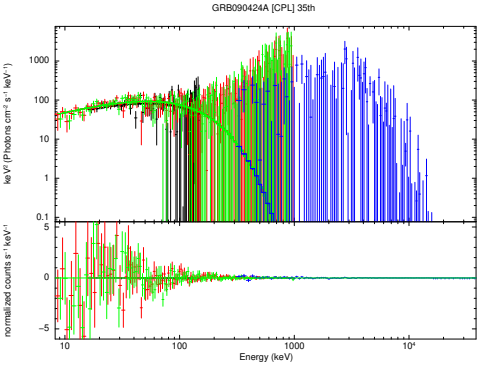
GRB090424A [CPL] 35th
keV² (Photons cm⁻² s⁻¹ keV⁻¹)
normalized counts s⁻¹ keV⁻¹
Energy (keV)

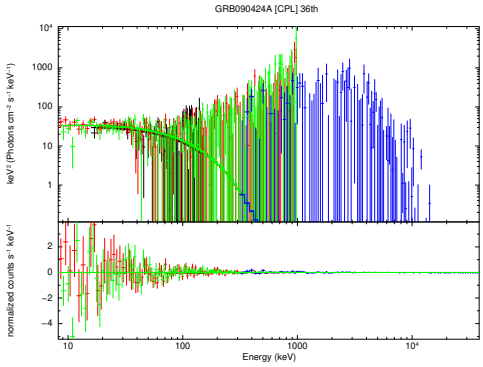
GRB090424A [CPL] 36th
keV² (Photons cm⁻² s⁻¹ keV⁻¹)
normalized counts s⁻¹ keV⁻¹
Energy (keV)

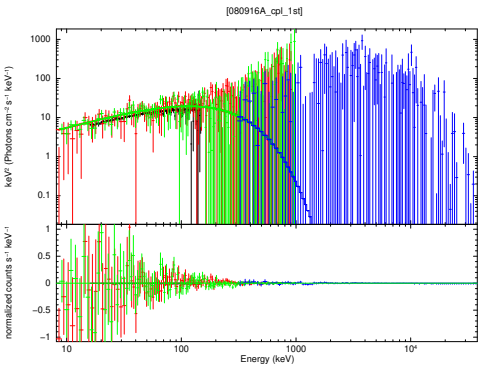
[080916A_cpl_1st]
keV² (Photons cm⁻² s⁻¹ keV⁻¹)
normalized counts s⁻¹ keV⁻¹
Energy (keV)

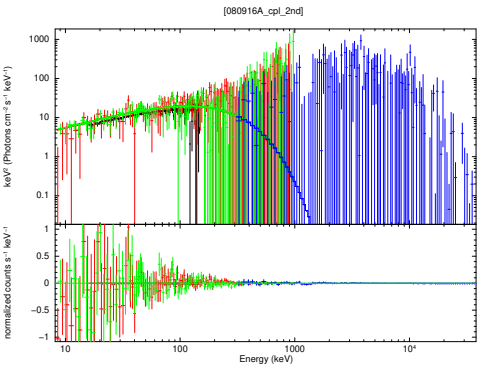
[080916A_cpl_2nd]
keV² (Photons cm⁻² s⁻¹ keV⁻¹)
normalized counts s⁻¹ keV⁻¹
Energy (keV)

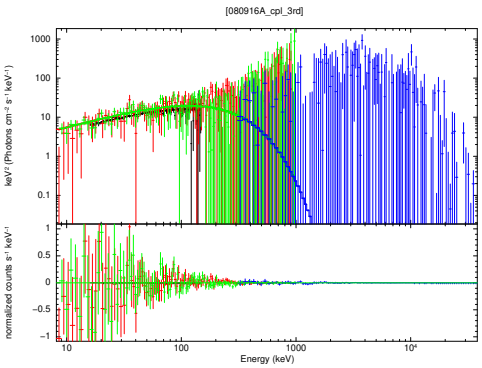
[080916A_cpl_3rd]
keV² (Photons cm⁻² s⁻¹ keV⁻¹)
normalized counts s⁻¹ keV⁻¹
Energy (keV)

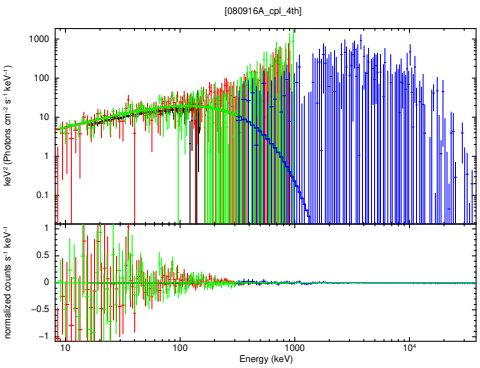
[080916A_cpl_4th]
keV² (Photons cm⁻² s⁻¹ keV⁻¹)
normalized counts s⁻¹ keV⁻¹
Energy (keV)

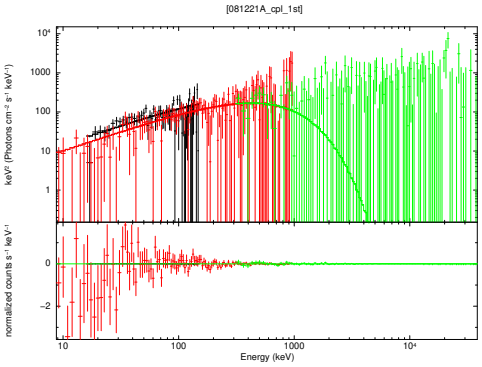
[081221A_cpl_1st]
keV² (Photons cm⁻² s⁻¹ keV⁻¹)
normalized counts s⁻¹ keV⁻¹
Energy (keV)

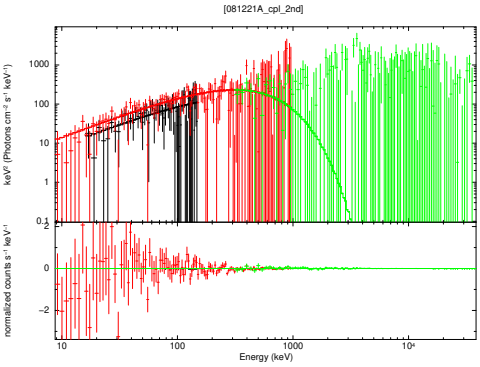
[081221A_cpl_2nd]
keV² (Photons cm⁻² s⁻¹ keV⁻¹)
normalized counts s⁻¹ keV⁻¹
Energy (keV)

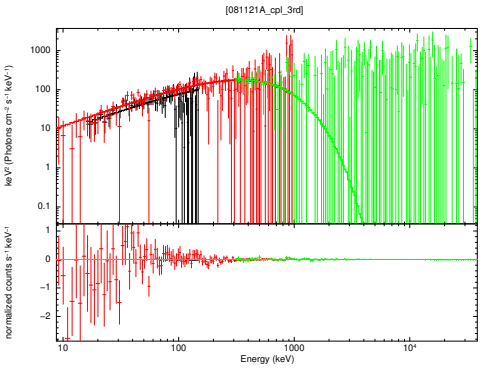
[081121A_cpl_3rd]
keV² (Photons cm⁻² s⁻¹ keV⁻¹)
normalized counts s⁻¹ keV⁻¹
Energy (keV)

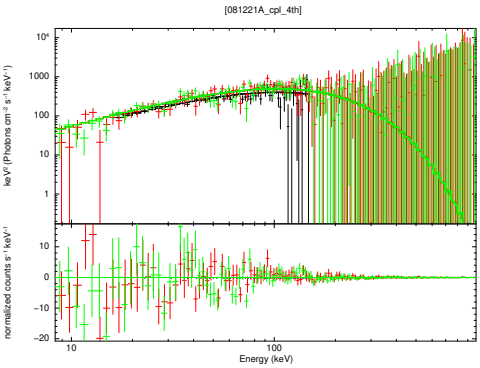
[081221A_cpl_4th]
keV² (Photons cm⁻² s⁻¹ keV⁻¹)
normalized counts s⁻¹ keV⁻¹
Energy (keV)

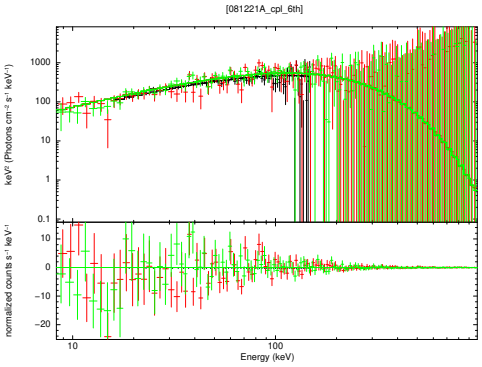
[081221A_cpl_6th]
keV² (Photons cm⁻² s⁻¹ keV⁻¹)
normalized counts s⁻¹ keV⁻¹
Energy (keV)

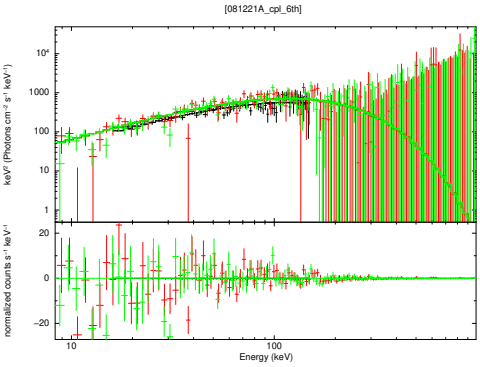
[081221A_cpl_6th]
keV² (Photons cm⁻² s⁻¹ keV⁻¹)
normalized counts s⁻¹ keV⁻¹
Energy (keV)

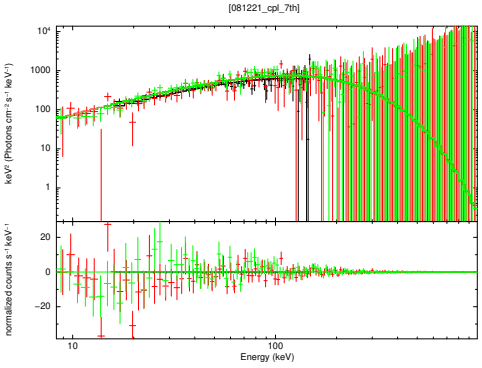
[081221_cpl_7th]
keV² (Photons cm⁻² s⁻¹ keV⁻¹)
normalized counts s⁻¹ keV⁻¹
Energy (keV)

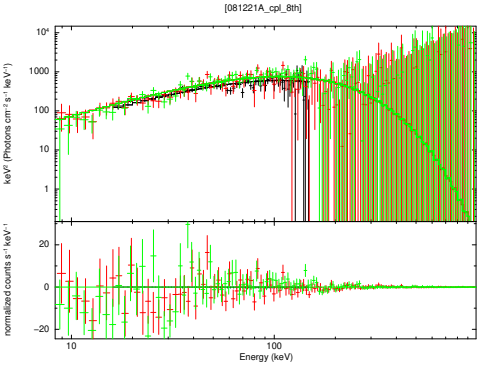
[081221A_cpl_8th]
keV² (Photons cm⁻² s⁻¹ keV⁻¹)
normalized counts s⁻¹ keV⁻¹
Energy (keV)

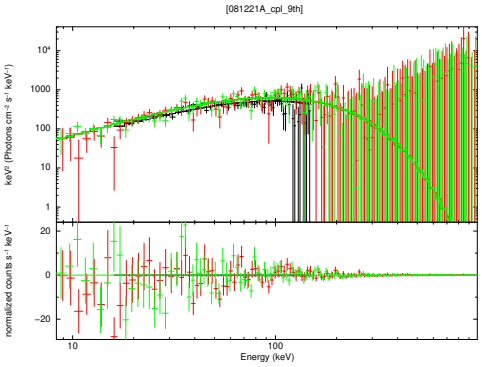
[081221A_cpl_9th]
keV² (Photons cm⁻² s⁻¹ keV⁻¹)
normalized counts s⁻¹ keV⁻¹
Energy (keV)

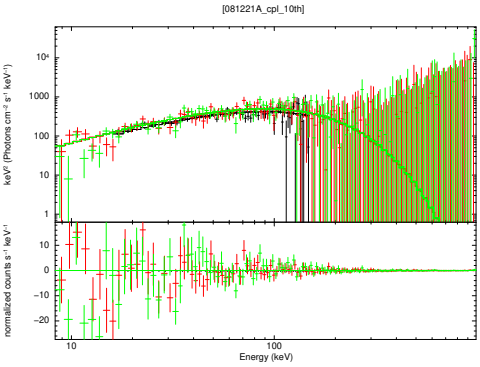
[081221A_cpl_10th]
keV² (Photons cm⁻² s⁻¹ keV⁻¹)
normalized counts s⁻¹ keV⁻¹
Energy (keV)

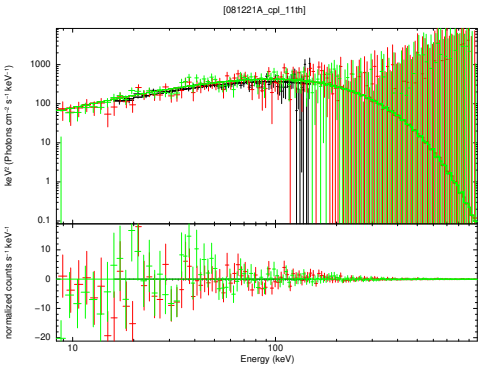
[081221A_cpl_11th]
keV² (Photons cm⁻² s⁻¹ keV⁻¹)
normalized counts s⁻¹ keV⁻¹
Energy (keV)

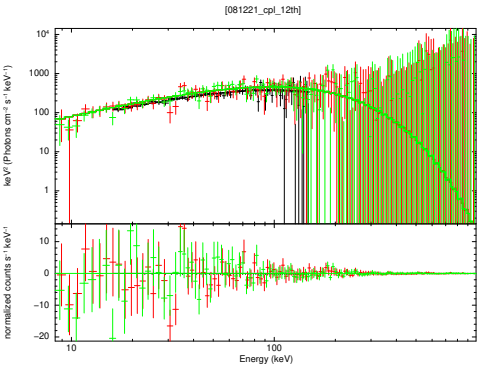
[081221_cpl_12th]
keV² (Photons cm⁻² s⁻¹ keV⁻¹)
normalized counts s⁻¹ keV⁻¹
Energy (keV)

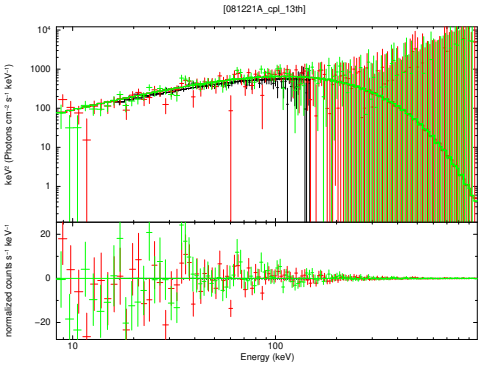
[081221A_cpl_13th]
keV² (Photons cm⁻² s⁻¹ keV⁻¹)
normalized counts s⁻¹ keV⁻¹
Energy (keV)

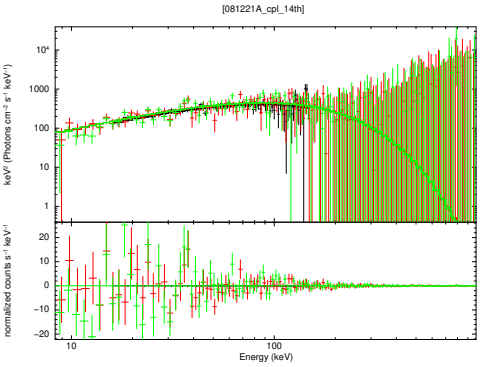
[081221A_cpl_14th]
keV² (Photons cm⁻² s⁻¹ keV⁻¹)
normalized counts s⁻¹ keV⁻¹
Energy (keV)

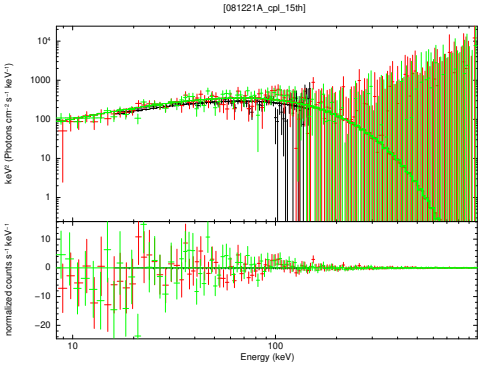
[081221A_cpl_15th]
keV² (Photons cm⁻² s⁻¹ keV⁻¹)
normalized counts s⁻¹ keV⁻¹
Energy (keV)

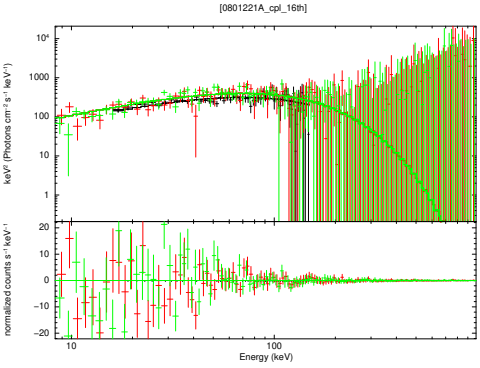
[0801221A_cpl_16th]
keV² (Photons cm⁻² s⁻¹ keV⁻¹)
normalized counts s⁻¹ keV⁻¹
Energy (keV)

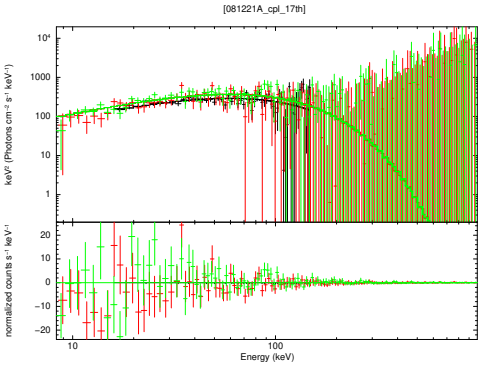
[081221A_cpl_17th]
keV² (Photons cm⁻² s⁻¹ keV⁻¹)
normalized counts s⁻¹ keV⁻¹
Energy (keV)

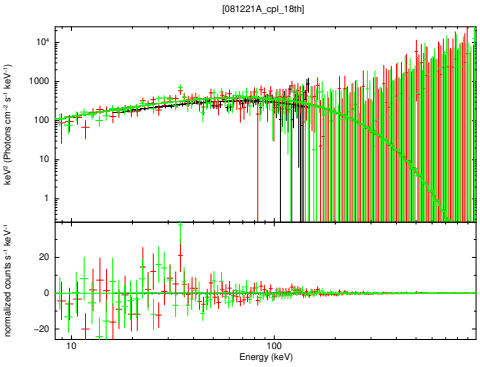
[081221A_cpl_18th]
keV² (Photons cm⁻² s⁻¹ keV⁻¹)
normalized counts s⁻¹ keV⁻¹
Energy (keV)

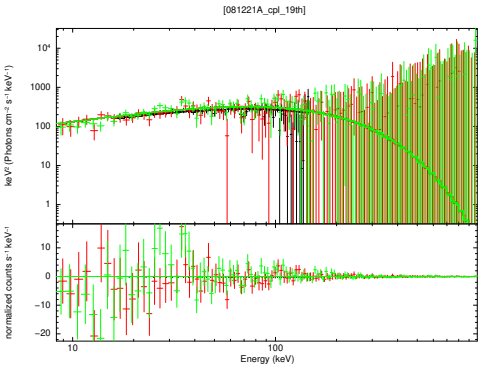
[081221A_cpl_19th]
keV² (Photons cm⁻² s⁻¹ keV⁻¹)
normalized counts s⁻¹ keV⁻¹
Energy (keV)

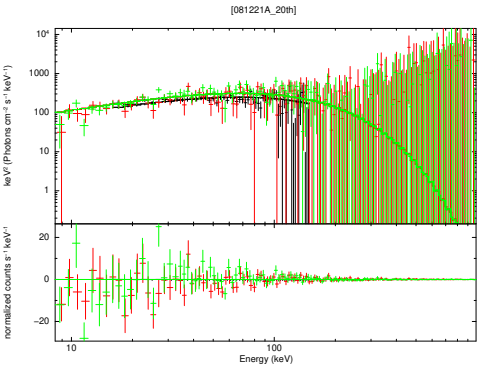
[081221A_cpl_20th]
keV² (Photons cm⁻² s⁻¹ keV⁻¹)
normalized counts s⁻¹ keV⁻¹
Energy (keV)

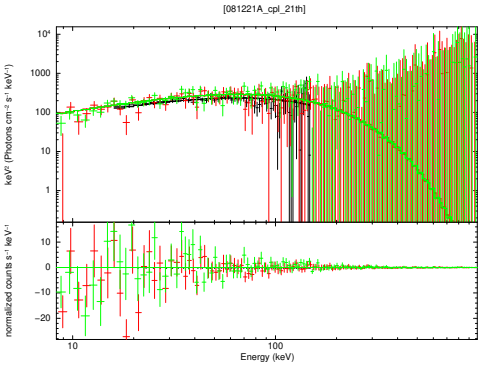
[081221A_cpl_21th]
keV² (Photons cm⁻² s⁻¹ keV⁻¹)
normalized counts s⁻¹ keV⁻¹
Energy (keV)

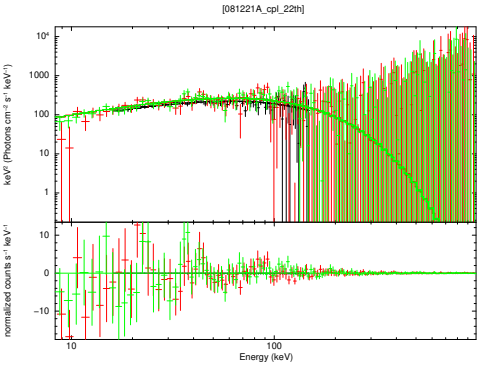
[081221A_cpl_22th]
keV² (Photons cm⁻² s⁻¹ keV⁻¹)
normalized counts s⁻¹ keV⁻¹
Energy (keV)

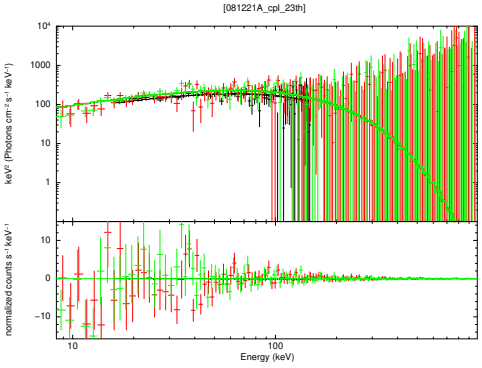
[081221A_cpl_23th]
keV² (Photons cm⁻² s⁻¹ keV⁻¹)
normalized counts s⁻¹ keV⁻¹
Energy (keV)

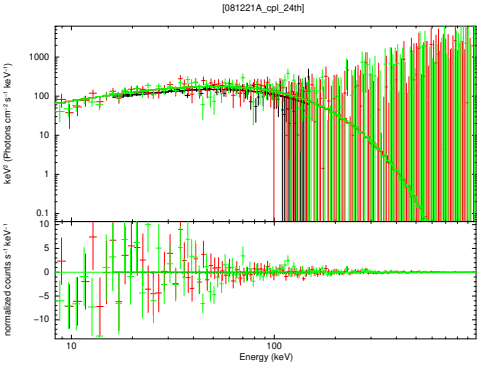
[081221A_cpl_24th]
keV² (Photons cm⁻² s⁻¹ keV⁻¹)
normalized counts s⁻¹ keV⁻¹
Energy (keV)

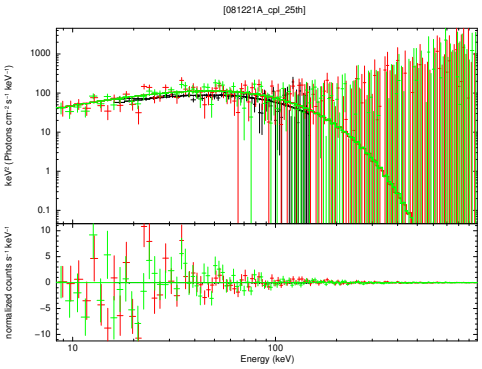
[081221A_cpl_25th]
keV² (Photons cm⁻² s⁻¹ keV⁻¹)
normalized counts s⁻¹ keV⁻¹
Energy (keV)

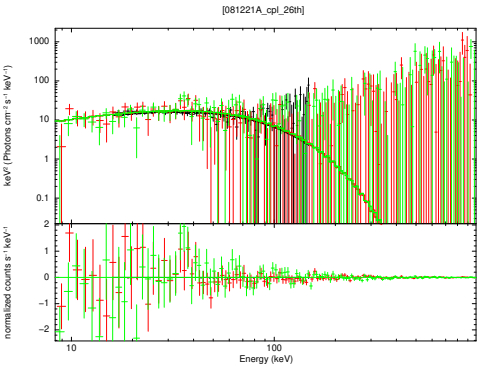
[081221A_cpl_26th]
keV² (Photons cm⁻² s⁻¹ keV⁻¹)
normalized counts s⁻¹ keV⁻¹
Energy (keV)

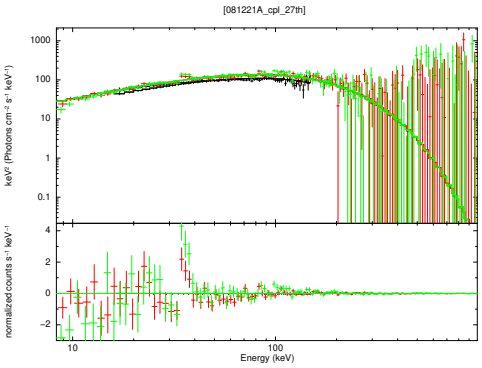
[081221A_cpl_27th]
keV² (Photons cm⁻² s⁻¹ keV⁻¹)
normalized counts s⁻¹ keV⁻¹
Energy (keV)

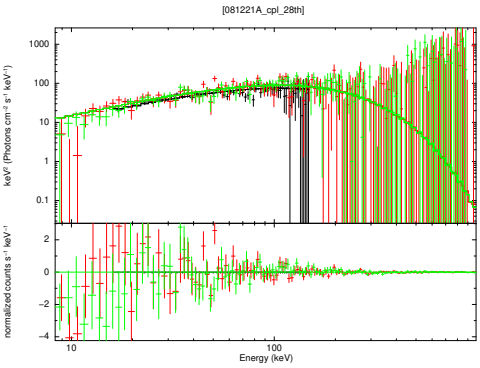
[081221A_cpl_28th]
keV² (Photons cm⁻² s⁻¹ keV⁻¹)
normalized counts s⁻¹ keV⁻¹
Energy (keV)

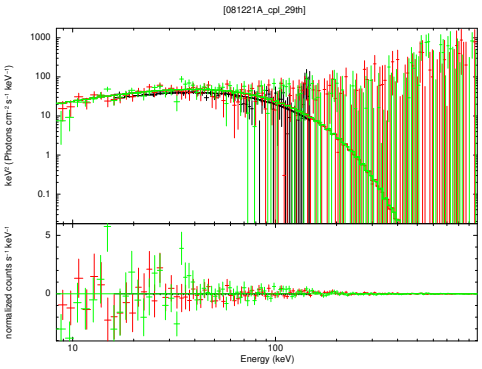
[081221A_cpl_29th]
keV² (Photons cm⁻² s⁻¹ keV⁻¹)
normalized counts s⁻¹ keV⁻¹
Energy (keV)

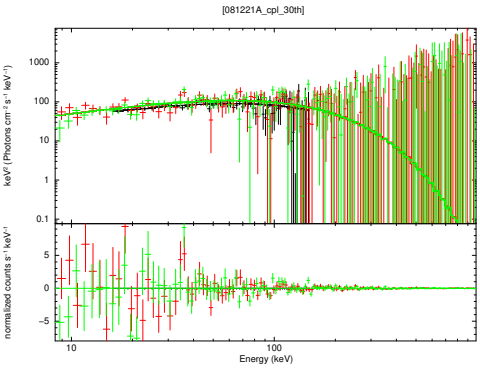
[081221A_cpl_30th]
keV² (Photons cm⁻² s⁻¹ keV⁻¹)
normalized counts s⁻¹ keV⁻¹
Energy (keV)

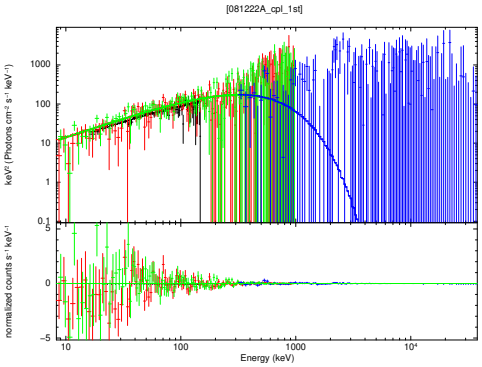
[081222A_cpl_1st]
keV² (Photons cm⁻² s⁻¹ keV⁻¹)
normalized counts s⁻¹ keV⁻¹
Energy (keV)

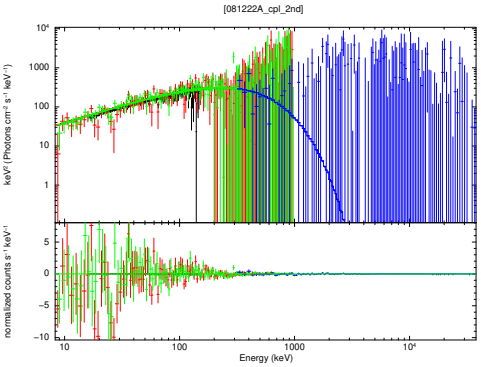
[081222A_cpl_2nd]
keV² (Photons cm⁻² s⁻¹ keV⁻¹)
normalized counts s⁻¹ keV⁻¹
Energy (keV)

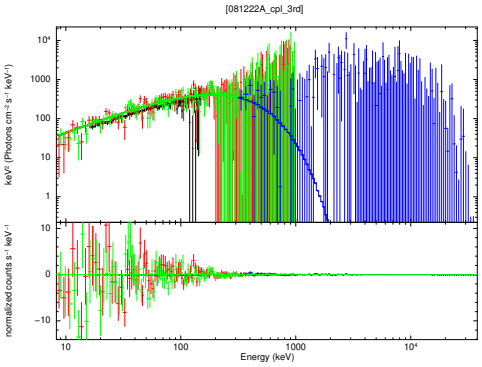
[081222A_cpl_3rd]
keV² (Photons cm⁻² s⁻¹ keV⁻¹)
normalized counts s⁻¹ keV⁻¹
Energy (keV)

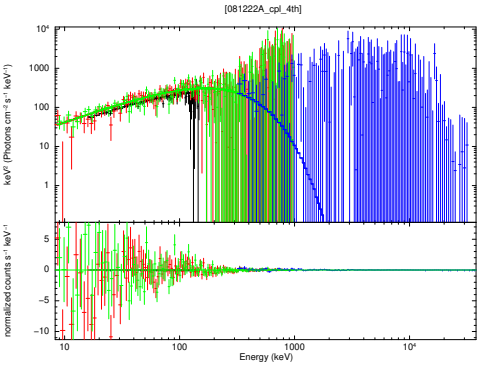
[081222A_cpl_4th]
keV² (Photons cm⁻² s⁻¹ keV⁻¹)
normalized counts s⁻¹ keV⁻¹
Energy (keV)

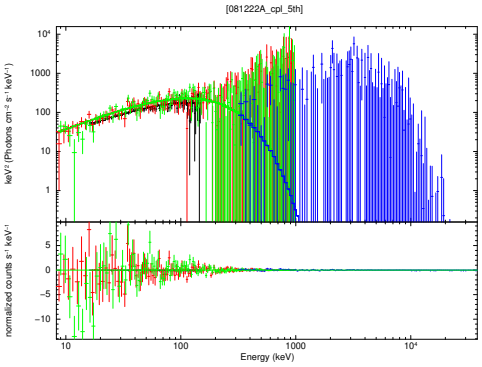
[081222A_cpl_5th]
keV² (Photons cm⁻² s⁻¹ keV⁻¹)
normalized counts s⁻¹ keV⁻¹
Energy (keV)

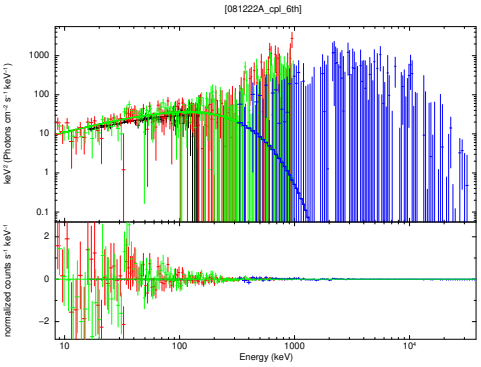
[081222A_cpl_6th]
keV² (Photons cm⁻² s⁻¹ keV⁻¹)
normalized counts s⁻¹ keV⁻¹
Energy (keV)

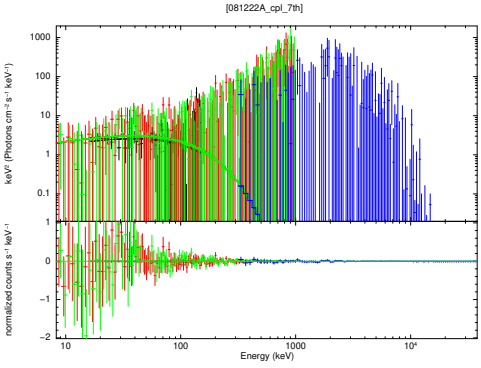
[081222A_cpl_7th]
keV² (Photons cm⁻² s⁻¹ keV⁻¹)
normalized counts s⁻¹ keV⁻¹
Energy (keV)

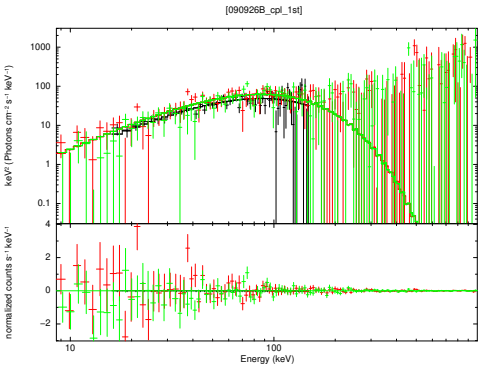
[090926B_cpl_1st]
keV² (Photons cm⁻² s⁻¹ keV⁻¹)
normalized counts s⁻¹ keV⁻¹
Energy (keV)

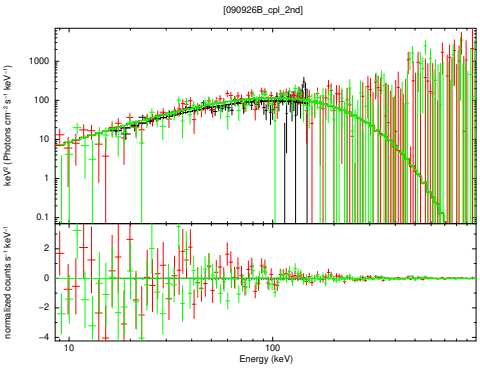
[090926B_cpl_2nd]
keV² (Photons cm⁻² s⁻¹ keV⁻¹)
normalized counts s⁻¹ keV⁻¹
Energy (keV)

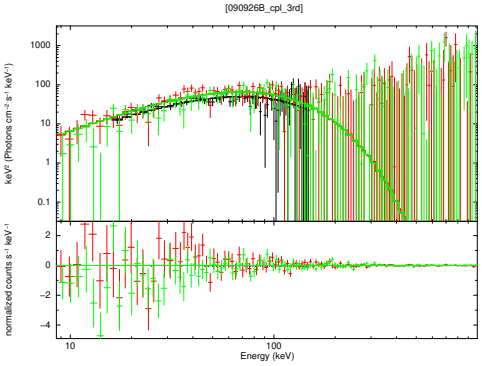
[090926B_cpl_3rd]
keV² (Photons cm⁻² s⁻¹ keV⁻¹)
normalized counts s⁻¹ keV⁻¹
Energy (keV)

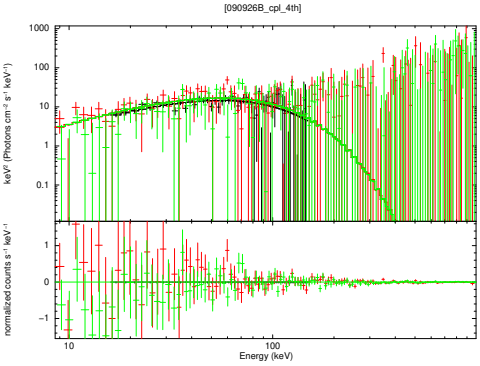
[090926B_cpl_4th]
keV² (Photons cm⁻² s⁻¹ keV⁻¹)
normalized counts s⁻¹ keV⁻¹
Energy (keV)

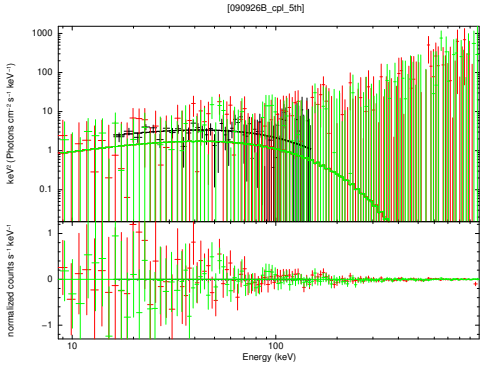
[090926B_cpl_5th]
keV² (Photons cm⁻² s⁻¹ keV⁻¹)
normalized counts s⁻¹ keV⁻¹
Energy (keV)

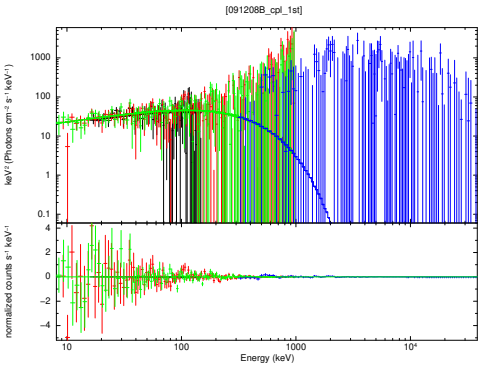
[091208B_cpl_1st]
keV² (Photons cm⁻² s⁻¹ keV⁻¹)
normalized counts s⁻¹ keV⁻¹
Energy (keV)

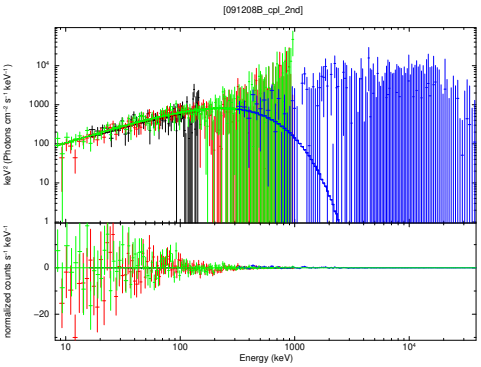
[091208B_cpl_2nd]
keV² (Photons cm⁻² s⁻¹ keV⁻¹)
normalized counts s⁻¹ keV⁻¹
Energy (keV)

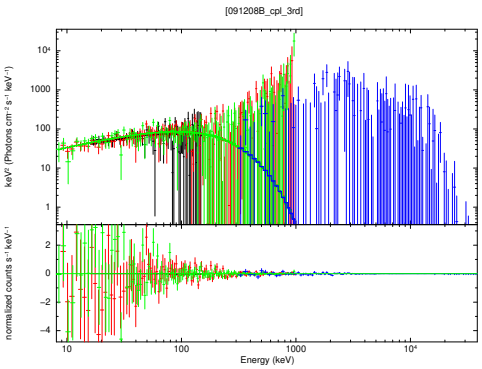
[091208B_cpl_3rd]
keV² (Photons cm⁻² s⁻¹ keV⁻¹)
normalized counts s⁻¹ keV⁻¹
Energy (keV)

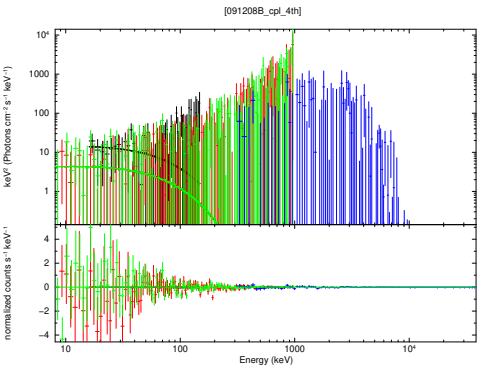
[091208B_cpl_4th]
keV² (Photons cm⁻² s⁻¹ keV⁻¹)
normalized counts s⁻¹ keV⁻¹
Energy (keV)

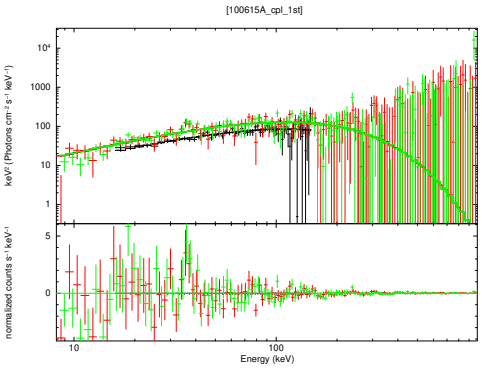
[100615A_cpl_1st]
keV² (Photons cm⁻² s⁻¹ keV⁻¹)
normalized counts s⁻¹ keV⁻¹
Energy (keV)

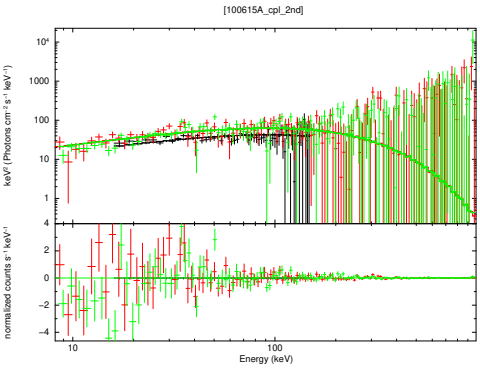
[100615A_cpl_2nd]
keV² (Photons cm⁻² s⁻¹ keV⁻¹)
normalized counts s⁻¹ keV⁻¹
Energy (keV)

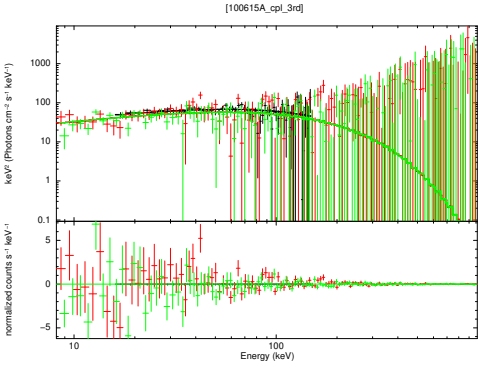
[100615A_cpl_3rd]
keV² (Photons cm⁻² s⁻¹ keV⁻¹)
normalized counts s⁻¹ keV⁻¹
Energy (keV)

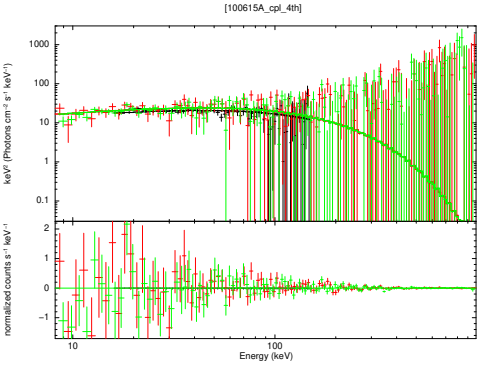
[100615A_cpl_4th]
keV² (Photons cm⁻² s⁻¹ keV⁻¹)
normalized counts s⁻¹ keV⁻¹
Energy (keV)

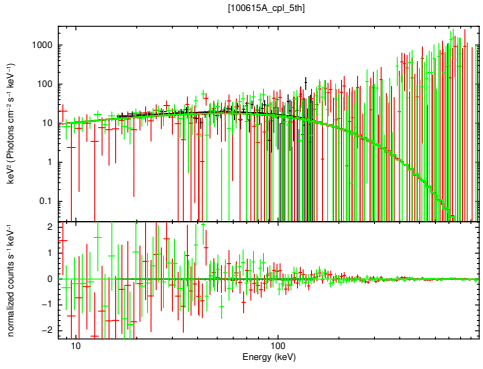
[100615A_cpl_5th]
keV² (Photons cm⁻² s⁻¹ keV⁻¹)
normalized counts s⁻¹ keV⁻¹
Energy (keV)

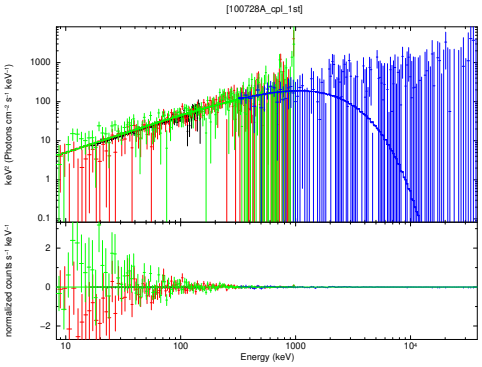
[100728A_cpl_1st]
keV² (Photons cm⁻² s⁻¹ keV⁻¹)
normalized counts s⁻¹ keV⁻¹
Energy (keV)

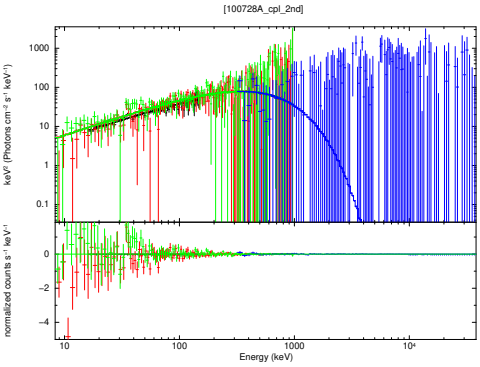
[100728A_cpl_2nd]
keV² (Photons cm⁻² s⁻¹ keV⁻¹)
normalized counts s⁻¹ keV⁻¹
Energy (keV)

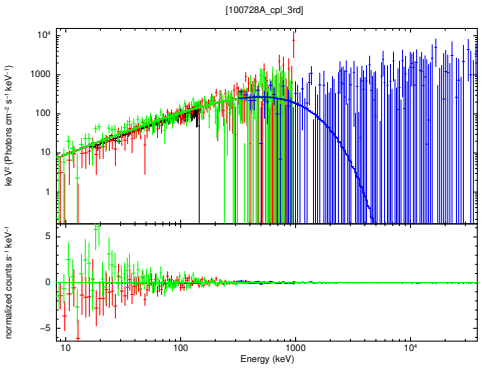
[100728A_cpl_3rd]
keV² (Photons cm⁻² s⁻¹ keV⁻¹)
normalized counts s⁻¹ keV⁻¹
Energy (keV)

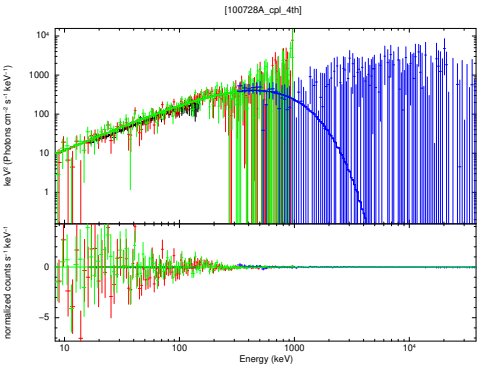
[100728A_cpl_4th]
keV² (Photons cm⁻² s⁻¹ keV⁻¹)
normalized counts s⁻¹ keV⁻¹
Energy (keV)

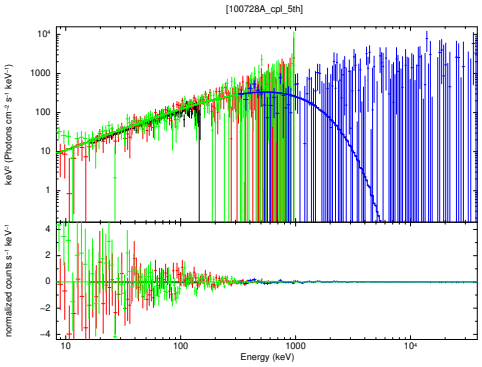
[100728A_cpl_5th]
keV² (Photons cm⁻² s⁻¹ keV⁻¹)
normalized counts s⁻¹ keV⁻¹
Energy (keV)

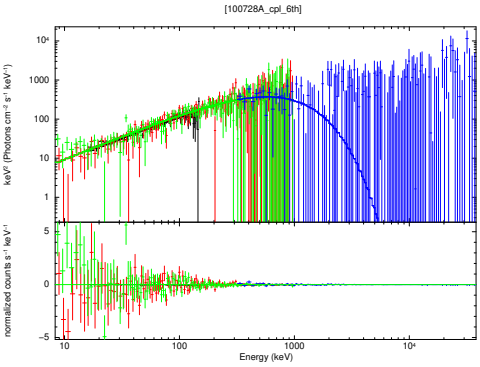
[100728A_cpl_6th]
keV² (Photons cm⁻² s⁻¹ keV⁻¹)
normalized counts s⁻¹ keV⁻¹
Energy (keV)

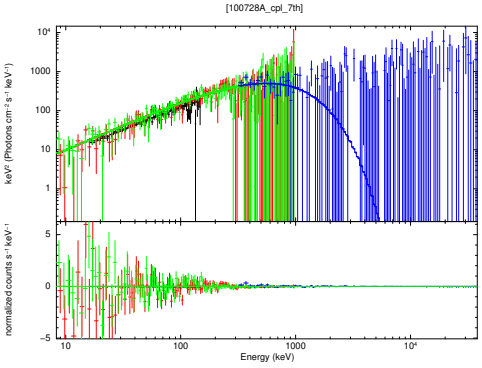
[100728A_cpl_7th]
keV² (Photons cm⁻² s⁻¹ keV⁻¹)
normalized counts s⁻¹ keV⁻¹
Energy (keV)

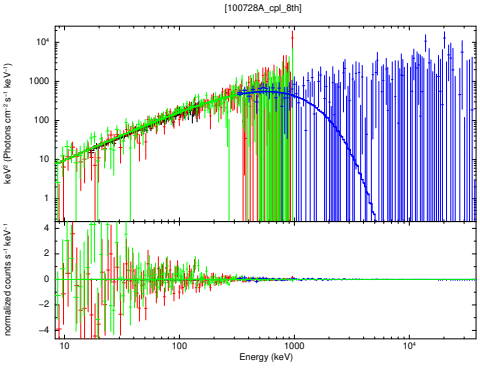
[100728A_cpl_8th]
keV² (Photons cm⁻² s⁻¹ keV⁻¹)
normalized counts s⁻¹ keV⁻¹
Energy (keV)

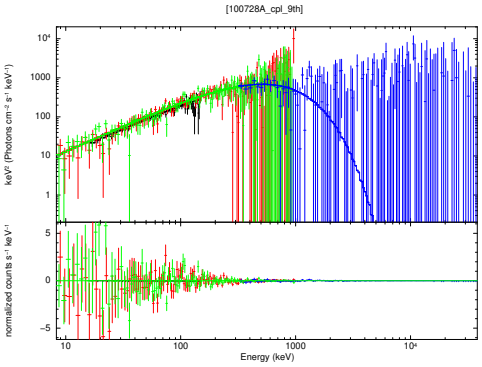
[100728A_cpl_9th]
keV² (Photons cm⁻² s⁻¹ keV⁻¹)
normalized counts s⁻¹ keV⁻¹
Energy (keV)

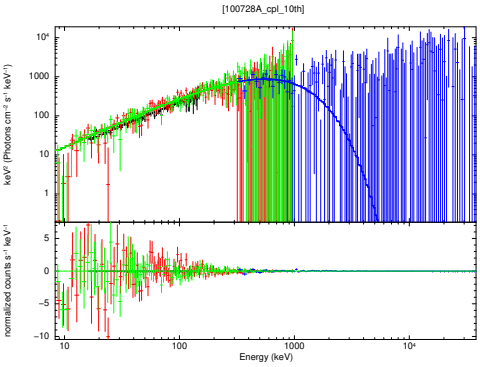
[100728A_cpl_10th]
keV² (Photons cm⁻² s⁻¹ keV⁻¹)
normalized counts s⁻¹ keV⁻¹
Energy (keV)

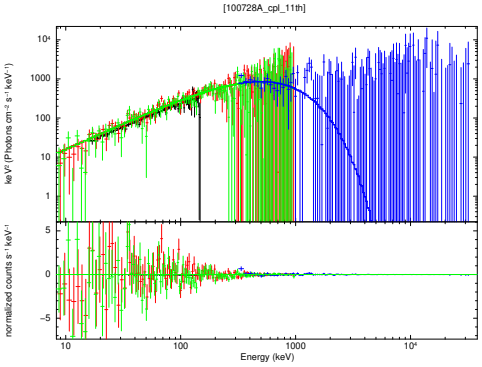
[100728A_cpl_11th]
keV² (Photons cm⁻² s⁻¹ keV⁻¹)
normalized counts s⁻¹ keV⁻¹
Energy (keV)

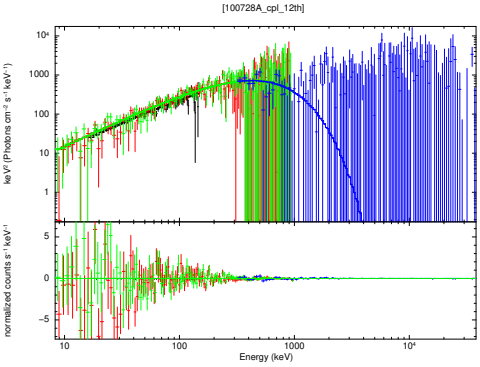
[100728A_cpl_12th]
keV² (Photons cm⁻² s⁻¹ keV⁻¹)
normalized counts s⁻¹ keV⁻¹
Energy (keV)

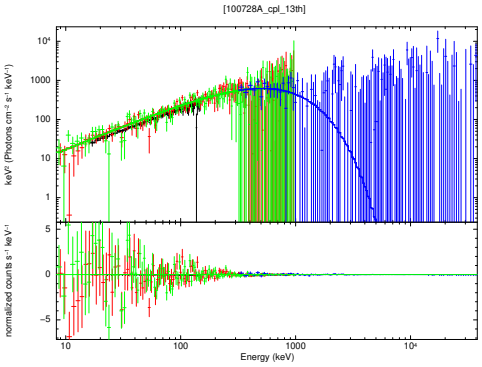
[100728A_cpl_13th]
keV² (Photons cm⁻² s⁻¹ keV⁻¹)
normalized counts s⁻¹ keV⁻¹
Energy (keV)

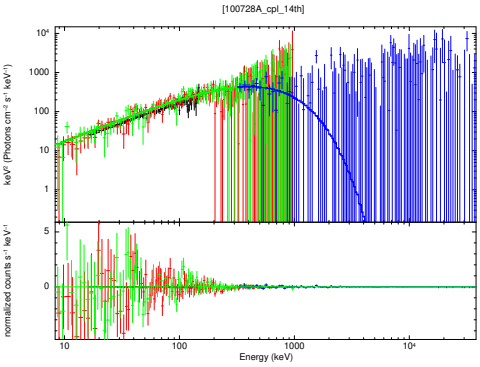
[100728A_cpl_14th]
keV² (Photons cm⁻² s⁻¹ keV⁻¹)
normalized counts s⁻¹ keV⁻¹
Energy (keV)

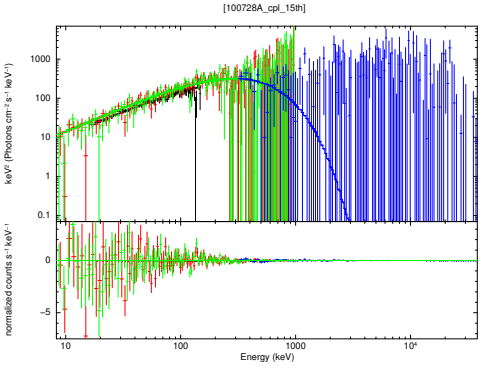
[100728A_cpl_15th]
keV² (Photons cm⁻² s⁻¹ keV⁻¹)
normalized counts s⁻¹ keV⁻¹
Energy (keV)

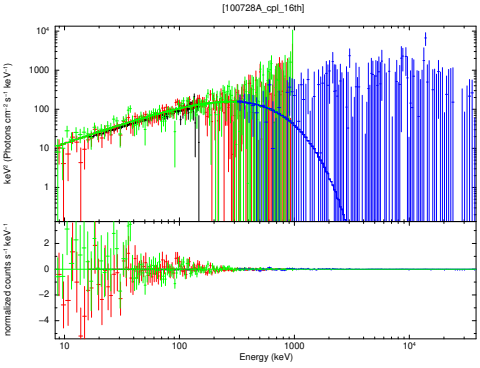
[100728A_cpl_16th]
keV² (Photons cm⁻² s⁻¹ keV⁻¹)
normalized counts s⁻¹ keV⁻¹
Energy (keV)

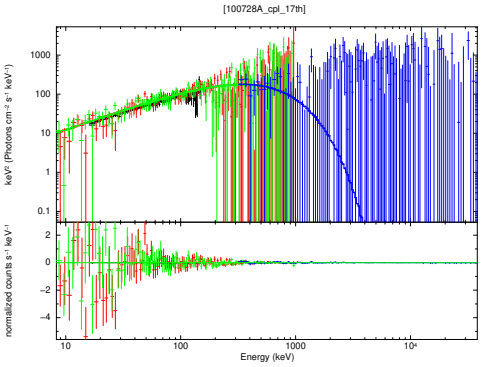
[100728A_cpl_17th]
keV² (Photons cm⁻² s⁻¹ keV⁻¹)
normalized counts s⁻¹ keV⁻¹
Energy (keV)

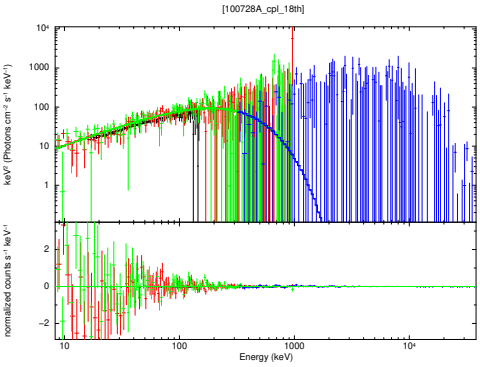
[100728A_cpl_18th]
keV² (Photons cm⁻² s⁻¹ keV⁻¹)
normalized counts s⁻¹ keV⁻¹
Energy (keV)

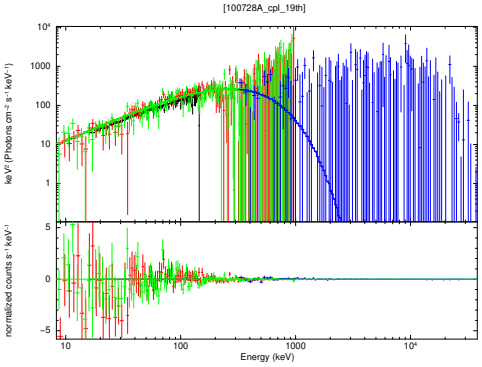
[100728A_cpl_19th]
keV² (Photons cm⁻² s⁻¹ keV⁻¹)
normalized counts s⁻¹ keV⁻¹
Energy (keV)

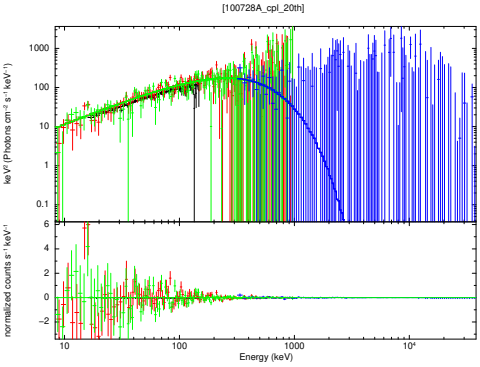
[100728A_cpl_20th]
keV² (Photons cm⁻² s⁻¹ keV⁻¹)
normalized counts s⁻¹ keV⁻¹
Energy (keV)

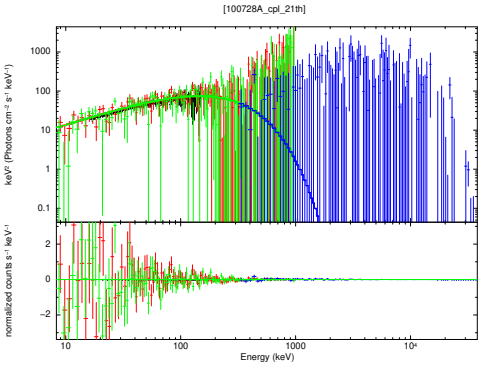
[100728A_cpl_21th]
keV² (Photons cm⁻² s⁻¹ keV⁻¹)
normalized counts s⁻¹ keV⁻¹
Energy (keV)

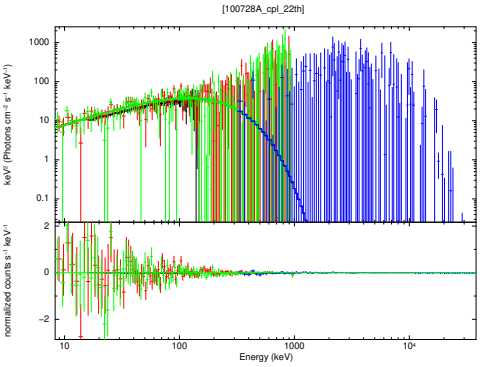
[100728A_cpl_22th]
keV² (Photons cm⁻² s⁻¹ keV⁻¹)
normalized counts s⁻¹ keV⁻¹
Energy (keV)

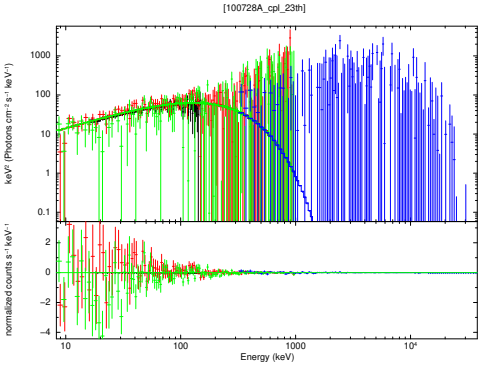
[100728A_cpl_23th]
keV² (Photons cm⁻² s⁻¹ keV⁻¹)
normalized counts s⁻¹ keV⁻¹
Energy (keV)

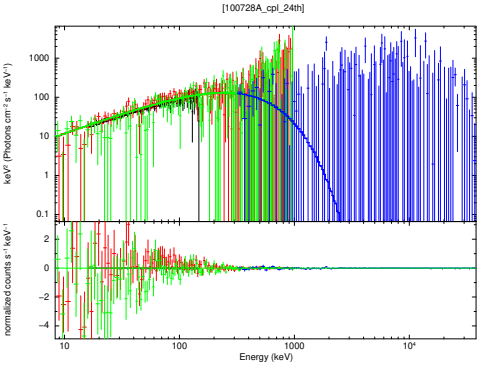
[100728A_cpl_24th]
keV² (Photons cm⁻² s⁻¹ keV⁻¹)
normalized counts s⁻¹ keV⁻¹
Energy (keV)

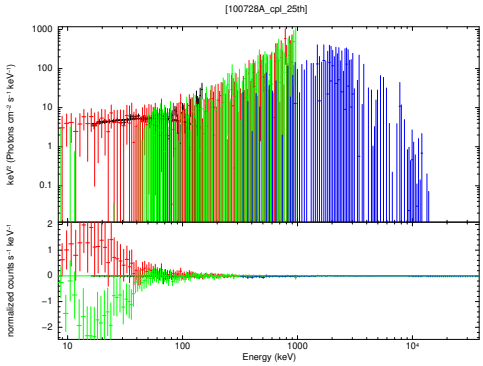
[100728A_cpl_25th]
keV² (Photons cm⁻² s⁻¹ keV⁻¹)
normalized counts s⁻¹ keV⁻¹
Energy (keV)

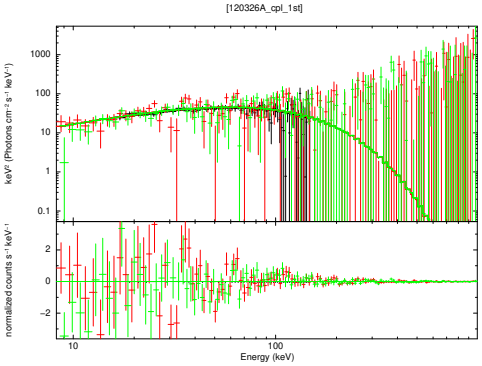
[120326A_cpl_1st]
keV² (Photons cm⁻² s⁻¹ keV⁻¹)
normalized counts s⁻¹ keV⁻¹
Energy (keV)

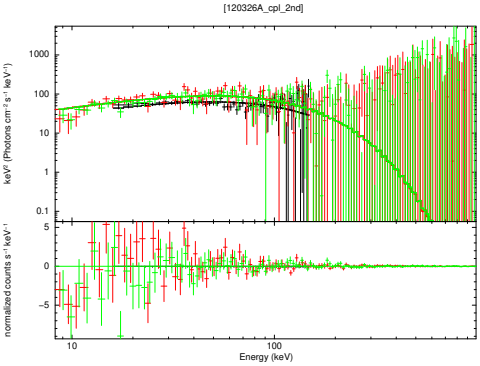
[120326A_cpl_2nd]
keV² (Photons cm⁻² s⁻¹ keV⁻¹)
normalized counts s⁻¹ keV⁻¹
Energy (keV)

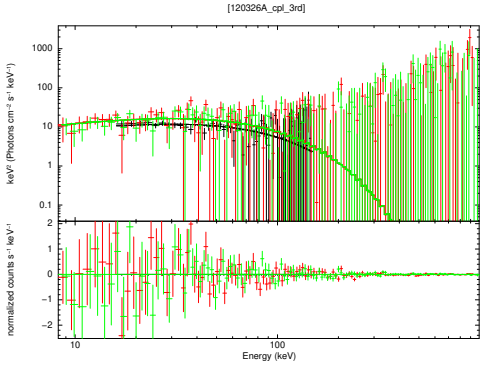
[120326A_cpl_3rd]
keV² (Photons cm⁻² s⁻¹ keV⁻¹)
normalized counts s⁻¹ keV⁻¹
Energy (keV)

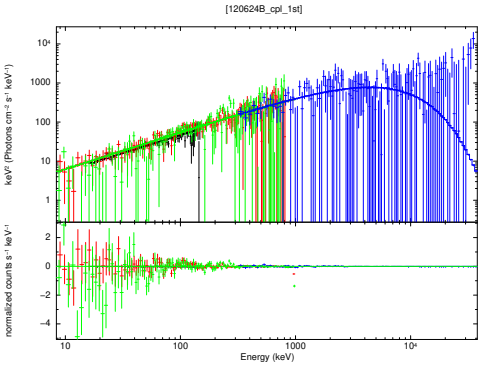
[120624B_cpl_1st]
keV² (Photons cm⁻² s⁻¹ keV⁻¹)
normalized counts s⁻¹ keV⁻¹
Energy (keV)

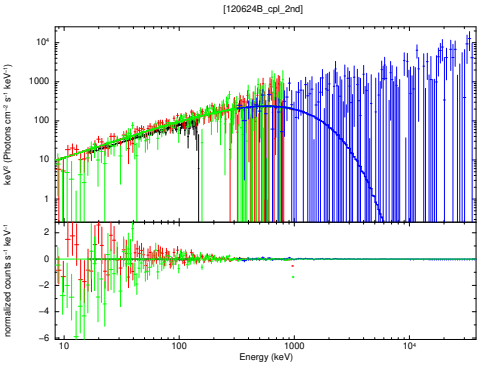
[120624B_cpl_2nd]
keV² (Photons cm⁻² s⁻¹ keV⁻¹)
normalized counts s⁻¹ keV⁻¹
Energy (keV)

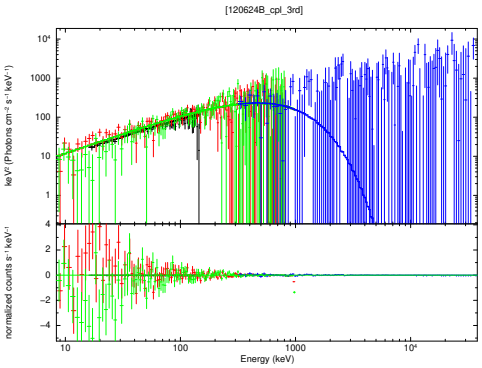
[120624B_cpl_3rd]
keV² (Photons cm⁻² s⁻¹ keV⁻¹)
normalized counts s⁻¹ keV⁻¹
Energy (keV)

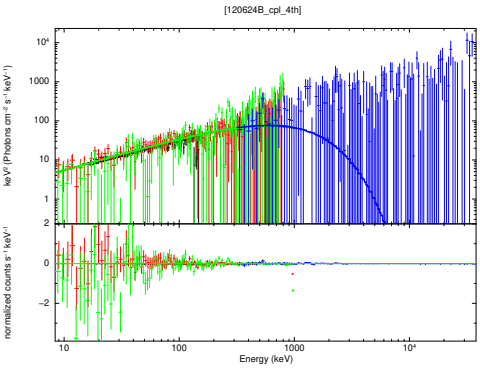
[120624B_cpl_4th]
keV² (Photons cm⁻² s⁻¹ keV⁻¹)
normalized counts s⁻¹ keV⁻¹
Energy (keV)

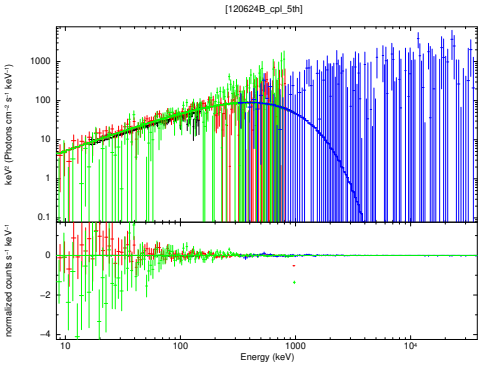
[120624B_cpl_5th]
keV² (Photons cm⁻² s⁻¹ keV⁻¹)
normalized counts s⁻¹ keV⁻¹
Energy (keV)

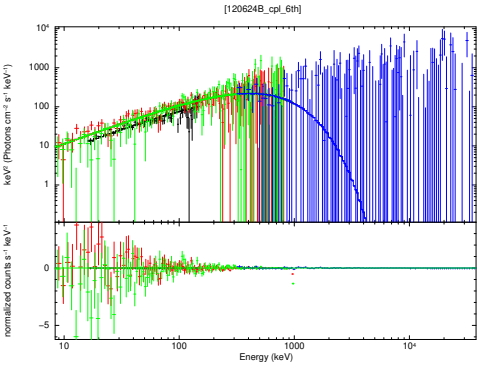
[120624B_cpl_6th]
keV² (Photons cm⁻² s⁻¹ keV⁻¹)
normalized counts s⁻¹ keV⁻¹
Energy (keV)

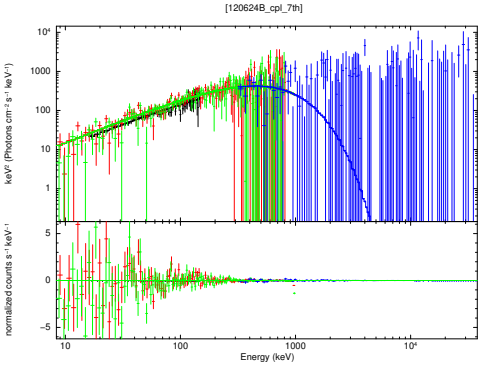
[120624B_cpl_7th]
keV² (Photons cm⁻² s⁻¹ keV⁻¹)
normalized counts s⁻¹ keV⁻¹
Energy (keV)

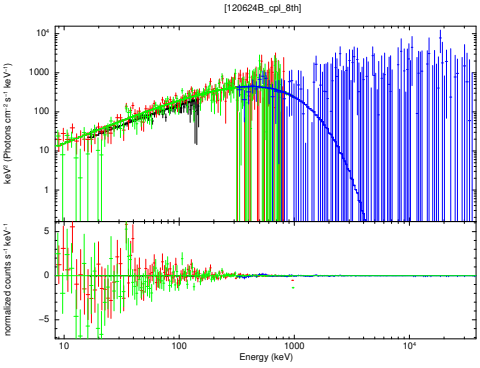
[120624B_cpl_8th]
keV² (Photons cm⁻² s⁻¹ keV⁻¹)
normalized counts s⁻¹ keV⁻¹
Energy (keV)

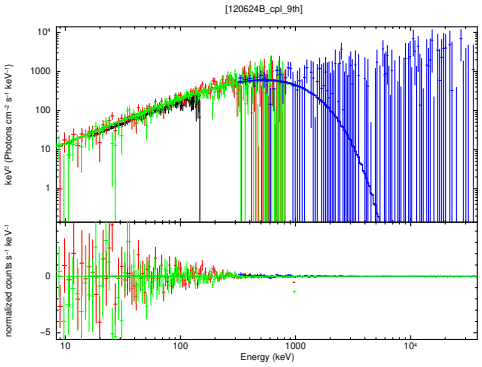
[120624B_cpl_9th]
keV² (Photons cm⁻² s⁻¹ keV⁻¹)
normalized counts s⁻¹ keV⁻¹
Energy (keV)

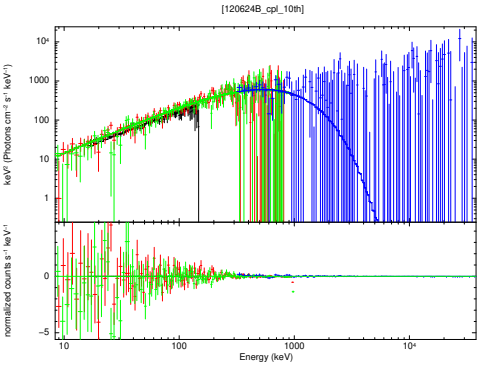
[120624B_cpl_10th]
keV² (Photons cm⁻² s⁻¹ keV⁻¹)
normalized counts s⁻¹ keV⁻¹
Energy (keV)

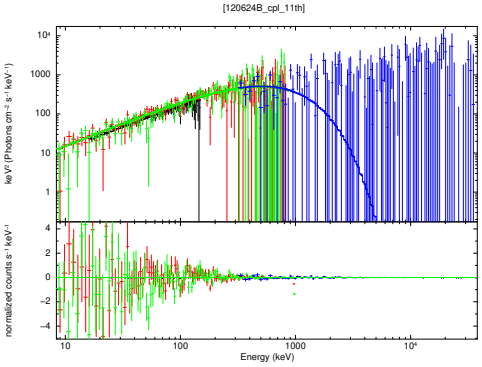
[120624B_cpl_11th]
keV² (Photons cm⁻² s⁻¹ keV⁻¹)
normalized counts s⁻¹ keV⁻¹
Energy (keV)

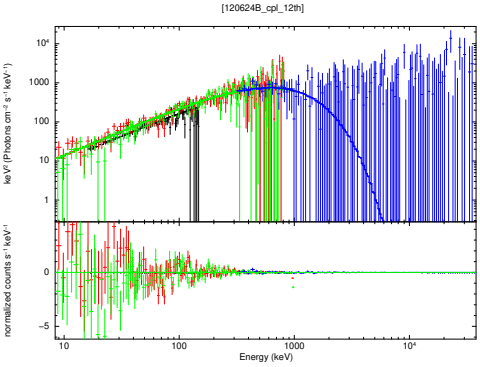
[120624B_cpl_12th]
keV² (Photons cm⁻² s⁻¹ keV⁻¹)
normalized counts s⁻¹ keV⁻¹
Energy (keV)

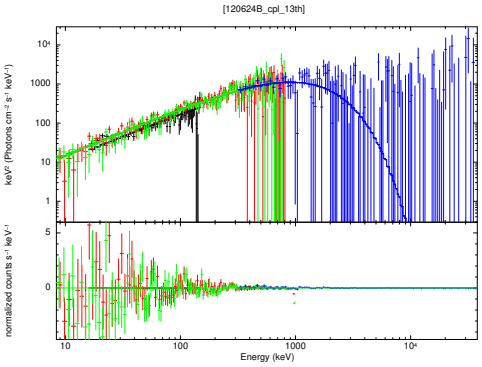
[120624B_cpl_13th]
keV² (Photons cm⁻² s⁻¹ keV⁻¹)
normalized counts s⁻¹ keV⁻¹
Energy (keV)

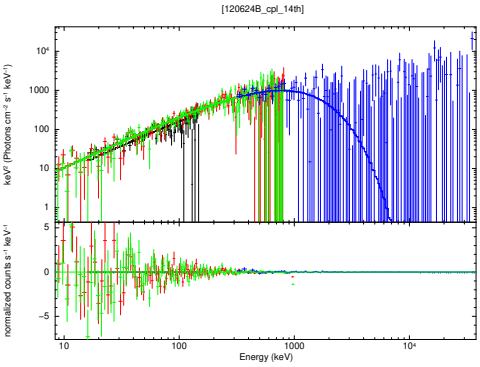
[120624B_cpl_14th]
keV² (Photons cm⁻² s⁻¹ keV⁻¹)
normalized counts s⁻¹ keV⁻¹
Energy (keV)

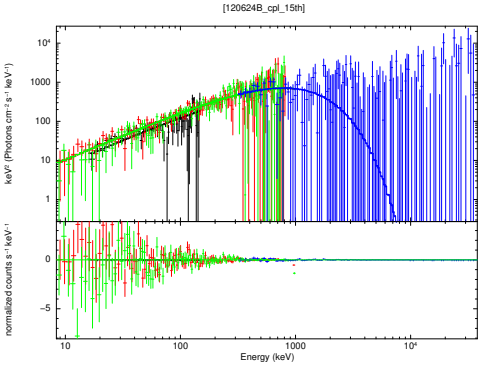
[120624B_cpl_15th]
keV² (Photons cm⁻² s⁻¹ keV⁻¹)
normalized counts s⁻¹ keV⁻¹
Energy (keV)

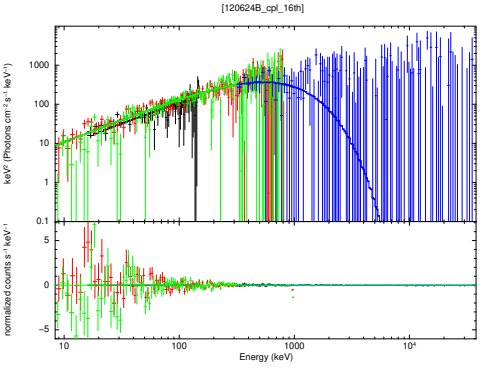
[120624B_cpl_16th]
keV² (Photons cm⁻² s⁻¹ keV⁻¹)
normalized counts s⁻¹ keV⁻¹
Energy (keV)

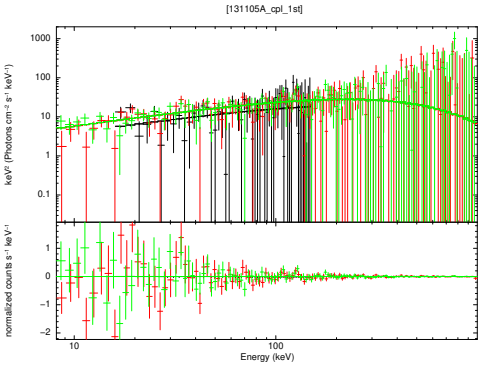
[131105A_cpl_1st]
keV² (Photons cm⁻² s⁻¹ keV⁻¹)
normalized counts s⁻¹ keV⁻¹
Energy (keV)

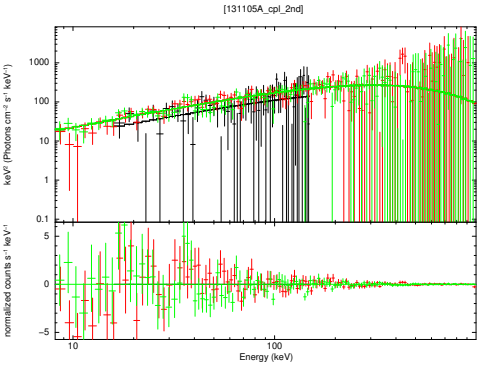
[131105A_cpl_2nd]
keV² (Photons cm⁻² s⁻¹ keV⁻¹)
normalized counts s⁻¹ keV⁻¹
Energy (keV)

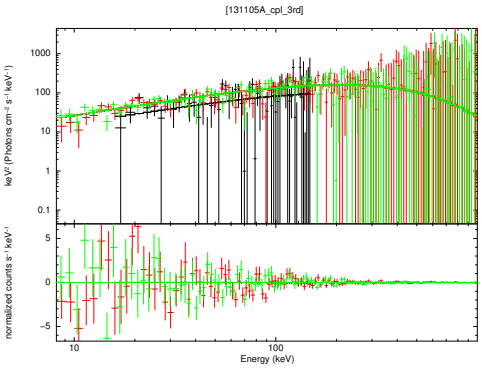
[131105A_cpl_3rd]
keV² (Photons cm⁻² s⁻¹ keV⁻¹)
normalized counts s⁻¹ keV⁻¹
Energy (keV)

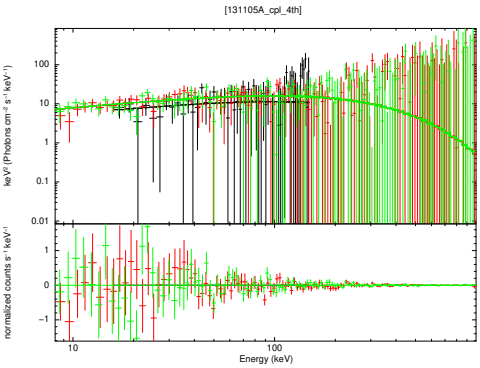
[131105A_cpl_4th]
keV² (Photons cm⁻² s⁻¹ keV⁻¹)
normalized counts s⁻¹ keV⁻¹
Energy (keV)

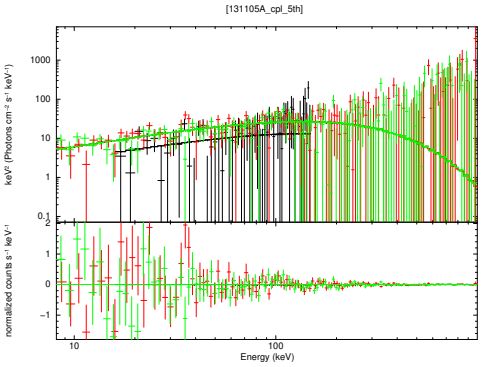
[131105A_cpl_5th]
keV² (Photons cm⁻² s⁻¹ keV⁻¹)
normalized counts s⁻¹ keV⁻¹
Energy (keV)

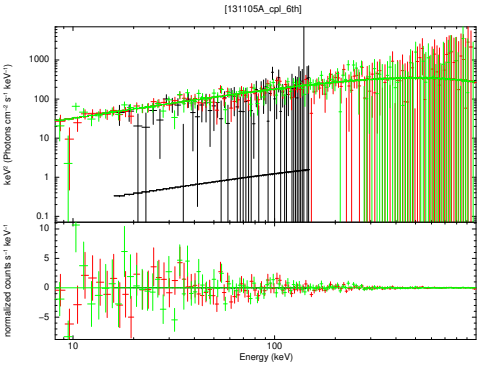
[131105A_cpl_6th]
keV² (Photons cm⁻² s⁻¹ keV⁻¹)
normalized counts s⁻¹ keV⁻¹
Energy (keV)

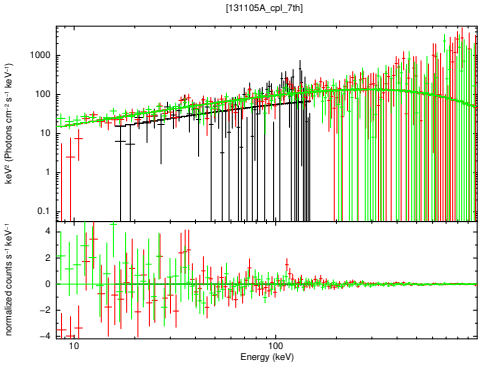
[131105A_cpl_7th]
keV² (Photons cm⁻² s⁻¹ keV⁻¹)
normalized counts s⁻¹ keV⁻¹
Energy (keV)

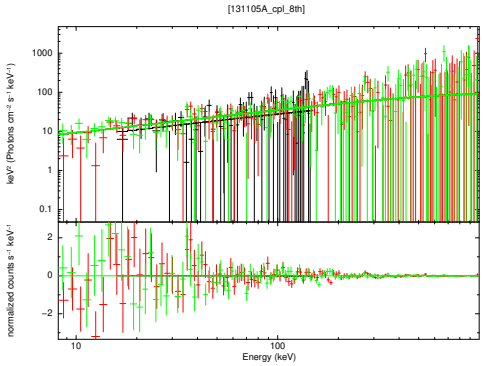
[131105A_cpl_8th]
1000
100
10
1
0.1
keV (Photons cm⁻² s⁻¹ keV⁻¹)
2
0
−2
normalized counts s⁻¹ keV⁻¹
10
100
Energy (keV)

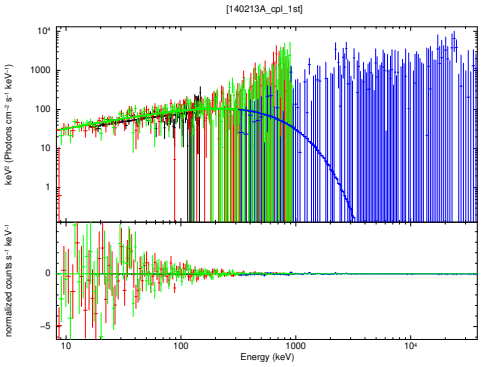
[140213A_cpl_1st]
keV² (Photons cm⁻² s⁻¹ keV⁻¹)
normalized counts s⁻¹ keV⁻¹
Energy (keV)

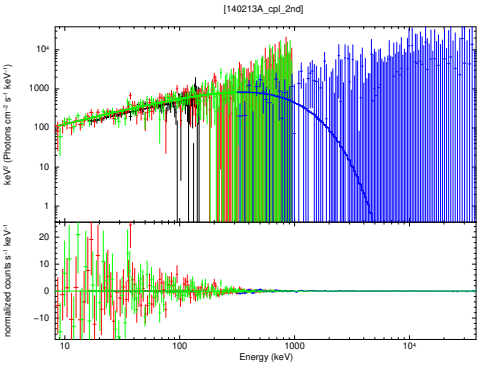
[140213A_cpl_2nd]
keV² (Photons cm⁻² s⁻¹ keV⁻¹)
normalized counts s⁻¹ keV⁻¹
Energy (keV)

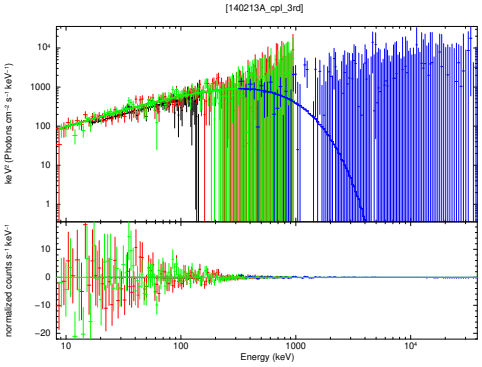
[140213A_cpl_3rd]
keV² (Photons cm⁻² s⁻¹ keV⁻¹)
normalized counts s⁻¹ keV⁻¹
Energy (keV)

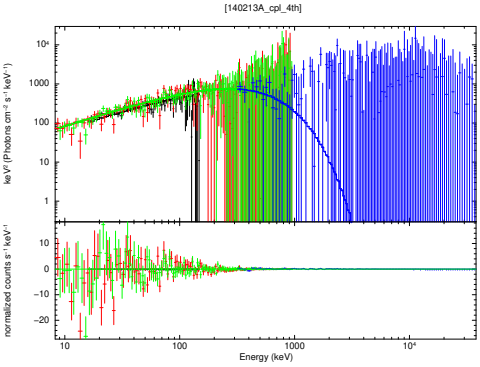
[140213A_cpl_4th]
keV² (Photons cm⁻² s⁻¹ keV⁻¹)
normalized counts s⁻¹ keV⁻¹
Energy (keV)

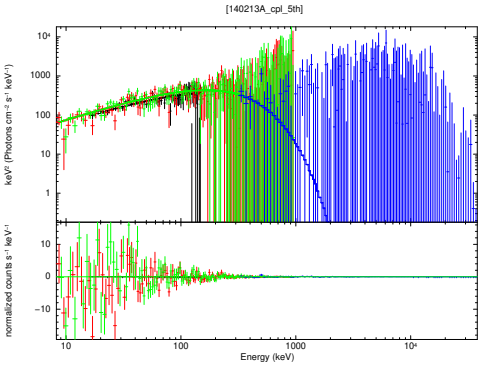
[140213A_cpl_5th]
keV² (Photons cm⁻² s⁻¹ keV⁻¹)
normalized counts s⁻¹ keV⁻¹
Energy (keV)

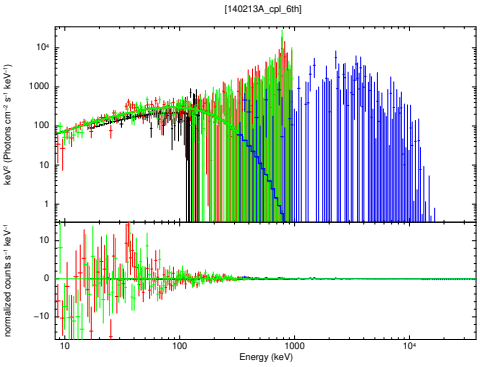
[140213A_cpl_6th]
keV² (Photons cm⁻² s⁻¹ keV⁻¹)
normalized counts s⁻¹ keV⁻¹
Energy (keV)

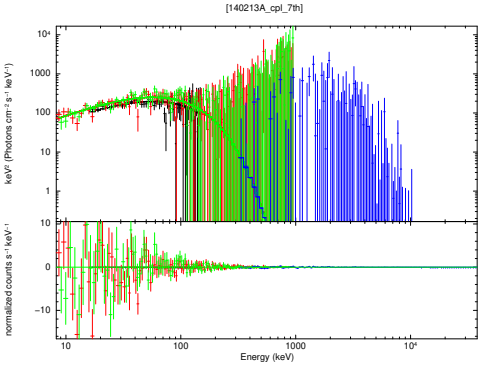
[140213A_cpl_7th]
keV² (Photons cm⁻² s⁻¹ keV⁻¹)
normalized counts s⁻¹ keV⁻¹
Energy (keV)

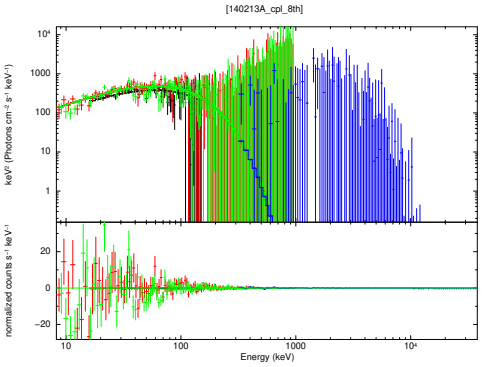
[140213A_cpl_8th]
keV² (Photons cm⁻² s⁻¹ keV⁻¹)
normalized counts s⁻¹ keV⁻¹
Energy (keV)

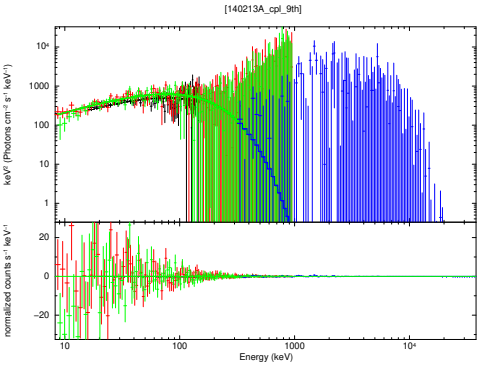
[140213A_cpl_9th]
keV² (Photons cm⁻² s⁻¹ keV⁻¹)
normalized counts s⁻¹ keV⁻¹
Energy (keV)

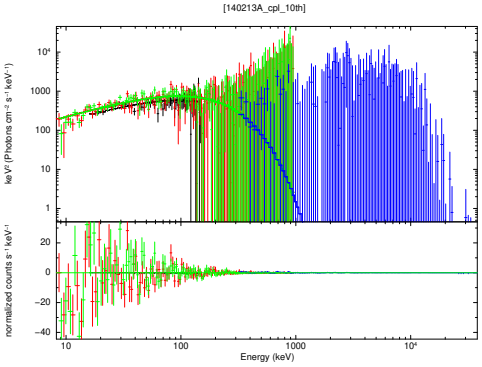
[140213A_cpl_10th]
keV² (Photons cm⁻² s⁻¹ keV⁻¹)
normalized counts s⁻¹ keV⁻¹
Energy (keV)

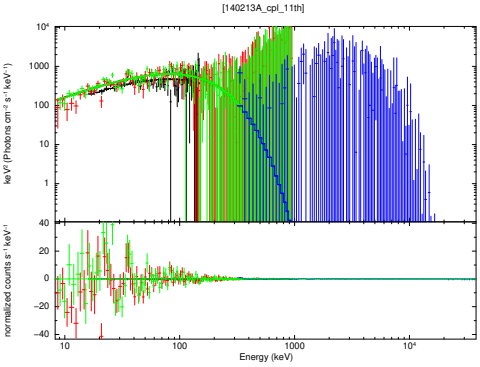
[140213A_cpl_11th]
keV² (Photons cm⁻² s⁻¹ keV⁻¹)
normalized counts s⁻¹ keV⁻¹
Energy (keV)

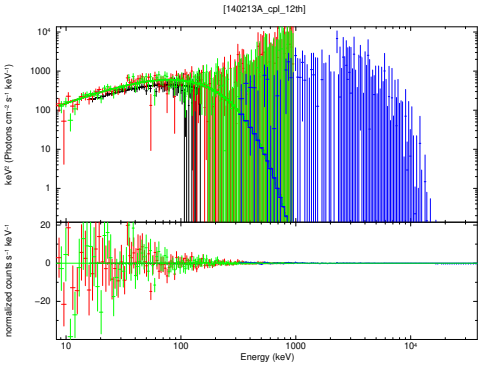
[140213A_cpl_12th]
keV² (Photons cm⁻² s⁻¹ keV⁻¹)
normalized counts s⁻¹ keV⁻¹
Energy (keV)

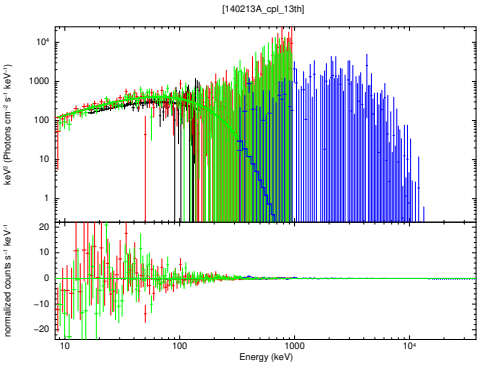
[140213A_cpl_13th]
keV² (Photons cm⁻² s⁻¹ keV⁻¹)
normalized counts s⁻¹ keV⁻¹
Energy (keV)

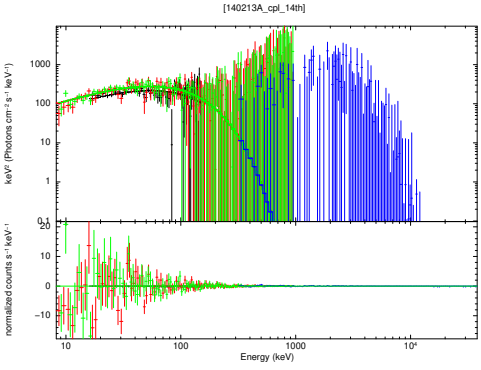
[140213A_cpl_14th]
keV² (Photons cm⁻² s⁻¹ keV⁻¹)
normalized counts s⁻¹ keV⁻¹
Energy (keV)

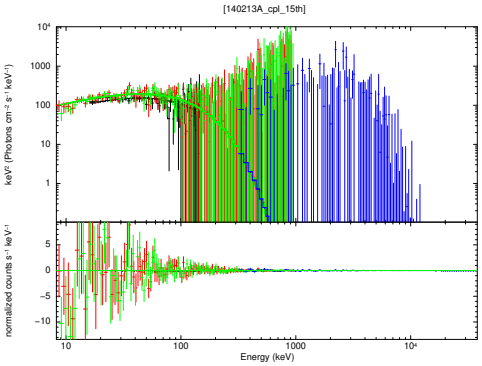
[140213A_cpl_15th]
keV² (Photons cm⁻² s⁻¹ keV⁻¹)
normalized counts s⁻¹ keV⁻¹
Energy (keV)

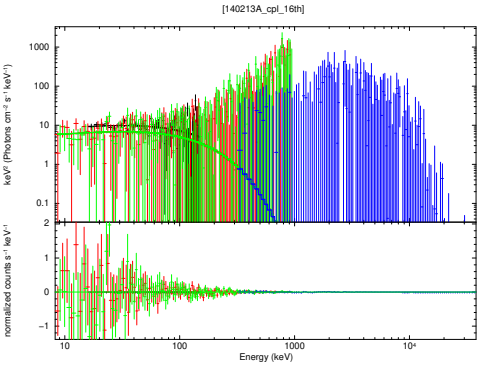
[140213A_cpl_16th]
keV² (Photons cm⁻² s⁻¹ keV⁻¹)
normalized counts s⁻¹ keV⁻¹
Energy (keV)

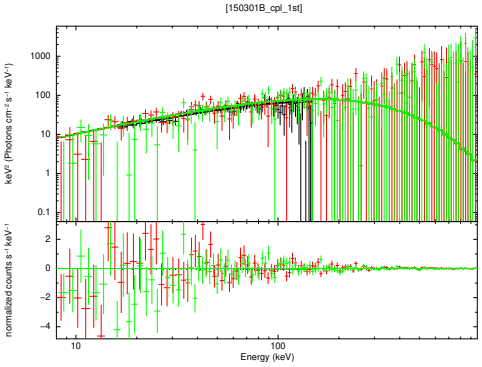
[150301B_cpl_1st]
keV² (Photons cm⁻² s⁻¹ keV⁻¹)
normalized counts s⁻¹ keV⁻¹
Energy (keV)

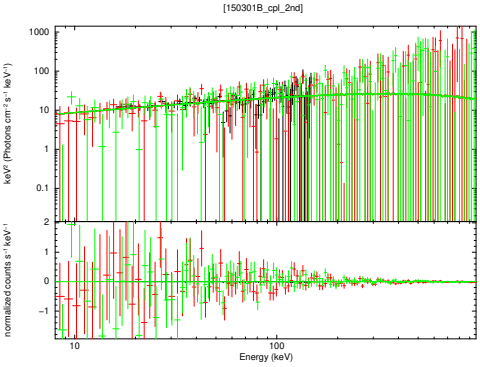
[150301B_cpl_2nd]
keV² (Photons cm⁻² s⁻¹ keV⁻¹)
normalized counts s⁻¹ keV⁻¹
Energy (keV)

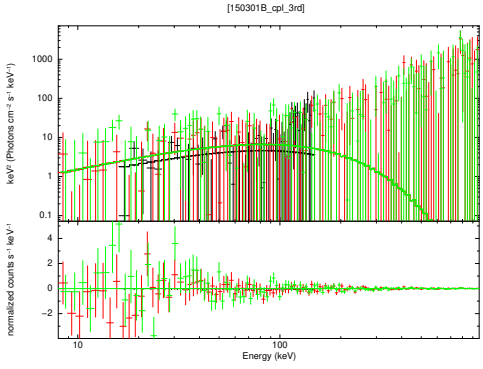
[150301B_cpl_3rd]
keV² (Photons cm⁻² s⁻¹ keV⁻¹)
normalized counts s⁻¹ keV⁻¹
Energy (keV)

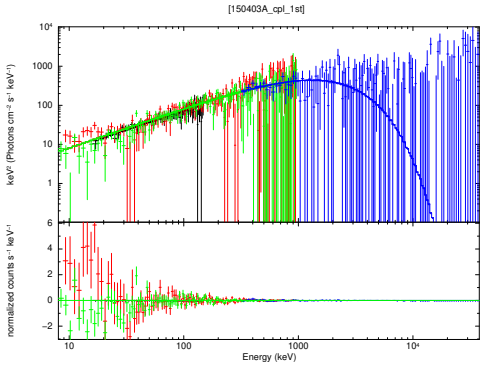
[150403A_cpl_1st]
keV² (Photons cm⁻² s⁻¹ keV⁻¹)
normalized counts s⁻¹ keV⁻¹
Energy (keV)

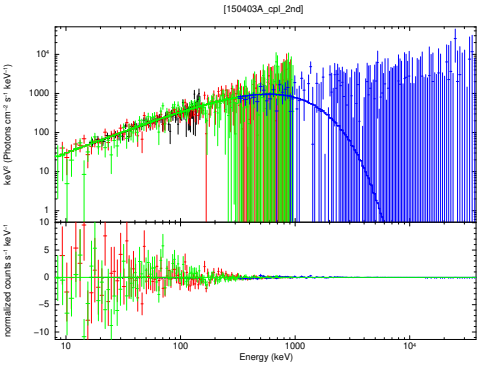
[150403A_cpl_2nd]
keV² (Photons cm⁻² s⁻¹ keV⁻¹)
normalized counts s⁻¹ keV⁻¹
Energy (keV)

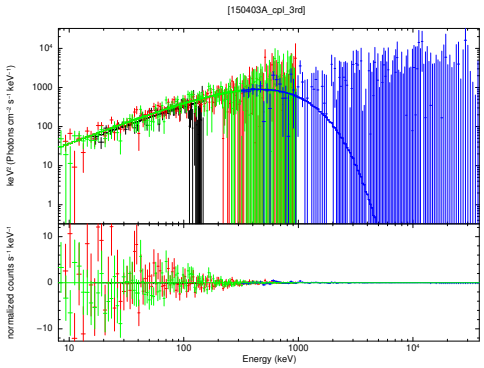
[150403A_cpl_3rd]
keV² (Photons cm⁻² s⁻¹ keV⁻¹)
normalized counts s⁻¹ keV⁻¹
Energy (keV)

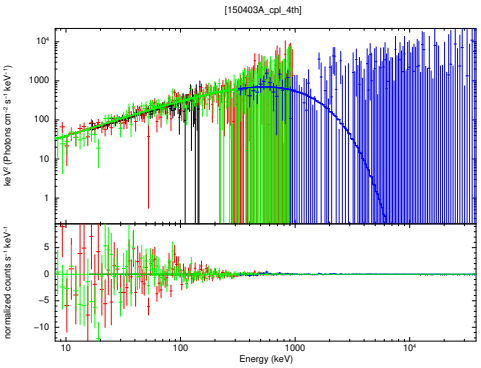
[150403A_cpl_4th]
keV² (Photons cm⁻² s⁻¹ keV⁻¹)
normalized counts s⁻¹ keV⁻¹
Energy (keV)

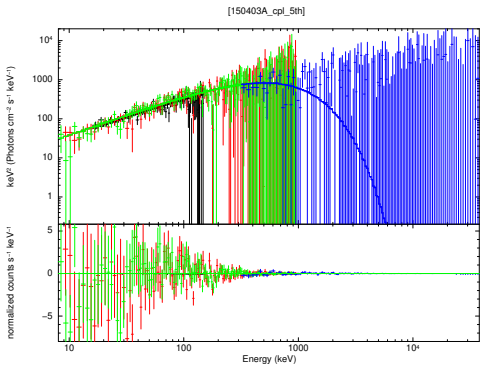
[150403A_cpl_5th]
keV² (Photons cm⁻² s⁻¹ keV⁻¹)
normalized counts s⁻¹ keV⁻¹
Energy (keV)

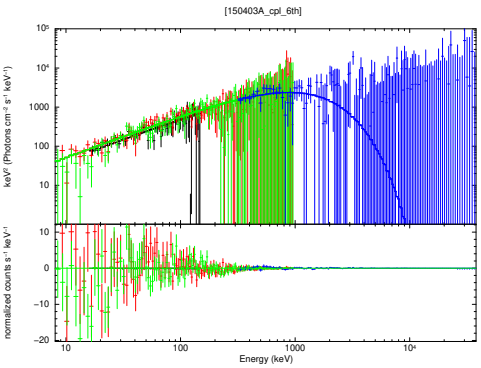
[150403A_cpl_6th]
keV² (Photons cm⁻² s⁻¹ keV⁻¹)
normalized counts s⁻¹ keV⁻¹
Energy (keV)

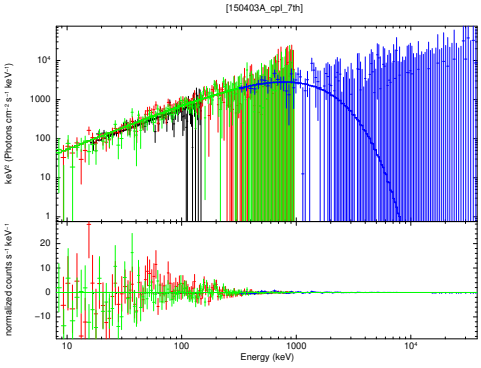
[150403A_cpl_7th]
keV² (Photons cm⁻² s⁻¹ keV⁻¹)
normalized counts s⁻¹ keV⁻¹
Energy (keV)

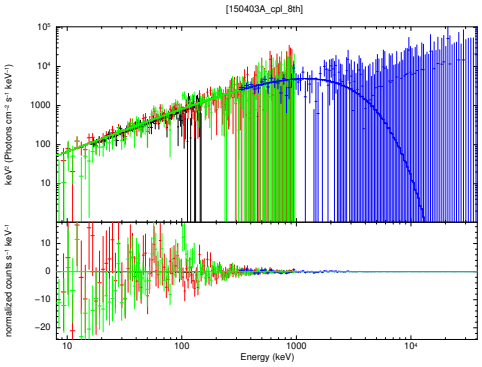
[150403A_cpl_8th]
keV² (Photons cm⁻² s⁻¹ keV⁻¹)
normalized counts s⁻¹ keV⁻¹
Energy (keV)

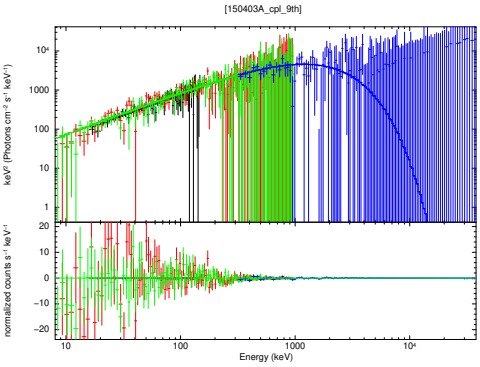
[150403A_cpl_9th]
keV² (Photons cm⁻² s⁻¹ keV⁻¹)
normalized counts s⁻¹ keV⁻¹
Energy (keV)

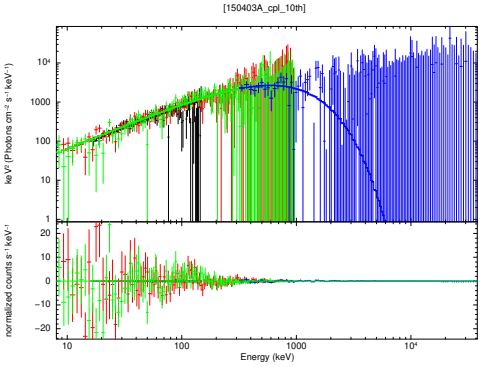
[150403A_cpl_10th]
keV² (Photons cm⁻² s⁻¹ keV⁻¹)
normalized counts s⁻¹ keV⁻¹
Energy (keV)

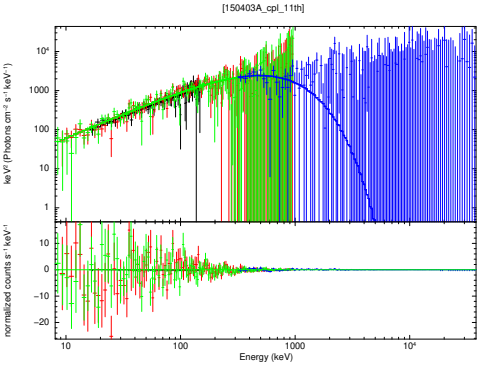
[150403A_cpl_11th]
keV² (Photons cm⁻² s⁻¹ keV⁻¹)
normalized counts s⁻¹ keV⁻¹
Energy (keV)

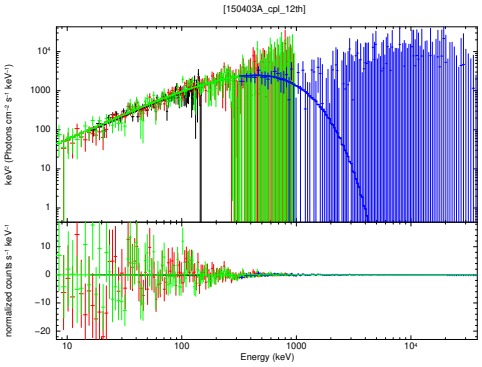
[150403A_cpl_12th]
keV² (Photons cm⁻² s⁻¹ keV⁻¹)
normalized counts s⁻¹ keV⁻¹
Energy (keV)

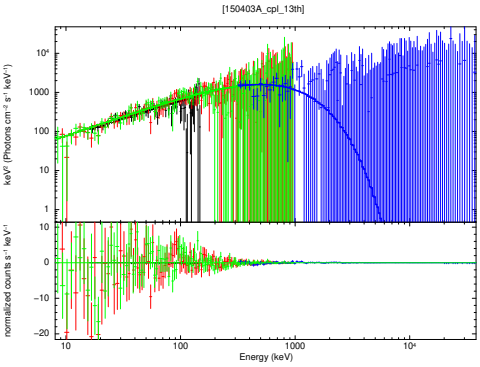
[150403A_cpl_13th]
keV² (Photons cm⁻² s⁻¹ keV⁻¹)
normalized counts s⁻¹ keV⁻¹
Energy (keV)

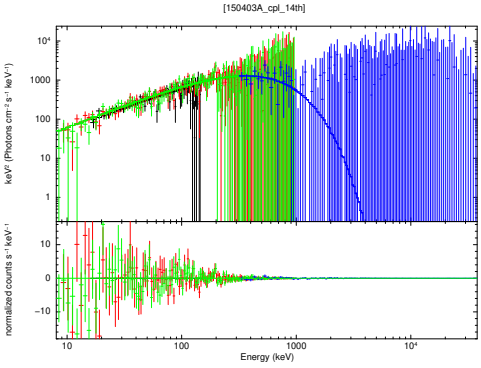
[150403A_cpl_14th]
keV² (Photons cm⁻² s⁻¹ keV⁻¹)
normalized counts s⁻¹ keV⁻¹
Energy (keV)

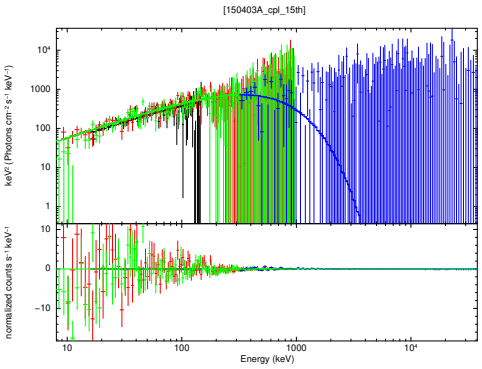
[150403A_cpl_15th]
keV² (Photons cm⁻² s⁻¹ keV⁻¹)
normalized counts s⁻¹ keV⁻¹
Energy (keV)

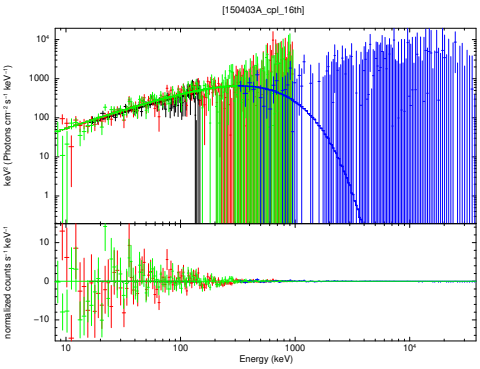
[150403A_cpl_16th]
keV² (Photons cm⁻² s⁻¹ keV⁻¹)
normalized counts s⁻¹ keV⁻¹
Energy (keV)

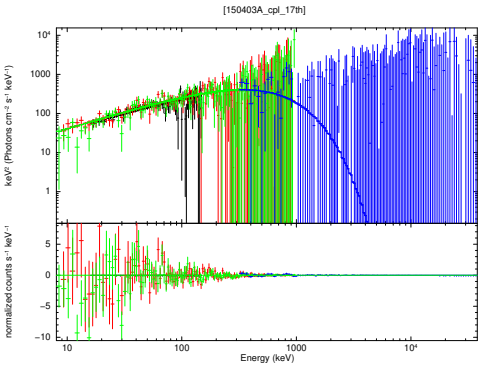
[150403A_cpl_17th]
keV² (Photons cm⁻² s⁻¹ keV⁻¹)
normalized counts s⁻¹ keV⁻¹
Energy (keV)

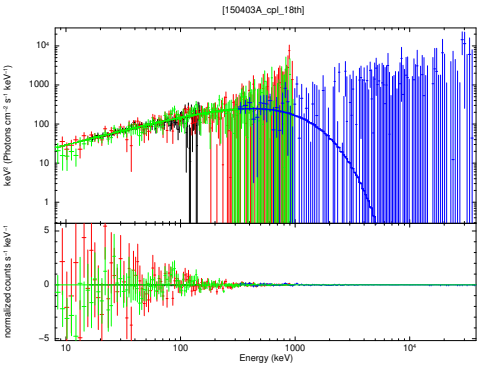
[150403A_cpl_18th]
keV² (Photons cm⁻² s⁻¹ keV⁻¹)
normalized counts s⁻¹ keV⁻¹
Energy (keV)

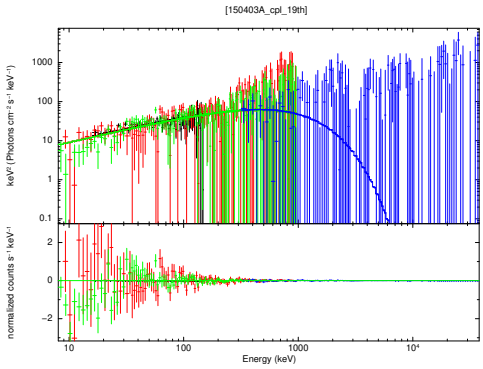
[150403A_cpl_19th]
keV² (Photons cm⁻² s⁻¹ keV⁻¹)
normalized counts s⁻¹ keV⁻¹
Energy (keV)

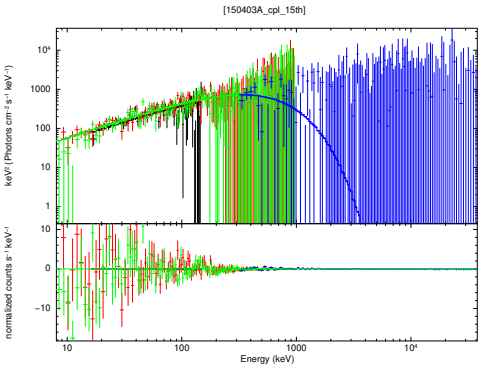
[150403A_cpl_15th]
keV² (Photons cm⁻² s⁻¹ keV⁻¹)
normalized counts s⁻¹ keV⁻¹
Energy (keV)

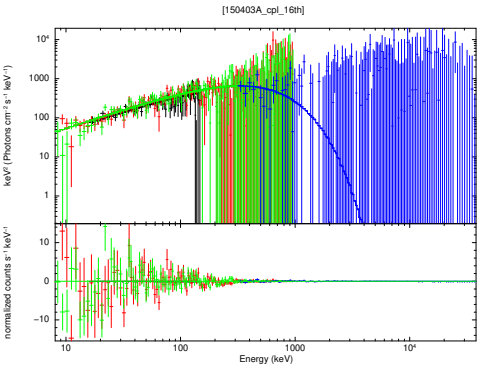
[150403A_cpl_16th]
keV² (Photons cm⁻² s⁻¹ keV⁻¹)
normalized counts s⁻¹ keV⁻¹
Energy (keV)

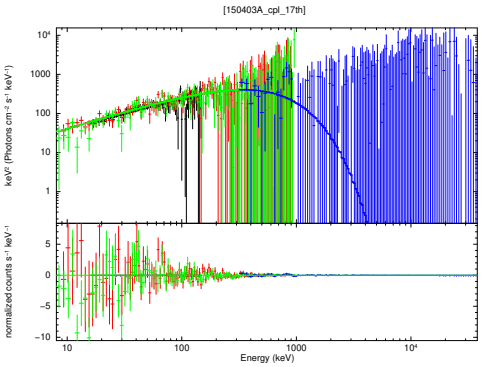
[150403A_cpl_17th]
keV² (Photons cm⁻² s⁻¹ keV⁻¹)
normalized counts s⁻¹ keV⁻¹
Energy (keV)

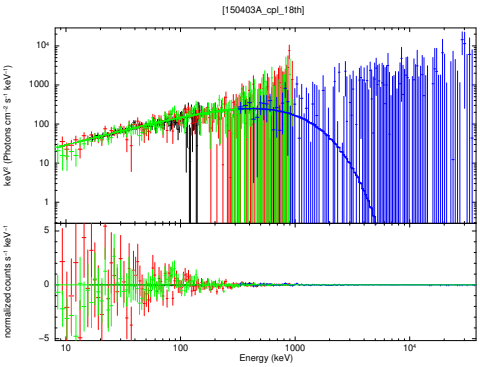
[150403A_cpl_18th]
keV² (Photons cm⁻² s⁻¹ keV⁻¹)
normalized counts s⁻¹ keV⁻¹
Energy (keV)

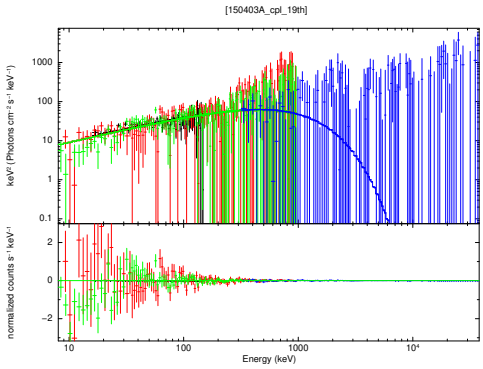
[150403A_cpl_19th]
keV² (Photons cm⁻² s⁻¹ keV⁻¹)
normalized counts s⁻¹ keV⁻¹
Energy (keV)

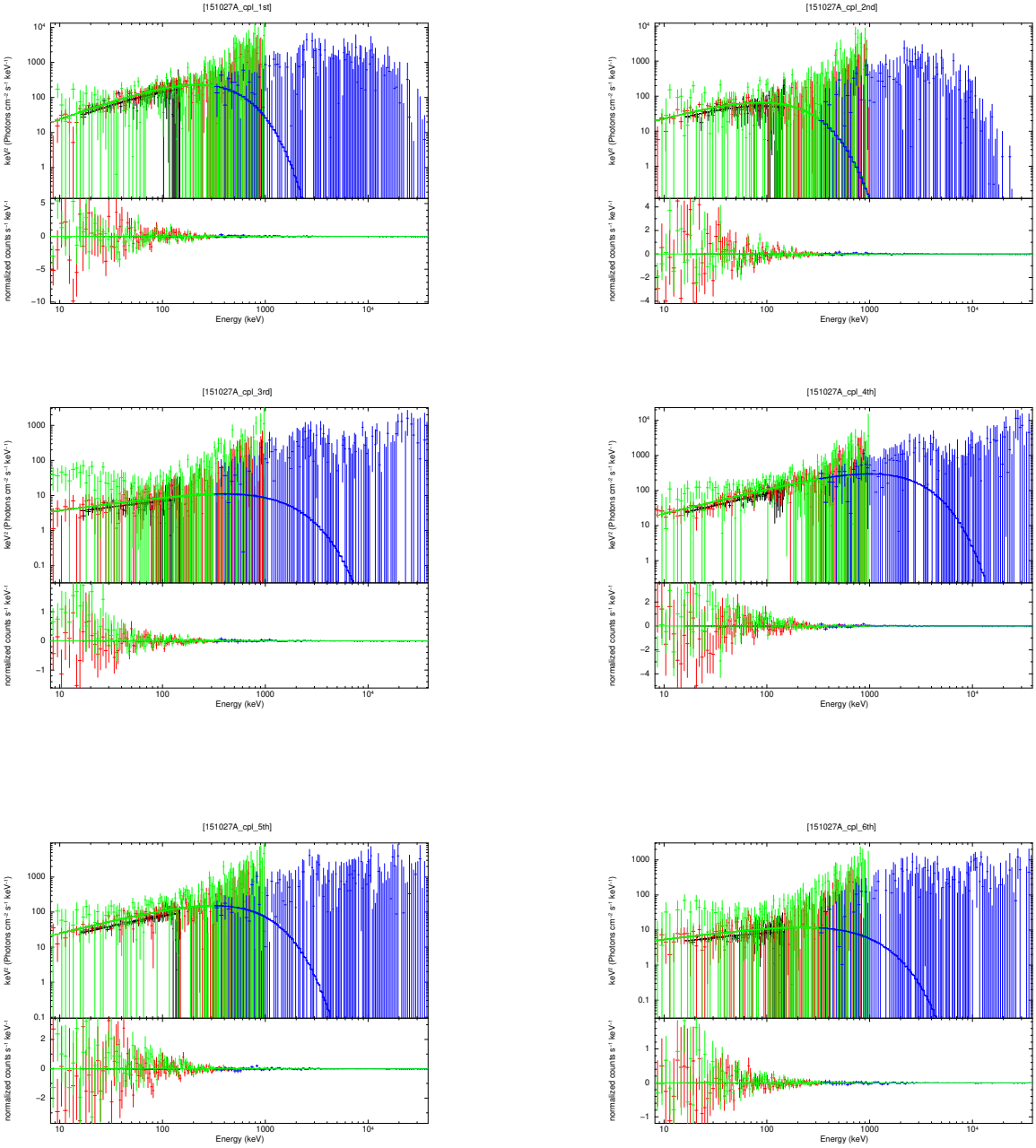

Figure A.2: The spectral analysis of the joint-fit (GBM+BAT) for the time-resolved spectra of the GRB sample.

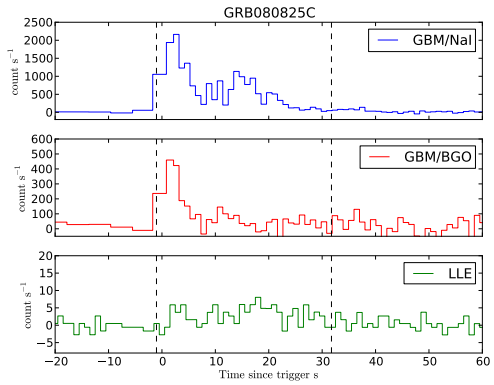
GRB080825C
GBM/NaI
GBM/BGO
LLE
count s^{-1}
Time since trigger s

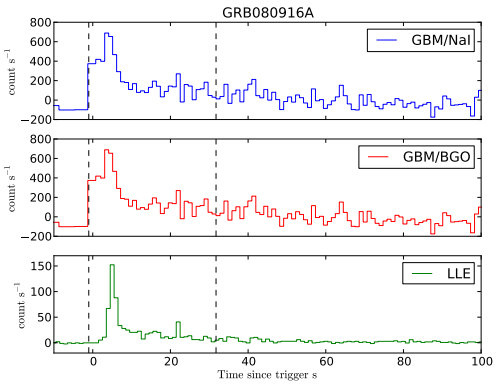
GRB080916A
GBM/NaI
GBM/BGO
LLE
count s^{-1}
Time since trigger s

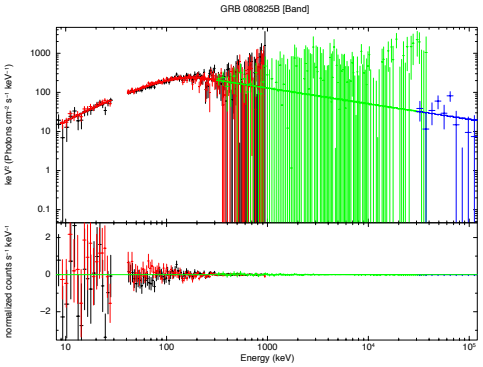
GRB 080825B [Band]
keV^2 (Photons cm^{-2} s^{-1} keV^{-1})
normalized counts s^{-1} keV^{-1}
Energy (keV)

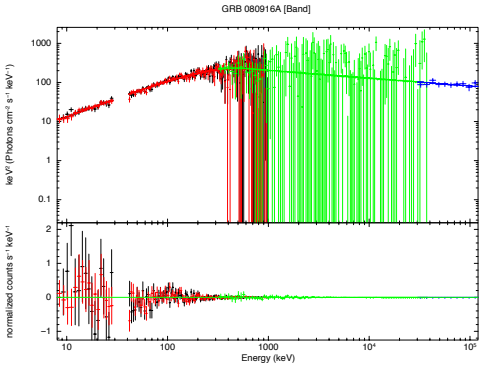
GRB 080916A [Band]
keV^2 (Photons cm^{-2} s^{-1} keV^{-1})
normalized counts s^{-1} keV^{-1}
Energy (keV)

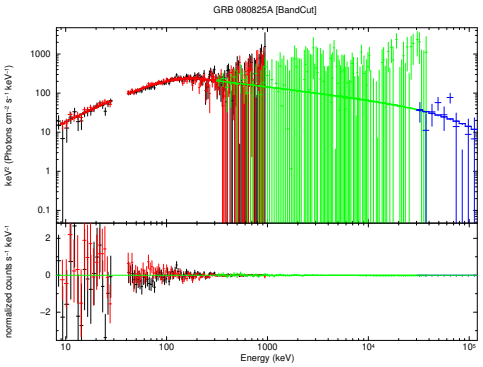
GRB 080825A [BandCut]
keV^2 (Photons cm^{-2} s^{-1} keV^{-1})
normalized counts s^{-1} keV^{-1}
Energy (keV)
eam27 6-Sep-2018 16:32

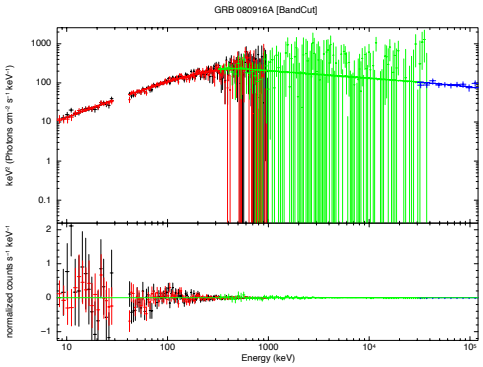
GRB 080916A [BandCut]
keV^2 (Photons cm^{-2} s^{-1} keV^{-1})
normalized counts s^{-1} keV^{-1}
Energy (keV)

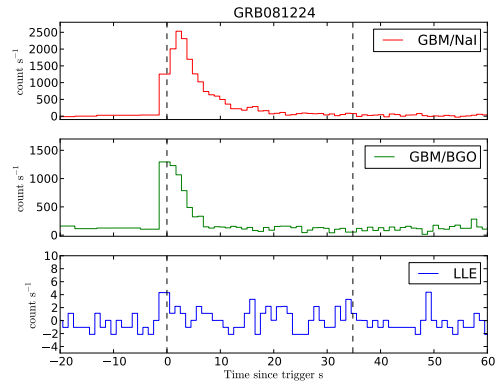
GRB081224
GBM/NaI
GBM/BGO
LLE
count s^{-1}
Time since trigger s

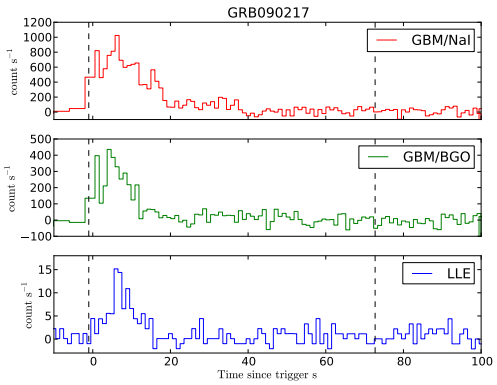
GRB090217
GBM/NaI
GBM/BGO
LLE
count s^{-1}
Time since trigger s

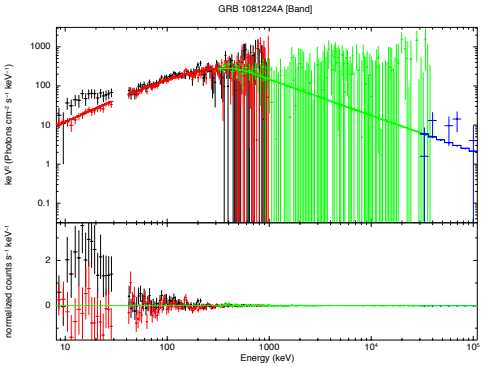
GRB 1081224A [Band]
keV^2 (Photons cm^{-2} s^{-1} keV^{-1})
normalized counts s^{-1} keV^{-1}
Energy (keV)

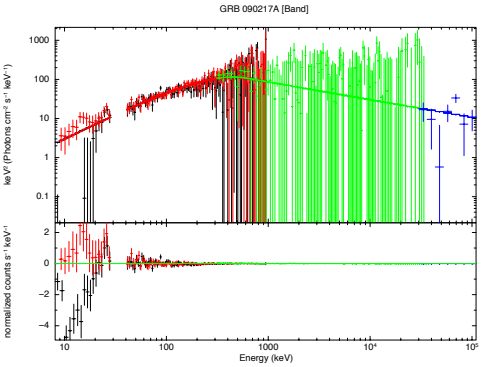
GRB 090217A [Band]
keV^2 (Photons cm^{-2} s^{-1} keV^{-1})
normalized counts s^{-1} keV^{-1}
Energy (keV)

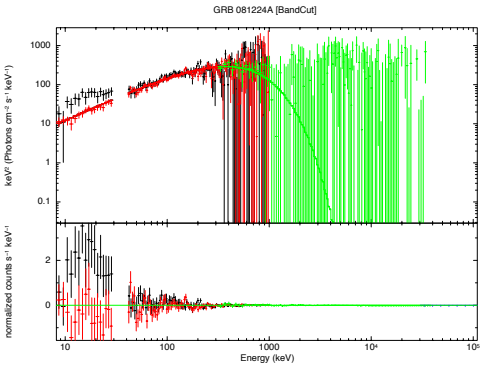
GRB 081224A [BandCut]
keV^2 (Photons cm^{-2} s^{-1} keV^{-1})
normalized counts s^{-1} keV^{-1}
Energy (keV)

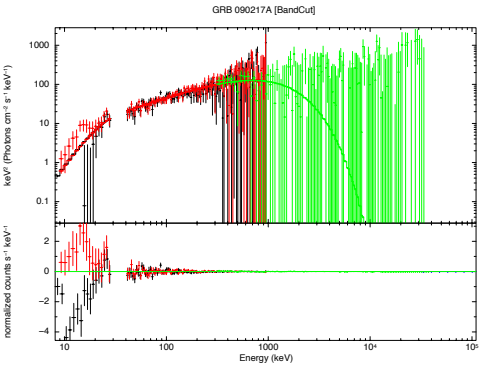
GRB 090217A [BandCut]
keV^2 (Photons cm^{-2} s^{-1} keV^{-1})
normalized counts s^{-1} keV^{-1}
Energy (keV)

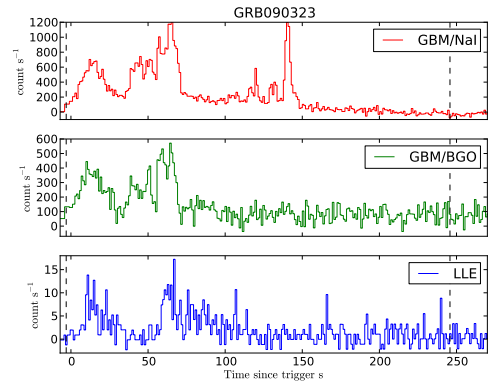
GRB090323
GBM/NaI
GBM/BGO
LLE
count s^{-1}
Time since trigger s

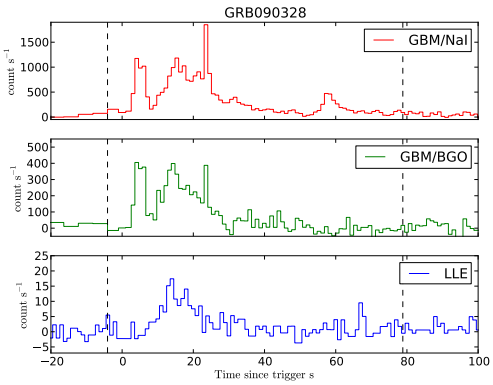
GRB090328
GBM/NaI
GBM/BGO
LLE
count s^{-1}
Time since trigger s

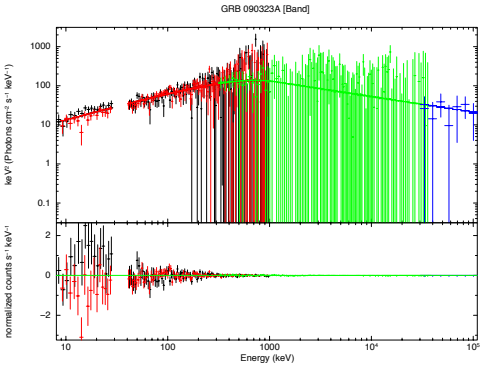
GRB 090323A [Band]
keV^2 (Photons cm^{-2} s^{-1} keV^{-1})
normalized counts s^{-1} keV^{-1}
Energy (keV)

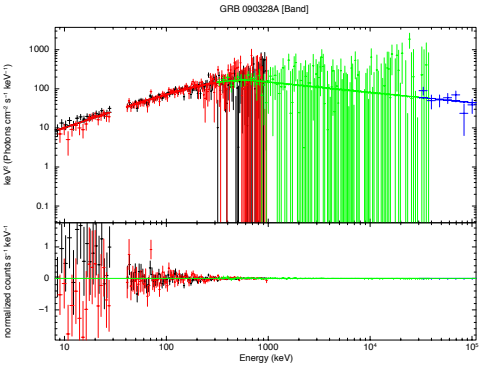
GRB 090328A [Band]
keV^2 (Photons cm^{-2} s^{-1} keV^{-1})
normalized counts s^{-1} keV^{-1}
Energy (keV)

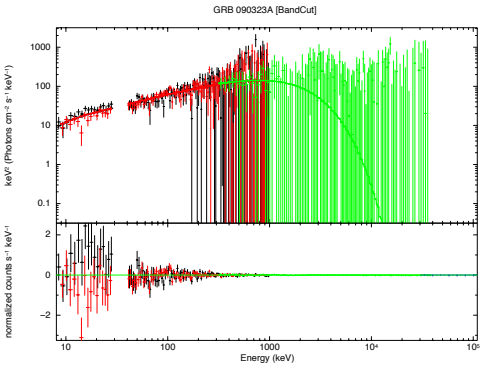
GRB 090323A [BandCut]
keV^2 (Photons cm^{-2} s^{-1} keV^{-1})
normalized counts s^{-1} keV^{-1}
Energy (keV)

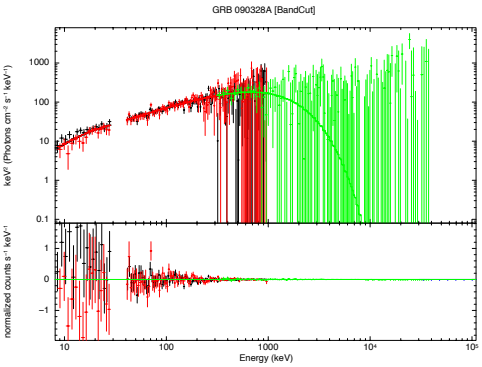
GRB 090328A [BandCut]
keV^2 (Photons cm^{-2} s^{-1} keV^{-1})
normalized counts s^{-1} keV^{-1}
Energy (keV)

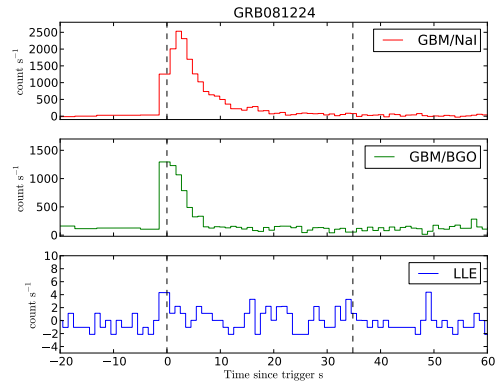
GRB081224
GBM/NaI
GBM/BGO
LLE
count s^{-1}
Time since trigger s

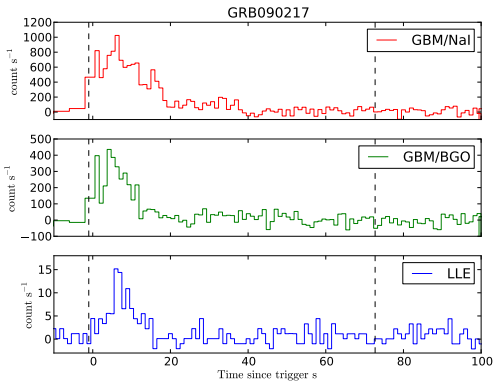
GRB090217
GBM/NaI
GBM/BGO
LLE
count s^{-1}
Time since trigger s

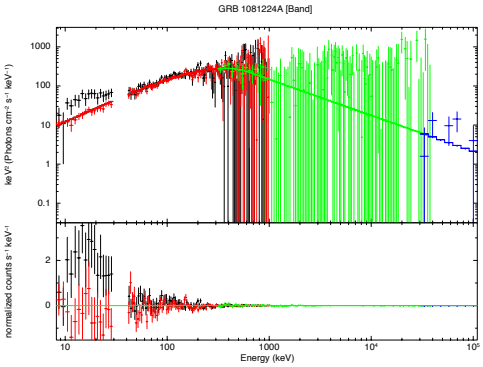
GRB 081224A [Band]
keV^2 (Photons cm^{-2} s^{-1} keV^{-1})
normalized counts s^{-1} keV^{-1}
Energy (keV)

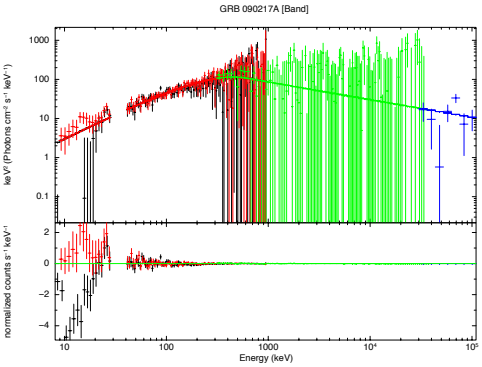
GRB 090217A [Band]
keV^2 (Photons cm^{-2} s^{-1} keV^{-1})
normalized counts s^{-1} keV^{-1}
Energy (keV)

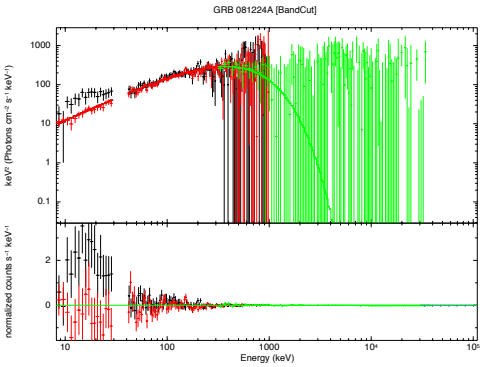
GRB 081224A [BandCut]
keV^2 (Photons cm^{-2} s^{-1} keV^{-1})
normalized counts s^{-1} keV^{-1}
Energy (keV)

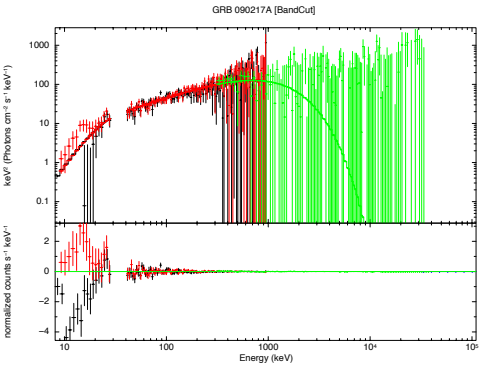
GRB 090217A [BandCut]
keV^2 (Photons cm^{-2} s^{-1} keV^{-1})
normalized counts s^{-1} keV^{-1}
Energy (keV)

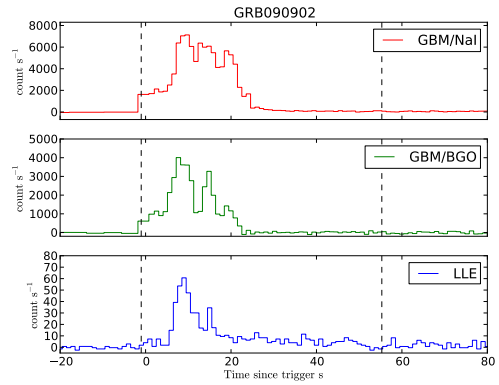
GRB090902
GBM/NaI
GBM/BGO
LLE
count s^{-1}
Time since trigger s

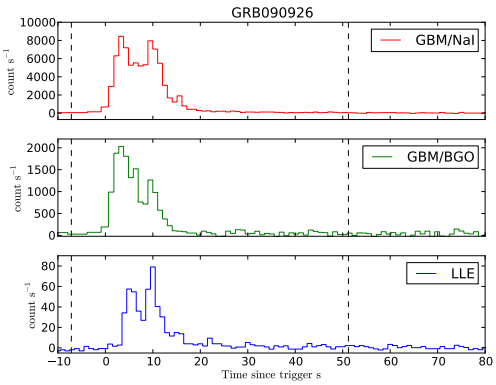
GRB090926
GBM/NaI
GBM/BGO
LLE
count s^{-1}
Time since trigger s

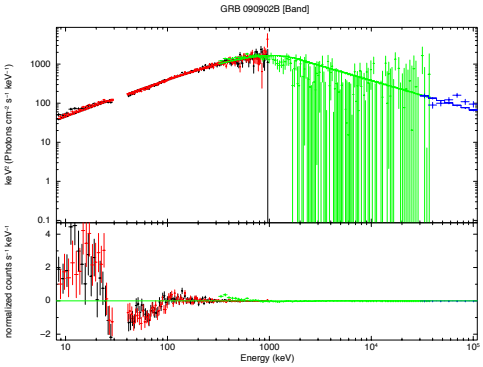
GRB 090902B [Band]
keV^2 (Photons cm^{-2} s^{-1} keV^{-1})
normalized counts s^{-1} keV^{-1}
Energy (keV)

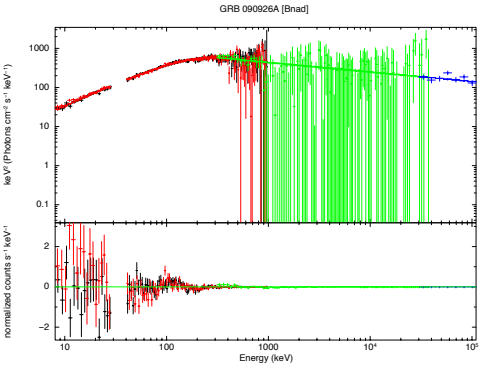
GRB 090926A [Bnad]
keV^2 (Photons cm^{-2} s^{-1} keV^{-1})
normalized counts s^{-1} keV^{-1}
Energy (keV)

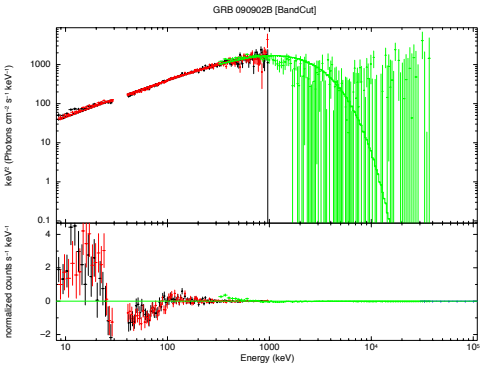
GRB 090902B [BandCut]
keV^2 (Photons cm^{-2} s^{-1} keV^{-1})
normalized counts s^{-1} keV^{-1}
Energy (keV)

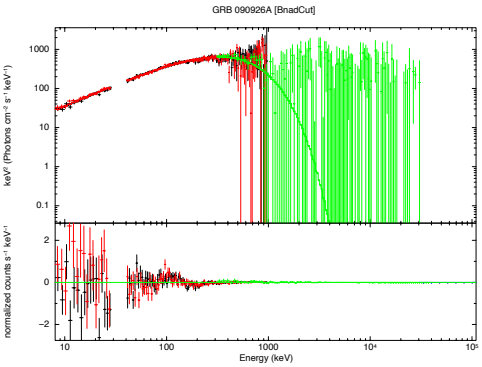
GRB 090926A [BnadCut]
keV^2 (Photons cm^{-2} s^{-1} keV^{-1})
normalized counts s^{-1} keV^{-1}
Energy (keV)

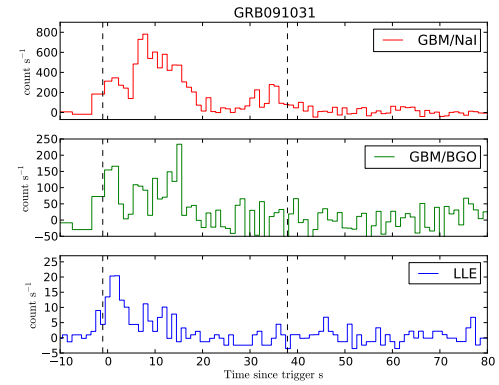
GRB091031
GBM/NaI
GBM/BGO
LLE
count s^{-1}
Time since trigger s

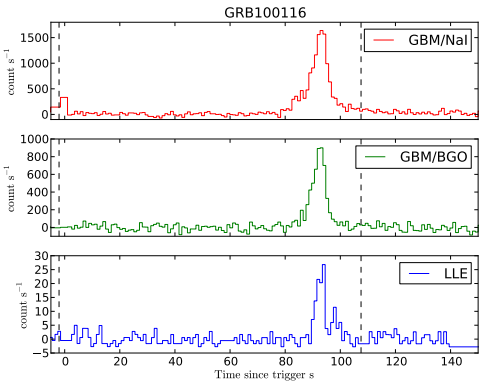
GRB100116
GBM/NaI
GBM/BGO
LLE
count s^{-1}
Time since trigger s

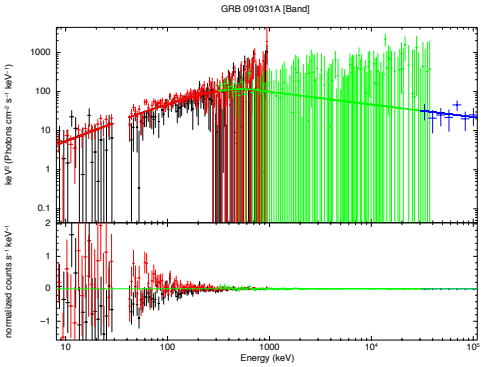
GRB 091031A [Band]
keV^2 (Photons cm^{-2} s^{-1} keV^{-1})
normalized counts s^{-1} keV^{-1}
Energy (keV)

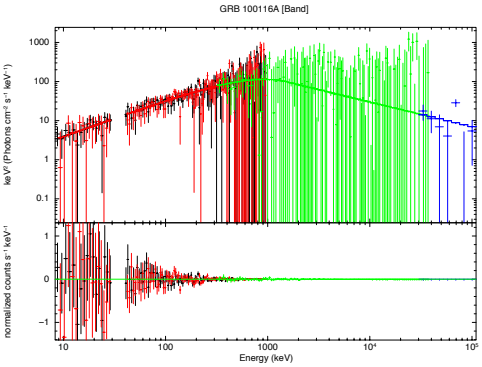
GRB 100116A [Band]
keV^2 (Photons cm^{-2} s^{-1} keV^{-1})
normalized counts s^{-1} keV^{-1}
Energy (keV)

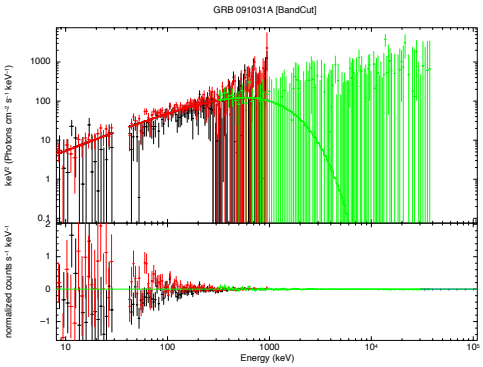
GRB 091031A [BandCut]
keV^2 (Photons cm^{-2} s^{-1} keV^{-1})
normalized counts s^{-1} keV^{-1}
Energy (keV)

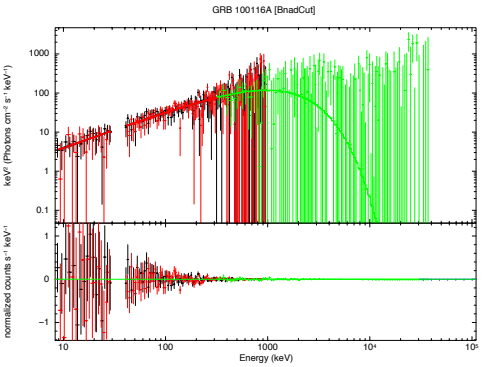
GRB 100116A [BnadCut]
keV^2 (Photons cm^{-2} s^{-1} keV^{-1})
normalized counts s^{-1} keV^{-1}
Energy (keV)

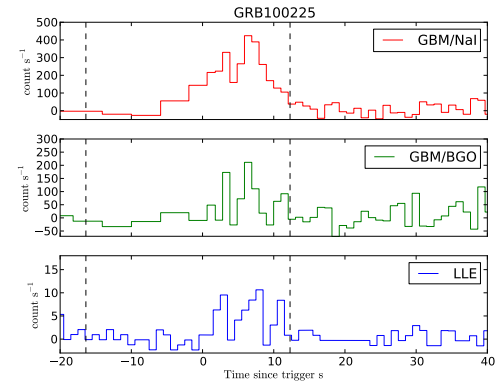
GRB100225
GBM/NaI
GBM/BGO
LLE
count s^{-1}
Time since trigger s

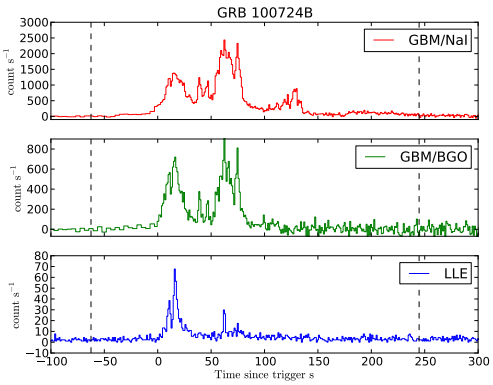
GRB 100724B
GBM/NaI
GBM/BGO
LLE
count s^{-1}
Time since trigger s

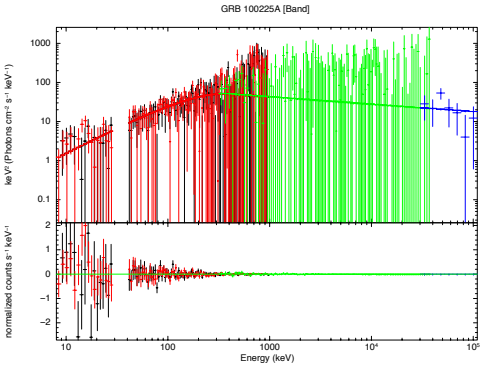
GRB 100225A [Band]
keV^2 (Photons cm^{-2} s^{-1} keV^{-1})
normalized counts s^{-1} keV^{-1}
Energy (keV)

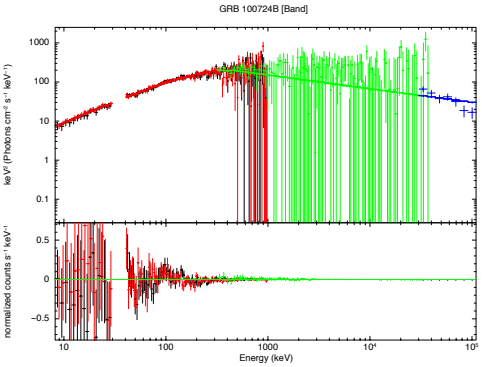
GRB 100724B [Band]
keV^2 (Photons cm^{-2} s^{-1} keV^{-1})
normalized counts s^{-1} keV^{-1}
Energy (keV)

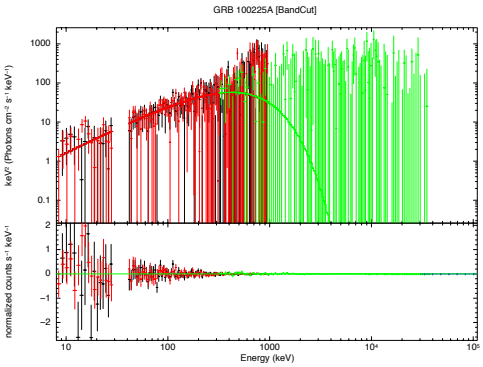
GRB 100225A [BandCut]
keV^2 (Photons cm^{-2} s^{-1} keV^{-1})
normalized counts s^{-1} keV^{-1}
Energy (keV)

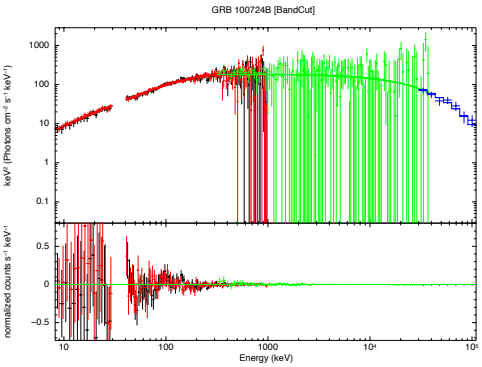
GRB 100724B [BandCut]
keV^2 (Photons cm^{-2} s^{-1} keV^{-1})
normalized counts s^{-1} keV^{-1}
Energy (keV)

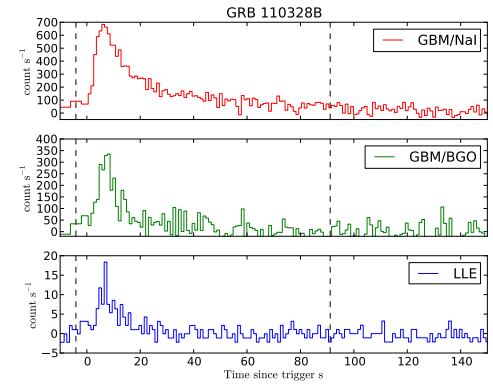
GRB 110328B
GBM/NaI
GBM/BGO
LLE
count s^{-1}
Time since trigger s

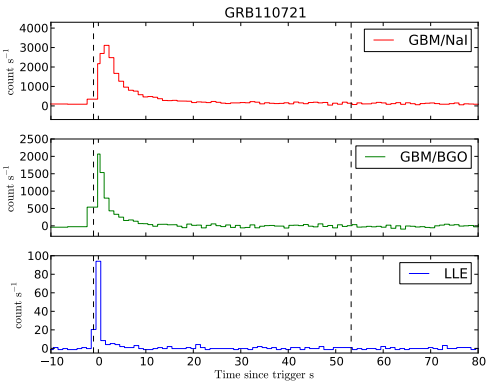
GRB110721
GBM/NaI
GBM/BGO
LLE
count s^{-1}
Time since trigger s

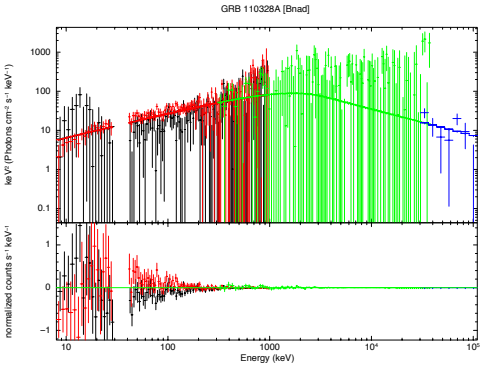
GRB 110328A [Bnad]
keV^2 (Photons cm^{-2} s^{-1} keV^{-1})
normalized counts s^{-1} keV^{-1}
Energy (keV)

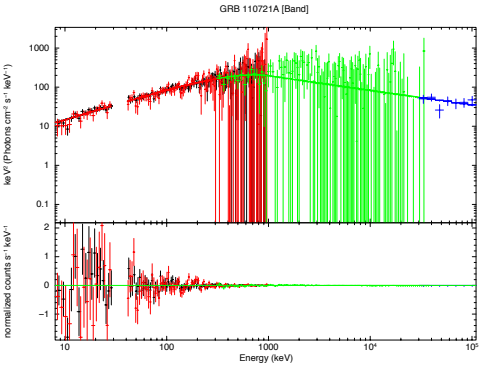
GRB 110721A [Band]
keV^2 (Photons cm^{-2} s^{-1} keV^{-1})
normalized counts s^{-1} keV^{-1}
Energy (keV)

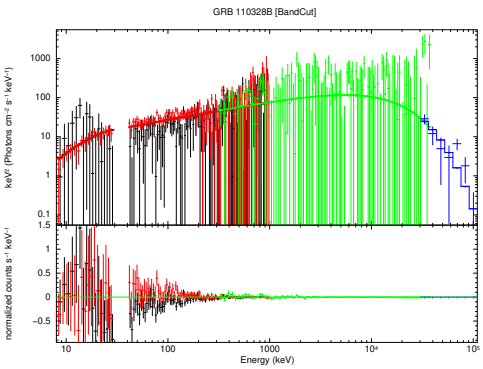
GRB 110328B [BandCut]
keV^2 (Photons cm^{-2} s^{-1} keV^{-1})
normalized counts s^{-1} keV^{-1}
Energy (keV)
eam27 6-Sep-2018 11:49

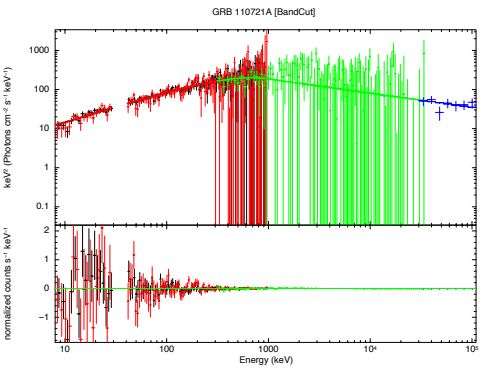
GRB 110721A [BandCut]
keV^2 (Photons cm^{-2} s^{-1} keV^{-1})
normalized counts s^{-1} keV^{-1}
Energy (keV)

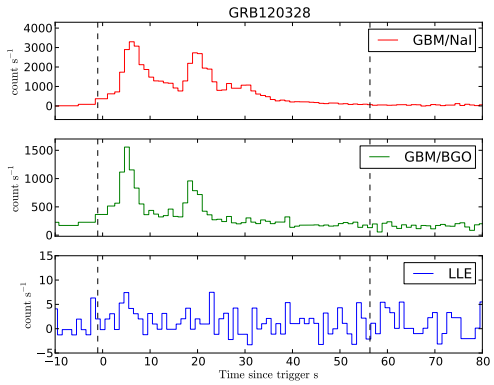
GRB120328
GBM/NaI
GBM/BGO
LLE
count s^{-1}
Time since trigger s

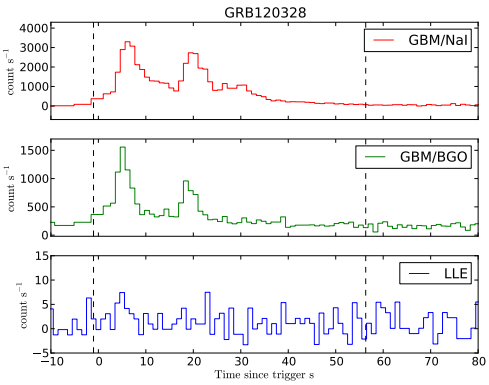
GRB120328
GBM/NaI
GBM/BGO
LLE
count s^{-1}
Time since trigger s

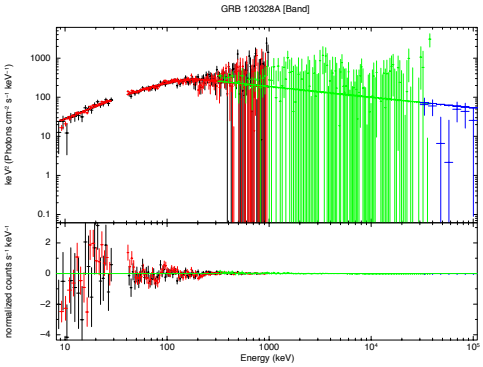
GRB 120328A [Band]
keV^2 (Photons cm^{-2} s^{-1} keV^{-1})
normalized counts s^{-1} keV^{-1}
Energy (keV)

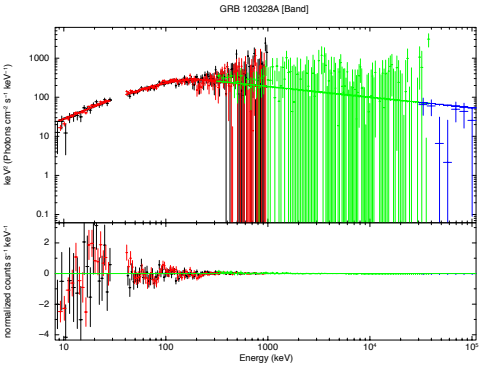
GRB 120328A [Band]
keV^2 (Photons cm^{-2} s^{-1} keV^{-1})
normalized counts s^{-1} keV^{-1}
Energy (keV)

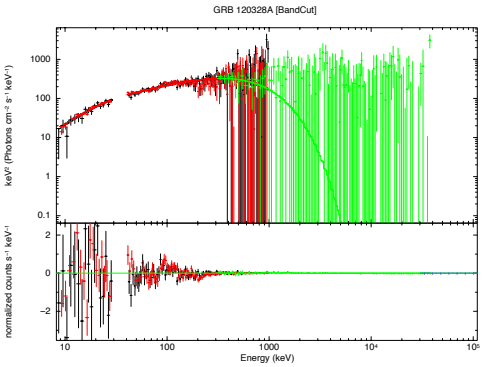
GRB 120328A [BandCut]
keV^2 (Photons cm^{-2} s^{-1} keV^{-1})
normalized counts s^{-1} keV^{-1}
Energy (keV)

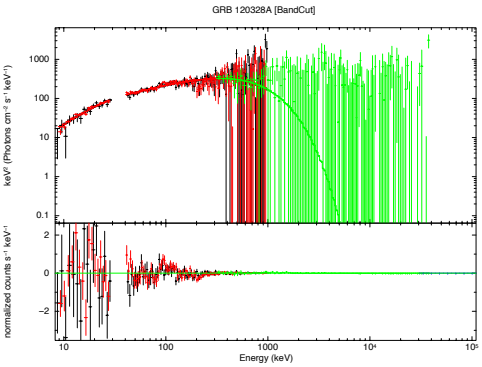
GRB 120328A [BandCut]
keV^2 (Photons cm^{-2} s^{-1} keV^{-1})
normalized counts s^{-1} keV^{-1}
Energy (keV)

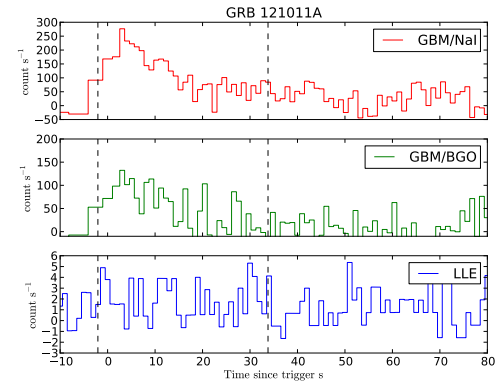
GRB 121011A
GBM/NaI
GBM/BGO
LLE
count s^{-1}
Time since trigger s

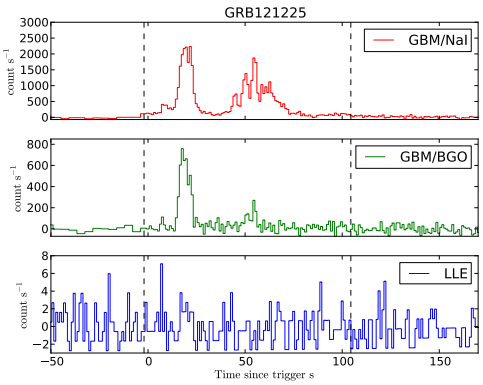
GRB121225
GBM/NaI
GBM/BGO
LLE
count s^{-1}
Time since trigger s

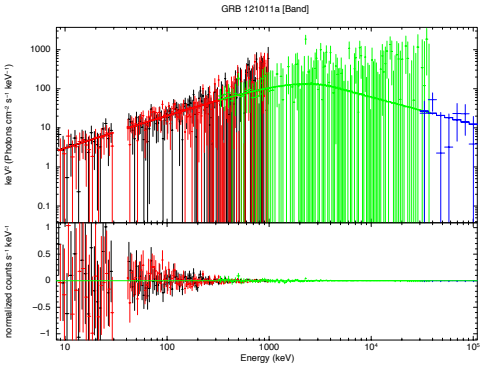
GRB 121011a [Band]
keV^2 (Photons cm^{-2} s^{-1} keV^{-1})
normalized counts s^{-1} keV^{-1}
Energy (keV)

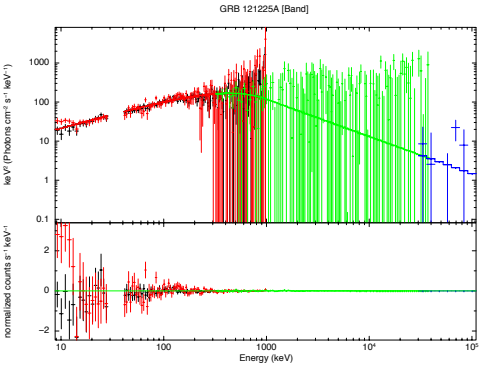
GRB 121225A [Band]
keV^2 (Photons cm^{-2} s^{-1} keV^{-1})
normalized counts s^{-1} keV^{-1}
Energy (keV)

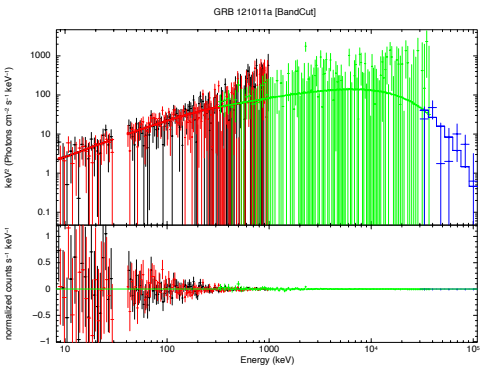
GRB 121011a [BandCut]
keV^2 (Photons cm^{-2} s^{-1} keV^{-1})
normalized counts s^{-1} keV^{-1}
Energy (keV)

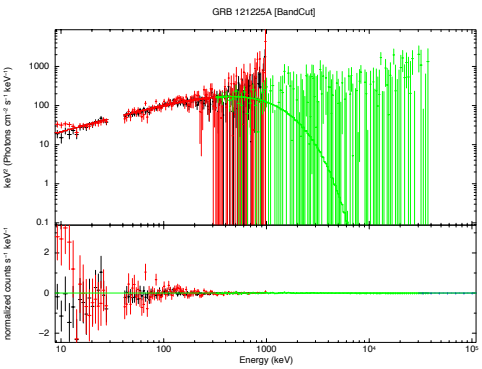
GRB 121225A [BandCut]
keV^2 (Photons cm^{-2} s^{-1} keV^{-1})
normalized counts s^{-1} keV^{-1}
Energy (keV)

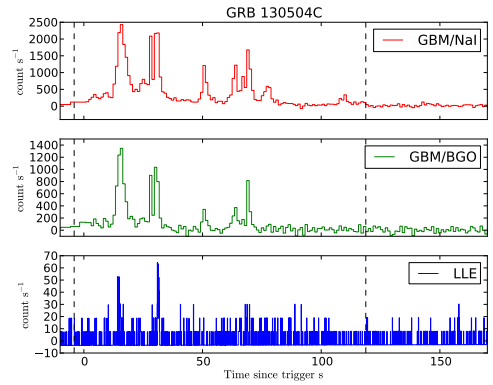
GRB 130504C
GBM/NaI
GBM/BGO
LLE
count s^{-1}
Time since trigger s

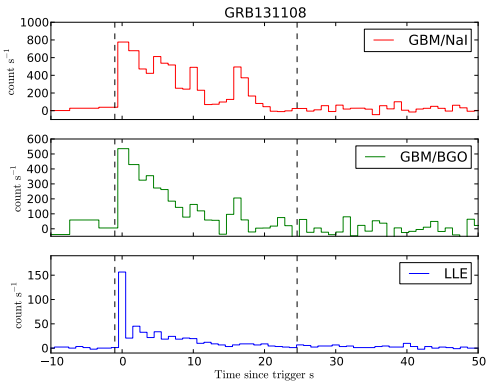
GRB131108
GBM/NaI
GBM/BGO
LLE
count s^{-1}
Time since trigger s

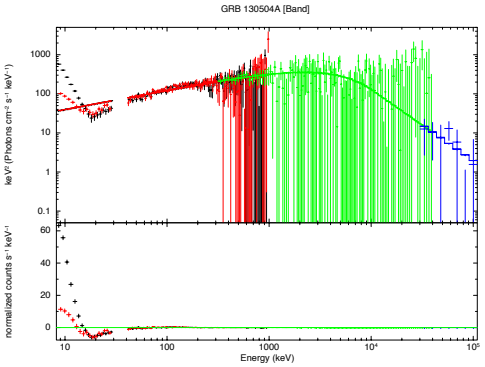
GRB 130504A [Band]
keV^2 (Photons cm^{-2} s^{-1} keV^{-1})
normalized counts s^{-1} keV^{-1}
Energy (keV)

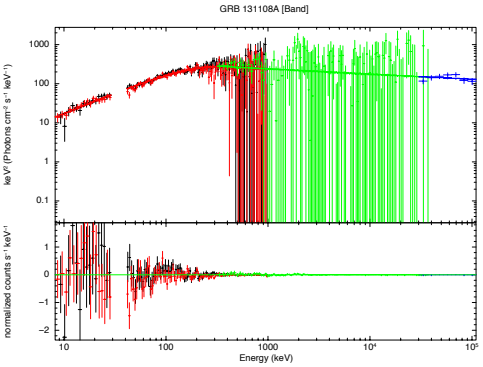
GRB 131108A [Band]
keV^2 (Photons cm^{-2} s^{-1} keV^{-1})
normalized counts s^{-1} keV^{-1}
Energy (keV)

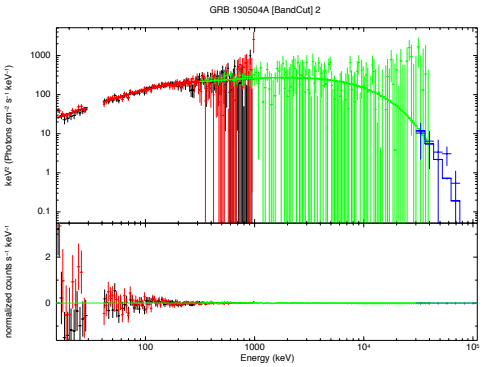
GRB 130504A [BandCut] 2
keV^2 (Photons cm^{-2} s^{-1} keV^{-1})
normalized counts s^{-1} keV^{-1}
Energy (keV)

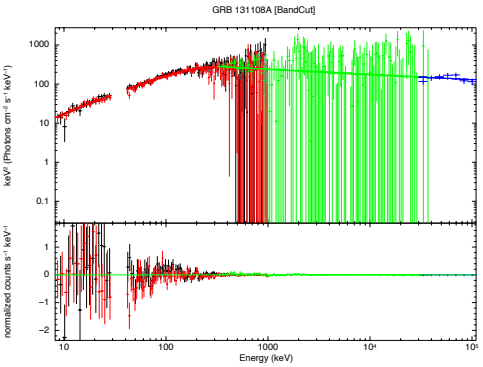
GRB 131108A [BandCut]
keV^2 (Photons cm^{-2} s^{-1} keV^{-1})
normalized counts s^{-1} keV^{-1}
Energy (keV)

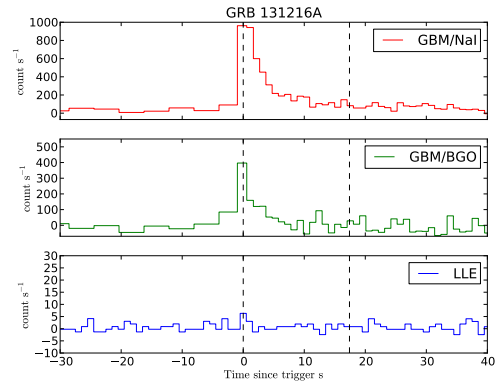
GRB 131216A
GBM/NaI
GBM/BGO
LLE
count s^{-1}
Time since trigger s

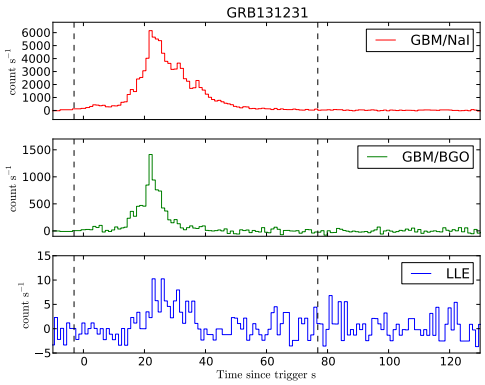
GRB131231
GBM/NaI
GBM/BGO
LLE
count s^{-1}
Time since trigger s

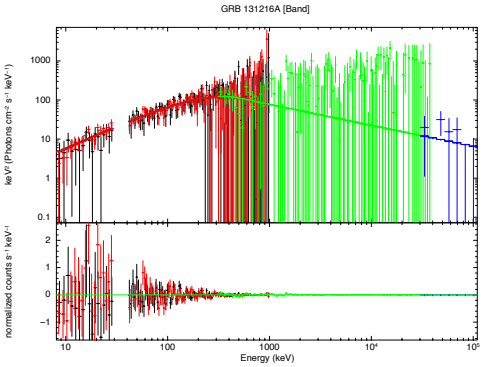
GRB 131216A [Band]
keV^2 (Photons cm^{-2} s^{-1} keV^{-1})
normalized counts s^{-1} keV^{-1}
Energy (keV)

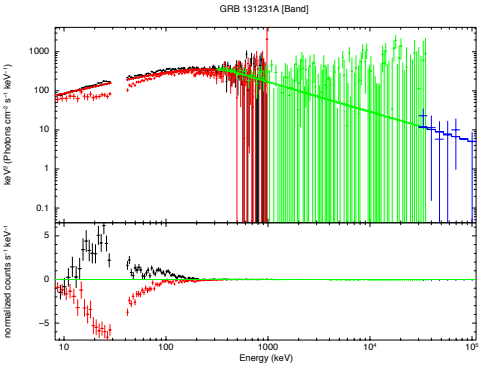
GRB 131231A [Band]
keV^2 (Photons cm^{-2} s^{-1} keV^{-1})
normalized counts s^{-1} keV^{-1}
Energy (keV)

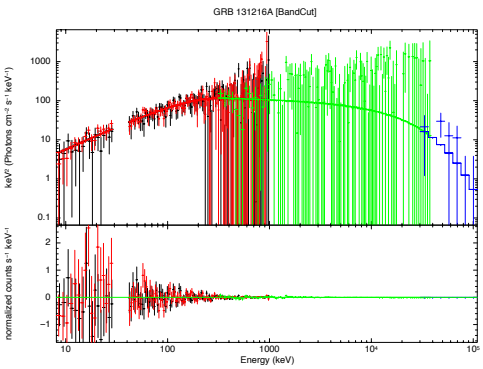
GRB 131216A [BandCut]
keV^2 (Photons cm^{-2} s^{-1} keV^{-1})
normalized counts s^{-1} keV^{-1}
Energy (keV)

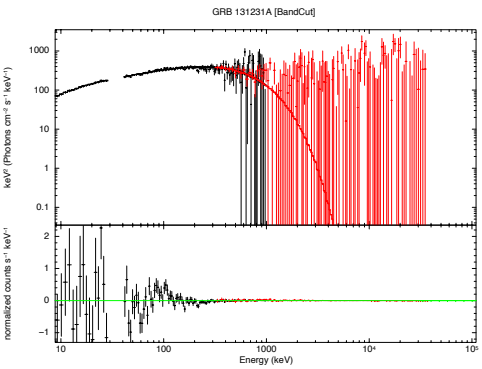
GRB 131231A [BandCut]
keV^2 (Photons cm^{-2} s^{-1} keV^{-1})
normalized counts s^{-1} keV^{-1}
Energy (keV)

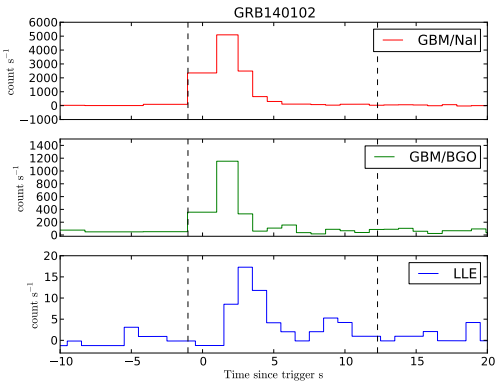
GRB140102
GBM/NaI
GBM/BGO
LLE
count s^{-1}
Time since trigger s

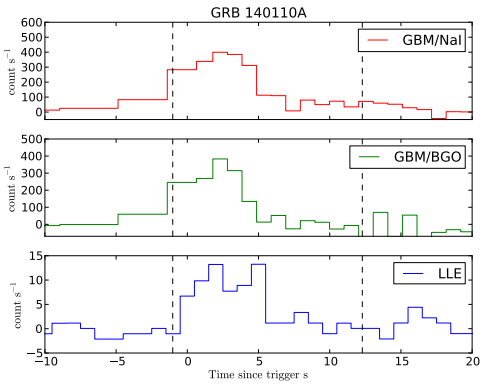
GRB 140110A
GBM/NaI
GBM/BGO
LLE
count s^{-1}
Time since trigger s

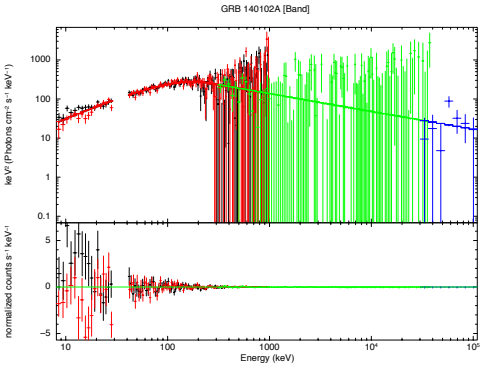
GRB 140102A [Band]
keV^2 (Photons cm^{-2} s^{-1} keV^{-1})
normalized counts s^{-1} keV^{-1}
Energy (keV)

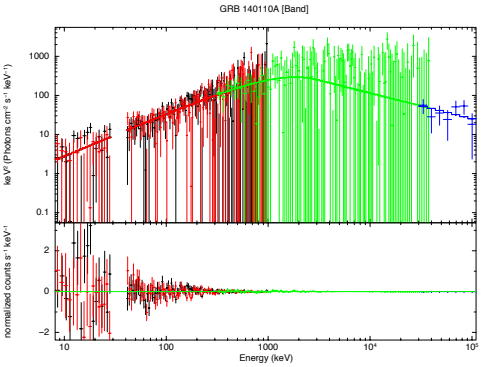
GRB 140110A [Band]
keV^2 (Photons cm^{-2} s^{-1} keV^{-1})
normalized counts s^{-1} keV^{-1}
Energy (keV)

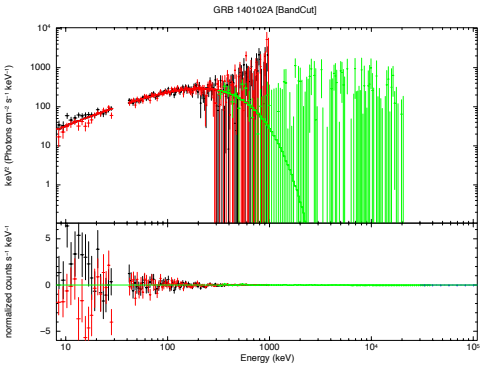
GRB 140102A [BandCut]
keV^2 (Photons cm^{-2} s^{-1} keV^{-1})
normalized counts s^{-1} keV^{-1}
Energy (keV)

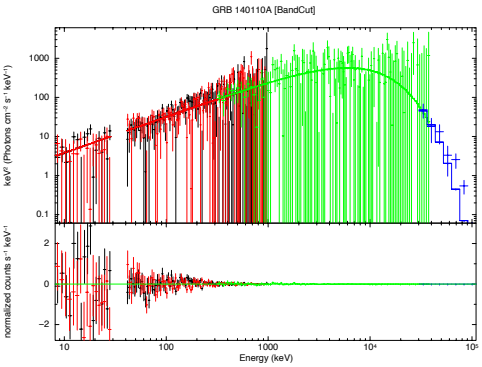
GRB 140110A [BandCut]
keV^2 (Photons cm^{-2} s^{-1} keV^{-1})
normalized counts s^{-1} keV^{-1}
Energy (keV)

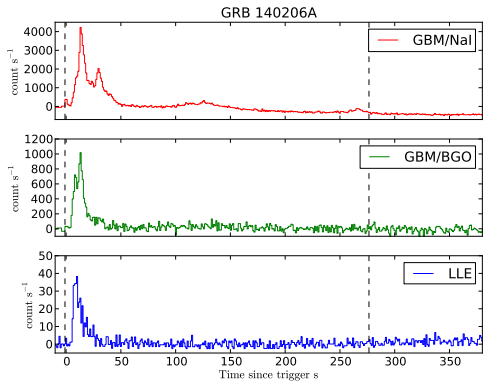
GRB 140206A
GBM/NaI
GBM/BGO
LLE
count s^{-1}
Time since trigger s

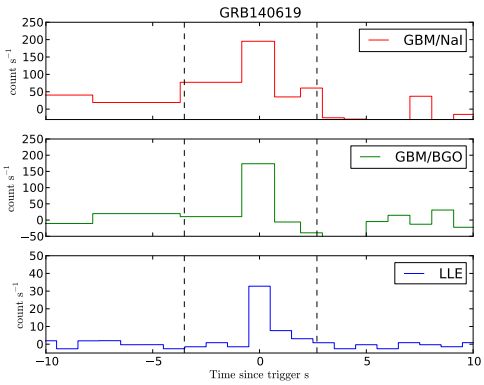
GRB140619
GBM/NaI
GBM/BGO
LLE
count s^{-1}
Time since trigger s

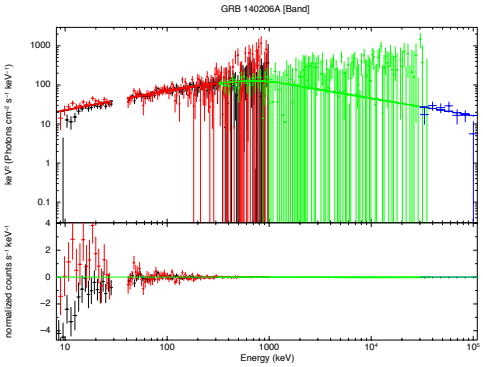
GRB 140206A [Band]
keV^2 (Photons cm^{-2} s^{-1} keV^{-1})
normalized counts s^{-1} keV^{-1}
Energy (keV)

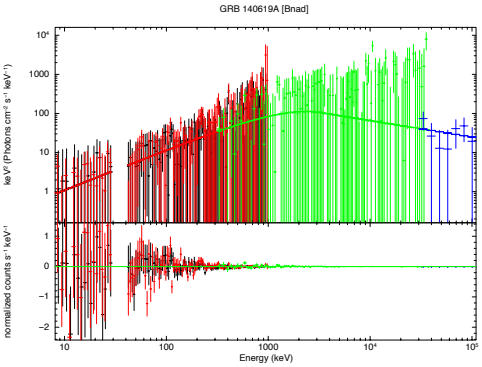
GRB 140619A [Bnad]
keV^2 (Photons cm^{-2} s^{-1} keV^{-1})
normalized counts s^{-1} keV^{-1}
Energy (keV)

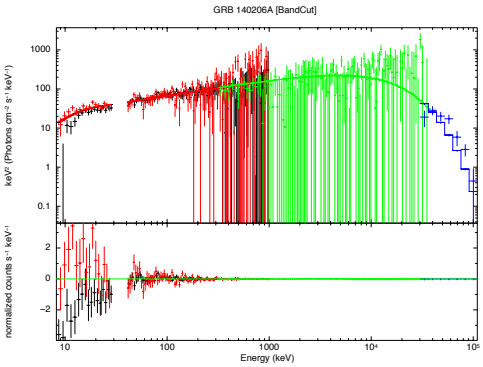
GRB 140206A [BandCut]
keV^2 (Photons cm^{-2} s^{-1} keV^{-1})
normalized counts s^{-1} keV^{-1}
Energy (keV)

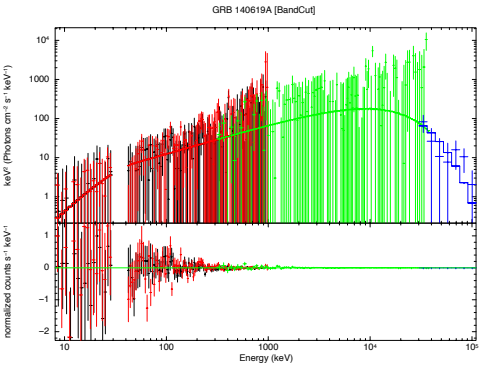
GRB 140619A [BandCut]
keV^2 (Photons cm^{-2} s^{-1} keV^{-1})
normalized counts s^{-1} keV^{-1}
Energy (keV)

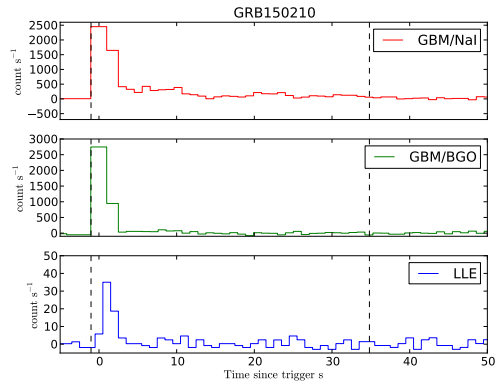
GRB150210
GBM/NaI
GBM/BGO
LLE
count s^{-1}
Time since trigger s

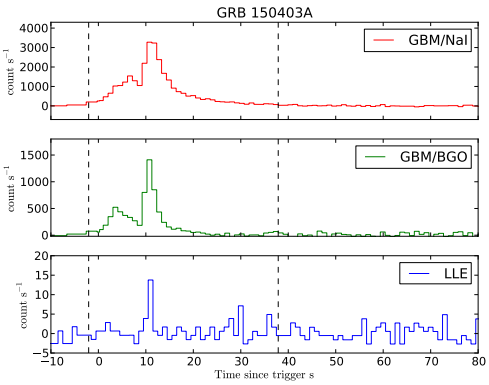
GRB 150403A
GBM/NaI
GBM/BGO
LLE
count s^{-1}
Time since trigger s

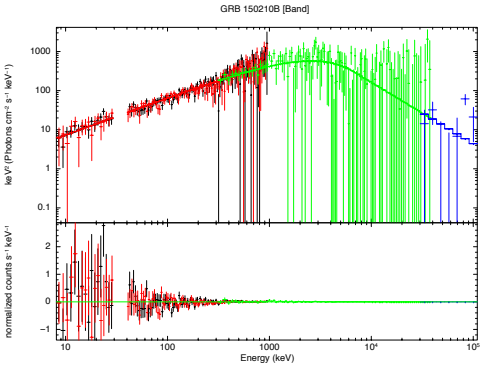
GRB 150210B [Band]
keV^2 (Photons cm^{-2} s^{-1} keV^{-1})
normalized counts s^{-1} keV^{-1}
Energy (keV)

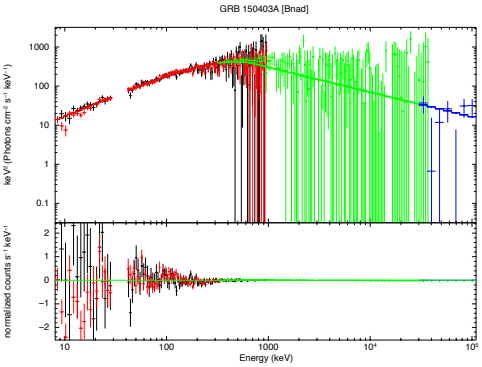
GRB 150403A [Bnad]
keV^2 (Photons cm^{-2} s^{-1} keV^{-1})
normalized counts s^{-1} keV^{-1}
Energy (keV)

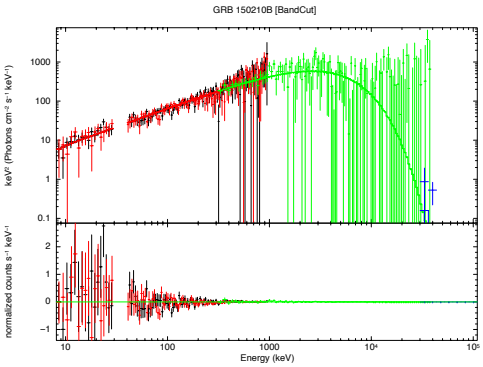
GRB 150210B [BandCut]
keV^2 (Photons cm^{-2} s^{-1} keV^{-1})
normalized counts s^{-1} keV^{-1}
Energy (keV)

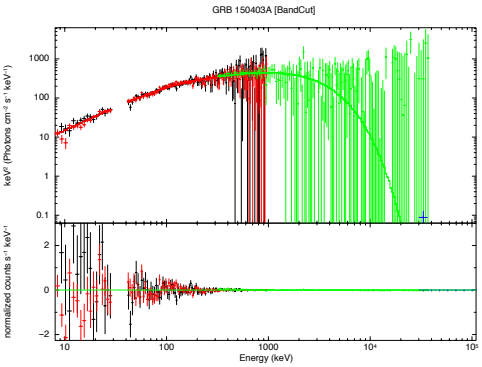
GRB 150403A [BandCut]
keV^2 (Photons cm^{-2} s^{-1} keV^{-1})
normalized counts s^{-1} keV^{-1}
Energy (keV)

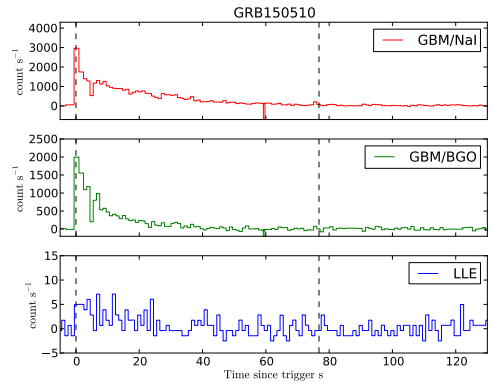
GRB150510
GBM/NaI
GBM/BGO
LLE
count s^{-1}
Time since trigger s

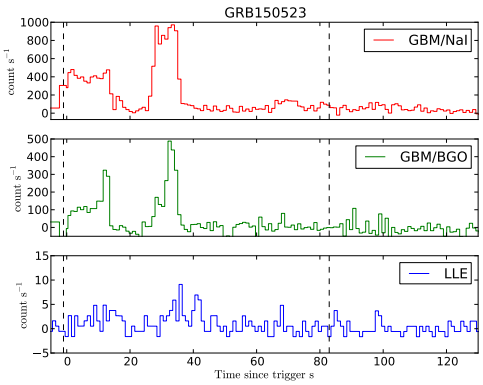
GRB150523
GBM/NaI
GBM/BGO
LLE
count s^{-1}
Time since trigger s

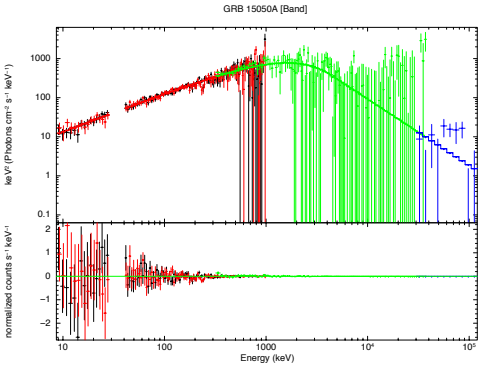
GRB 15050A [Band]
keV^2 (Photons cm^{-2} s^{-1} keV^{-1})
normalized counts s^{-1} keV^{-1}
Energy (keV)

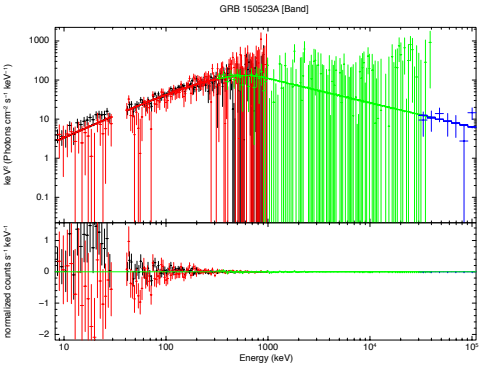
GRB 150523A [Band]
keV^2 (Photons cm^{-2} s^{-1} keV^{-1})
normalized counts s^{-1} keV^{-1}
Energy (keV)

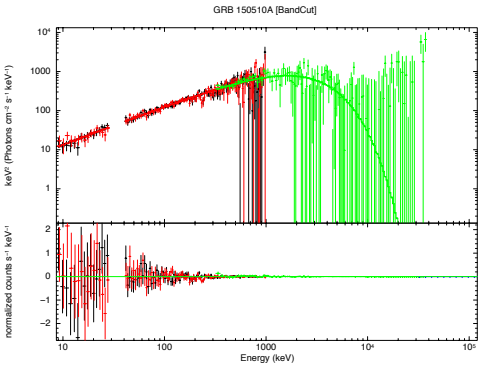
GRB 150510A [BandCut]
keV^2 (Photons cm^{-2} s^{-1} keV^{-1})
normalized counts s^{-1} keV^{-1}
Energy (keV)

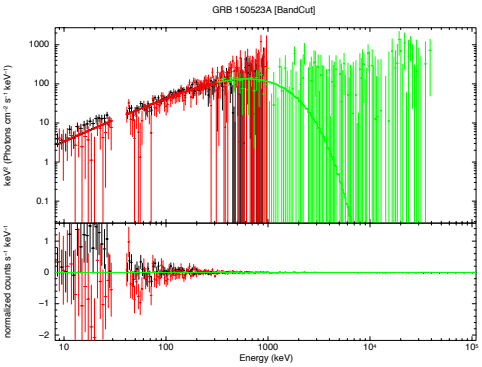
GRB 150523A [BandCut]
keV^2 (Photons cm^{-2} s^{-1} keV^{-1})
normalized counts s^{-1} keV^{-1}
Energy (keV)

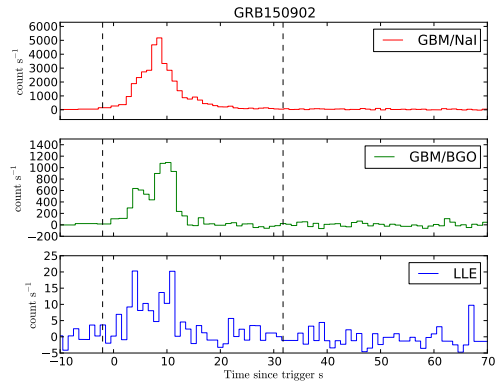
GRB150902
GBM/NaI
GBM/BGO
LLE
count s^{-1}
Time since trigger s

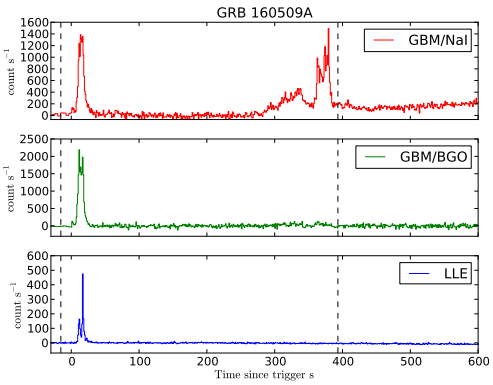
GRB 160509A
GBM/NaI
GBM/BGO
LLE
count s^{-1}
Time since trigger s

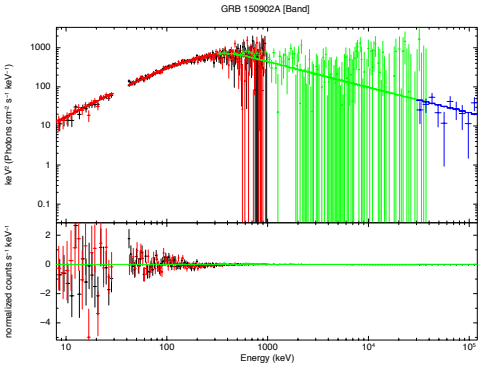
GRB 150902A [Band]
keV^2 (Photons cm^{-2} s^{-1} keV^{-1})
normalized counts s^{-1} keV^{-1}
Energy (keV)

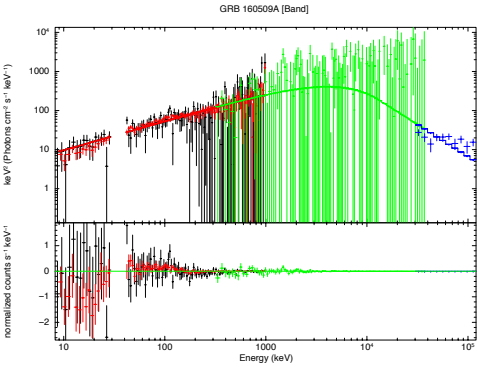
GRB 160509A [Band]
keV^2 (Photons cm^{-2} s^{-1} keV^{-1})
normalized counts s^{-1} keV^{-1}
Energy (keV)

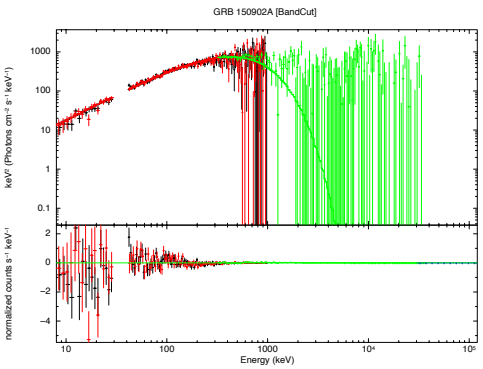
GRB 150902A [BandCut]
keV^2 (Photons cm^{-2} s^{-1} keV^{-1})
normalized counts s^{-1} keV^{-1}
Energy (keV)

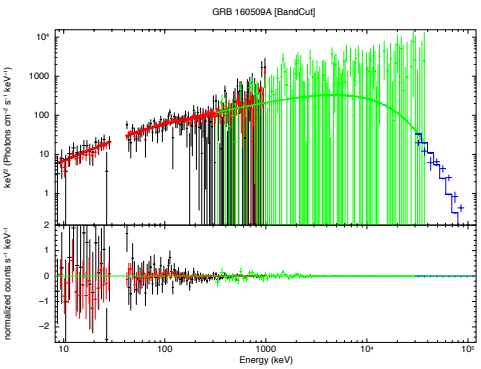
GRB 160509A [BandCut]
keV^2 (Photons cm^{-2} s^{-1} keV^{-1})
normalized counts s^{-1} keV^{-1}
Energy (keV)

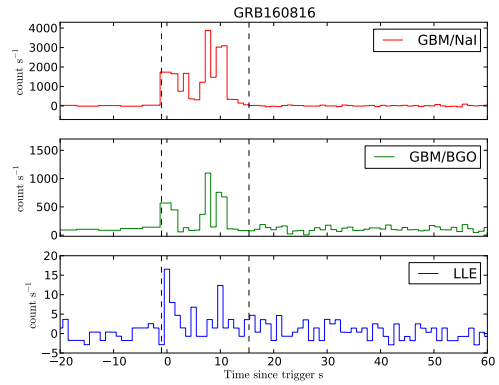
GRB160816
GBM/NaI
GBM/BGO
LLE
count s^{-1}
Time since trigger s

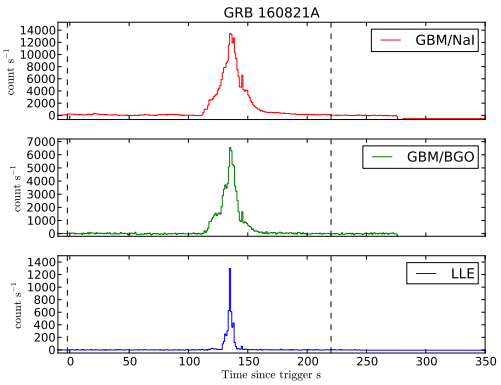
GRB 160821A
GBM/NaI
GBM/BGO
LLE
count s^{-1}
Time since trigger s

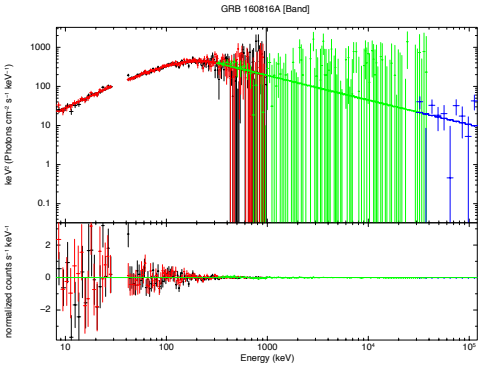
GRB 160816A [Band]
keV^2 (Photons cm^{-2} s^{-1} keV^{-1})
normalized counts s^{-1} keV^{-1}
Energy (keV)

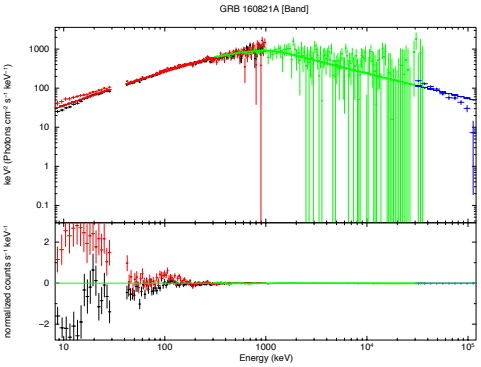
GRB 160821A [Band]
keV^2 (Photons cm^{-2} s^{-1} keV^{-1})
normalized counts s^{-1} keV^{-1}
Energy (keV)

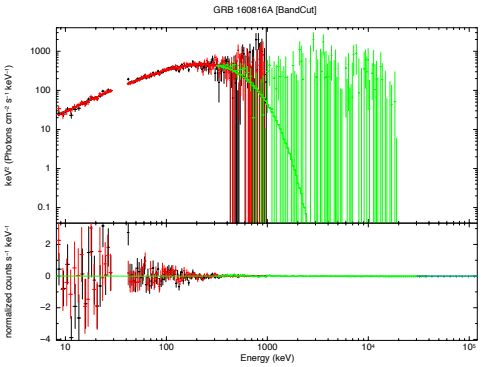
GRB 160816A [BandCut]
keV^2 (Photons cm^{-2} s^{-1} keV^{-1})
normalized counts s^{-1} keV^{-1}
Energy (keV)

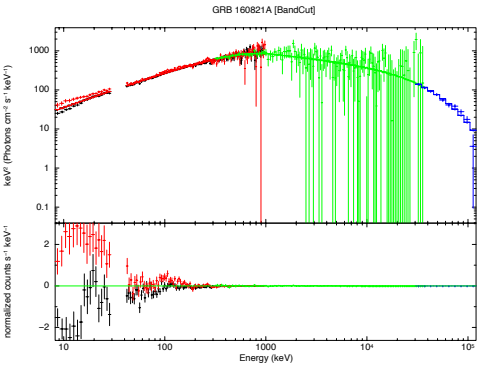
GRB 160821A [BandCut]
keV^2 (Photons cm^{-2} s^{-1} keV^{-1})
normalized counts s^{-1} keV^{-1}
Energy (keV)

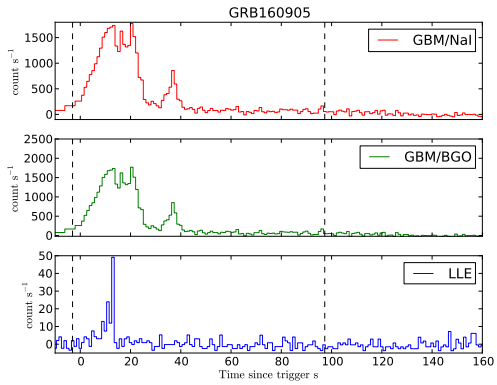
GRB160905
GBM/NaI
GBM/BGO
LLE
count s^{-1}
Time since trigger s

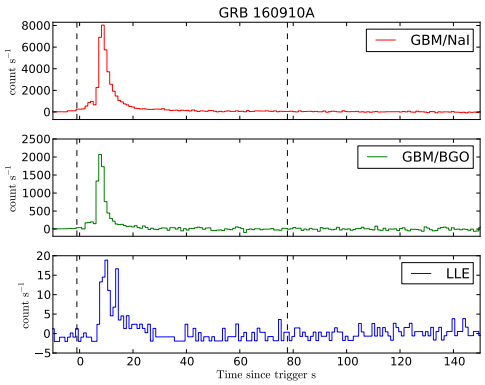
GRB 160910A
GBM/NaI
GBM/BGO
LLE
count s^{-1}
Time since trigger s

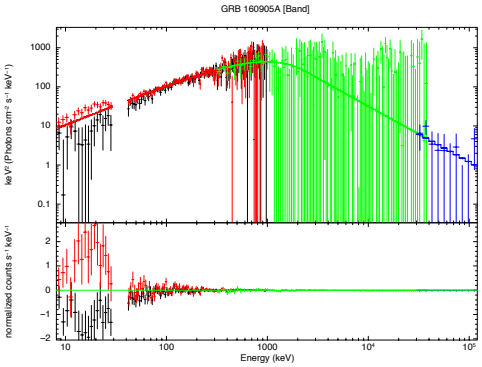
GRB 160905A [Band]
keV^2 (Photons cm^{-2} s^{-1} keV^{-1})
normalized counts s^{-1} keV^{-1}
Energy (keV)

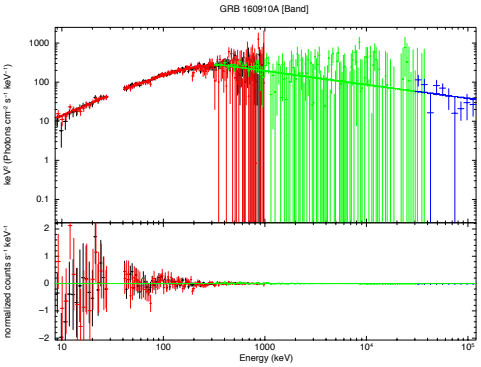
GRB 160910A [Band]
keV^2 (Photons cm^{-2} s^{-1} keV^{-1})
normalized counts s^{-1} keV^{-1}
Energy (keV)

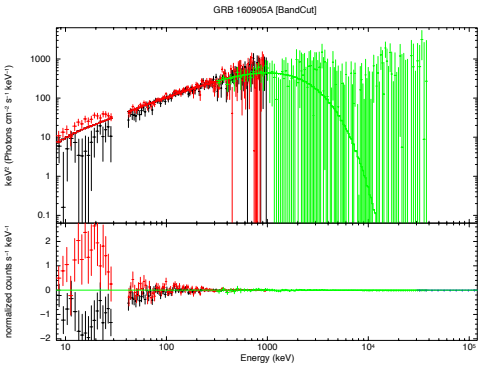
GRB 160905A [BandCut]
keV^2 (Photons cm^{-2} s^{-1} keV^{-1})
normalized counts s^{-1} keV^{-1}
Energy (keV)

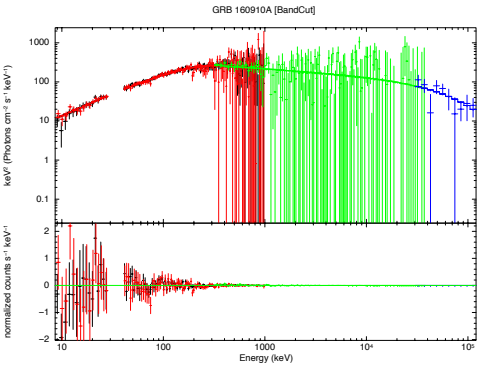
GRB 160910A [BandCut]
keV^2 (Photons cm^{-2} s^{-1} keV^{-1})
normalized counts s^{-1} keV^{-1}
Energy (keV)

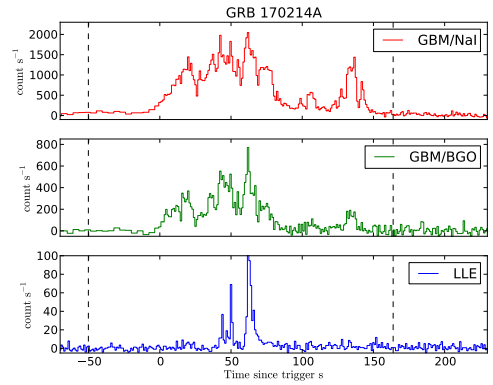
GRB 170214A
GBM/NaI
GBM/BGO
LLE
count s^{-1}
Time since trigger s

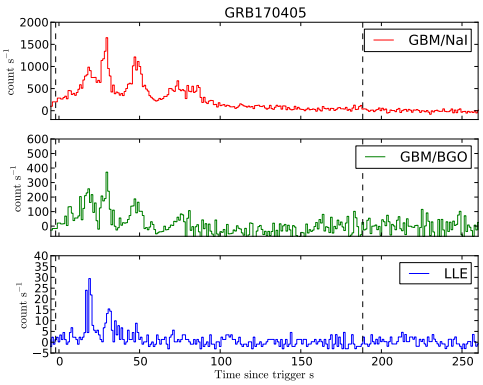
GRB170405
GBM/NaI
GBM/BGO
LLE
count s^{-1}
Time since trigger s

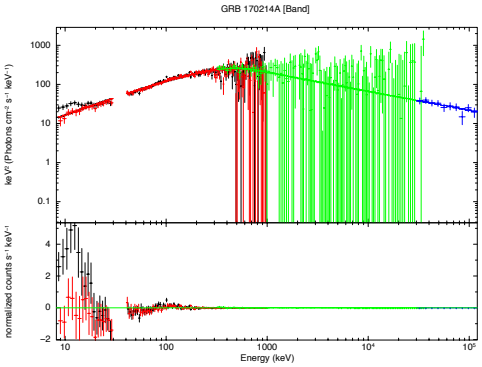
GRB 170214A [Band]
keV^2 (Photons cm^{-2} s^{-1} keV^{-1})
normalized counts s^{-1} keV^{-1}
Energy (keV)

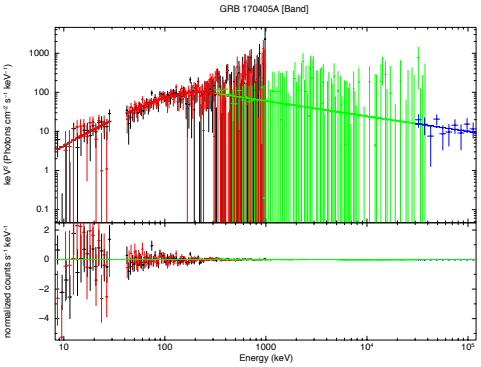
GRB 170405A [Band]
keV^2 (Photons cm^{-2} s^{-1} keV^{-1})
normalized counts s^{-1} keV^{-1}
Energy (keV)

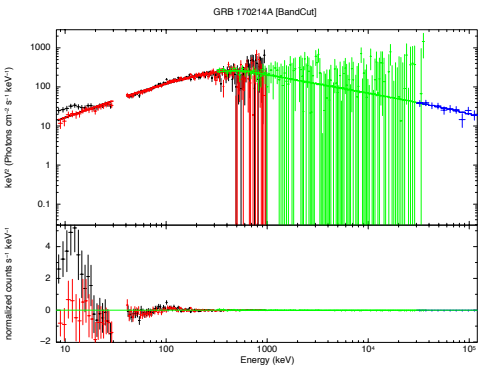
GRB 170214A [BandCut]
keV^2 (Photons cm^{-2} s^{-1} keV^{-1})
normalized counts s^{-1} keV^{-1}
Energy (keV)

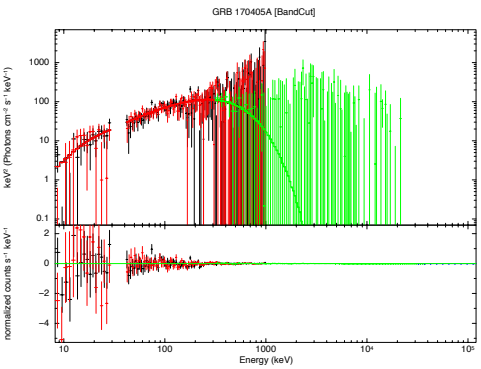
GRB 170405A [BandCut]
keV^2 (Photons cm^{-2} s^{-1} keV^{-1})
normalized counts s^{-1} keV^{-1}
Energy (keV)

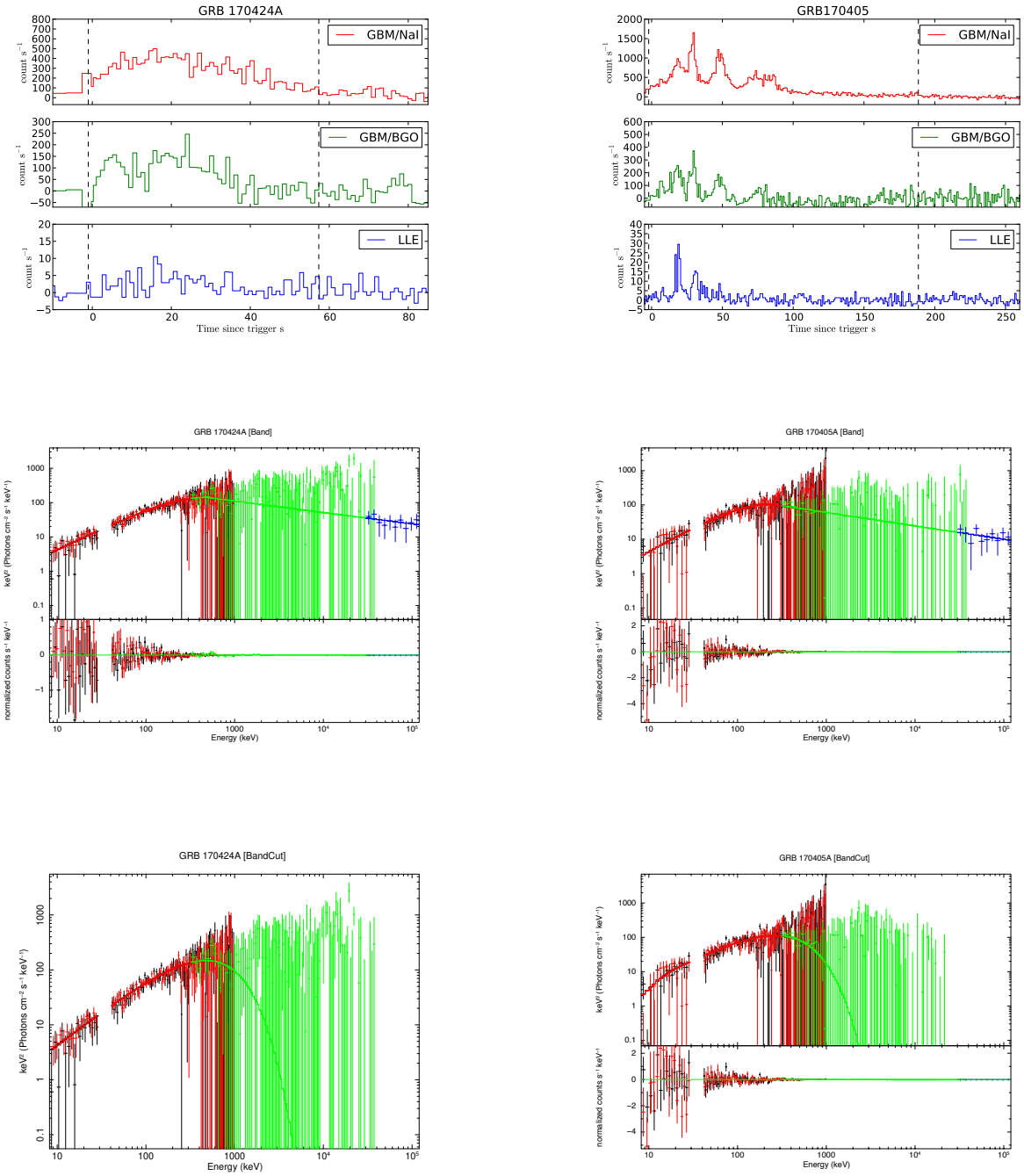

Figure A.3: LLE+GBM spectral joint-fit for a sample of 50 GRBs fitted with the simple Band and BandCut models, and the light curves for both GBM (NaI & BGO) and BAT.

Bibliography

Abdo A. A., et al., 2009a, Nat, 462, 331

Abdo A. A., et al., 2009b, ApJ, 706, L138

Abdo A. A., et al., 2011, ApJ, 734, L27

Ackermann M., et al., 2011, prl, 107, 241302

Ackermann M., et al., 2012, ApJ, 761, 91

Ackermann M., et al., 2013, The Astrophysical Journal Supplement Series, 209, 34

Amati L., 2003, Chinese Journal of Astronomy and Astrophysics Supplement, 3, 455

Amati L., 2006, MNRAS, 372, 233

Amati L., 2010, preprint, pp Proceedings of "The Shocking Universe – Gamma–Ray Bursts and High Energy Shock phenomena", Venice (Italy), September 14–18, 2009 (arXiv:1002.2232)

Amati L., et al., 2002, A&A, 390, 81

Amati L., Guidorzi C., Frontera F., Della Valle M., Finelli F., Landi R., Montanari E., 2008, MNRAS, 391, 577

Amati L., Frontera F., Guidorzi C., 2009, A&A, 508, 173

Aptekar R. L., et al., 1995, ssr, 71, 265

Arimoto M., Axelsson M., Racusin J., Bissaldi E., Kocevski D., 2015, GRB Coordinates Network, 18228, 1

Arimoto M., Axelsson M., Dirirsa F., Longo F., 2016, GRB Coordinates Network, 19836, 1

Atwood W. B., et al., 2009a, ApJ, 697, 1071

Atwood W. B., et al., 2009b, ApJ, 697, 1071

Band D. L., 1997, preprint, pp Proceedings of "The Eight Marcel Grossmann Meeting on General Relativity" held in Jerusalem, Israel, in June 1997 (arXiv:astro-ph/9712193)

Band D. L., Preece R. D., 2005, ApJ, 627, 319

Band D., et al., 1992, in Paciesas W. S., Fishman G. J., eds, Vol. 265, American Institute of Physics Conference Series. p. 169

Band D., et al., 1993, ApJ, 413, 281

Band D. L., Norris J. P., Bonnell J. T., 2004, ApJ, 613, 484

Baring M. G., Braby M. L., 2004, ApJ, 613, 460

Baring M. G., Harding A. K., 1997, ApJ, 481, L85

Barraud C., et al., 2003, A&A, 400, 1021

Barthelmy S. D., et al., 1994, in Fishman G. J., ed., Vol. 307, Gamma-Ray Bursts. p. 643, doi:10.1063/1.45819

Barthelmy S. D., et al., 2005, ssr, 120, 143

Basak R., Rao A. R., 2012a, in 39th COSPAR Scientific Assembly. p. 106

Basak R., Rao A. R., 2012b, ApJ, 745, 76

Basak R., Rao A. R., 2012c, ApJ, 745, 76

Basak R., Rao A. R., 2013a, MNRAS, 436, 3082

Basak R., Rao A. R., 2013b, ApJ, 768, 187

Belczynski K., Perna R., Bulik T., Kalogera V., Ivanova N., Lamb D. Q., 2006, ApJ, 648, 1110

Belczynski K., et al., 2016, A&A, 594, A97

Beniamini P., Granot J., 2016, MNRAS, 459, 3635

Beniamini P., Guetta D., Nakar E., Piran T., 2011, MNRAS, 416, 3089

Berger E., 2014, Annual Review of Astronomy and Astrophysics, 52, 43

Berger E., Rauch M., 2008, GRB Coordinates Network, 8542, 1

Bhat P. N., Fishman G. J., Meegan C. A., Wilson R. B., Brock M. N., Paciesas W. S., 1992, Nat, 359, 217

Bhat P. N., Fishman G. J., Meegan C. A., Wilson R. B., Kouveliotou C., Paciesas W. S., Pendleton G. N., Schaefer B. E., 1994, ApJ, 426, 604

Bhat P. N., et al., 2012, ApJ, 744, 141

Bissaldi E., Briggs M. S., Piron F., Takahashi H., Uehara T., 2009, GRB Coordinates Network, 9972, 1

Bissaldi E., et al., 2011, ApJ, 733, 97

Bissaldi E., Vianello G., Longo F., Desiante R., Racusin J., 2014, GRB Coordinates Network, 15791, 1

Bissaldi E., Vianello G., Yassine M., 2015, GRB Coordinates Network, 17864, 1

Blandford R., Eichler D., 1987, physrep, 154, 1

Bloom J. S., Frail D. A., Kulkarni S. R., 2003, ApJ, 594, 674

Bouvier A., et al., 2008, GRB Coordinates Network, 8183, 1

Burgess J. M., et al., 2014, ApJ, 784, 17

Burlon D., Ghirlanda G., Ghisellini G., Lazzati D., Nava L., Nardini M., Celotti A., 2008, ApJ, 685, L19

Burlon D., Ghirlanda G., Ghisellini G., Greiner J., Celotti A., 2009, A&A, 505, 569

Burrows D. N., et al., 2005, ssr, 120, 165

Butler N. R., Kocevski D., Bloom J. S., Curtis J. L., 2007, ApJ, 671, 656

Cabrera J. I., Firmani C., Avila-Reese V., Ghirlanda G., Ghisellini G., Nava L., 2007, MNRAS, 382, 342

Cai Y.-F., Li C., Saridakis E. N., Xue L.-Q., 2018, prd, 97, 103513

Campana S., et al., 2006, Nat, 442, 1008

Cannizzo J. K., Ukwatta T. N., Palmer D. M., Margutti R., de Pasquale M., 2009, GCN Report, 221, 1

Cash W., 1979, ApJ, 228, 939

Cavallo G., Rees M. J., 1978, MNRAS, 183, 359

Cenko S. B., Bloom J. S., Morgan A. N., Perley D. A., 2009, GRB Coordinates Network, 9053, 1

Chandra P., Frail D. A., 2009, GRB Coordinates Network, 9260, 1

Chapman R., Levan A. J., Priddey R. S., Tanvir N. R., Wynn G. A., King A. R., Davies M. B., 2007, in Napiwotzki R., Burleigh M. R., eds, Vol. 372, 15th European Workshop on White Dwarfs. p. 415

Cheng L. X., Ma Y. Q., Cheng K. S., Lu T., Zhou Y. Y., 1995, A&A, 300, 746

Chornock R., Perley D. A., Cenko S. B., Bloom J. S., 2009, GRB Coordinates Network, 9028, 1

Ciolfi R., 2016, ApJ, 829, 72

Costa E., et al., 1997, International Astronomical Union Circular, 6576, 1

Creminelli P., Vernizzi F., 2017, prl, 119, 251302

Crider A., Liang E. P., Preece R. D., Briggs M. S., Pendleton G. N., Paciesas W. S., Band D. L., Matteson J. L., 1999, ApJ, 519, 206

Cucchiara A., Fox D. B., Cenko S. B., Berger E., 2008, GRB Coordinates Network, 8713, 1

Cucchiara A., Fox D. B., Tanvir N., Berger E., 2009, GRB Coordinates Network, 9873, 1

Cucchiara A., et al., 2011, ApJ, 736, 7

Cutini S., Vasileiou V., Chiang J., 2009, GRB Coordinates Network, 9077, 1

Daigne F., Mochkovitch R., 1998, MNRAS, 296, 275

Dermer C. D., 2004, ApJ, 614, 284

Desiante R., Kocevski D., Vianello G., Longo F., Bissaldi E., Troja E., 2013, GRB Coordinates Network, 15333, 1

Dezalay J. P., Lestrade J. P., Barat C., Talon R., Sunyaev R., Terekhov O., Kuznetsov A., 1996, ApJ, 471, L27

Dingus B. L., 1995, Ap&SS, 231, 187

East W. E., Paschalidis V., Pretorius F., 2015, ApJ, 807, L3

Esposito J. A., et al., 1999, The Astrophysical Journal Supplement Series, 123, 203

Evans P. A., et al., 2009, MNRAS, 397, 1177

Fan Y., Piran T., 2006, MNRAS, 370, L24

Fargion D., Khlopov M. Y., Oliva P., 2018, International Journal of Modern Physics D, 27, 1841001

Fenimore E. E., 1998, in Olinto A. V., Frieman J. A., Schramm D. N., eds, Eighteenth Texas Symposium on Relativistic Astrophysics. p. 506 (arXiv:astro-ph/9705028)

Fenimore E. E., Ramirez-Ruiz E., 2000, preprint, pp Submitted to ApJ Report No. LA–UR 00–1791 (arXiv:astro-ph/0004176)

Fenimore E., RamirezRuiz E., 2000, preprint, pp Proceedings of "The Eight Marcel Grossmann Meeting on General Relativity" held in Jerusalem, Israel, in June 1997 (arXiv:astro-ph/0004176)

Fenimore E. E., Epstein R. I., Ho C., 1993a, Astronomy and Astrophysics Supplement Series, 97, 59

Fenimore E. E., Epstein R. I., Ho C., 1993b, Astronomy and Astrophysics Supplement Series, 97, 59

Fenimore E. E., Madras C. D., Nayakshin S., 1996, ApJ, 473, 998

Fishman G. J., Meegan C. A., 1995, Annual Review of Astronomy and Astrophysics, 33, 415

Flores H., et al., 2010, GRB Coordinates Network, 11317, 1

Ford L., et al., 1994, in Fishman G. J., ed., Vol. 307, Gamma-Ray Bursts. p. 261, doi:10.1063/1.45801

Ford L. A., et al., 1995, ApJ, 439, 307

Frail D. A., Kulkarni S. R., Nicastro L., Feroci M., Taylor G. B., 1997, Nat, 389, 261

Frail D. A., et al., 2001, ApJ, 562, L55

Freedman W. L., et al., 2001, ApJ, 553, 47

Frontera F., Amati L., Guidorzi C., Landi R., La Parola V., 2009, preprint, pp Presented at the Conference "Neutron Stars and gamma–ray Bursts", 30 March – 4 April, Cairo and Alexandria; to be published in AIP procs (on–line only) and in ASR (arXiv:0909.3451)

Fryer C. L., Woosley S. E., Hartmann D. H., 1999, ApJ, 526, 152

Fynbo J. P. U., Malesani D., Hjorth J., Sollerman J., Thoene C. C., 2008, GRB Coordinates Network, 8254, 1

Fynbo J. P. U., Malesani D., Jakobsson P., D'Elia V., 2009, GRB Coordinates Network, 9947, 1

Galama T. J., et al., 1998, Nat, 395, 670

Gao H., Zhang B., 2015, ApJ, 801, 103

Gehrels N., Mészáros P., 2012, Science, 337, 932

Gehrels N., Razzaque S., 2013, Frontiers of Physics, 8, 661

Gehrels N., Swift 2004, in American Astronomical Society Meeting Abstracts. p. 116.01

Gehrels N., Swift Team 2005, in American Astronomical Society Meeting Abstracts. p. 96.01

Gendre B., et al., 2013, preprint, pp 7th Huntsville Gamma–Ray Burst Symposium, GRB 2013: paper 19 in eConf Proceedings C1304143,8 pages, 1 color figure (arXiv:1308.1001)

Ghirlanda G., Celotti*A., GhiselliniG.,* 2002*, A&A,* 393*,* 409

Ghirlanda G., Ghisellini G., Lazzati D., 2004a, ApJ, 616, 331

Ghirlanda G., Ghisellini G., Lazzati D., 2004b, ApJ, 616, 331

Ghirlanda G., Nava L., Ghisellini G., Celotti A., Firmani C., 2009, A&A, 496, 585

Ghirlanda G., Nava L., Ghisellini G., 2010a, A&A, 511, A43

Ghirlanda G., Nava L., Ghisellini G., 2010b, A&A, 511, A43

Ghirlanda G., Nava L., Ghisellini G., Celotti A., Burlon D., Covino S., Melandri A., 2012, MNRAS, 420, 483

Ghirlanda G., et al., 2018, A&A, 609, A112

Ghisellini G., Celotti A., Lazzati D., 2000, MNRAS, 313, L1

Ghisellini G., Ghirlanda G., Nava L., Celotti A., 2010, MNRAS, 403, 926

Giannios D., Mimica P., Aloy M. A., 2008, A&A, 478, 747

Giblin T. W., Connaughton V., van Paradijs J., Preece R. D., Briggs M. S., Kouveliotou C., Wijers R. A. M. J., Fishman G. J., 2002, ApJ, 570, 573

Gill R., Thompson C., 2014, ApJ, 796, 81

Giuliani A., et al., 2008, A&A, 491, L25

Goldstein A., et al., 2012, The Astrophysical Journal Supplement Series, 199, 19

Goldstein A., Preece R. D., Mallozzi R. S., Briggs M. S., Fishman G. J., Kouveliotou C., Paciesas W. S., Burgess J. M., 2013, The Astrophysical Journal Supplement Series, 208, 21

Goldstein A., et al., 2017, ApJ, 848, L14

Golenetskii S. V., Mazets E. P., Aptekar R. L., Ilinskii V. N., 1983, Nat, 306, 451

Goodman J., 1986, ApJ, 308, L47

Granot J., Cohen-Tanugi J., Silva E. d. C. e., 2008, ApJ, 677, 92

Granot J., for the Fermi LAT Collaboration the GBM Collaboration 2010, preprint, pp Proceedings of "The Shocking Universe – Gamma–Ray Bursts and High Energy Shock phenomena", Venice (Italy), September 14–18, 2009 (arXiv:1003.2452)

Granot J., Piran T., Bromberg O., Racusin J. L., Daigne F., 2015, ssr, 191, 471

Green M. A., Moffat J. W., Toth V. T., 2018, Physics Letters B, 780, 300

Gruber D., 2012, GRB Coordinates Network, 13383, 1

Gruber D J., et al., 2011, A&A, 531, A20

Gruber D., et al., 2014, The Astrophysical Journal Supplement Series, 211, 12

Guidorzi C., Frontera F., Montanari E., Amati F. R. L., Gomboc A., Hurley K., Mundell C. G., 2005, Nuovo Cimento C Geophysics Space Physics C, 28, 307

Guiriec S., et al., 2010, ApJ, 725, 225

Guiriec S., et al., 2011, ApJ, 727, L33

Guiriec S., et al., 2013, ApJ, 770, 32

Gupta N., Zhang B., 2008, MNRAS, 384, L11

Hakkila J., Giblin T. W., 2004, ApJ, 610, 361

Hakkila J., Preece R. D., 2011, ApJ, 740, 104

Hakkila J., Preece R. D., 2014, ApJ, 783, 88

Hakkila J., Giblin T. W., Norris J. P., Fragile P. C., Bonnell J. T., 2008, ApJ, 677, L81

Hanabata Y., et al., 2009, GRB Coordinates Network, 9270, 1

Hascoët R., Daigne F., Mochkovitch R., Vennin V., 2012, MNRAS, 421, 525

Heise J., in 't Zand J., 2001, preprint, pp Proceedings of the jan van Paradijs Memorial Symposium "From X–ray Binaries to Gamma Ray Bursts", held in Amsterdam, june 6–8, 2001 (arXiv:astro-ph/0112353)

Heise J., in't Zand J., 2003, in van den Heuvel E. P., Kaper L., Rol E., Wijers R. A. M. J., eds, Vol. 308, From X-ray Binaries to Gamma-Ray Bursts: Jan van Paradijs Memorial Symposium. p. 365

Hjorth J., et al., 2003, Nat, 423, 847

Hoversten E. A., et al., 2008, GRB Coordinates Network, 8687, 1

Hu Y.-D., Liang E.-W., Xi S.-Q., Peng F.-K., Lu R.-J., Lü L.-Z., Zhang B., 2014, ApJ, 789, 145

Hughes E. B., et al., 1980, IEEE Transactions on Nuclear Science, 27, 364

Inoue T., Asano K., Ioka K., 2011, ApJ, 734, 77

Ioka K., Nakamura T., 2001, ApJ, 554, L163

Jakobsson P., et al., 2006, in Holt S. S., Gehrels N., Nousek J. A., eds, American Institute of Physics Conference Series Vol. 836, Gamma-Ray Bursts in the Swift Era. pp 552–557 (arXiv:astro-ph/0602071), doi:10.1063/1.2207953

Jenke P., Xiong S., 2014, GRB Coordinates Network, 15644, 1

Jin Z.-P., et al., 2013, ApJ, 774, 114

Kanbach G., et al., 1988, ssr, 49, 69

Kaneko Y., Preece R. D., Briggs M. S., Paciesas W. S., Meegan C. A., Band D. L., 2006, The Astrophysical Journal Supplement Series, 166, 298

Kargatis V. E., Liang E. P., Hurley K. C., Barat C., Eveno E., Niel M., 1994, ApJ, 422, 260

Kasen D., Badnell N. R., Barnes J., 2013, ApJ, 774, 25

Katz J., 1994, ApJ, 422, 248

Katz J. I., 1997, ApJ, 490, 633

Kippen R. M., Paciesas W. S., Pendleton G. N., Swartz D. A., 2000, IEEE Transactions on Nuclear Science, 47, 2050

Klebesadel R. W., Strong I. B., Olson R. A., 1973a, ApJ, 182, L85

Klebesadel R. W., Strong I. B., Olson R. A., 1973b, ApJ, 182, L85

Kobayashi S., Sari R., 2001, ApJ, 551, 934

Kobayashi S., Piran T., Sari R., 1997, ApJ, 490, 92

Kocevski D., 2012, ApJ, 747, 146

Kocevski D., Liang E., 2003, in Ricker G. R., Vanderspek R. K., eds, Vol. 662, Gamma-Ray Burst and Afterglow Astronomy 2001: A Workshop Celebrating the First Year of the HETE Mission. pp 130–133, doi:10.1063/1.1579318

Kocevski D., Ryde F., Liang E., 2003, ApJ, 596, 389

Kocevski D., Racusin J. L., Sonbas E., 2012, GRB Coordinates Network, 14101, 1

Kocevski D., Omodei N., Racusin J., Zhu S., Guiriec S., Troja E., 2013, GRB Coordinates Network, 15115, 1

Koshut T. M., 1996, PhD thesis, UNIVERSITY OF ALABAMA IN HUNTSVILLE.

Kouveliotou C., Meegan C. A., Fishman G. J., Bhat N. P., Briggs M. S., Koshut T. M., Paciesas W. S., Pendleton G. N., 1993, ApJ, 413, L101

Krolik J. H., Pier E. A., 1991, ApJ, 373, 277

Kruehler T., Malesani D., Xu D., Fynbo J. P. U., Levan A. J., Tanvir N. R., D'Elia V., Perley D., 2013, GRB Coordinates Network, 14264, 1

Kruehler T., Schady P., Greiner J., Tanvir N. R., 2017, GRB Coordinates Network, 20686, 1

Kumar P., 1999, ApJ, 523, L113

Kumar P., Narayan R., 2009, MNRAS, 395, 472

Kumar P., Panaitescu A., 2000, ApJ, 541, L51

Kumar P., Zhang B., 2015, physrep, 561, 1

Lazarian A., Beresnyak A., Yan H., Opher M., Liu Y., 2009, ssr, 143, 387

Lazarian A., Eyink G. L., Vishniac E. T., Kowal G., 2015, in Lazarian A., de Gouveia Dal Pino E. M., Melioli C., eds, Vol. 407, Magnetic Fields in Diffuse Media. p. 311 (arXiv:1407.6356)

Lazzati D., 2005, MNRAS, 357, 722

Levan A. J., et al., 2014, ApJ, 781, 13

Li B., Li Z., 2012, Research in Astronomy and Astrophysics, 12, 1519

Li L.-X., Paczyński B., 1998, ApJ, 507, L59

Liang E. P., Kargatis V., 1996, in Kouveliotou C., Briggs M. F., Fishman G. J., eds, Vol. 384, American Institute of Physics Conference Series. pp 202–203, doi:10.1063/1.51664

Liang E., Zhang B., 2005, ApJ, 633, 611

Liang E., Zhang B., 2006, MNRAS, 369, L37

Liang E.-W., Yi S.-X., Zhang J., Lü H.-J., Zhang B.-B., Zhang B., 2010, ApJ, 725, 2209

Lichti G. G., et al., 2004, Baltic Astronomy, 13, 311

Lien A., et al., 2016, ApJ, 829, 7

Lipunov V., Kornilov V., Gorbovskoy E., Lipunova G., Vlasenko D., Panchenko I., Tyurina N., Grinshpun V., 2018, na, 63, 48

Lithwick Y., Sari R., 2001, ApJ, 555, 540

Lloyd N. M., Petrosian V., 2000, in Kippen R. M., Mallozzi R. S., Fishman G. J., eds, Vol. 526, Gamma-ray Bursts, 5th Huntsville Symposium. pp 465–469 (arXiv:astro-ph/9912205)

Longo F., Bissaldi E., Arimoto M., Zhu S., 2015, GRB Coordinates Network, 17667, 1

Longo F., et al., 2016, GRB Coordinates Network, 19413, 1

Lu R. J., Qin Y. P., Zhang Z. B., Yi T. F., 2006, MNRAS, 367, 275

Lu R. J., Hou S. J., Liang E.-W., 2010, ApJ, 720, 1146

Lu R.-J., Wei J.-J., Liang E.-W., Zhang B.-B., Lü H.-J., Lü L.-Z., Lei W.-H., Zhang B., 2012, ApJ, 756, 112

Lyutikov M., Blandford R., 2003, preprint, pp astro–ph/0312347 (arXiv:astro-ph/0312347)

MacFadyen A. I., Woosley S. E., 1999, ApJ, 524, 262

Malesani D., et al., 2009, GRB Coordinates Network, 9942, 1

McEnery J., Chiang J., Omodei N., Nakamori T., 2010, GRB Coordinates Network, 10333, 1

McEnery J. E., Longo F., Bissaldi E., Kocevski D., 2016, GRB Coordinates Network, 19890, 1

McMahon E., Kumar P., Piran T., 2006, MNRAS, 366, 575

Medvedev M. V., Loeb A., 1999, ApJ, 526, 697

Meegan C., et al., 2009, ApJ, 702, 791

Mészáros P., 2001, Science, 291, 79

Mészáros P., Rees M. J., 1997, ApJ, 482, L29

Metzger M. R., 1997, in American Astronomical Society Meeting Abstracts. p. 55.02

Metzger B. D., Berger E., 2012, ApJ, 746, 48

Metzger B. D., et al., 2010, MNRAS, 406, 2650

Molinari E., et al., 2007, A&A, 469, L13

Murakami T., Yonetoku D., Izawa H., Ioka K., 2003, Publications of the Astronomical Society of Japan, 55, L65

Mészáros P., 2002, Annual Review of Astronomy and Astrophysics, 40, 137

Mészáros P., 2006a, Reports on Progress in Physics, 69, 2259

Mészáros P., 2006b, Reports on Progress in Physics, 69, 2259

Mészáros P., Rees M. J., 1993, ApJ, 405, 278

Mészáros P., Rees M. J., 1994, MNRAS, 269, L41

Mészáros P., Rees M. J., 1997a, ApJ, 476, 232

Mészáros P., Rees M., 1997b, ApJ, 476, 232

Mészáros P., Rees M. J., Papathanassiou H., 1994, ApJ, 432, 181

Nappo F., Ghisellini G., Ghirlanda G., Melandri A., Nava L., Burlon D., 2014, MNRAS, 445, 1625

Narayan R., Paczynski B., Piran T., 1992, ApJ, 395, L83

Nava L., 2018, International Journal of Modern Physics D, 27, 1842003

Nava L., Ghirlanda G., Ghisellini G., Firmani C., 2008, MNRAS, 391, 639

Nava L., Ghirlanda G., Ghisellini G., Celotti A., 2010, arXiv e-prints, p. arXiv:1004.1410

Nava L., Ghirlanda G., Ghisellini G., Celotti A., 2011, A&A, 530, A21

Nava L., et al., 2012, MNRAS, 421, 1256

Nava L., Sironi L., Ghisellini G., Celotti A., Ghirlanda G., 2013, MNRAS, 433, 2107

Norris J. P., Bonnell J. T., 2006, ApJ, 643, 266

Norris J. P., Share G. H., Messina D. C., Dennis B. R., Desai U. D., Cline T. L., Matz S. M., Chupp E. L., 1986, ApJ, 301, 213

Norris J. P., Nemiroff R. J., Bonnell J. T., Scargle J. D., Kouveliotou C., Paciesas W. S., Meegan C. A., Fishman G. J., 1996, ApJ, 459, 393

Norris J. P., Marani G. F., Bonnell J. T., 2000, ApJ, 534, 248

Norris J. P., Bonnell J. T., Kazanas D., Scargle J. D., Hakkila J., Giblin T. W., 2005, ApJ, 627, 324

Oganesyan G., Nava L., Ghirlanda G., Celotti A., 2017, ApJ, 846, 137

Oganesyan G., Nava L., Ghirlanda G., Celotti A., 2018, A&A, 616, A138

Ohno M., Fermi LAT/GBM Collaboration 2010, in The Energetic Cosmos: from Suzaku to ASTRO-H. pp 394–395

Ohno M., Cutini S., McEnery J., Chiang J., Koerding E., 2009, GRB Coordinates Network, 9021, 1

Omodei N., McEnery J., 2013, GRB Coordinates Network, 14675, 1

Paciesas W. S., Pendleton G. N., Kouveliotou C., Fishman G. J., Meegan C. A., Wilson R. B., 1992, in Paciesas W. S., Fishman G. J., eds, Vol. 265, American Institute of Physics Conference Series. p. 190

Paciesas W. S., et al., 2012, The Astrophysical Journal Supplement Series, 199, 18

Paczynski B., 1986, ApJ, 308, L43

Paczynski B., 1990, ApJ, 363, 218

Paczynski B., Rhoads J. E., 1993, ApJ, 418, L5

Page K. L., et al., 2009, MNRAS, 400, 134

Page K. L., et al., 2011, MNRAS, 416, 2078

Panaitescu A., Kumar P., 2001, ApJ, 560, L49

Panaitescu A., Mészáros P., 2000, ApJ, 544, L17

Panaitescu A., Mészáros P., 1998, preprint, p. submitted to the ApJ (10/05/98) (arXiv:astro-ph/9810258)

Pe'Er A., Mészáros P., Rees M. J., 2006, in Holt S. S., Gehrels N., Nousek J. A., eds, Vol. 836, Gamma-Ray Bursts in the Swift Era. pp 181–184, doi:10.1063/1.2207885

Pe'Er A., Zhang B.-B., Ryde F., McGlynn S., Zhang B., Preece R. D., Kouveliotou C., 2012, MNRAS, 420, 468

Pe'er A., 2008, ApJ, 682, 463

Pe'er A., Casella P., 2009, ApJ, 699, 1919

Pe'er A., Waxman E., 2004a, ApJ, 613, 448

Pe'er A., Waxman E., 2004b, ApJ, 613, 448

Pe'er A., Waxman E., 2005, ApJ, 633, 1018

Pe'er A., Mészáros P., Rees M. J., 2005, ApJ, 635, 476

Pe'er A., Ryde F., Wijers R. A. M. J., Mészáros P., Rees M. J., 2007, ApJ, 664, L1

Pelassa V., Preece R., Piron F., Omodei N., Guiriec S., Fermi LAT Collaboration Fermi GBM Collaboration 2010, preprint, p. Proceedings for the 2009 Fermi Symposium. eConf Proceedings C091122 (arXiv:1002.2617)

Pendleton G. N., et al., 1994, ApJ, 431, 416

Peng F.-K., Liang E.-W., Wang X.-Y., Hou S.-J., Xi S.-Q., Lu R.-J., Zhang J., Zhang B., 2014, ApJ, 795, 155

Perley D., 2015, The Swift GRB Host Galaxy Legacy Survey, Keck Observatory Archive MOSFIRE

Perley D. A., et al., 2009, ApJ, 696, 1871

Pilla R. P., Loeb A., 1998, ApJ, 494, L167

Piran T., 1995, preprint, pp astro–ph/9507114 (arXiv:astro-ph/9507114)

Piran T., 1999, physrep, 314, 575

Piran T., 2005, Rev. Mod. Phys., 76, 1143

Piran T., Sari R., 1998, in Meegan C. A., Preece R. D., Koshut T. M., eds, Vol. 428, Gamma-Ray Bursts, 4th Hunstville Symposium. pp 662–666, doi:10.1063/1.55395

Piron F., Ohno M., de Palma F., Moretti E., McEnery J., 2010, GRB Coordinates Network, 10450, 1

Planck Collaboration et al., 2018, arXiv e-prints, p. arXiv:1807.06209

Preece R. D., Briggs M. S., Pendleton G. N., Paciesas W. S., Matteson J. L., Band D. L., Skelton R. T., Meegan C. A., 1996, ApJ, 473, 310

Preece R. D., Briggs M. S., Mallozzi R. S., Pendleton G. N., Paciesas W. S., Band D. L., 2000, The Astrophysical Journal Supplement Series, 126, 19

Preece R. D., Briggs M. S., Giblin T. W., Mallozzi R. S., Pendleton G. N., Paciesas W. S., Band D. L., 2002, ApJ, 581, 1248

Pugliese V., Xu D., Tanvir N. R., Wiersema K., Fynbo J. P. U., Milvang-Jensen B., D'Elia V., 2015, GRB Coordinates Network, 17672, 1

Qin Y.-P., Zhang Z.-B., Zhang F.-W., Cui X.-H., 2004, ApJ, 617, 439

Qin Y. P., Gupta A. C., Fan J. H., Lu R. J., 2008, Journal of Cosmology and Astro-Particle Physics, 2008, 004

Racusin J. L., Kocevski D., 2016a, GRB Coordinates Network, 19902, 1

Racusin J. L., Kocevski D., 2016b, GRB Coordinates Network, 19902, 1

Racusin J. L., Axelsson M., Yassine M., Kocevski D., 2015, GRB Coordinates Network, 17806, 1

Rao A. R., et al., 2011, ApJ, 728, 42

Ravasio M. E., Oganesyan G., Ghirlanda G., Nava L., Ghisellini G., Pescalli A., Celotti A., 2018, A&A, 613, A16

Razzaque S., Mészáros P., Waxman E., 2004, prd, 69, 023001

Rees M. J., Mészáros P., 1993, in Friedlander M., Gehrels N., Macomb D. J., eds, Vol. 280, American Institute of Physics Conference Series. pp 987–991, doi:10.1063/1.44213

Rees M. J., Mészáros P., 2005, ApJ, 628, 847

Rees M. J., Mészáros P., 1992, MNRAS, 258, 41

Rees M. J., Mészáros P., 1994a, ApJ, 430, L93

Rees M. J., Mészáros P., 1994b, ApJ, 430, L93

Reichart D. E., 1997, ApJ, 485, L57

Reichart D. E., Lamb D. Q., Fenimore E. E., Ramirez-Ruiz E., Cline T. L., Hurley K., 2001, ApJ, 552, 57

Riess A. G., Casertano S., Yuan W., Macri L. M., Scolnic D., 2019, arXiv e-prints, p. arXiv:1903.07603

Roming P. W. A., et al., 2005, ssr, 120, 95

Romoli C., Taylor A. M., Aharonian F., 2017, Astroparticle Physics, 88, 38

Rosswog S., Ramirez-Ruiz E., Davies M. B., 2003, MNRAS, 345, 1077

Ruderman M., 1975, in Bergman P. G., Fenyves E. J., Motz L., eds, Vol. 262, Seventh Texas Symposium on Relativistic Astrophysics. pp 164–180, doi:10.1111/j.1749-6632.1975.tb31430.x

Ruderman M. A., Sutherland P. G., 1975, ApJ, 196, 51

Ryde F., 2004, ApJ, 614, 827

Ryde F., 2005, in 22nd Texas Symposium on Relativistic Astrophysics. pp 65–69 (arXiv:astro-ph/0504539)

Ryde F., Pe'Er A., 2009, in Meegan C., Kouveliotou C., Gehrels N., eds, Vol. 1133, American Institute of Physics Conference Series. pp 312–316, doi:10.1063/1.3155908

Ryde F., Petrosian V., 2002, ApJ, 578, 290

Sakamoto T., et al., 2004, in Fenimore E., Galassi M., eds, Vol. 727, Gamma-Ray Bursts: 30 Years of Discovery. pp 106–110 (arXiv:astro-ph/0309455)

Sakamoto T., et al., 2005, ApJ, 629, 311

Sakamoto T., et al., 2006, ApJ, 636, L73

Sakamoto T., et al., 2008a, The Astrophysical Journal Supplement Series, 175, 179

Sakamoto T., et al., 2008b, ApJ, 679, 570

Sakamoto T., et al., 2009, ApJ, 693, 922

Sakamoto T., et al., 2011, The Astrophysical Journal Supplement Series, 195, 2

Salafia O. S., Ghisellini G., Ghirlanda G., Colpi M., 2017, preprint, p. arXiv:1711.03112 (arXiv:1711.03112)

Salmonson J. D., 2000, ApJ, 544, L115

Sanchez-Ramirez R., Gorosabel J., Castro-Tirado A. J., Cepa J., Gomez-Velarde G., 2013, GRB Coordinates Network, 14685, 1

Sari R., 1999, ApJ, 524, L43

Sari R., Piran T., 1997, MNRAS, 287, 110

Sari R., Piran T., 1999a, ApJ, 517, L109

Sari R., Piran T., 1999b, ApJ, 520, 641

Sari R., Narayan R., Piran T., 1996, ApJ, 473, 204

Sari R., Piran T., Narayan R., 1998, ApJ, 497, L17

Savchenko V., et al., 2013, GRB Coordinates Network, 15259, 1

Schaefer B. E., 2004, ApJ, 602, 306

Schaefer B. E., et al., 1992, ApJ, 393, L51

Schmidt W. K. H., 1978, Nat, 271, 525

Schulze S., Wiersema K., Xu D., Fynbo J. P. U., 2014, GRB Coordinates Network, 15831, 1

Shemi A., Piran T., 1990, ApJ, 365, L55

Shen R.-F., Song L.-M., Li Z., 2005, MNRAS, 362, 59

Siegel D. M., Ciolfi R., 2016, ApJ, 819, 14

Sonbas E., Racusin J. L., Kocevski D., McEnery J., 2013, GRB Coordinates Network, 15640, 1

Sonbas E., Vianello G., Longo F., 2014, GRB Coordinates Network, 15659, 1

Spruit H. C., Daigne F., Drenkhahn G., 2001, A&A, 369, 694

Stamatikos M., 2009, preprint, (arXiv:0907.3190)

Stanek K. Z., et al., 2003, ApJ, 591, L17

Starling R. L. C., et al., 2011, MNRAS, 411, 2792

Stratta G., et al., 2013, ApJ, 779, 66

Strong I. B., 1975, International Cosmic Ray Conference, 1, 237

Strong I. B., Klebesadel R. W., 1974, in Bulletin of the American Astronomical Society. p. 270

Strong I. B., Klebesadel R. W., Olson R. A., 1974, ApJ, 188, L1

Tajima H., Bregeon J., Chiang J., Thayer G., 2008, GRB Coordinates Network, 8246, 1

Tanaka Y., Ohno M., Takahashi H., Uehara T., Omodei N., Chiang J., Guiriec S., 2010, GRB Coordinates Network, 10978, 1

Tang Q.-W., Peng F.-K., Wang X.-Y., Tam P.-H. T., 2015, ApJ, 806, 194

Tanvir N. R., et al., 2009, Nat, 461, 1254

Tanvir N. R., Levan A. J., Fruchter A. S., Hjorth J., Hounsell R. A., Wiersema K., Tunnicliffe R. L., 2013, Nat, 500, 547

Tavani M., 1996, ApJ, 466, 768

Tavani M., 1997, ApJ, 483, L87

Tavani M., et al., 2008, Nuclear Instruments and Methods in Physics Research A, 588, 52

Tavani M., et al., 2009, Nat, 462, 620

Tello J. C., Sanchez-Ramirez R., Gorosabel J., Castro-Tirado A. J., Rivero M. A., Gomez-Velarde G., Klotz A., 2012, GRB Coordinates Network, 13118, 1

Thompson C., 1994, MNRAS, 270, 480

Thompson D. J., et al., 1993, The Astrophysical Journal Supplement Series, 86, 629

Tierney D., et al., 2013, A&A, 550, A102

Tikhomirova Y. Y., Stern B. E., 2005, Astronomy Letters, 31, 291

Tsutsui R., Yonetoku D., Nakamura T., Takahashi K., Morihara Y., 2013, MNRAS, 431, 1398

Uhm Z. L., Zhang B., 2016, ApJ, 825, 97

Usov V. V., 1992, Nat, 357, 472

Usov V. V., 1994, MNRAS, 267, 1035

Vasileiou V., Omodei N., Chiang J., Vianello G., Kocevski D., Racusin J., 2011, GRB Coordinates Network, 11835, 1

Vianello G., Kocevski D., 2012, GRB Coordinates Network, 13379, 1

Vianello G., Kocevski D., 2017, GRB Coordinates Network, 20987, 1

Vianello G., Omodei N., Racusin J., Ohno M., 2013, GRB Coordinates Network, 15472, 1

Vianello G., Gill R., Granot J., Omodei N., Cohen-Tanugi J., Longo F., 2018, ApJ, 864, 163

Vietri M., 1997, ApJ, 478, L9

Virgili F. J., Qin Y., Zhang B., Liang E., 2012, MNRAS, 424, 2821

Wang X.-Y., Li Z., Mészáros P., 2006, ApJ, 641, L89

Waxman E., 1997, ApJ, 489, L33

Wei D. M., Gao W. H., 2003, MNRAS, 345, 743

Wiersema K., de Ugarte Postigo A., Levan A., 2009, GRB Coordinates Network, 9250, 1

Wijers R. A. M. J., Galama T. J., 1999, ApJ, 523, 177

Wijers R. A. M. J., Rees M. J., Mészáros P., 1997, MNRAS, 288, L51

Willingale R., et al., 2007, ApJ, 662, 1093

Wilms J., Allen A., McCray R., 2000, ApJ, 542, 914

Wilson C., Connaughton V., Longo F., Omodei N., 2008, GRB Coordinates Network, 8723, 1

Woods E., Loeb A., 1995, ApJ, 453, 583

Woosley S. E., 1993, ApJ, 405, 273

Woosley S. E., Bloom J. S., 2006, Annual Review of Astronomy and Astrophysics, 44, 507

Xu D D., Tanvir N., Kruehler T., Fynbo J., 2013, GRB Coordinates Network, 15450, 1

Yonetoku D., Murakami T., Nakamura T., Yamazaki R., Inoue A. K., Ioka K., 2004, ApJ, 609, 935

Yu H.-F., van Eerten H. J., Greiner J., Sari R., Narayana Bhat P., von Kienlin A., Paciesas W. S., Preece R. D., 2015, A&A, 583, A129

Yu H.-F., et al., 2016, A&A, 588, A135

Zhang B., 2005, in Bulik T., Rudak B., Madejski G., eds, Vol. 801, Astrophysical Sources of High Energy Particles and Radiation. pp 106–113 (`arXiv:astro-ph/0509571`)

Zhang F.-W., 2012, Ap&SS, 339, 123

Zhang B. B., Bhat N., 2014, GRB Coordinates Network, 15669, 1

Zhang B., Mészáros P., 2002, ApJ, 566, 712

Zhang B., Mészáros P., 2004, International Journal of Modern Physics A, 19, 2385

Zhang B., Mészáros P., 2004, International Journal of Modern Physics A, 19, 2385

Zhang B., Yan H., 2011a, ApJ, 726, 90

Zhang B., Yan H., 2011b, ApJ, 726, 90

Zhang B.-B., Zhang B., Liang E.-W., Wang X.-Y., 2009a, ApJ, 690, L10

Zhang B., et al., 2009b, ApJ, 703, 1696

Zhang B., et al., 2009c, ApJ, 703, 1696

Zhang B.-B., et al., 2011, ApJ, 730, 141

Zhang B., Lu R.-J., Liang E.-W., Wu X.-F., 2012, ApJ, 758, L34

Zhang B., Lü H.-J., Liang E.-W., 2016, ssr, 202, 3

Zhao X.-H., Li Z., Bai J.-M., 2011, ApJ, 726, 89

Zheng W., et al., 2012, ApJ, 751, 90

Zou Y.-C., Fan Y.-Z., Piran T., 2011, ApJ, 726, L2

Zou Y.-C., Cheng K. S., Wang F. Y., 2015, ApJ, 800, L23

Zrake J., 2014, ApJ, 794, L26

Zrake J., East W. E., 2016a, ApJ, 817, 89

Zrake J., East W. E., 2016b, ApJ, 817, 89

de Palma F., Omodei N., McEnery J., Vasileiou V., 2009, GRB Coordinates Network, 10163, 1

de Ugarte Postigo A., Thoene C. C., Gorosabel J., Sanchez-Ramirez R., Fynbo J. P. U., Tanvir N. R., Cabrera-Lavers A., Garcia A., 2013, GRB Coordinates Network, 15470, 1

van Paradijs J., et al., 1997, Nat, 386, 686

von Kienlin A., Bhat P. N., 2014, GRB Coordinates Network, 15796, 1

von Kienlin A., et al., 2014, The Astrophysical Journal Supplement Series, 211, 13